Contribution to the Numerical Study of Turbulence-Mass Transfer Interactions in Evaporating Two-Phase Flows

Marcos Martin Onofre Ramos

THÈSE

Pour l'obtention du grade de

DOCTEUR DE L'ÉCOLE NATIONALE SUPÉRIEURE

DE MÉCANIQUE ET D'AÉROTECHNIQUE

(Diplôme national — Arrêté du 25 mai 2016)

École doctorale :

Sciences et Ingénierie en Matériaux, Mécanique, Énergétique et Aéronautique

Secteur de recherche :

Énergétique, Thermique, Combustion

Présentée par :

Marcos Martín ONOFRE RAMOS

****

Contribution to the numerical study of turbulence-mass transfer interactions in evaporating two-phase flows

****

Directeur de thèse : **Arnaud MURA**

Co-encadrant : **Zakaria BOUALI**

****

Soutenue le 14 décembre 2021

devant la commission d'examen

****

Jury

Président :

M. Serge Simoëns — Directeur de recherche cnrs–lmfa

Rapporteurs :

M. Francesco Picano — Professeur université padoue

M. François-Xavier Demoulin — Professeur université de rouen

Membres du jury :

Mme. Veronique Fortune — Maître de conférences université de poitiers

M. Zakaria Bouali — Maître de conférences ensma, poitiers

M. Arnaud Mura — Directeur de recherche cnrs–pprime

Tener éxito es equivocarte en tus propios términos, porque es llegar a donde quieres haciendo lo que quieres.

Guillermo del Toro.

«De parvis grandis acervus erit»

Acknowledgement

A mi madre, Sra. Emilia Evangelina Ramos Andreani, quien me ha llenado de amor y ha sido no solamente mi maestra de vida, sino también mi apoyo incondicional en todas y cada una de las decisiones en mi vida.

A mi padre, Sr. José Martín Onofre Muñoz, quien sé estaría muy orgulloso de ver el hombre y profesionista en quien me he convertido.

A mi hermano, Erick Heberto Onofre Ramos, quien siempre me apoya y sabe escuchar.

A mi abuela, Sra. Ernestina Andreani Yardela, de quien aprendí que no hay nada más satisfactorio que el trabajar en lo que uno ama.

J'adresse ma profonde gratitude à mon directeur de thèse Arnaud Mura et mon co-encadrant Zakaria Bouali , sans qui, ce voyage d'apprentissage, de découverte de soi et de maturation n'aurait jamais eu lieu. Je n'oublierai jamais les leçons de vie personnelle et professionnelle apprises, ni leur disponibilité pour les moments de doute. Je suis infiniment reconnaissant pour les conseils fournis au cours du doctorat, ainsi que l'autonomie que m'a permis de mener ma recherche. Je me souviendrai toujours de toutes les expériences que nous partageons, qui, sans aucun doute, auront un impact permanent sur ma carrière de chercheur et ma vie.

Mes remerciements ensuite à MM. Vincent Robin et Yves Gervais de m'avoir accueilli dans le département Fluides, Thermique, Combustion de l'Institut Pprime.

Je souhaite remercier le personnel de l'ENSMA pour son accueil chaleureux. À cet égard, je tiens à exprimer ma reconnaissance à Jocelyne, Isabelle, Marie-Cannelle,

Audrey, Céline, Corinne et Valerie, pour les efforts qu'elles réalisent afin d'offrir les meilleures conditions de travail.

I would like to extend my thanks especially to Josué Melguizo Gavilanes, Armando Oropeza Osornio, Armando Estrada Parra, Mauricio Torres Arellano, Abraham Medina Ovando, Alfredo Arias Montaño, Francisco Castillo Acosta and Oliver Huerta Chávez, who apart from being a deep inspiration, have become invaluable and dear friends, who always have cared about my personal and professional development.

My gratitude also goes to those who have been my office colleagues and friends : Luis, Song, Nguyen, Francesco, Fabio, Anthony and Xiadong . First of all for their welcome, but above all for the many scientific and personal discussions we had during this journey. I also express my thanks to all the doctoral students (former and current) of the P 'institute : Camille, Gabriel, Gad, Jorge, Melissa, Ožbej, Said, and all the *"thésards"* from the ADDICT who have become dear friends. Thank you all for the excellent moments shared. I do not want to lose the opportunity to mention my dear friends Carlos, Alisson, Hamadi, Lina, Laura, Evgeniia, Irina, Lamia, Cveta, Marion, Diego, Maksym, Bastian, and Attila ; whom I met outside the doctoral environment and which I have forge a nice friendship. There are also my friends whom the geographical distance has not discouraged to follow the progress of my thesis. I have a thought for Abel García, Alfonso Olvera, Arqueles Estrada, Arturo Sánchez, Bryan Sánchez, Carlos Brena, Emilio García, Fernanda Salinas, Gabriela Meneses, Karen Aguilar, Marcelino Soto, Paola Espíndola, Rafael Trujillo, Ricardo Ruíz and their families, with whom I have lived many of the best moments of my life and who always support and encourage me to pursuit and follow my goals.

To all my former teachers, former school-and-work colleagues, and all those who have contributed something good or bad in both my professional and personal life, I thank you, because without the sum of each and every one of those experiences, I would not be the human being and professional of today.

Last but not least, I would like to recognize the invaluable economical support from CONACyT (Consejo Nacional de Ciencia y Tecnología), that was a milestone in the completion of this thesis project through the scholarship CVU622998.

le 14 décembre 2021
Marcos ONOFRE

Contents

Nomenclature

For the sake of brevity, we only report here the notations used continuously in the manuscript (the others will be presented as and when they are used).

Acronyms

ARCHER	Academic Research Code for Hydrodynamic Equations Resolution
CFD	Computational Fluid Dynamics
CLSVOF	Coupled level-set/volume-of-fluid method
CPU	Central Processing Unit
DNS	Direct Numerical Simulation
GFM	Ghost-Fluid Method
HIT	Homogeneous Isotropic Turbulence
JPDF	Joint Probability Density Function
LEE's	Lagrangian Evolution Equations
LS	Level-set
MCT's	Mean Conditional Trajectories
MPI	Message Passing Interface
PDF	Probability Density Function
RANS	Reynolds Average Navier–Stokes Simulation
RMS	Root Mean Square
SDR	Scalar Dissipation Rate
TSI	Turbulence-Scalar-Interaction
VGT	Velocity Gradient Tensor
VOF	Volume of fluid
W(ENO)	Weighted (Essentially Non-Oscillatory)

Non-dimensional numbers

Re	Reynolds number (inertia / viscosity)
We	Weber number (inertia / surface tension)

Operators

$\overline{f}$	Average in the sense of Reynolds
$\widetilde{f}$	Average in the sense of Favre

Exponents

$(.)'$	Fluctuation in the sense of Reynolds
$(.)''$	Fluctuation in the sense of Favre
$(.)^T$	Transposed
$(.)_0$	Initial value of the preliminary convergence phase
$(.)_1$	Final value of the preliminary convergence phase

Symbol Definitions

Roman letters

A_{ij}, $\boldsymbol{A}$	Velocity gradient tensor
A^*_{ij}, $\boldsymbol{A}^*$	Traceless velocity gradient tensor
b_{ij}	Normalized (traceless) Reynolds stress anisotropy tensor
B	Forcing coefficient
$\boldsymbol{D}$	Viscous deformation tensor
$\mathcal{D}$	Mixture fraction molecular diffusivity
$\boldsymbol{e}_i$	Eigenframe of the strain-rate tensor
f	Source term to induces linear forcing, $f = C\boldsymbol{u}'_{\boldsymbol{i}}$
G	Level-set function
h	Mass enthalpy
$\boldsymbol{I}$	Identity tensor
$\mathcal{L}_t$	Integral space scale
$\boldsymbol{n}$	Normal unit vector pointing towards the liquid phase, $\boldsymbol{n} = \boldsymbol{\nabla} G / \lvert \boldsymbol{\nabla} G \rvert$
$\boldsymbol{\nabla} \cdot \boldsymbol{n}$	Curvature evaluated from the level set function, $k(G)$
$\boldsymbol{n}_\xi$	Scalar gradient vector, $\boldsymbol{n}_{\xi_i} = \boldsymbol{\nabla} \xi = \xi_{,i}$
N_ξ	Scalar dissipation rate (SDR), $N_\xi = 2\mathcal{D} \boldsymbol{\nabla} \xi \boldsymbol{\nabla} \xi = 2\mathcal{D} \xi_{,i} \xi_{,i}$
$P(\,)$	PDF in graphs
$P_{\boldsymbol{A}}$	First invariant of the VGT
$P^*_{\boldsymbol{A}}$	First invariant of the traceless VGT
$P_{\boldsymbol{S}}$	First invariant of the strain-rate tensor
$P^*_{\boldsymbol{S}}$	First invariant of the traceless Strain rate tensor
$Q_{\boldsymbol{A}}$	Second invariant of the VGT
$Q^*_{\boldsymbol{A}}$	Second invariant of the traceless VGT
$Q_{\boldsymbol{S}}$	Second invariant of the strain-rate tensor
$Q^*_{\boldsymbol{S}}$	Second invariant of the traceless strain-rate tensor
$Q_{\boldsymbol{\Omega}}$	Second invariant of the rotational-rate tensor
$Q^*_{\boldsymbol{\Omega}}$	Second invariant of the traceless rotational-rate tensor
$R_{\boldsymbol{A}}$	Third invariant of the VGT
$R^*_{\boldsymbol{A}}$	Third invariant of the traceless VGT
$R_{\boldsymbol{S}}$	Third invariant of the strain-rate tensor
$R^*_{\boldsymbol{S}}$	Third invariant of the traceless strain-rate tensor
p	Fluid pressure
$\boldsymbol{S}$, S_{ij}	Symmetric part of $\boldsymbol{A}$, strain rate tensor
$\boldsymbol{S}^*$, S^*_{ij}	Traceless strain-rate tensor
$\boldsymbol{S}_\xi$	Segregation rate of the mixing fraction xi
$\mathcal{T}$	Kurtosis coefficient
t	Physical time
t^+	Normalized time for statistics without evaporation, $t^* = t - t_0 / \tau_{T_0}$
t^*	Normalized time for statistics with evaporation, $t^* = t - t_1 / \tau_{T_1}$
$\boldsymbol{u}$, u_i	Component of the velocity following the i direction
ΔU	Accumulated RMS

$\mathcal{RMS}$	Root mean square, $U = (2/3\kappa)^{1/2}$, with κ the TKE
x_i	Cartesian coordinate following the *i th* direction
Y_v	Level of vapor mass fraction
Y_{vs}	Saturation level of vapor mass fraction
ξ	Mixing rate, passive scalar

Greek letters

δ_{ij}	Dirac delta
ϵ_{ijk}	Levi-Civita or permutation symbol
ε	Turbulent dissipation rate
η^*	Normalized third invariant of b_{ij}
η_K	Kolmogorov spatial scale
κ	TKE
λ	Taylor length scale
λ_i	Eigenvalues of A_{ij}
$\dot{\lambda}_i$	Normalized eigenvalues of A_{ij}, $\dot{\lambda}_i = \lambda_i \nu \eta_K^{-2}$
μ	Molecular dynamic (shear) viscosity
ν	Molecular kinematic viscosity
ξ	Normalized passive scalar, i.e., mixture fraction
ξ^*	Normalized second invariant of b_{ij}
ρ	Density
σ	Surface tension force
τ_{ij}	Tensor of viscous stresses
τ_K	Kolmogorov time scale
τ_λ	Taylor time scale
τ_T	Turbulent time scale
Ψ	Sum of the TSI contributions, $\Psi = \sum_{i=1}^{i=3} \lambda_i \cos^2\left(\boldsymbol{n}_{\tilde{\xi}_i}, \boldsymbol{e}_i\right)$
ϕ	Fraction of liquid
$\boldsymbol{\omega}$	Vorticity of the velocity field
$\delta_{\boldsymbol{\omega}}$	Vorticity thickness
$\boldsymbol{\Omega}$, Ω_{ij}	Rotational-rate tensor
$\boldsymbol{\omega}_k$	Vorticity vector
$\dot{\boldsymbol{\omega}}_\xi$	Source term of vapor
$\boldsymbol{\nabla}$	Gradient operator

Turbulent Topologies

UF/C	*unstable-focus compressing*
SF/S	*stable-focus stretching*
SN/S/S	*stable-node saddle-saddle*
UN/S/S	*unstable-node saddle-saddle*

1 Introduction

Content of the chapter

« La semplicità è la sofisticatezza finale »
This famous quote from Leonardo Da Vinci denotes the spirit of this thesis.

1.1 State of the art

1.1.1 Brief review of fluid mechanics and combustion science

Fluid mechanics and combustion science have been played a central role in human life since the oldest *"river"* civilizations like Mesopotamia, Egypt, China, just to mention a few. In the one hand, fluid mechanics is the branch of physics concerned to the study of how fluids behave in steady, transitional and fully unsteady motion. Some of the most prominent scientists and philosophers from the ancient Greece were the first to attempt to formally conceptualize certain fluids characteristics and their motions (Tokaty [103]), so for example Aristotle used for the first time the *"continuity principle"* and developed a distinction between natural and forced motion,

Archimedes based the actual fluid statics, and Hero of Alexandria invented the *"Herons Reactive Motor"*, which is considered the father of actual jet, rocket and turbine engines. Some centuries after, one of the most prominent Italian scientist of the renaissance period, Leonardo Da Vinci, gave the mathematical and physical basis to the concept of continuity, and was the first to point out a distinction between the physical and mathematical concept of point. Later, the Swiss mathematician Leonhard Paul Euler introduced the basic concepts of the modern fluid mechanics developing the concept of fluid particle, and deducing : i) the differential equation of the streamline, ii) the law of mass conservation, and iii) the differential equations of continuity and of fluid motion for potential (non-viscous) flows. Then, the first attempt to mathematically describe the motion of viscous fluids was made by the french engineer and physicist Claude-Louis Navier and the Anglo-Irish physicist and mathematician George Gabriel Stokes. Together with the deduction of the Navier-Stokes equations and the contributions of the Irish engineer and physicist Osborne Reynolds, see Fig. 1.1 : i) the non-dimensional Reynolds number (Re), and ii) the discovery of the laminar and turbulent modes of fluids flow ; the turbulence research field was formally created.

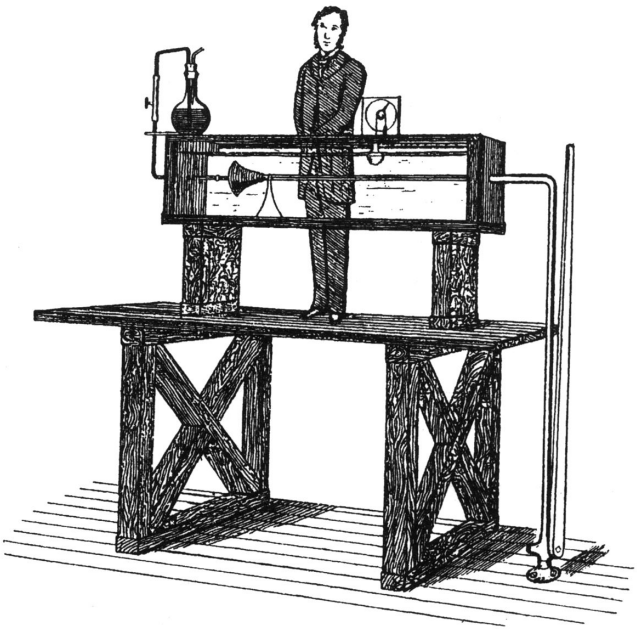

Figure 1.1. *Sketch of Osborne Reynolds and his fluid turbulence experiment from 1883*

On the other hand, in regards to combustion science, maybe the earliest scientific attempt to define the concept of *"combustion"* was made by the Flemish physicist and alchemist Johannes Baptista van Helmont, as he understood that there are gases of different nature from atmospheric air while he studied the combustion process of charcoal, and observing the interaction among the fuel, oxidizer (atmosphere)

and flame/heat; so he stated that combustion involves the escape of a "wild spirit" (spiritus silvestre), i.e., smoke/soot from the fuel-oxidizer interaction (Harris [46]). With this experiment he discovered the carbon dioxide (CO_2), and introduced the word *gas* to the scientific language. Nevertheless, modern combustion science was founded by the french chemist Antoine Laurent Lavoisier, so when he studied : i) the phosphoric acid production, and ii) the calcination of sulfates; which at the end of the process gain weight due to the absorption of carbon dioxide. This discovery also gathered him the title of *"father of modern Chemistry"* (Kohler [56]). Even though combustion science has had an important role in human civilizations, its research and development was strongly encouraged during the 19^{th} century owing to different facts : i) the demand for power issued for the industrial revolution, ii) scientist started to understand the key concepts upon which the internal combustion engine was built, and iii) the fuel needed to power the engine was becoming available in large amounts.

In 1862 the Belgian inventor Jean-Joseph Etienne Lenoir invented the world first automobile using an engine invented by himself. Then in 1876, the German engineer Nicolaus August Otto, after several years of experimentation with the Lenoir motor, invented the first "Otto" four-stroke engine which ran on petroleum gas and used a timed spark plug-ignition. From the contributions of Otto, the next challenge was to use liquid fuels, since then, spray and vaporization processes become central subjects of study for engineers. At the end of the 19^{th} century, three different processes were invented to accomplish this task : i) carburetor, ii) hot bulb vaporization, and iii) diesel engine, see Fig. 1.2; this last one was introduced in 1897 by the German engineer Rudolf Christian Karl Diesel (Sass [86]).

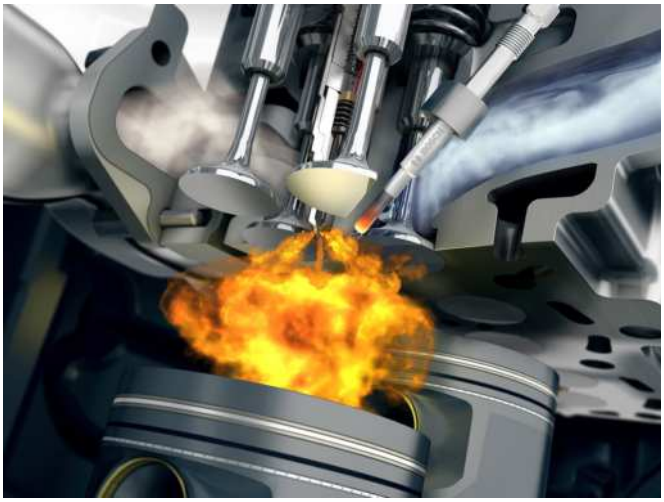

Figure 1.2. *Schematic of a Diesel engine performing combustion*

1.1.2 Direct numerical simulation (DNS) of turbulent flows

Since the contributions of Leonhard Paul Euler and until the second half of the twentieth century, experimental and theoretical approaches were the only possible approaches to tackle the problems posed by the fluid mechanics. The first calculation of a practical turbulent flow was achieved by Prandtl (1925) [80], when the mixing length concept was introduced, and with which the eddy viscosity was successfully determined ; but the emergence in the 1960_s of the Computational Fluid Dynamics (CFD) supposed a game-changer in the field, see Fig. 1.3 [1] [2]. This relative-new third approach to the study and development of fluid mechanics was made possible thanks to the merge of the improvements in memory capacity and computational speed of computers achieved in the 1950_s, together with the development of numerical methods and algorithms, so CFD consist on taking advantage of the significant amount of calculations that computers can perform in a relative short time, implementing in them several numerical algorithms as programs, so together can tackle fluid flow problems. The first proper CFD solvers were presented at the 1968 Stanford conference on computation of turbulent boundary layers [20], and at the 1968 NASA symposium on compressible turbulent boundary layers organized at Langley research center [68]. The solvers presented at those conferences worked by discretizing Reynolds stress transport models, i.e., were based on the Reynolds-averaged Navier-Stokes (RANS) modeling framework, but unfortunately (for research purposes), the solutions of the ensemble-averaged equations provided by RANS approach were lacking of information on the unsteady features of the flow i.e., real transition and turbulence phenomena cannot be studied in detail by this mean. Nevertheless, advanced CFD modeling frameworks were developed to overcome the limitations that RANS framework presents : i) large eddy simulation (LES), proposed by Smagorinsky (1963) [91], and firstly explored by Deardorff (1970) [22] ; where the large scale motions (large eddies) of turbulent flow are computed directly and only the sub-grid scale (SGS) motions are modeled, and ii) direct numerical simulations (DNS), which foundations were laid by Douglas and Douglas (1972) [24] (researches at the National Center for Atmospheric Research), where no turbulence model is taken into account, which means that the whole range of spatial and temporal scales of the turbulence must be resolved. LES and DNS have opened new opportunities to simulate fluid flows with higher fidelity and to investigate physical insights of many complex flow systems that are very difficult to obtain and/or to measure at the laboratory, such as : spray,

1. By Jitze Couperus-Flickr : Supercomputer-The Beginnings, CC BY 2.0, https://commons.wikimedia.org/w/index.php?curid=19382150
2. By Penalva-Own work, CC BY-SA 4.0, https://commons.wikimedia.org/w/index.php?curid=47918630

atomization, evaporation and combustion.

Figure 1.3. *On the left side the supercomputer CDC 6600 with its console, launched in 1964, and on the right side the supercomputer Occigen installed by GENCI at CINES, in Montpellier ; with which the databases presented in this thesis where obtained.*

In regards to combustion science, during the first half of the 20^{th} century, by means of theoretical and experimental advances, big progress on regards to improve the Otto and Diesel engines were achieved, even the first jet engine was introduced in 1936 by the German physicist Joachim Pabst von Ohain, when he designed the first operational jet aircraft, the **Heinkel He** 178, and only eight years after, by the end of the 2^{nd} World War, the deutsche Luftwaffe put in operation the first jet-powered fighter aircraft, the **Messerschmitt Me** 262. Even though the improvement and/or creation of new-and-more efficient and reliable internal combustion engines have strongly boosted the research field of combustion science, it is paramount to point out that it was not possible to employ CFD-DNS tools to perform proper research in the combustion field until the 1990_s ; this is due to the fact that in any combustion process, several phenomena of : i) chemical kinetics, ii) thermochemistry, iii) transport (molecular diffusion coefficients of species and diffusivity of heat), and iv) fluid mechanics. All these phenomena take place simultaneously and interact between them in complex ways, which –numerically speaking– is very difficult to take into account all together, therefore CFD codes that simulate combustion are pretty different from those used to study internal and external non-reactive flows.

In this context, even laminar flame codes can easily become pretty complex, so it is only necessary to recall that even for the most common fuel models like : methane (CH_4), octane (C_8H_{18}) and kerosene $(C_{12}H_{26})$; when burned in presence of air $(O_2 + 3.76N_2)$, due to the high temperatures reached at the flame front $\left(\delta_l^0 \sim 10e^{-4}\,[m]\right)$: i) thousands of chemical reactions take place, and ii) hundreds of chemical species are created (Westbrook et al. [111]).

On the other hand, turbulent flames happen more commonly in real life. In this

respect, the first DNS research studies were devoted to :

- flamelets in premixed turbulent combustion by Girimaji and Pope (1992) [39]
- passive scalar mixing by Pumir (1994) [82], Jaberi et al. (1996) [50], Overholt and Pope (1996) [76], and Juneja and Pope (1996) [53]

Nevertheless, for industrial applications, the confined turbulent flames become the subject of study due to the necessity to recover heat and transform it into mechanical work, which in turn not only turbulence add complexity to the physics of the system, but also do : radiation, acoustics, heat transfer, fluid/structure interaction and the coupling of multi-physics ; among extra numerical and computational difficulties, i.e., suited computational algorithms for complex domain discretization. The sum of all this multi-physics requires the use of models in the industrial/engineering CFD codes (i.e., RANS and some LES). Nonetheless, these models are obtained by studying experimentally and numerically (i.e., some LES and DNS) specific aspects of canonical flames.

1.1.3 Challenges in DNS of multi-phase turbulent mixing flows

At this point is important to remember that, in practice, the systems based on non-premixed or partially-premixed combustion modes are strongly preferred due to their transport and storage safety advantages, although they do offer lower efficiency than premixed systems. This fact makes the micro-mixing processes, i.e., interaction between turbulence and scalar field, a key ingredient to characterize and to model properly the mixture fraction field (i.e., the composition of the fresh mixture). When the fuel enters in liquid state in non-premixed and partially-premixed systems (i.e., internal combustion engine), the possible influence of mass transfer between the two phases (i.e., evaporation) becomes also a key issue to study from both research and technical viewpoints. However, atomization and evaporation processes such as those which takes place in automotive, aeronautical and space engines are remarkably difficult to study experimentally due to the complex multi-physics coupling that happens in the combustion chamber (Faeth [31]), so here is where DNS of turbulent multi-phase flows has become a powerful tool to tackle these problematic.

In regard to the DNS framework, is important to bear in mind that it has been thought to resolve the turbulent length scales greater or equal to the Kolmogorov length scale η_K, and this point poses a big deal when multi-phase turbulent mixing flows are intended to be resolved with this framework. Firstly, when there exist deformable droplets in movement with a length scale smaller than the Kolmogorov length scale η_K of the carrier fluid, then it is currently impossible to fully resolve the motion

of the dispersed phase, so in order to overcome this limitation, phenomenological models (like those used in the RANS and LES approaches), are used to compute the deformation of the dispersed phase. Such phenomenological models are discussed by e.g., Elghobashi (2019) [28].

Moreover, to resolve the deforming interfaces of the liquid clusters with a characteristic length larger than the Kolmogorov length scale η_K of the carrier fluid, three approaches has been developed and successfully implemented into DNS codes :

- Tracking points : consist in to treat the interface through marked points advected by the flow, as in the front tracking method (FTM) developed by Unverdi and Tryggvason (1992) [106]
- Tracking scalar functions : consist in to numerical methods that track a specific scalar function, so there exist :
  - The volume of fluid (VOF) method ; where the volume fraction of the local phase of both sides of the interface is the relevant scalar function. The VOF method foundations were posed by Noh and Woodward (1976) [69]. An introductory-level review of this method have been written by Scardovelli and Zaleski (1999) [87]
  - The level-set method ; where the signed distance between any point of the computational domain and the zero iso-contour. i.e., the interface, is the relevant scalar function (Sussman et al. [98])
  - The lattice Bolzmann method (LBM) ; where the probability density function, $f_i^n(\mathbf{x},t)$, of finding a fluid particle of fluid phase n at position $\mathbf{x}$, at time t, and moving in one of the discretized i^{th} lattice velocity directions ; is the relevant scalar function (Shan and Chen [88])
  - The phase-field model (PFM) ; where the scalar phase field, i.e., the order parameter, $\gamma(\mathbf{x},t)$, is the relevant scalar function. Here γ represents a physical property of the mixture. In contrast to the previous methods (VOF, level-set & PFM), here a continuum model of $f(\gamma)$ replaced the surface tension forces (Jacqmin [51]). The PFM foundations were posed in the work of Cahn and Hilliard (1959) [10]
- Immersed boundary method (IBM) : consist in establish interaction equations, by the Dirac delta function, among an Eulerian and Lagrangian set of variables, so the numerical scheme of the method uses two different meshes, the first one is a fixed Cartesian mesh (where the Eulerian variables are discretized), the second is a curvilinear mesh (where the Lagrangian variables are discretized) ; the movement of the curvilinear mesh is not constrained in any way to adapt

to the fixed Cartesian mesh. This method was originally thought for the numerical simulation of fluid–structure interaction. It was introduced by Peskin (1972) [78], but an IBM with an interaction potential model (IPM) for fully resolved deformable interfaces and membranes has been proposed by Spandan et al. (2017) [93], and has been used to study ellipsoidal bubbles in Taylor-Couette flow (Spandan et al. [94]).

1.1.3.1 Jet breakup and atomization

The process of jet breakup in internal combustion engines consist into injecting a certain quantity of fuel (sometimes oxidizer in space applications) as a turbulent liquid spray, mixed it with the carrier fluid (commonly the oxidizer) and then burn the fresh mixture in gaseous form ; in order to arrive at this gaseous state the liquid jet must breakup (i.e., split) into multiple liquid clusters and through atomization processes eventually become into droplets small enough so they will be able to release vapor into the carrier stream fluid, which will allow the combustion process to take place in the combustion chamber. At this point it is important to recall that the droplet size and droplet distribution are essential to predict accurately spray flames. The jet breakup phenomenon in spray combustion consist on four elementary processes interacting between them in complex ways (Jenny et al. [52]), through which combustion efficiency and combustion stability can be enhanced and maintained, and also through which pollutant emissions can be minimized :

- atomization
- spray dispersion
- evaporation and mixing
- combustion

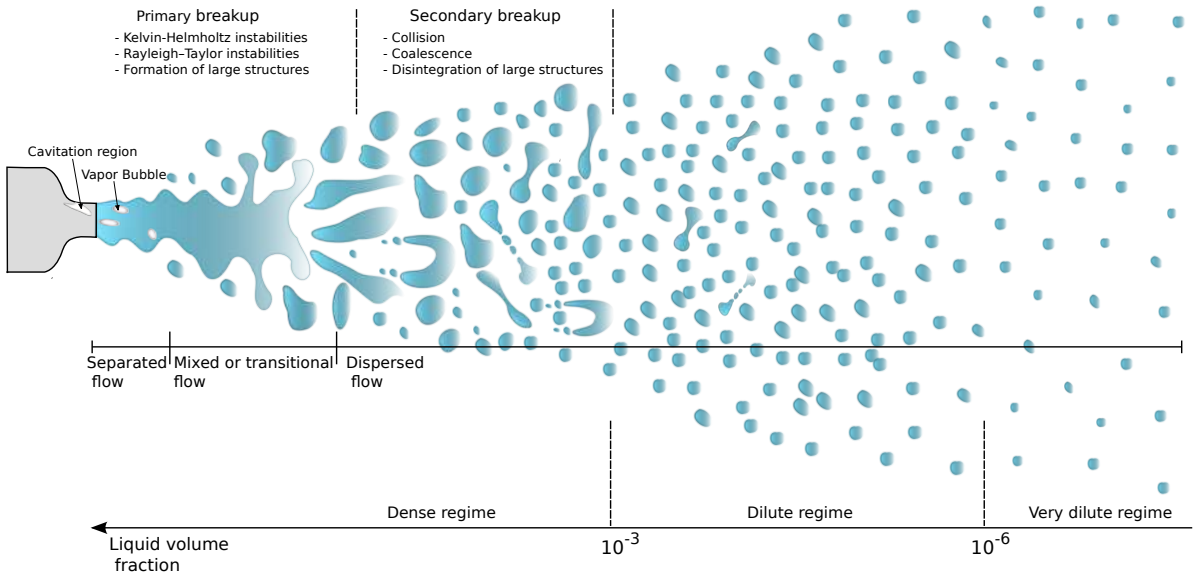

Figure 1.4. *Jet breakup phenomenon can be analyzed through three different viewpoints : in function of the atomization level, in function of the spray dispersion and in function of the liquid volume fraction* (ϕ_ℓ)

Figure 1.4 also shows that the spray can be divided into three distinct regimes based on the volume fraction occupied by the dispersed phase, i.e., ϕ_ℓ (Bouali et al. [7]) :

- dense regime $\left[\phi_\ell \geq 10^{-3}\right]$
- dilute regime $\left[10^{-3} < \phi_\ell > 10^{-6}\right]$
- very dilute regime $\left[\phi_\ell \leq 10^{-6}\right]$

Each regime enclose characteristic physical phenomena.

Dense regime

This regime is dominated by atomization phenomenon, which means that droplet collision and coalescence dominate the dynamics of the dispersed phase (Elghobashi and Truesdell [29]). Here both primary and secondary atomization take place (Jenny et al. [52]) :

- Primary atomization : consists on the disintegration of the liquid jet into large liquid clusters (i.e., droplets and strips called ligaments), due to Kelvin-Helmholtz instabilities developed at the liquid-gas interface when the jet is injected into the gaseous carrier stream, then eventually Rayleigh-Taylor instabilities develops. The interested reader may find useful information about pioneering and recent numerical works devoted to the spray region in the reviews of Gorokhovski and Herrmann (2008) [42] and Junji (2018) [54], respectively.
- Secondary atomization : is dominated by aerodynamic forces originated by the inter-facial velocity gradient, that provoke more instabilities and further

disintegration of the liquid structures formed at the primary breakup, resulting into even smaller droplets and ligaments. In this sense, Weber (1931) [110] proposed a well accepted breakup criterion of the secondary liquid clusters based on : i) the deformation time, and ii) the Weber number (We = *fluid's inertia / surface tension*) ; which is a meaningful dimensionless quantity when the characteristic length of the liquid bodies, i.e., diameter of the droplets, is larger than the Kolmogorov length scale η_K. Such number is briefly refereed below but widely explained by Zeoli and Gu (2006) [114] :

* bag breakup $[11 \leq We < 80]$
* stripping breakup $[80 \leq We < 350]$
* catastrophic breakup $[We > 850]$

Dilute and very dilute regimes

The very first and at the same time distinctive driving phenomenon of both dilute and very dilute regimes is dispersion. In this sense, and analogously to the *dense regime* (i.e., We number), the capillary number (Ca = *viscous forces / surface tension forces*) is the meaningful dimensionless quantity which is the base of the breakup criterion for the *dilute regime*. For an accurate computation of the *dilute regime*, a two-way coupling source term in the momentum equation must be taken into account, because the turbulence–statistics of the carried gas phase is influenced by the droplet velocity, and vice versa. In other words, turbulence modulation takes place, because the size of the liquid clusters is larger than the Kolmogorov length scale, so they alter the momentum and mass transport rates (Iliopoulos and Hanratty [49]), modifying the turbulence spectrum of the carried fluid through different mechanisms (Balachandar and Eaton [3]) such as :

- damping due to large liquid clusters (mostly droplets), which enhanced dissipation
- kinetic energy transfer from droplets to the carrier flow stream
- wakes and vortex generation behind the larger droplets

so the acceleration of the droplets attenuate the turbulence of the carrier fluid flow due to the energy taken from it, but the wakes generated by the large droplets enhance the turbulence of the continuous phase-flow (Zaichik and Pershukov [113]).

On the other hand, very far from the injector, the probability of liquid-liquid interactions become negligible. In those regions, the droplet characteristic size is very small, so the surface tension forces will become dominant and minimize the surface to its maximum, which has the effect to make the droplets practically spherical. Therefore, for accurately compute this regime, Lagrangian tracking methods must be

used to follow the dispersed phase, because the whole domain can be considered as a droplet-laden turbulent flow, as showed by Dodd and Jofre (2019) [23].

Vapor mixing

Now, for the *dense*, *dilute*, and *very dilute regimes*, there exist two phenomena that happen in all these three which, in turn, have a big impact on spray dynamics and combustion (Faeth [32]) :

- Droplet density : influence the local volume fraction occupied by the liquid clusters, which agglomerate in vortex fields, where the droplets of the dispersed phase change their inertial trajectory (Fessler et al. [34])
- Evaporation and micro-mixing : control the topology of the mixture-fraction field, so is the very key ingredient to control ignition and combustion in non-premixed and partially-premixed systems, because mixing happens at the molecular levels.

in this sense, Turbulence is such an enhanced mechanism to mixing, due to the improvement action that has over stirring, i.e., turbulent convection. The role played by stirring is to distort and increase the surface area of the scalar field interface (produced by evaporation).

It is paramount to mention that in the framework of spray combustion, it is common to assume that dense spray does not take place, but only *isolated* fuel droplets, i.e., droplets in low-or-non vapor concentration zones, so each droplet experience a rapid evaporation rate and the droplet-droplet interaction is negligible. Notwithstanding, Reveillon and Demoulin (2007) [83] have described two successive micro-mixing scenarios to this one (all three scenarios are naturally related to the droplet evaporation rates). The second takes place when regions of high vapor concentrations are formed, which happens because zones with the highest droplet density reach quickly a vapor concentration close to the saturation value, therefore the evaporation rate decrease dramatically fast almost up to zero. The third scenario consider that the vaporization of droplets can continue only if transport phenomena enter in to the game, either if turbulent mixing and diffusion translate vapor from droplet-cluster regions with high vapor concentrations, i.e., if they dilute the vapor concentration ; or, by effect of turbulence, the droplets are transported to a lower vapor concentration zone.

Mathematically, the mixture fraction ξ (the mixture of the released fuel vapor with the surrounding oxidizer), commonly is defined as a normalized mass fraction. This quantity is a key ingredient to model combustion properly : in diffusion flames it affects the reaction rate through the direct influence of the scalar dissipation rate (SDR, $N_{\tilde{\xi}}$) ; whereas in premixed flames it affects the propagation speed of the flame

through the direct influence of the local equivalence ratio.

At this point, it is important to specify that the consideration of *dilute* and *very dilute regimes* are beyond the scope of this thesis work, but the secondary atomization which takes place at the *dense regime* is the center of the study. The reader interested in numerical research on primary atomization may find further details in the work of Chein and Chung (1987) [13], Kalyan and William (1992) [55], Umemura (1994) [105], Sirignano (1999) [90], and Hasslberger et al. (2019) [47].

1.1.3.2 Recent numerical works

Nowadays, for the sake prioritizing safe storage and safe operating conditions, most of the industrial devices that perform two-phase flow combustion processes work under non-premixed or partially premixed conditions. In such cases, when turbulent regimes must be taken into account, it may be require the consideration of the mixture composition probability density function (PDF). However, for practicality, the composition of the mixture may be characterized thanks to a reduced set of scalar quantities including a mixture fraction variable, or fuel inlet tracer ξ, the marginal PDF of which is presumed from the knowledge of its first two moments by using a beta function. Thus, it seems necessary to consider specific additional modeling of the transport equations for the variance, $\widetilde{\xi}_v = \widetilde{\xi^2} - \widetilde{\xi}^2 = \widetilde{\xi''^2}$, and the mean, $\widetilde{\xi}$ of the mixture fraction, in order to obtain a more reliable turbulent combustion closure for two-phase flow conditions. The quantity $\widetilde{q} = \overline{\rho q}/\overline{\rho}$ denotes the Favre- or mass-averaged value of q, while $\overline{q}$ is its ensemble-averaged value. The scalar variance transport equation that characterizes the energy of composition fluctuations requires a specific closure to be proposed for the turbulent scalar dissipation rate (SDR) contribution, whereas the closure of the transport equation for the averaged mixture fraction value $\widetilde{\xi}$ does not pose any specific modeling difficulty. The SDR is defined by $\widetilde{\varepsilon}_\xi = \overline{\rho \mathcal{D} (\partial \xi''/\partial x_i)(\partial \xi''/\partial x_i)}/\overline{\rho}$ with $\mathcal{D}$ being the molecular diffusivity. In standard gaseous conditions, this quantity is often represented with a simplified algebraic closure, which implies the linear relaxation of the scalar fluctuations $\widetilde{\varepsilon}_\xi = \widetilde{\xi}_v/(C_\xi \tau_T)$ with τ_T a characteristic time scale of the turbulence and C_ξ a modeling constant (Gomet et al. [40]). Its relevance has been investigated for a wide variety of gaseous flows including conditions associated to high-speed flows (Buttay et al. [9]). The use of such a linear relaxation model (LRM) is quite appealing since it avoids the consideration of an additional modeled transport equation for the mean SDR (Gomet et al. [40]). However, it is rightful to question its validity for less standard configurations, such as the two-phase flow conditions featuring mass transfer through

vaporization considered herein. Such question is legitimate when attention is turned to the behavior of the leading-order terms present in the SDR transport equation including the turbulence-scalar interaction (TSI) term. The analysis of the TSI term already concentrate much effort in incompressible turbulence conditions, e.g., Gibson (1968) [38], Ashurst et al. (1987) [1], Ruetsch and Maxey (1991) [84], and Tsinober (2009) [104]. It has been recently extended to compressible flows by Buttay et al. (2016) [9] and Boukharfane et al. (2018) [8]; and it must also be emphasized that it has received considerable attention for premixed combustion conditions over the last ten years, e.g., Swaminathan and Chakraborty (2007) [99], Mura et al. (2008) [65], and Chakraborty et al. (2011) [12]. This is in contrast with the case of two-phase flows with mass transfer for which the SDR transport equation and associated TSI term were more seldom analyzed by Bouali et al. (2016) [6] and Zhao et al. (2020) [116].

1.2 Motivation of the study

The aim of the present work is to provide new insights into the corresponding small-scale physics of turbulent mixing in vaporizing two-phase flows. This work gathers theoretical analyses and numerical computations conducted with the DNS solver ARCHER. The scientific issue is placed on the influence of the liquid-gas interface and the possible mass-transfer between them due to evaporation, over the structure of the turbulent flow field and the scalar field properties. Considering its impact on the resulting equivalence ratio distribution the subject is especially relevant for turbulent combustion modeling in such conditions, since either ignition or flame propagation phenomena display a first-order dependence to the corresponding quantity.

1.2.1 Research target

Bring a deeper understanding of the underlying physics of turbulent mixing in vaporizing two-phase flows, its modeling and numerical simulation, so as to improve combustion performance.

1.2.1.1 Specific objectives and research targets

The first target is to use the ARCHER solver to generate DNS databases for the study of small-scale scalar and turbulence dynamics in turbulent flows with evaporation. The

first data-set will be gathered for two-phase flow homogeneous isotropic turbulence (HIT), resorting to a forcing approach as to maintain the turbulent kinetic energy at a prescribed level and considering several values of the liquid volume fraction and surface tension, thus allowing for (i) variations of the mass transfer rate between the liquid and gaseous phases and (ii) associated variations of the corresponding effects on the smallest scales of the turbulent two-phase flow. The liquid volume fraction will be varied from 0% to 10%, while the range of surface tension variations will be bounded between 0.8 and 1.4 (times) a reference value σ_{ref}.

Along with the generation of the first data-set, the second target is the development of the post-processing to perform the analysis of the small-scale structure of scalar and turbulence. Special attention was payed to the study of the small-scale scalar structure under the influence of liquid interface and evaporation, i.e., to the analysis of micro-geometric properties of the scalar gradient for the different cases featuring increasing values of the liquid volume fraction and varying levels of surface tension, which allowed to quantify the influence of the liquid-gas interface and the possible mass-transfer between them due to evaporation on the structure of the turbulent flow at small scales, and the scalar field properties.

1.3 Organization of the thesis

This dissertation is made up of seven (7) chapters and three (3) appendices. It is organized as follows :

§2«Presentation of ARCHER solver» this chapter briefly recalls the equations governing incompressible, viscous and evaporative fluid-flows ; as well as the presentation of the numerical tools used by the ARCHER solver.

§3«Initialization and parameters of the DNS simulations» this chapter presents the numerical set-up of the DNS HIT reference case and the DNS HIT two-phase flow cases, following by the corresponding characterization of the turbulent and mixture fraction fields.

§4«Velocity field analysis of evaporative two-phase flows in HIT» this chapter presents the statistical characterization of the turbulent velocity field. Firstly are addressed the results concerning the velocity fluctuations, e.g., turbulent kinetic energy or associated Reynolds stress tensor, which characterize the energetic scales. Then attention is turned to the velocity gradient tensor (VGT), which is relevant to the dissipative scales. It is worth recalling that the velocity gradient tensor $\boldsymbol{A} = \boldsymbol{\nabla} \otimes \boldsymbol{u}$ contains key information about the rates of deformation of

infinitesimal material lines, surfaces, and volumes [63]. The evolution of the turbulence characteristics is scrutinized at various distances from the interface, in such a manner that that the gas phase is divided into several sub-regions according to the values of the level-set G, i.e., the distance from the liquid-gas interface. The acquisition of the statistics proceed in this way because the liquid-gas interface does not only alter the isotropy of velocity fluctuations but also the dissipative (i.e., small-scale) structure of the turbulent flow-field. It should be emphasized that, in the gaseous phase, the distance to the interface is defined in such a manner that the level-set value, G, is negative.

§5«Scalar field analysis of evaporative two-phase flows in HIT» this chapter presents the statistical characterization of the mixture fraction field of an evaporative multi-phase DNS simulation database set featuring two distinct values of the liquid volume fraction ϕ_ℓ. On the first part, results concerning the mixing scalar field are reported. Then attention is turned to the geometrical properties and alignment statistics of the scalar mixing and scalar dissipation. Such statistics are gathered at various distances from the interface, in such a manner that that the gas phase is divided into several sub-regions according to the values of the level-set G, i.e., the distance from the liquid-gas interface.

§6«Lagrangian evolution equations analysis» this chapter enclosed the Lagrangian-statistical characterization of the turbulent velocity field. First the mathematical formalisms of the Lagrangian evolution equations (LEE) and conditional mean trajectories (CMT) are presented. This is followed by a detailed description of the methodology used to gather such CMT. This methodology includes a novel consideration, which allows, for the first time, to scrutinize not only the direction, but also the magnitude of the trajectories computed from the terms of the LEE. Then a detailed inspection of the Lagrangian dynamics of the HIT reference case is presented. Finally the analysis concerning to the multi-phase cases featuring evaporation with different levels of volume of fluids, $\phi_\ell = 0.05$ and $\phi_\ell = 0.10$ is reported. The acquisition of the statistics is gathered at various distances from the interface, in such a manner that the gaseous phase is divided into several sub-regions according to the values of the level-set G, i.e., the distance from the liquid/gas interface.

§7«Conclusions and perspectives»

§A«Lagrangian evolution equations for the invariants of the VGT tensor»

§B«Lagrangian evolution equations for the traceless invariants of the VGT tensor»

§C«Résumé de la thèse de l'école doctorale SIMME»

2 Presentation of ARCHER solver

Content of the chapter

2.1 Introduction

The massively parallel ARCHER solver [1] (which stands for *Academic Research Code for Hydrodynamic Equations Resolution*), has been developed at CORIA laboratory with the aim of investigating phenomena involved in two-phase flows that may be turbulent, incompressible, and with phase changes. To conduct this research, ARCHER was used to solve the three-dimensional incompressible form of the Navier-Stokes equations. ARCHER makes use of a *fifth-order precision WENO scheme* for convective terms, a *second-order central finite difference scheme* to evaluate viscous and diffusion contributions,

1. https://www.coria-cfd.fr/index.php/Archer

and a *third-order precision Runge-Kutta scheme* for temporal integration. A *multi-grid algorithm* is employed for the preconditioning of the conjugate gradient method in the Poisson equation. A *ghost fluid (GF) method* is used for discontinuous variables at the liquid/gas interfaces and the *coupled level-set/volume-of-fluid (CLSVOF) method* is retained to ensure mass conservation of the system. In this chapter the numerical tools used to generate the vaporizing two-phase flow data-set are only briefly presented since a detailed presentation of the methods and solved equations can be found in the thesis works of Tanguy (2004) [100], Ménard (2007) [66] and Duret (2013) [25].

2.2 Numerical methods description

2.2.1 Coupled level-set/volume-of-fluid (CLSVOF) method

The most important aim of the *volume of fluid (VOF) method*, for the simulation of two-phase flows, is to enforce the conservation of mass. This method discretizes a given volume fraction (of gas or liquid) over the computational domain, in such a way that the conservation of the volume fraction is guaranteed when it is transported by the velocity field [57, 44, 81, 5]. However, within an Eulerian formalism (fixed mesh, for example) the *VOF* describes poorly the topology of the interface, therefore it is not the best suited to compute characteristic quantities of the surface such as : normal and tangent directions, as well as curvature. In addition, physical effects that are critical to be considered arise as factors that rest precision to the *VOF method*, such as :

- breakup and coalescence induce in some regions of the domain the formation of droplets or ligaments with a thickness of the order of only a few times the typical mesh size, so making the topological description of fine structures difficult, and
- steep jumps in some fields (like density or viscosity) may prevent the computation in the corresponding zone.

Moreover, for three-dimensional simulations, the formalism becomes more complex and expensive, since it is necessary to perform a reconstruction of the interface from the fraction function, a discontinuous scalar function used to follow the liquid phase.

On the contrary, the *level-set method*, developed by Osher and Sethian (1988) [75], is based on continuous scalar function, G, that measures the distance to the interface that we are trying to describe in the computational domain. Such function, by means of the resolution of a convection equation, allows to track the deformation of the interface in a given velocity field. Howbeit, the level-set method implementation for the simulation of two-phase flows cannot be direct, because :

- losses of mass arise from dissipative numerical errors in the resolution of the transport equation, and
- remarkable changes of the physical properties are induced by the spreading or tightening of the G-field iso-contours.

Considering the pros and cons offered by both the *level-set method* and the *volume of fluid (VOF) method*, Sussman and Puckett (2000) [97] introduced the *coupled level-set/volume-of-fluid (CLSVOF) method*, the main goal of which is to take advantage of the precise geometrical description of the *level-set method* (accurate computation of the normal direction and curvature) and, at the same time, benefit from the implicit mass conservation offered by the *volume of fluid (VOF) method*. Such a coupling requires a special procedure to recalculate the distance to the interface at each time step.

2.2.2 Fifth order weighted essentially non-oscillatory (WENO) scheme

As it has already been mentioned, the generation of small droplets and thin ligaments pose a computational discretization challenge, being that their description must be optimal. Therefore, so as to guarantee that these regions will be well resolved, a *fifth-order precision weighted essentially non oscillatory (WENO) method*, proposed by Guang-Shan and Chi-Wang (1996) [43], is used. The *weighted ENO* formulation consists into taking into account a combination of the different possible *ENO* approximations, in such a way that if one of the *ENO* approximations is interpolated across a discontinuity, its contribution will get a minimum weight, then minimizing the resulting numerical errors.

In the various simulations reported in this thesis two kinds of error can happen in the context of the resolution of small droplets and thin ligaments, the first one is related to the *level-set method*, the second to the *volume of fluid (VOF) method* :

- the disappearance of the structure from where losses of mass become not be negligible, and
- the artificial fragmentation of ligaments into several filaments, with, however, good conservation of the mass.

In order to improve these mass losses with the *level-set method*, the smoothing and weighting procedure are applied not on the derivatives but on the variable to be discretized and then the smoothed solution is derived using a centered scheme. This modified form of the *fifth order WENO scheme* has been proposed by Estivalezes (2002) [30]. Such improvements are also documented in the thesis of Tanguy (2004) [100].

2.2.3 Third order Runge Kutta (RK3) scheme

The *Runge-Kutta methods* are a family of implicit and explicit iterative methods used for temporal discretization to approximate solutions of ordinary differential equations. They are widely used because of their good compromise between numerical stability and precision. The order of the method gives the number of steps of the scheme with which several intermediate values of the integrated variable within a time step will be evaluated. By increasing the number of steps the precision is increased too, but it goes together with an increased computational time of each time-step. ARCHER makes use of a *third-order precision Runge-Kutta scheme*.

2.2.4 Ghost fluid method

For incompressible two-phase flows simulations, the surface of discontinuities, i.e., liquid clusters, are introduced explicitly in the equations, so the displacement of the liquid bodies interfaces is calculated by means of the *level-set method*, and the jump conditions are explicitly imposed as additional constraints which depend on the local characteristics of the interface. Thanks to this, the *ghost fluid method*, which was developed by Fedkiw et al. (1999) [33], allows to extend the discontinuous variables by continuity beyond the interface before proceeding with differentiation it, which in turn allows to impose a very realistic jump condition. Then the derivation of the extended variable does not pose a problem since it has been made differentiable thanks to the extension by continuity.

2.3 Solved equations

2.3.1 Navier-Stokes equations

To resolve the Navier-Stokes equations (Eq. 2.1), the *coupled level-set/volume-of-fluid (CLSVOF) method* is used in conjunction with an incompressible flow projection algorithm

$$\frac{\partial \boldsymbol{u}}{\partial t} + (\boldsymbol{u} \cdot \boldsymbol{\nabla})\,\boldsymbol{u} = -\frac{\boldsymbol{\nabla} p}{\rho} + \frac{1}{\rho}\boldsymbol{\nabla} \cdot (2\,\mu\,\boldsymbol{D}) + \boldsymbol{f} + \frac{1}{\rho}\sigma k \delta(G)\,\boldsymbol{n} \tag{2.1}$$

where $\boldsymbol{u}$ denotes the velocity vector, ρ is the density, p the dynamic component of the pressure field, $\mu = \rho\nu$ the dynamic viscosity (with ν the molecular kinematic

viscosity), $\boldsymbol{D}$ the viscous deformation tensor and finally $\boldsymbol{f}$ the source term associated to the linear forcing used to counteract the decay of homogeneous isotropic turbulence (HIT). At the liquid-gas interface, the influence of surface tension σ is taken into account, $\boldsymbol{n} = \boldsymbol{\nabla} G / \mid\mid \boldsymbol{\nabla} G \mid\mid$ denotes the normal unit vector pointing towards the liquid phase, while $k = \boldsymbol{\nabla} \cdot \boldsymbol{n}$ is the curvature of the interface, as evaluated from the level-set function G, and δ is the Kronecker delta.

2.3.2 Poisson solver

The spatial derivatives for convective terms are evaluated using the *fifth order WENO scheme* (Guang-Shan and Chi-Wang [43]), (Tanguy [100]), while the viscous and molecular diffusion terms are computed using a *second-order central finite difference scheme*. The temporal integration is performed using a *third-order precision Runge-Kutta (RK3) scheme*. The resolution consider a (staggered) Cartesian mesh. Unlike scalar variables (including pressure) which are defined at the center of cells, a *first-order multi-grid projection algorithm* for the preconditioning of the conjugate gradient method in the Poisson equation is used. It consists first in calculating an intermediate velocity $\boldsymbol{u}^*$ from the momentum equation, but without the pressure term.

$$\boldsymbol{u}^* = \boldsymbol{u}^n + \Delta t \left(-(\boldsymbol{u} \cdot \boldsymbol{\nabla})\boldsymbol{u} + \frac{1}{\rho}\boldsymbol{\nabla} \cdot (2\mu \boldsymbol{D}) + \boldsymbol{f} + \frac{1}{\rho}\sigma\kappa|\boldsymbol{\nabla} G|\delta(G)\boldsymbol{n} \right) \tag{2.2}$$

The zero-divergence of the velocity $\boldsymbol{u}^*$ in Eq. 2.2 is not ensured. The obtainment of a velocity $\boldsymbol{u}^{n+1}$ with zero divergence is seeked. Thus the gradient of pressure $\boldsymbol{\nabla} p^{n+1}$ is introduced in Eq. 2.3 as follows :

$$\boldsymbol{u}^{n+1} = \boldsymbol{u}^* - \frac{\boldsymbol{\nabla} p^{n+1}}{\rho}\Delta t \tag{2.3}$$

Then the divergence operator is applied to Eq. 2.3. The continuity equation imposes zero divergence for the speed $\boldsymbol{u}^{n+1}$, therefore $\boldsymbol{\nabla} \cdot \boldsymbol{u}^{n+1} = 0$, which gives the following Poisson equation as a constrain applied to $\boldsymbol{u}^*$:

$$\boldsymbol{\nabla} \cdot \boldsymbol{u}^* = \boldsymbol{\nabla} \cdot \frac{\boldsymbol{\nabla} p^{n+1}}{\rho}\Delta t \tag{2.4}$$

Eq. 2.4 is solved using a *conjugate-gradient solver* with multi-grid preconditioning. It is paramount to mention that dividing by the density (ρ) introduce a matrix with

non-constant coefficients, scilicet, the resolution of the system become more difficult, therefore the *ghost fluid method* is used, to impose a jump condition for the density ratio is ρ_l/ρ_g at the liquid-gas interface (such ratio can be as large as one thousand). Finally, the pressure obtained by the Poisson solver is used to obtain the speed at the following instant, as is read in Eq. 2.3. This projection method gives a velocity field at instant $n+1$ with zero-divergence.

2.3.3 Interface tracking

The level-set method uses a continuous function to describe the interface, Eq. 2.5. Such function is defined as the signed distance between any point of the computational domain and the zero iso-contour $(G=0)$, i.e,. the liquid-gas interface (Osher and Fedkiw [74]). In ARCHER, the level-set method is used in conjunction with the VOF method in the solver part of the code.

$$\frac{\partial G}{\partial t} + (\boldsymbol{u}\cdot\boldsymbol{\nabla})\,G = 0 \tag{2.5}$$

The level-set Eq. 2.5 is the hyperbolic type, therefore its discretization must combine high convergence order with robustness. Thus, the *fifth-order WENO scheme* is used to discretized the convective term. Unfortunately, the level-set G no longer remains a distance function as Eq. 2.5 is solved numerically and a re-normalization algorithm must be applied to keep it as the signed distance to the interface. The *coupled level-set and volume-of-fluid (CLSVOF) method* has been proposed to address this specific issue (Sussman and Puckett [97]) and has been successfully applied to the numerical simulation of atomization processes by Ménard et al. (2007) [67] and Lebas et al. (2009) [58]. The main concept behind the *CLSVOF* method is to take advantage of both level-set and VOF strategies : mass loss is limited through the use of the VOF method and a detailed description of interface is ensured within the level-set framework. Density and viscosity depend on the value (sign) of the level-set (liquid and gas). Jump conditions across the interface are taken into account within the *ghost fluid (GF) method*. In the *GF method*, ghost cells are defined on each side of the interface (Liu et al. [59]), which prolongs the description of each phase beyond the interface location so as to allow smooth derivative computations in the vicinity of the interface.

The scalar used in the *VOF method* is the liquid volume fraction $\phi_\ell = V_l/V$, where V_l is the volume of liquid in the cell and V is the cell volume, i.e., $V = dx^3$ with $dx\,[m]$

the characteristic mesh size. This scalar is governed by the transport equation read in Eq. 2.6 :

$$\frac{\partial \phi_\ell}{\partial t} + (\boldsymbol{u} \cdot \boldsymbol{\nabla})\, \phi_\ell = 0 \tag{2.6}$$

The *piecewise linear interface calculation (PLIC)* reconstruction is used, which represents the interface by plans in each cell of the domain. The position of the interface in each cell is slightly modified according to the volume given by the VOF method. The geometric characteristics are determined by the level-set using the relationships detailed by the normal unit vector pointing towards the liquid phase $\boldsymbol{n} = \boldsymbol{\nabla} G / \mid\mid \boldsymbol{\nabla} G \mid\mid$ and the curvature $k = \boldsymbol{\nabla} \cdot \boldsymbol{n}$.

Finally, discontinuities require special care. In general, the term "jump conditions" is used when there is a sudden discontinuity in a variable. In the case of two-phase flows of liquid and gas, there is a jump in the density ratio ρ_l / ρ_g, which can be of the order of 1000 at the liquid-gas interface. These jump conditions are imposed because a "single-fluid" formalism is solved, i.e., a single set of equations is solved for the whole domain. Therefore, during the resolution of the equations it is necessary to estimate derivatives near interface. If the computation of a derivative in the gas domain requires points in the liquid, several jump conditions will come into play so that the points used take into account the jump in density (ρ), pressure (p), and dynamic viscosity (μ) ; in our case. To take them into account, the *ghost fluid (GF) method* is used. The principle consists in extrapolating the considered variable by continuity, rather than submitting it to a sudden discontinuity, which would have the effect of making the computational schemes unstable and/or oscillating. The numerical scheme remains unchanged but the jump condition is directly integrated into the Ghost cells of the studied variable (only applied close to the interface).

2.3.4 Mixture fraction

Assuming local thermodynamic equilibrium, the mass fraction of fuel evaporated at the liquid-gas interface $Y_{F,s}$ can be determined from the Clausius-Clapeyron law. The mixture fraction ξ is herein defined as the normalized value of the fuel mass fraction : $\xi = Y_F / Y_{F,s}$. It is thus bounded between zero in the pure oxidizer and unity at the liquid-gas interface for the sake of simplicity, and it evolves in the gaseous phase due to convection and molecular diffusion. Based on previous investigations of Duret et al. (2012) [26] and Bouali et al. (2016) [6], it is considered that the amount of mass transferred from the liquid into the gas remains sufficiently small to be neglected. This is relevant provided that the equilibrium is reached rapidly. Therefore, the mass

of liquid present in the computational domain remains approximately constant, while the evolution of the vapor concentrations is analyzed. This computational framework allows to study scalar mixing induced by mass transfer between the two phases for conditions associated to characteristic velocity fluctuations that remain larger than the Stefan flow velocity. It should be emphasized that the consideration of the whole vaporization process from a more general viewpoint still remains very challenging and requires several additional equations, including energy and species budgets, as well as additional jump conditions [37]. The mixture fraction evolution equation may be written as follows :

$$\frac{\partial \rho \xi}{\partial t} + \boldsymbol{\nabla} \left(\rho \boldsymbol{u} \xi \right) = \boldsymbol{\nabla} \cdot \left(\rho \mathcal{D} \boldsymbol{\nabla} \xi \right) + \rho \dot{\omega}_{\xi} \tag{2.7}$$

where $\dot{\omega}_{\xi}$ denotes a mixture fraction source term resulting from the influence of mass transfer induced by vaporization. The influence of the corresponding mass transfer term requires to sustain a value of ξ equal to unity at the liquid-gas interface in Eq. 2.7. This boundary condition must be imposed at the interface location, thus allowing for the resolution of Eq. 2.7 to analyze the vaporization processes. Further details in regard to this special point have been previously provided by Duret et al. (2012) [26] and Bouali et al. (2016) [6].

For the evolution equation of the mixture fraction field, Eq. 2.7, the same schemes employed to solve momentum equation are used to compute the convective term, while the molecular contribution is evaluated with the *second-order central finite difference scheme*. The time integration is performed with a *third-order precision Runge-Kutta (RK3) scheme*. At the vicinity of interface, the evaluation of the spatial derivatives are based on ghost values deduced from the *Aslam extension method* [2]. This method is used to obtain an extension of the normal derivative of the scalar field across the interface, thus enhancing the numerical accuracy of the estimation of the convective term close to the interface. The boundary conditions are enforced with the *Aslam-Chiu method* [15], which consists in applying a Dirichlet condition, at the liquid-gas interface Duret (2013) [25], compatible with the *Aslam extension method*, see appendix A of Bouali et al. (2016) [6]. At the initial time of the simulation, the value of ξ is set to zero in the gas and to unity at the interface. The scalar equation is then solved only in the gas phase. In the liquid, the values of ξ are given by the *Aslam-Chiu method* and they are subsequently used as ghost values during the resolution of the scalar transport equation.

2.3.5 Turbulence forcing method

The turbulence is maintained by a linear forcing method with two different phases, which is added to Eq. 2.1 as the source term $\boldsymbol{f} = B\boldsymbol{u}'$, where B is the forcing coefficient. At this point is convenient to state that a standard Reynolds decomposition is applied to both velocity and scalar field, e.g., $\boldsymbol{u} = \overline{\boldsymbol{u}} + \boldsymbol{u}'$, with $\overline{\boldsymbol{u}}$ the mean flow velocity and $\boldsymbol{u}'$ the associated velocity fluctuation.

The evolution equation of the TKE $\kappa = \frac{1}{2}\overline{\boldsymbol{u}'^2}$ can be written as follows :

$$\frac{\partial \kappa}{\partial t} + \boldsymbol{\nabla}\left(\overline{\boldsymbol{u}}\kappa\right) = C_\kappa + 2B\kappa \tag{2.8}$$

Where C_κ groups the typical contributions to the TKE evolution, i.e., without forcing, and $\overline{\boldsymbol{u}}$ is the average speed in the domain. This term includes the liquid-gas interface, so it is complex to estimate B directly from Eq. 2.8. Therefore, the following procedure was employed :

1 Estimate of C_κ^{n-1} based on the value of the constant B^{n-1} :

$$C_\kappa^{n-1} = \frac{\kappa^n - \kappa^{n-1}}{\Delta t} - 2B^{n-1} - \kappa^{n-1} \tag{2.9}$$

2 Calculation of the forcing coefficient B^n based on C_κ^{n-1} :

$$2B^n - \kappa^n = \frac{\kappa_c - \kappa^n}{\tau_f} - C_\kappa^{n-1} \tag{2.10}$$

Where κ_c is the kinetic energy level chosen beforehand, τ_f is a characteristic relaxation time $\left(\tau_f = 3\Delta t\right)$, to avoid any abrupt change in the value of the forcing term. Consequently, the forcing coefficient B is calculated at each time step to introduce the term $\boldsymbol{f}$ in the Navier-Stokes equations 2.1. This method maintains a temporally constant averaged kinetic energy.

However, this type of forcing has some drawbacks : energy is added to all turbulence scales, unlike spectral forcing (frequently used in the case of single-phase) where the forcing term is applied only to a chosen wave-number range. However, the application of spectral forcing in two-phase flow DNS is complex because of the discontinuities across the interface, it is also more expensive in computing time (use of a fast Fourier transform algorithm). The choice of linear forcing was made for its simplicity and because of the lack of extensive studies dedicated to two-phase flow DNS forcing methods.

3 Initialization and parameters of the DNS simulations

Content of the chapter

3.1 Set-up of the direct numerical simulation

The studied configuration corresponds to two-phase flows in a three-dimensional homogeneous isotropic turbulence (HIT) cube featuring periodic boundaries. Such simulations of the flow were performed on regular meshes featuring a resolution of $256 \times 256 \times 256$ computational points. The physical properties are almost the same as those previously documented in the works of Duret et al. (2012) [26] and Bouali et al. (2016) [6] : the value of the surface tension is $\sigma = 0.0108 kg \cdot s^{-2}$ while the gas and liquid viscosities are $\mu_g = 1.879 \times 10^{-5} kg \cdot m^{-1} \cdot s^{-1}$ and $\mu_\ell = 5.65 \times 10^{-4} kg \cdot m^{-1} \cdot s^{-1}$, respectively. The density ratio between the two phases ρ_ℓ / ρ_g is set to 30, and the

liquid volume fraction is $\phi_\ell = V_\ell / V$, where V_ℓ denotes the volume of liquid and $V = V_\ell + V_g$ is the total volume, i.e., $V = L^3$ with $L = 1.5 \times 10^{-4} m$ the characteristic length of the computational domain. In the present study, two different values of the liquid volume fraction are considered : $\phi_\ell = 0.05$ and $\phi_\ell = 0.10$.

It is noteworthy that similar HIT and two-phase-HIT box configurations have been already reported by Bouali et al. (2016) [6], but considering decaying turbulence. Here the DNS databases correspond to forced turbulence with a value of the turbulent kinetic energy (TKE, κ) maintained at low constant level of $\kappa = 3.6$ m^2·s^{-2}. The TKE is defined in Eq. 3.3.

The current simulations were constructed in two successive steps. The first one consists in generating the initial spray conditions based on statistically-converged HIT numerical simulations conducted with the same level of resolution but without any consideration of the mass transfer. These preliminary two-phase flow HIT simulations are run until convergence of the second-order moments is reached based on the values of the normalized turbulent kinetic energy ΔU, defined below in Eq. 3.1. This is obtained once $t^+ = (t - t_0) / \tau_{T_0}$ reaches $t^+ = 12.0$ for $\phi_\ell = 0.05$ and $t^+ = 9$ for $\phi_\ell = 0.10$. Evaporation is activated in a second step and the data are gathered from $t^* = 0.0$ to $t^* = 6.0$ with $t^* = (t - t_1) / \tau_{T_1}$. In the above expression, the turbulent time scales are evaluated from $\tau_{T_0} = \kappa_0 / \varepsilon_0$ and $\tau_{T_1} = \kappa_1 / \varepsilon_1$, respectively, with ε the TKE dissipation rate. The subscripts zero and unity correspond to the initial and final values of the preliminary convergence phase, which is conducted without any consideration of the evaporation processes.

$$\Delta \mathrm{U} = 100 \times \left(\frac{\mathrm{U}(t) - \mathrm{U}(t_1)}{\mathrm{U}(t_1)} \right) \tag{3.1}$$

where

$$\mathrm{U} = \left(\frac{2\kappa}{3} \right)^{1/2} \tag{3.2}$$

The convergence of the multi-phase cases is inspected through their normalized RMS, ΔU, which are reported in Fig. 3.1 for $\phi_\ell = 0.05$ (—), and $\phi_\ell = 0.10$ (- - -). Both cases depict a tendency to converge to zero, no matter if breakup or coalescence phenomenon predominates.

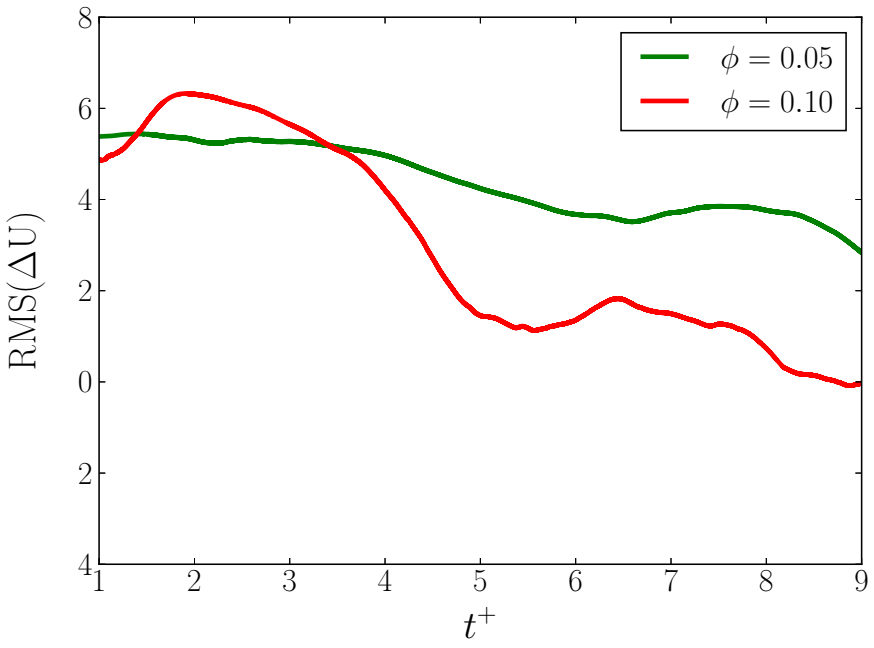

Figure 3.1. *Evolution of the normalized RMS, ΔU, as a function of the non-dimensionalized time, t^+, for the preliminary multi-phase HIT simulations with $\phi_\ell = 0.05$ (—), and $\phi_\ell = 0.10$ (—).*

3.2 Characterization of the HIT configuration

Before characterizing the multi-phase cases featuring turbulence forcing and evaporation, the firs step is to evaluate the standard HIT configuration but with forced turbulence.

Instantaneous snapshots of the HIT reference case are displayed in Fig. 3.2. The displayed contours corresponds to three different Q_A iso-values : $Q_A = 3$, $Q_A = 1.5$ and $Q_A = -1.5$, which are colored by the value of the normalized vorticity magnitude, $||\boldsymbol{\omega}||$. The Q_A-criterion is used to identify turbulent structures in numerical data-sets. It makes use of the second invariant of the velocity gradient tensor, $\boldsymbol{A}$, i.e., Q_A, since the viscous stresses are functions of the strain rate only, $\tau = \mu\left[\left(\partial u_i/\partial x_j + \partial u_j/\partial x_i\right)\right]$. The corresponding set of figures shows vortical structures $(Q_A > 0)$, as well as strain-dominated structures $(Q_A < 0)$.

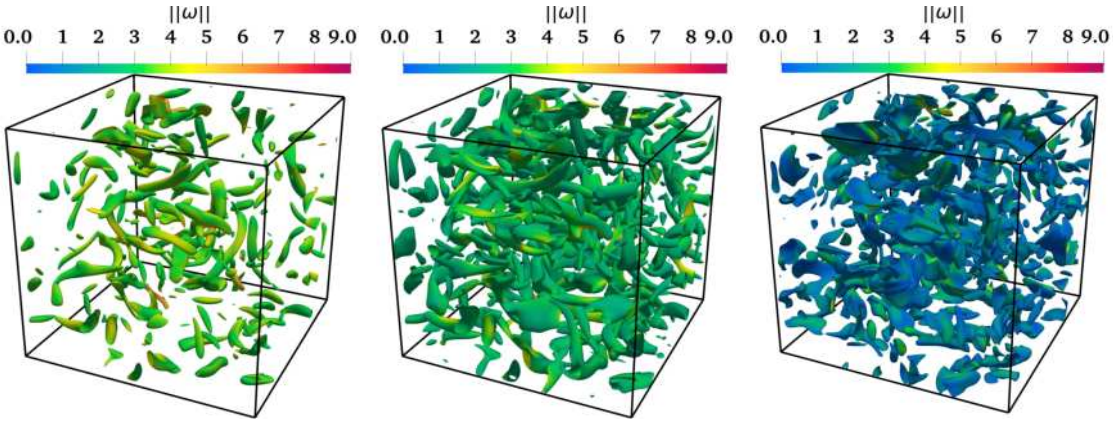

(a) $Q_A = 3$ **(b)** $Q_A = 1.5$ **(c)** $Q_A = -1.5$

Figure 3.2. *Instantaneous 3D-snapshots of the HIT reference case at the non-dimensional time,* $t^+ = 2.5$*. The displayed contours correspond to different* Q_A*-criterion values : (a) and (b) display iso-surfaces of vortex structures* $(Q_A > 0)$*, meanwhile (c) depict regions with higher strain* $(Q_A < 0)$*. The three iso-surfaces are colored by the normalized vorticity magnitude,* $||\boldsymbol{\omega}||$*.*

3.2.1 Forcing and dissipation

The mean TKE, $\overline{\kappa}$, converges very quickly to the imposed value of $\kappa = 3.6$, and this value is maintained without any large fluctuation, as can be seen in Fig. 3.3. At this point it seems convenient to introduced also the definition of the TKE dissipation rate, see Eq. 3.4. Its mean evolution, $\overline{\varepsilon}$, is presented in Fig. 3.4. These results confirms the potential and stability of the 5^{th} *order WENO scheme* implemented in the ARCHER solver to accurately reproduce the balance between turbulence production, i.e., forcing, and dissipation.

$$\kappa = \frac{\overline{\boldsymbol{u}' \cdot \boldsymbol{u}'}}{2} \tag{3.3}$$

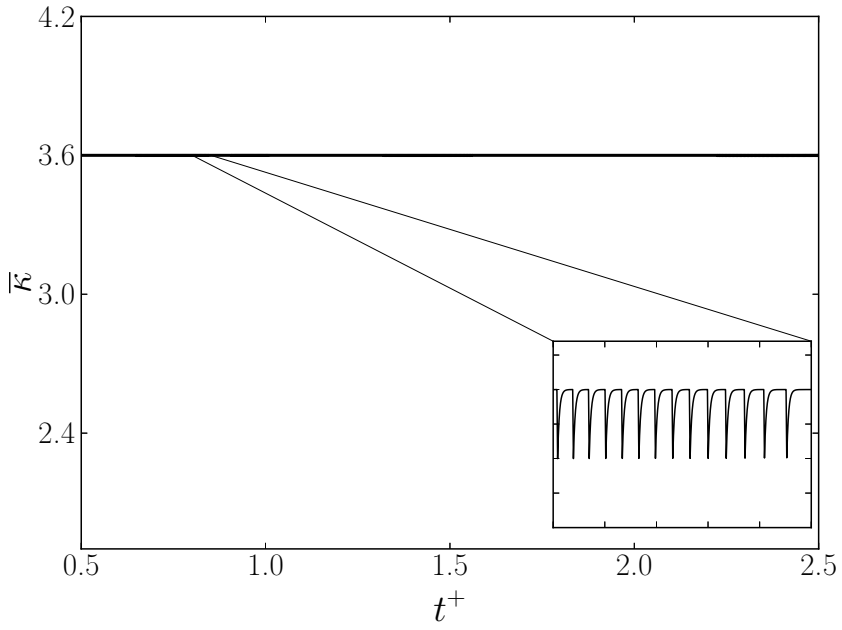

Figure 3.3. *Evolution of the mean turbulent kinetic energy, $\overline{\kappa}$ (—), as function of the non-dimensionalized time, t^+, for the HIT reference case.*

$$\overline{\varepsilon} = \overline{\nu_g \left(\frac{\partial u'}{\partial x_j}\right)_g \left(\frac{\partial u'}{\partial x_j}\right)_g} + \overline{\nu_\ell \left(\frac{\partial u'}{\partial x_j}\right)_\ell \left(\frac{\partial u'}{\partial x_j}\right)_\ell} \tag{3.4}$$

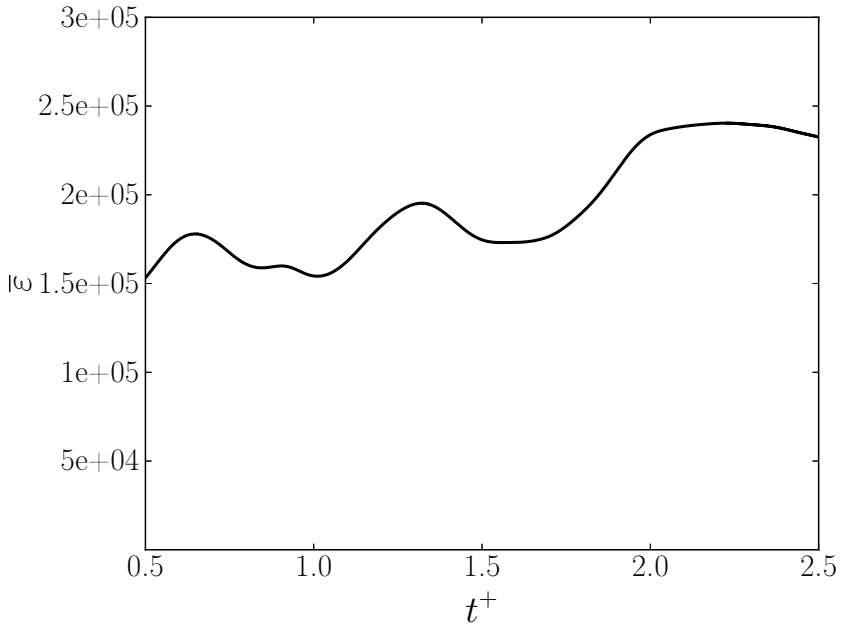

Figure 3.4. *Evolution of the mean dissipation rate of the turbulent kinetic energy, $\overline{\varepsilon}$ (—), as function of the non-dimensionalized time, t^+, for the HIT reference case.*

3.2.2 Turbulent and dissipative scales

Motions in a turbulent flow exist over a broad range of length and time scales and observations indicate that eddies lost most of their energy after one or two turnovers [89]. Therefore, the rate of energy transferred from the largest eddies is proportional to their energy (times) their rotational frequency. Since, by definition, the Reynolds number shows the relationship between inertial forces (here generated by the turbulence production), and dissipative forces, it becomes interesting to take a closer look at the evolution – over the non-dimensionalized time, t^+ – of some length scales and Reynolds numbers enlisted and defined below :

- turbulent or integral length scale, ℓ_t, defined in Eq. 3.5. This scale correspond to the scale of the largest vortices. Its corresponding Reynolds number is defined in Eq. 3.6.

$$\ell_t = \frac{\kappa^{3/2}}{\varepsilon} \tag{3.5}$$

$$Re_t = \frac{\kappa^2}{\nu\varepsilon} = \frac{\boldsymbol{u}' \cdot \ell_t}{\nu} \tag{3.6}$$

- Kolmogorov micro-scale, η_K, defined in Eq. 3.7. This is relevant to the smallest scale presented in any turbulent flow. At the Kolmogorov scale, viscosity dominates over inertia and the turbulent kinetic energy is dissipated into heat. By definition, the Kolmogorov Reynolds number is unity, $Re_K = 1$.

$$\eta_K = \left(\frac{\nu^3}{\varepsilon}\right)^{1/4} \tag{3.7}$$

- Taylor length scale, λ, defined in Eq. 3.8. This scale correspond to an intermediate scale between the macro-scale, ℓ_t, and the micro-scale, η_K, of turbulence. The Reynolds number based on the Taylor length scale, Re_λ defined in Eq. 3.9, is widely used to characterize turbulent flow. In general, it is assumed that a flow is turbulent when its Re_λ values becomes significantly larger than 10.

$$\lambda = \sqrt{10}\eta_k^{2/3}\ell_t^{1/3} \tag{3.8}$$

$$Re_\lambda = \frac{u' \lambda}{\nu} \tag{3.9}$$

The evolution of the Taylor and integral length scales tend to stabilize, and their corresponding Reynolds numbers keep an almost constant value, as depicted in Fig. 3.5.

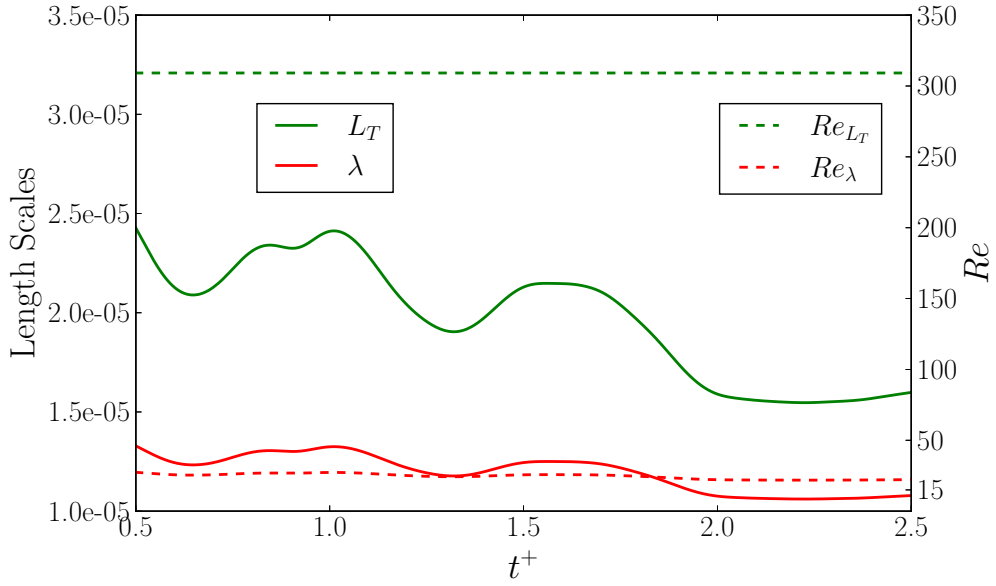

Figure 3.5. *Evolution of the integral, ℓ_t (—), and Taylor, λ (—), length scales; together with their corresponding turbulent, Re_{ℓ_t} (- - -), and Taylor, Re_λ (- - -), Reynolds numbers, as a function of the non-dimensionalized time, t^+, for the HIT reference case.*

The values of Re_λ represents a weakly turbulent flow. However, in Table 3.1 are gathered for the single-phase HIT reference case, some classical turbulence flow parameters that correspond to the non-dimensionalized time $t^+ = 2.5$: turbulent velocity fluctuation (u_{RMS}), the integral (ℓ_t), Taylor (λ), and Kolmogorov (η_K) length scales; as well as two Reynolds numbers, the integral (Re_t), and the Taylor (Re_λ).

Case	u_{RMS} (m/s)	ℓ_t (μm)	λ (μm)	η_K (μm)	Re_t (-)	Re_λ (-)	τ_{T_0} (μs)
HIT	1.55	16.71	11.03	1.18	309.2	22.7	44.6

Table 3.1 – *Turbulence flow parameters for the reference HIT case, at the non-dimensionalized time $t^+ = 2.5$.*

3.3 Characterization of the multi-phase flows non-evaporative cases

Instantaneous snapshots of the three-dimensional turbulent two-phase flow of the case with $\phi_\ell = 0.10$ are displayed in Fig. 3.6. The displayed contour corresponds to an iso-value of the level-set, G, which is a signed distance from the liquid-gas interface to any point of the domain. Such iso-contour value corresponds to the liquid-gas interface, i.e., $G = 0$. The interface is colored by the value of the normalized vorticity magnitude, $||\omega||$, and it is plotted for two distinct values of non-dimensional times : (a) $t^+ = 0.0$, which corresponds to the initialization of the domain, and (b) $t^+_{\text{end}} = 9.0$, the last time step before the activation of the evaporation module. The corresponding set of figures shows different liquid structures such as drops but also ligaments, or even larger liquid structures of any shape. This confirms that there exists very strong interactions between liquid clusters. They will frequently collide and may eventually coalesce, but in any situation the interface may display significant levels of curvature and wrinkling.

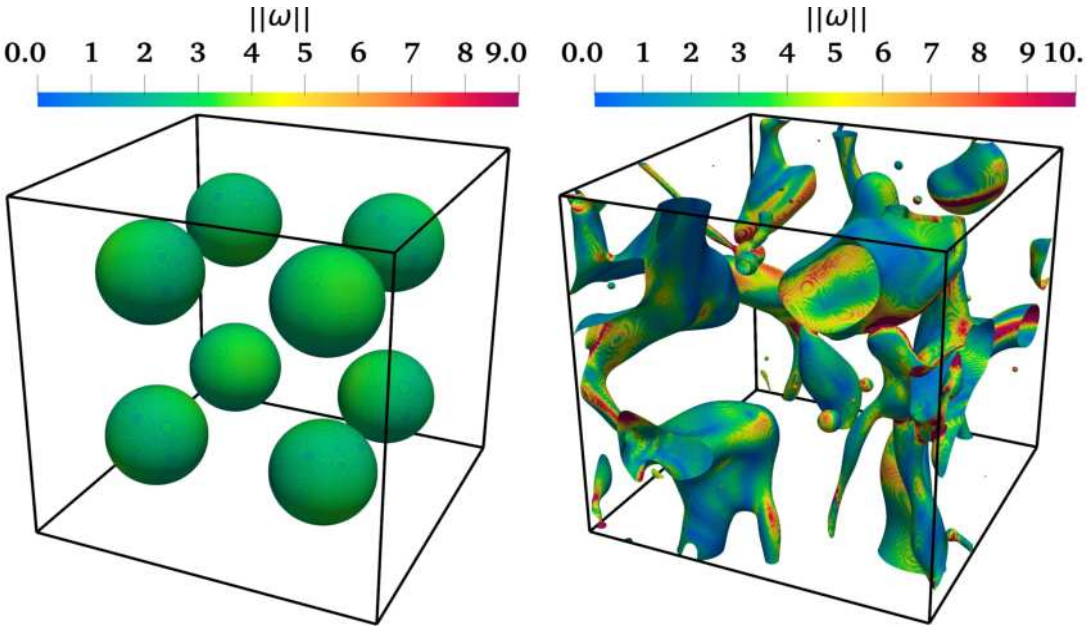

(a) $t^+ = 0.0$ **(b)** $t^+ = 9.0$

Figure 3.6 – *Instantaneous 3D-snapshots of the turbulent two-phase flow case with* $\phi_\ell = 0.10$ *at two different non-dimensional times : (a) initialization of the domain* $(t^+ = 0.0)$*, and (b) last time step before the activation of the evaporation module* $\left(t^+ = \frac{t-t_0}{\tau_{t_0}} = 9.0\right)$*. The displayed contours correspond to the liquid-gas interface, i.e., the level-set value, G, equal to zero; colored by the normalized vorticity magnitude,* $||\omega||$*.*

3.3.1 Interface behavior

From the *CLSVOF* method, the mean interface density, $\overline{\Sigma}$, can be directly evaluated and it is reported in Fig. 3.7 for $\phi_\ell = 0.05$ (—), and $\phi_\ell = 0.10$ (—). Its evolution over the non-dimensionalized time t^+, is due to breakup and coalescence of the liquid structures, that will "reduce" or "increase" the interface density, respectively. Although the case with $\phi_\ell = 0.10$ depicts large variations of the values taken by Σ, coalescence phenomenon prevails if compared against the case with $\phi_\ell = 0.05$, where conversely breakup is the dominant process.

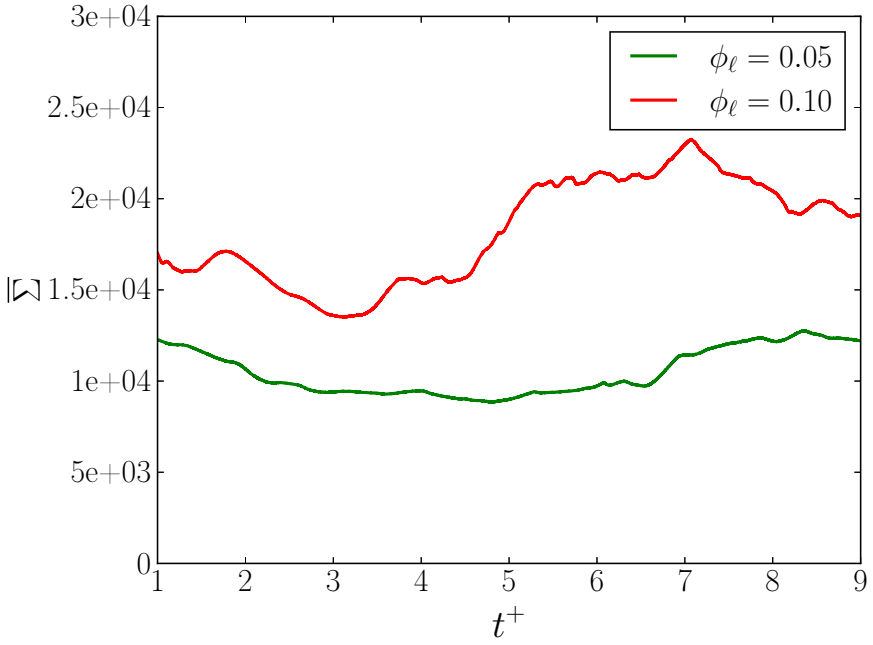

Figure 3.7. *Evolution of the mean liquid-gas interface, $\overline{\Sigma}$, as a function of the non-dimensionalized time, t^+, for the preliminary multi-phase HIT simulations with $\phi_\ell = 0.05$ (—), and $\phi_\ell = 0.10$ (—).*

The mass conservation of the liquid phase is a critical parameter in multi-phase simulations. This is checked through the evolution of the ratio of the mass of liquid over its initial value, m/m_{init}, reported in Fig. 3.8. The corresponding values of the initial mass of liquid for each case are $m_{init} = 0.127$ (ng) for $\phi_\ell = 0.05$ (—), and $m_{init} = 0.254$ (ng) for $\phi_\ell = 0.10$ (—). For both cases, the variation of the mass of liquid over time is remains below 0.12%, which confirms the ability of the *CLSVOF* approach to accurately simulate this kind of flows.

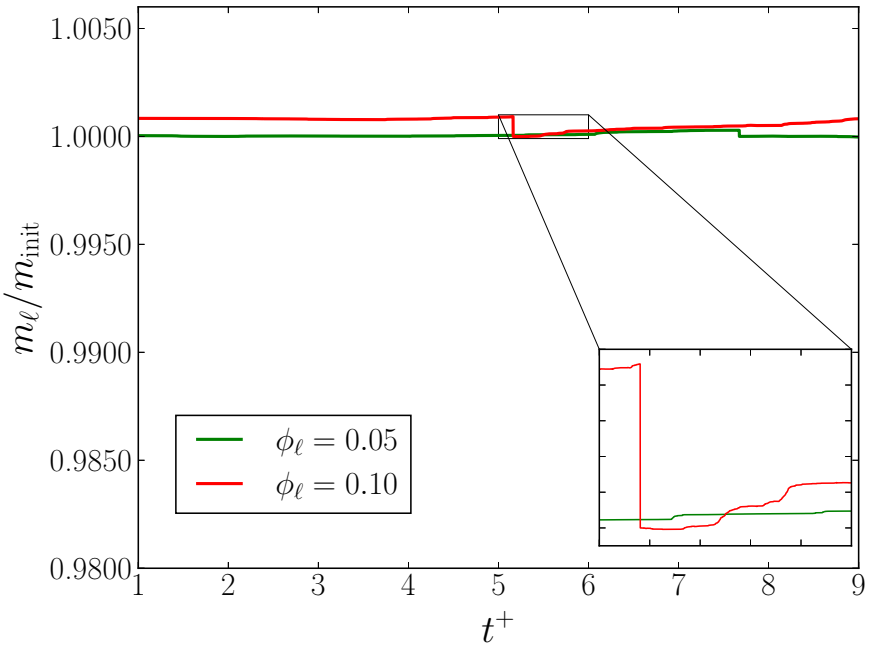

Figure 3.8. *Evolution of the mass of the liquid phase normalized by its initial value, m_ℓ / m_{init}, as a function of the non-dimensionalized time, t^+, for the preliminary multi-phase HIT simulations with $\phi_\ell = 0.05$ (—), and $\phi_\ell = 0.10$ (—).*

3.3.2 Turbulent fields

As previously mentioned in chapter 1, it is very difficult to assess the influence of two-phase flow on turbulence. However, it remains possible to conduct "classical" analysis developed for single-phase turbulence to such multi-phase databases.

In Fig. 3.9 the evolution of the mean TKE, $\overline{\kappa}$, is reported for $\phi_\ell = 0.05$ (—), and $\phi_\ell = 0.10$ (- - -). For both cases the TKE level is maintained at the constant value of $\kappa = 3.6$.

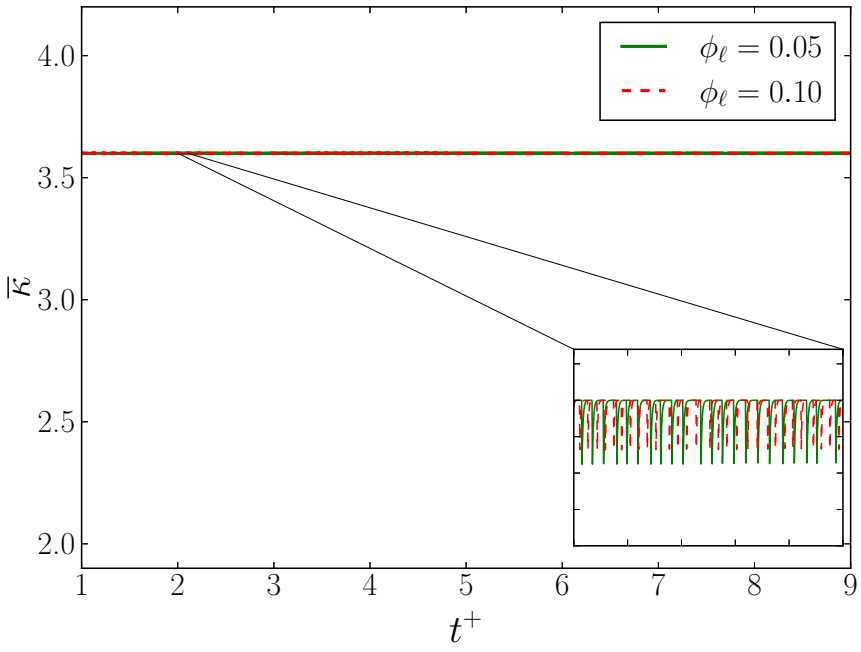

Figure 3.9. *Evolution of the mean turbulent kinetic energy, $\overline{\kappa}$, as a function of the non-dimensionalized time, t^+, for the preliminary multi-phase HIT simulations with $\phi_\ell = 0.05$ (—), and $\phi_\ell = 0.10$ (- - -).*

The mean dissipation rate of the TKE, $\overline{\varepsilon}$, is reported In Fig. 3.10 for $\phi_\ell = 0.05$ (—), and $\phi_\ell = 0.10$ (—). Such evolution, in comparison to the HIT reference case, Fig. 3.4, also display some oscillation, but does not tend to increase due to the presence of the liquid phase. The case governed by breakup phenomenon, i.e., $\phi_\ell = 0.05$, exhibit a more fluctuating behavior than the case where coalescence prevails. The later indeed shows a more stable development before the first turnover.

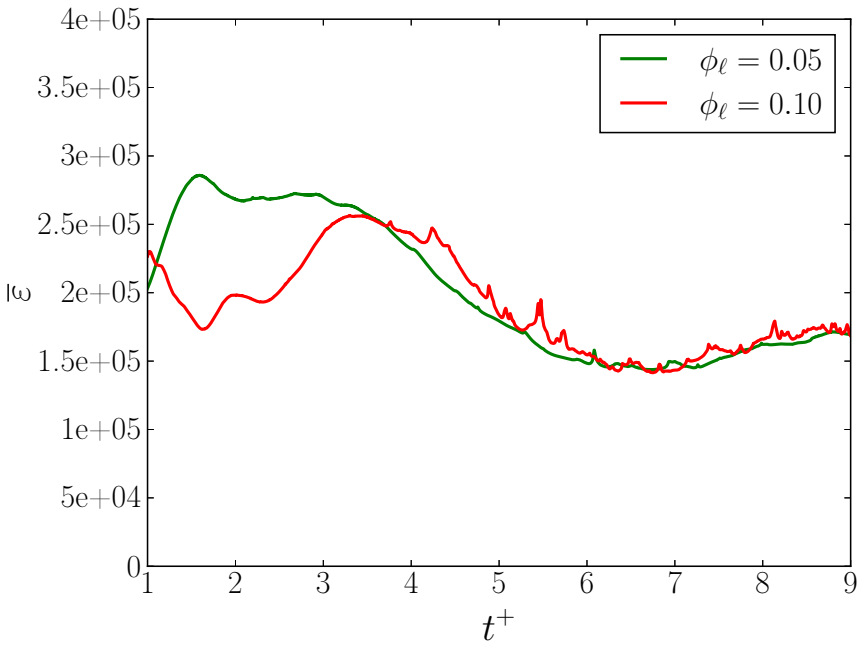

Figure 3.10. *Evolution of the mean dissipation rate of the turbulence kinetic energy, $\bar{\varepsilon}$, as a function of the non-dimensionalized time, t^+, for the preliminary multi-phase HIT simulations with $\phi_\ell = 0.05$ (—), and $\phi_\ell = 0.10$ (—).*

Figure 3.11 present the evolution of the Taylor (—) and integral (—) length scales and their corresponding turbulent, Re_{ℓ_t} (- - -), and Taylor, Re_λ (- - -), Reynolds numbers, for both cases, $\phi_\ell = 0.05$ (—), and $\phi_\ell = 0.10$ (—). Such length scales display a more fluctuating behavior in comparison to those evaluated in the HIT reference case. This reflects the impact of the wrinkling, coalescence and breakup of the biggest liquid clusters. Nonetheless, their corresponding Reynolds numbers, keep an almost constant value.

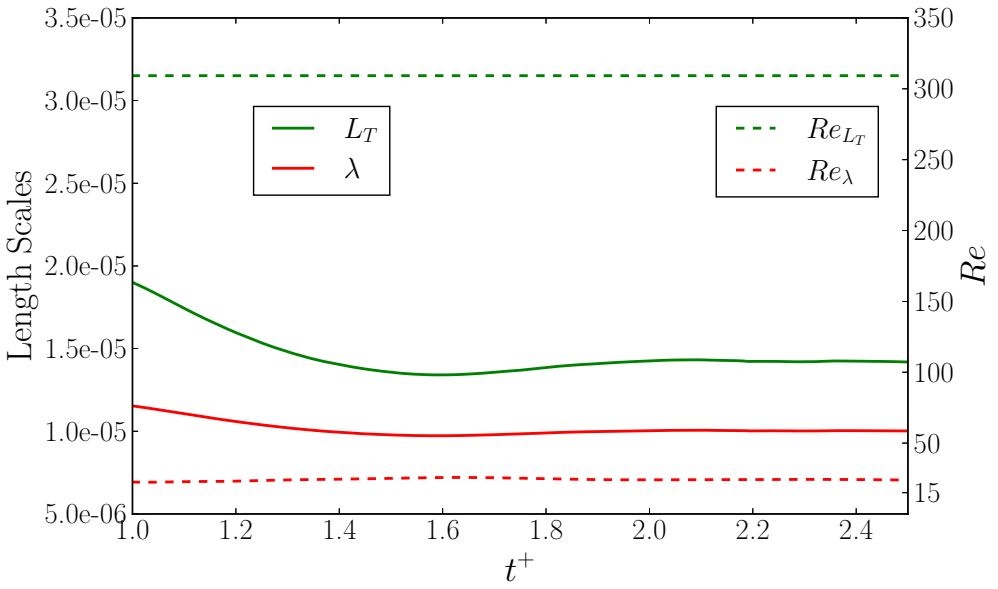

Figure 3.11. *Evolution of the integral, ℓ_t (—), and Taylor, λ (—), length scales; together with their corresponding turbulent, Re_{ℓ_t} (- - -), and Taylor, Re_λ (- - -), Reynolds numbers, as a functions of the non-dimensionalized time, t^+, for the preliminary multi-phase HIT simulations with $\phi_\ell = 0.05$ (—), and $\phi_\ell = 0.10$ (—).*

Table 3.2 reports the same turbulence flow parameters as Table 3.1, but for the non-evaporative multi-phase cases $\phi_\ell = 0.05$ and $\phi_\ell = 0.10$ at the non-dimensionalized time $t^+ = 12$ and $t^+ = 9$, respectively.

Case	u_{RMS} (m/s)	ℓ_t (μm)	λ (μm)	η_K (μm)	Re_t (-)	Re_λ (-)	τ_{T_0} (μs)
$\phi_\ell = 0.05$	1.51	17.53	11.86	1.22	300.4	23.0	21.4
$\phi_\ell = 0.10$	1.52	20.17	12.67	1.26	309.3	24.8	30.8

Table 3.2 – *Turbulence flow parameters for the two multi-phase non-evaporative cases with $\phi_\ell = 0.05$ and $\phi_\ell = 0.10$, at the non-dimensionalized time $t^* = 12.0$ and $t^+ = 9$, respectively.*

3.4 Characterization of the multi-phase flows evaporative cases

Instantaneous snapshots of the three-dimensional turbulent two-phase flow with $\phi_\ell = 0.10$ are presented in Fig. 3.12. The displayed iso-contour value corresponds to the liquid-gas interface, i.e., $G = 0$. The considered non-dimensional time ($t^* = 6.0$), correspond to a mean mixture fraction value of $\overline{\xi} = 0.56$. On the left, the interface

is colored by the normalized vorticity magnitude, $||\omega||$. On the right, the mixture fraction, ξ, is presented at the planes settled at the boundaries, the iso-contours are set to a certain level of transparency so that the planes can be visualized.

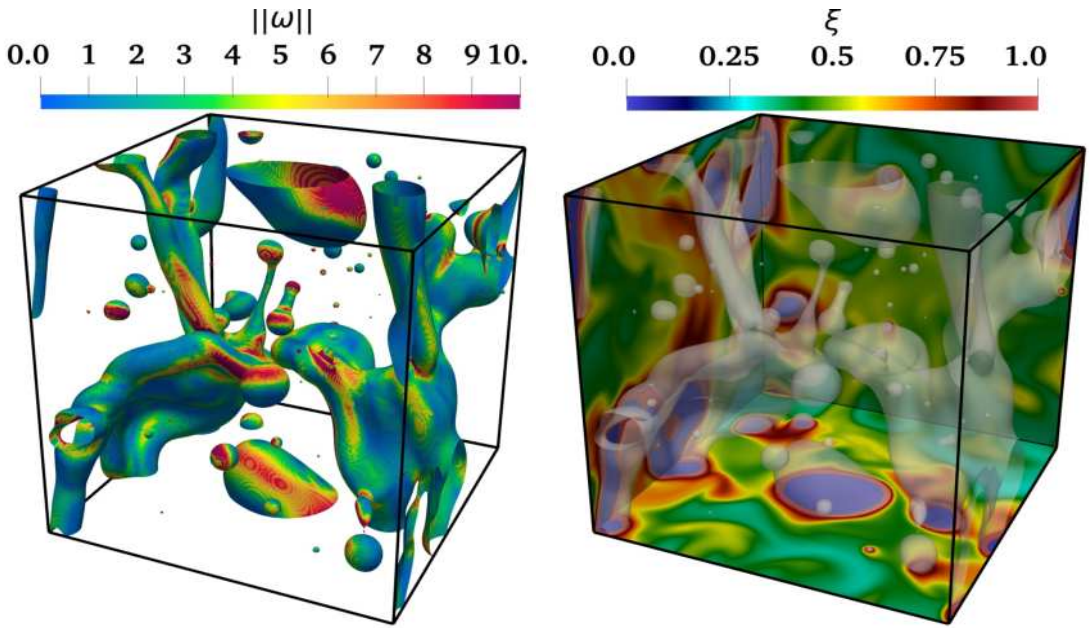

(a) $t^* = 6.0$ **(b)** $t^* = 6.0$

Figure 3.12. *Instantaneous 3D-snapshots of the turbulent two-phase flow case with* $\phi_\ell = 0.10$ *at the non-dimensional time,* $t^* = 6.0$*, when the value of the mean mixture fraction of* $\overline{\xi} = 0.56$ *is reached. The displayed contours corresponds to the liquid-gas interface, i.e., the level-set value, G, equal to zero. On the left, the interface is colored by the normalized vorticity magnitude,* $||\omega||$*. On the right, the iso-contours are set to a certain level of transparency, so the planes where the mixture fraction is displayed,* ξ*, can be visualized.*

3.4.1 Mixture fraction evolution

Figure 3.13 shows the evolution of the mean mixture fraction, $\overline{\xi}$, as a function of the non-dimensionalized time, t^*, for $\phi_\ell = 0.05$ (—), and $\phi_\ell = 0.10$ (- - -). As can be expected, the case with a larger quantity of liquid presents higher levels of evaporation.

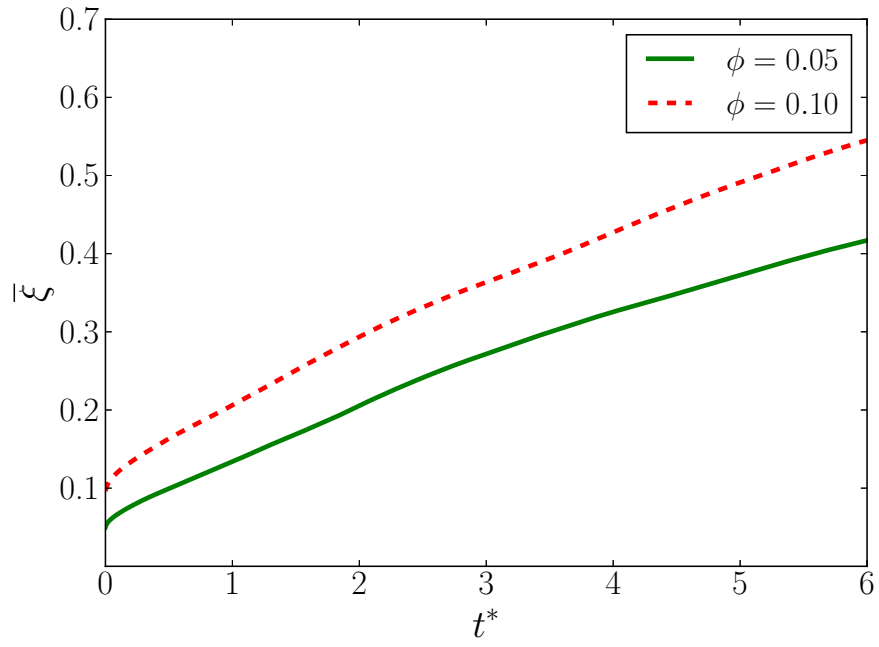

Figure 3.13. *Evolution of the mean mixture fraction, $\overline{\xi}$, as a function of the non-dimensionalized time, t^*, for the evaporative multi-phase HIT simulations with $\phi_\ell = 0.05$ (——), and $\phi_\ell = 0.10$ (- - -).*

3.4.2 Turbulent fields

Some classical turbulence flow parameters for both evaporative multi-phase cases $\phi_\ell = 0.05$ and $\phi_\ell = 0.10$ are gathered in Table 3.3.

Case	u_{RMS} (m/s)	ℓ_t (μm)	λ (μm)	η_K (μm)	Re_t (-)	Re_λ (-)	τ_{T_1} (μs)
$\phi_\ell = 0.05$	1.54	18.57	11.82	1.21	306.9	23.9	17.5
$\phi_\ell = 0.10$	1.47	23.30	14.26	1.33	293.0	26.1	19.9

Table 3.3 – *Turbulence flow parameters for the reference HIT case, and the two multi-phase evaporative cases with $\phi_\ell = 0.05$ and $\phi_\ell = 0.10$, at the non-dimensionalized time $t^* = 6.0$.*

Table 3.4 contains some important turbulent two-phase flow parameters for both multi-phase simulated cases. The dimensionless numbers corresponding to this data-set (extracted at the time $t^* = 6.0$) are : mean evaporation $\left(\overline{\xi}\right)$, gaseous Weber number $\left(We_g = \rho_g \kappa L/\sigma\right)$, liquid Weber number $\left(We_\ell = \rho_\ell \kappa L/\sigma\right)$, Reynolds number based on the liquid $\left(Re_\ell = \sqrt{\frac{2}{3}\kappa} L/\nu_\ell\right)$, and the Ohnesorge number based on the liquid $\left(Oh_\ell = \sqrt{We_\ell}/Re_\ell\right)$.

Simulation	$\overline{\xi}$	We_g (-)	We_ℓ (-)	Re_ℓ (-)	Oh_ℓ (-)
$\phi_\ell = 0.05$	0.44	1.23	48.2	350	0.02
$\phi_\ell = 0.10$	0.56	1.12	72.7	430	0.02

Table 3.4 – *Multi-phase flow parameters at post-processed time* $t^* = 6.0$ *for both cases,* $\phi_\ell = 0.05$ *and* $\phi_\ell = 0.10$.

3.5 Summary and conclusions

In this chapter the technical details considered to set-up the numerical simulations are presented, and followed by the inspection of the resolution capacity and stability of the code ARCHER to tackle : HIT, non-evaporative and evaporative two-phase flow simulations. The physical properties of the simulations, summarized in Table 3.5 and Table 3.6, are relevant to the secondary breakup regime of a jet, so interactions between the turbulence and the liquid-gas interface such as collision, coalescence and disintegration of large structures take place and are captured accurately with these numerical solver. It is worthy to point out that such regime has a significant engineering relevance for spray combustion devices.

Instantaneous snapshots of the three-dimensional turbulent two-phase flow with $\phi_\ell = 10$ are displayed in Fig. 3.14. The displayed contour corresponds to a given iso-value of the level-set (G), which is a signed distance from the liquid-gas interface to any point of the domain. Such iso-contour value is $G = -2\Delta x$, i.e., a surface in the gaseous phase but in the vicinity of the liquid-gas interface, which are colored by the value of the normalized second invariant Q_A/Q_Ω of the VGT. Three distinct values of non-dimensional times are presented : (a) $t^+ = 0.0$, (b) $t^* = 0.0$, and (c) $t^* = 6.0$. The corresponding set of figures clearly confirms that the interface displays significant levels of curvature and wrinkling, which may conversely alter the behavior of the turbulence field, the mixture fraction and the scalar dissipation rate (SDR) in the vicinity of the interface.

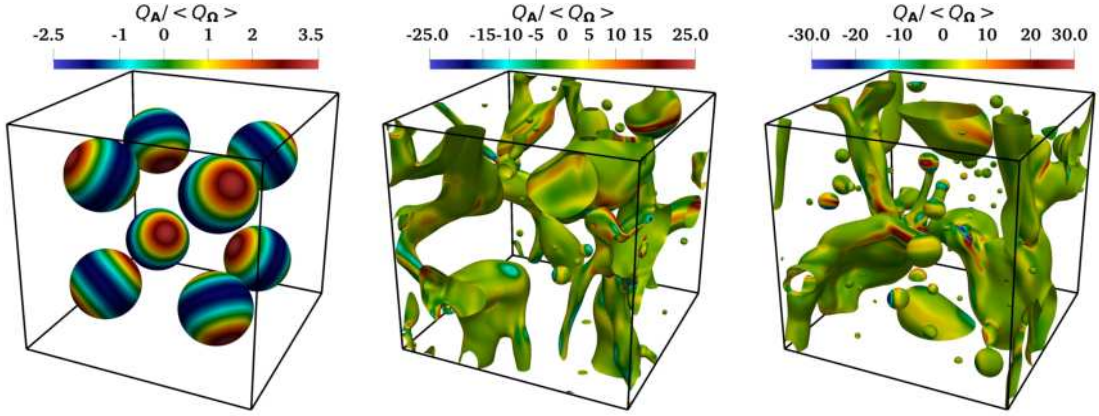

(a) $t^+ = 0.0$ **(b)** $t^* = 0.0$ **(c)** $t^* = 6.0$

Figure 3.14. *Instantaneous 3D-snapshots of the turbulent two-phase flow case with* $\phi_\ell = 0.10$ *at three different non-dimensional times : (a) initialization of the domain* $(t^+ = 0.0)$*, (b) activation of the evaporation module* $(t^* = 0.0)$*, and (c) time-step with a mean vapor concentration of* $\overline{\xi} = 0.56$ $(t^* = 6.0)$*. The displayed contours correspond to the level-set value of* $G = -2\Delta x$*, which are colored by the second invariant* Q_A *normalized by the average value of the second invariant of the rotation tensor, i.e.,* $\langle Q_\Omega \rangle = \langle -\Omega_{ij}\Omega_{ji}/2 \rangle$*.*

Case	u_{RMS} (m/s)	ℓ_t (μm)	λ (μm)	η_K (μm)	Re_t (-)	Re_λ (-)	τ_{T_0} (μs)	τ_{T_1} (μs)
HIT	1.55	16.71	11.03	1.18	309.2	22.7	44.6	-
$\phi_\ell = 0.05$	1.54	18.57	11.82	1.21	306.9	23.9	21.4	17.5
$\phi_\ell = 0.10$	1.47	23.30	14.26	1.33	293.0	26.1	30.8	19.9

Table 3.5 – *Turbulence flow parameters for the reference HIT case at the non-dimensionalized time* $t^+ = 2.5$*, and for the two multi-phase evaporative cases with* $\phi_\ell = 0.05$ *and* $\phi_\ell = 0.10$*, at the non-dimensionalized time* $t^* = 6.0$*.*

Simulation	$\overline{\xi}$	We_g (-)	We_ℓ (-)	Re_ℓ (-)	Oh_ℓ (-)
$\phi_\ell = 0.05$	0.44	1.23	48.2	350	0.02
$\phi_\ell = 0.10$	0.56	1.12	72.7	430	0.02

Table 3.6 – *Multi-phase flow parameters at post-processed time* $t^* = 6.0$ *for both cases,* $\phi_\ell = 0.05$ *and* $\phi_\ell = 0.10$*.*

4

Velocity field analysis of evaporative two-phase flows in HIT

Content of the chapter

The chapter presents the statistical characterization of the turbulent velocity field. Firstly are addressed the results concerning the velocity fluctuations, e.g., turbulent kinetic energy or associated Reynolds stress tensor, which characterize the energetic scales. Then attention is turned to the velocity gradient tensor (VGT), which is relevant to the dissipative scales. It is worth recalling that the velocity gradient tensor $\boldsymbol{A} = \boldsymbol{\nabla} \otimes \boldsymbol{u}$ contains key information about the rates of deformation of infinitesimal material lines, surfaces, and volumes [63]. The evolution of the turbulence characteristics is scrutinized at various distances from the interface, in such a manner that that the gas phase is divided into several sub-regions according to the values of the level-set G, i.e., the distance from the liquid-gas interface, as shown in Table 4.1. The acquisition of the statistics proceed in this way because the liquid-gas interface does not only alter the isotropy of velocity fluctuations but also the dissipative (i.e., small-scale) structure of the turbulent flow-field. It should be emphasized that, in the gaseous phase, the distance to the interface is defined in such a manner that the level-set value, G, is negative.

gas phase region	range of level-set values
far [♦]	$G \leq -20\Delta x$
intermediate [■]	$-20\Delta x < G \leq -5\Delta x$
near [●]	$-5\Delta x < G \leq 0.0$

Table 4.1 – *Definition of three sub-regions in the gas phase based on the level-set value.*

4.1 Theoretical background

Lumley triangles

This 2D-space, originally introduced by Lumley and Newman (1977) [61], provides a geometrical proof where any tensor whose eigenvalues are invariably non-negative should remain inside the triangle delineated by the limiting values of the second and third invariants of the considered tensor. Its labels are two independent invariants that can be determined at any point or for any time in the flow from the normalized (traceless) Reynolds-stress anisotropy tensor b_{ij}

$$b_{ij} = \frac{a_{ij}}{2\kappa} = \frac{\overline{u_i u_j}}{\overline{u_k u_k}} - \frac{1}{3}\delta_{ij}$$

Originally these invariants are $\mathrm{II} = \left(-b_{ij}b_{ji}/2\right)$, and $\mathrm{III} = \left(-b_{ij}b_{jk}b_{ki}/3\right)$, the non-linear behavior in the return to isotropy is not so easy to visualize, therefore a modified presentation of the invariants i.e., a modified Lumley triangle [60], has been introduced, based on the quantities η^* and ξ^*, such that :

$$\eta^* = \left(b_{ij}b_{ji}\right)^{1/2} \quad 6\xi^* = \left(b_{ij}b_{jk}b_{ki}\right)^{1/3}$$

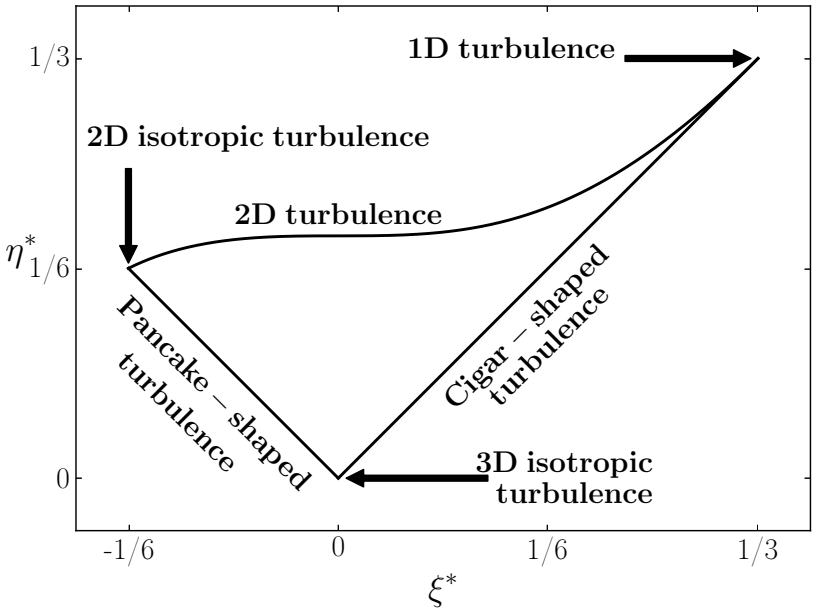

Figure 4.1. *Modified Lumley triangle.*

(R_A, Q_A)-phase plane

The components of the velocity gradient tensor, $\boldsymbol{A}$, are given by

$$A_{ij} \equiv \frac{\partial u_i}{\partial x_j} = S_{ij} + W_{ij} \ , \tag{4.1}$$

with $\boldsymbol{S}$ its symmetric part

$$S_{ij} \equiv \frac{1}{2}\left(A_{ij} + A_{ji}\right) = \frac{1}{2}\left(\frac{\partial u_i}{\partial x_j} + \frac{\partial u_j}{\partial x_i}\right) \ , \tag{4.2}$$

and $\boldsymbol{W}$ its anti-symmetric part

$$W_{ij} \equiv \frac{1}{2}\left(A_{ij} - A_{ji}\right) = \frac{1}{2}\left(\frac{\partial u_i}{\partial x_j} - \frac{\partial u_j}{\partial x_i}\right) \ . \tag{4.3}$$

The eigen-values of the VGT, i.e., λ_1, λ_2 and λ_3 (in decreasing order $\lambda_1 \geq \lambda_2 \geq \lambda_3$) are the roots of its characteristic equation

$$\det[\boldsymbol{A} - \lambda \boldsymbol{I}] = 0.0 \ , \tag{4.4}$$

while the invariants P_A, Q_A, and R_A of the VGT are defined as the normalized

coefficients of this characteristic equation

$$\lambda^3 + P_A\lambda^2 + Q_A\lambda + R_A = 0 \tag{4.5}$$

They can be expressed as [17]

$$P_A = -\text{tr}[\boldsymbol{A}] = -A_{kk}\ , \tag{4.6a}$$
$$Q_A = \frac{1}{2}\left(P_A^2 - \text{tr}[\boldsymbol{AA}]\right) = \frac{1}{2}\left(P_A^2 - A_{ij}A_{ji}\right)\ , \tag{4.6b}$$
$$R_A = \frac{1}{3}\left(-P_A^3 + 3P_AQ_A - \text{tr}[\boldsymbol{AAA}]\right) = \frac{1}{3}\left(-P_A^3 + 3P_AQ_A - A_{ij}A_{jk}A_{ki}\right) \tag{4.6c}$$

In general the (P_A, Q_A, R_A)-phase space allows to classify the streamlines topology (Perry and Chong, Chong et al. [77, 17]) of turbulent flow-fields in terms of elementary flow patterns. In other words, the (P_A, Q_A, R_A)-phase space reveals the relationship between the turbulent topology and the vortex-stretching / compressing mechanisms. The first invariant of the VGT, P_A, represents the local volumetric dilatation rate, i.e., the local change of an infinitesimal fluid volume, in such a way that the fluid volume experiments compression in the region where P_A has positive values $(P_A > 0.0)$, meanwhile it may experiments expansion in the region where P_A has negative values, $(P_A < 0.0)$. There exists a region in this invariant-space of singular interest where zero dilatation takes place, which corresponds to the phase-plane where this firs VGT invariant is zero, $(P_A \equiv 0.0, Q_A, R_A)$. Such (R_A, Q_A)-phase plane, depicted in Figure 4.2, displays four distinct non-degenerative regions delineated by considering the vertical axis $(R_A = 0.0)$ and two lines originating from the origin $(Q_A = 0.0, R_A = 0.0)$ that are often referred to as the Vieillefosse discriminant tails [107]. Such Vieillefosse discriminant curve gathers solutions to $\Delta^* \equiv (27/4)R_A^2 + Q_A^3 = 0.0$, i.e., zero values of the discriminant of the VGT characteristic polynomial. The topologies above the zero-discriminant lines $(\Delta^* > 0.0)$, are spiraling in nature (governed by vortex mechanisms), and are often referred to as focal topologies, whereas the topologies below these lines $(\Delta^* < 0.0)$, do not spiral about a focus, (governed by strain mechanisms), and are therefore termed as non-focal topologies. The third VGT invariant, R_A, defines two critical points in this phase-plane, the stable for $R_A < 0.0$ and the unstable for $R_A > 0.0$. Now it is easy to describe the different mechanisms that are shown in this (R_A, Q_A)-phase plane. In the vorticity-dominated regions $(\Delta^* > 0.0)$, enstrophy-production is associated to vortex-stretching mechanisms $(R_A < 0.0)$, whereas enstrophy-dissipation is related to vortex-compressing mechanisms $(R_A < 0.0)$. In the strain-dominated regions $(\Delta^* < 0.0)$, bi-axial compression generates tube-like structures $(R_A < 0.0)$, albeit bi-axial stretching generates sheet-like structures $(R_A > 0.0)$. The four regions mentioned above, according to the terminology of Perry

and Chong [77], correspond to : unstable-focus compressing (UF/C), stable-focus stretching (SF/S), stable-node saddle-saddle (SN/S/S), and unstable-node saddle-saddle (UN/S/S) from the top right-hand corner to the bottom right-hand corner (counter clockwise). These four regions will also be hereafter denoted by quadrants Q_1, Q_2, Q_3, and Q_4, respectively.

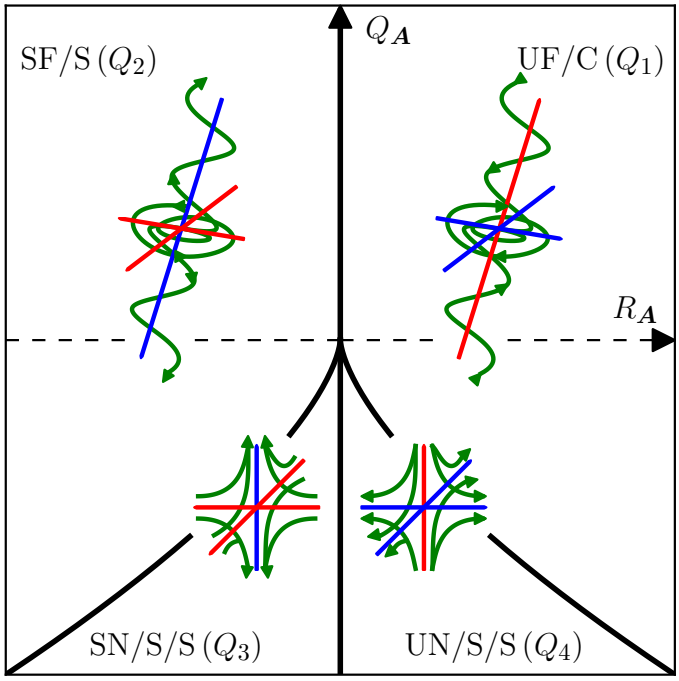

Figure 4.2. *Classification of streamline topology in the (R_A, Q_A)-phase plane : unstable-focus compressing (UF/C), stable-focus stretching (SF/S), stable-node saddle-saddle (SN/S/S), and unstable-node saddle-saddle (UN/S/S).*

It is paramount to mention that is possible to work in this (R_A, Q_A)-phase plane with zero dilatation, independently of the flow condition considered, e.g., multi-phase, reactive, compressible, etc. To this purpose, the deviatoric counterparts of 4.6 may be considered. Such deviatoric invariants are defined from the traceless part of the VGT tensor $\boldsymbol{A}^*$

$$A^*_{ij} \equiv A_{ij} - \frac{\theta}{3}\delta_{ij} \,, \tag{4.7}$$

with δ_{ij} the Kronecker tensor and $\theta \equiv \mathrm{tr}[\boldsymbol{A}] = A_{kk} = -P$ the dilatation-rate, i.e., the trace of $\boldsymbol{A}$. Similarly, the symmetric and anti-symmetric parts of $\boldsymbol{A}^*$ are denoted as $\boldsymbol{S}^*$ and $\boldsymbol{W}^*$, respectively, and the invariants of $\boldsymbol{A}^*$ can be expressed as [79]

$$P^*_A = -A^*_{kk} \equiv 0 \,, \tag{4.8a}$$

$$Q^*_A = -\frac{1}{2}A^*_{ij}A^*_{ji} \,, \tag{4.8b}$$

$$R_A^* = -\frac{1}{3} A_{ij}^* A_{jk}^* A_{ki}^* \,. \tag{4.8c}$$

Straining processes

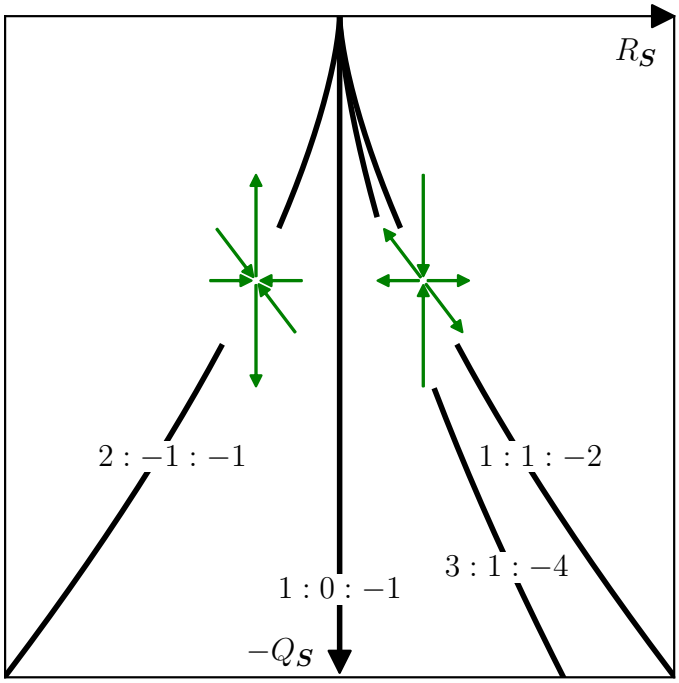

Figure 4.3. *Definitions of some lines corresponding to different ratios of principal strains* $(\lambda_1 : \lambda_2 : \lambda_3)$ *in* (R_S, Q_S)*-phase plane : axi-symmetric expansion, i.e., axial stretching* $(1:1:-2)$*; axi-symmetric contraction, i.e., axial contraction* $(2:-1:-1)$*; two-dimensional flow* $(1:0:-1)$*; and straining by bi-axial stretching* $(3:1:-4)$.

The JPDF of the normalized second and third invariants of the strain-rate tensor $\boldsymbol{S} = (\boldsymbol{A} + \boldsymbol{A}^{\boldsymbol{T}})/2$, i.e., Q_S and R_S, can be analyzed to get further insights into the straining processes. Thus, different regions can be delineated in the (R_S,Q_S)-plane, see Fig. 4.3. In fact, Q_S is negative-definite and the topology mainly depends on the sign of R_S with sheet-like structures associated to $R_S > 0.0$ and tube-like structures to $R_S < 0.0$. Further information can be obtained by dividing the (R_S, Q_S)-phase plane into various sub-regions, which are defined according the eigenvalue ratios $(\lambda_1 : \lambda_2 : \lambda_3)$. In this manner, the right branch of the Vieillefosse discriminant line $(1:1:-2)$ corresponds to axi-symmetric expansion, i.e., axial stretching, while the left branch of the Vieillefosse discriminant line $(2:-1:-1)$ represents axi-symmetric contraction, i.e., axial contraction. The two-dimensional straining limit can be associated to the line $R_S = 0$, which corresponds to $(1:0:-1)$. Finally, the fourth region represents bi-axial stretching $(3:1:-4)$, it is located between the line $R_S = 0.0$ and

the right branch of the Vieillefosse discriminant tail.

Topology of dissipative and vortical regions

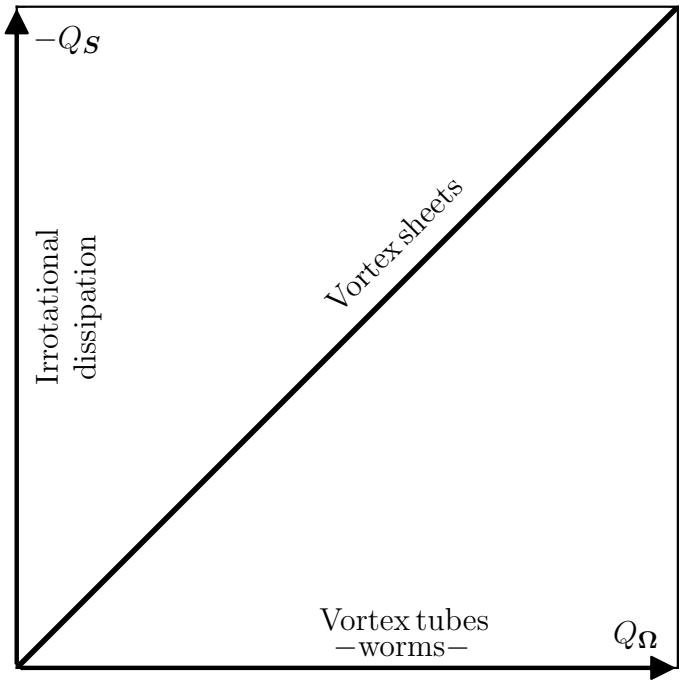

Figure 4.4. *Classification of streamline topology of the dissipative and vortical regions of the* $(Q_\Omega, -Q_S)$*-phase plane.*

The $(Q_\Omega, -Q_S)$-phase plane, Fig. 4.4, provide information on the topology of the dissipative and vortical regions. Since the quantities Q_Ω and $-Q_S$ are positive, the topology information depends on the direction along which the JPDF contours are aligned : the Q_Ω-axis is relevant to vortex tubes, i.e., structures featuring high enstrophy levels and moderate dissipation rates (similar to solid-body rotation) whereas the $-Q_S$-axis represents irrotational dissipation with high level of strain and negligible vorticity. Finally, the zone of high correlation (i.e., the vicinity of the first bisecting line) is relevant to vortex sheets, i.e., structures featuring both high strain and vorticity levels.

Dynamics of 'worms' formation

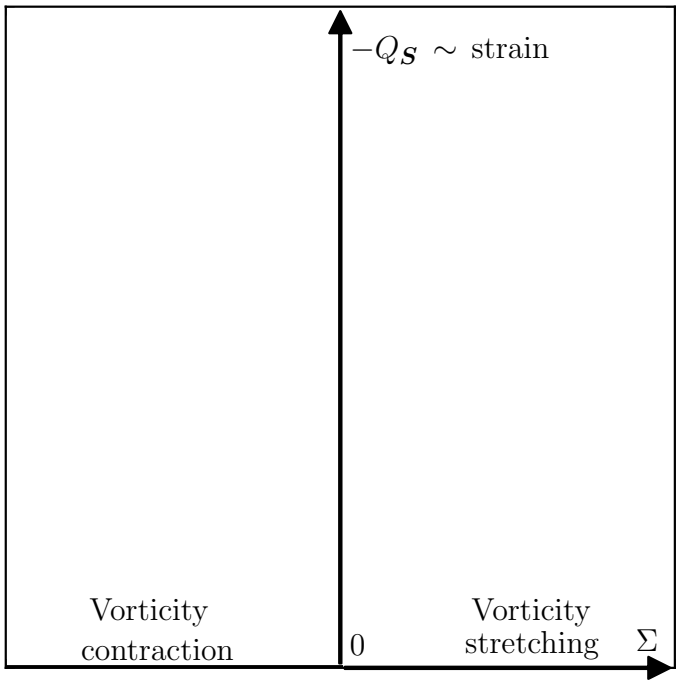

Figure 4.5. *Classification of streamline topology related to the strain dynamics of the worms formation in the* $(\Sigma, -Q_S)$*-phase plane.*

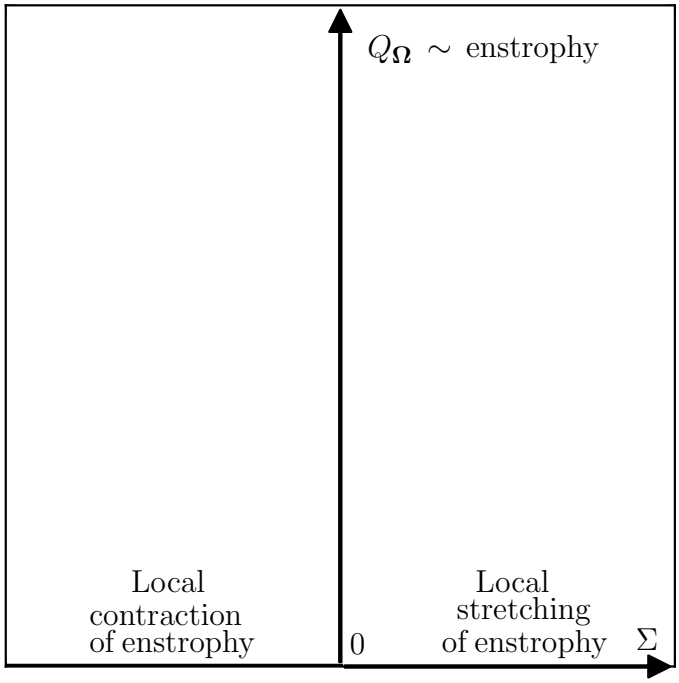

Figure 4.6. *Classification of streamline topology related to the enstrophy dynamics of the worms formation in the* (Σ, Q_Ω)*-phase plane.*

The dynamics of worms formation is analyzed in Figs. 4.5 and 4.6, in the light of the joint statistics of the second invariant (either $-Q_S$ or Q_Ω) together with the normalized vorticity stretching-contracting rate $\Sigma = \boldsymbol{\omega} \cdot \boldsymbol{S} \cdot \boldsymbol{\omega} / Q_\Omega = (R_S - R_A)/Q_\Omega$. The corresponding JPDF of $(\Sigma, -Q_S)$ and (Σ, Q_Ω) are displayed for the three regions in Fig. 4.5 and Fig. 4.6. Since the quantities $-Q_S$ and Q_Ω are positive, the topology information mostly depends upon the sign of Σ : its positiveness in the $(\Sigma, -Q_S)$-phase plane is relevant to vorticity-stretching whereas, in the $(\Sigma, -Q_\Omega)$-phase plane, it is associated to local enstrophy-stretching. On the contrary, negative values of Σ corresponds to either vorticity or enstrophy contraction. It is worthy to point out that once the vorticity is stretched to a sufficiently high amplitude, it decouples from the original strain field and looses its orientation relative to it.

Vorticity-eigenframe alignments

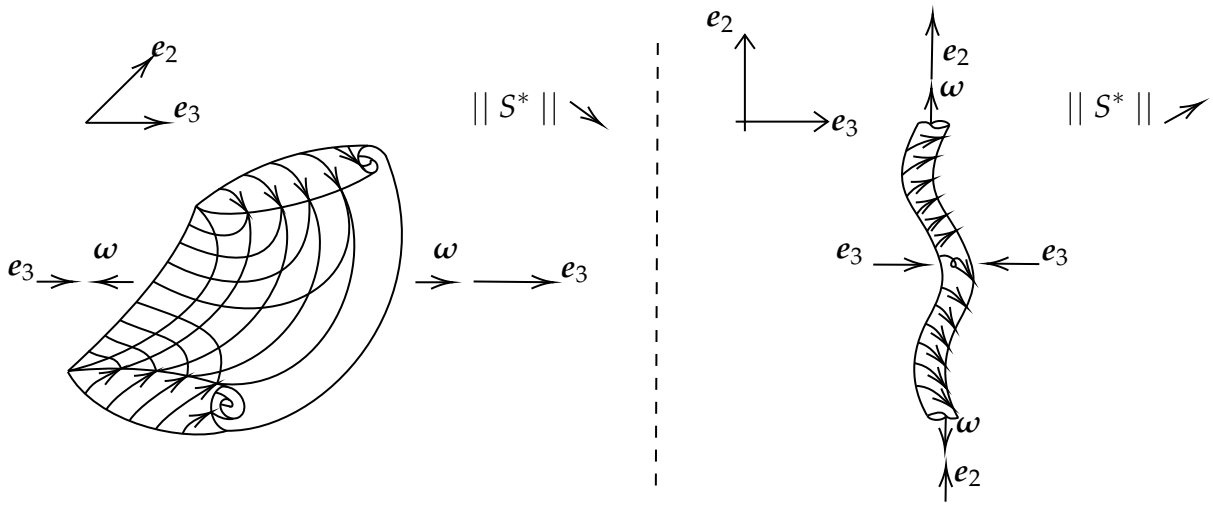

Figure 4.7. *Schematic of the different vortical structures. On the left is depicted the sheet-like-strain-dominated structure, and on the right is the tube-like-strain-dominated structure. Here, S^* is the normalized enstrophy production term associated with the vortex-stretching effects $\left(S^* = \boldsymbol{\omega} \cdot \boldsymbol{S} \cdot \boldsymbol{\omega} / (\nu/\eta^2)^3\right)$.*

The vortical structures gathered in isotropic homogeneous turbulence are presented in Fig.4.7. On the left is depicted the sheet-like-strain-dominated structure, gathered when the vorticity vector $\boldsymbol{\omega}$ is aligned with the most compressive eigen-vector $(\boldsymbol{e}_3)$. Such alignment is relevant to enstrophy decrease $(|| S^* ||\downarrow)$. On the right is depicted the tube-like-strain-dominated structure, gathered when the vorticity vector $(\boldsymbol{\omega})$ is aligned with the intermediate eigen-vector $(\boldsymbol{e}_2)$. Such alignment is relevant to enstrophy increase $(|| S^* ||\uparrow)$. Here, S^* is the normalized enstrophy production term associated with the vortex-stretching effects $\left(S^* = \boldsymbol{\omega} \cdot \boldsymbol{S} \cdot \boldsymbol{\omega} / (\nu/\eta^2)^3\right)$. In isotropic

homogeneous turbulence, vorticity $(\boldsymbol{\omega})$ displays high transversality with the most extensive $(\boldsymbol{e}_1)$ and the most compressing $(\boldsymbol{e}_3)$ directions, and preferential alignment with the intermediate $(\boldsymbol{e}_2)$ eigenvector. Such alignment reflects the enhancement of the energy transfer due to vortex-stretching mechanisms [104].

Vorticity-vorticity stretching vector alignment

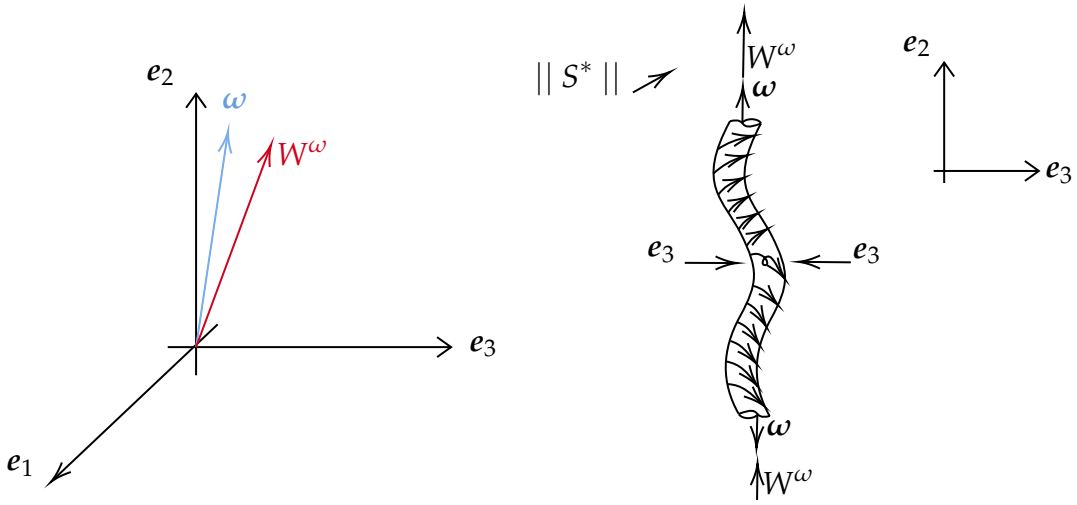

Figure 4.8. *On the left the eigen-space and the alignment between the vorticity $(\boldsymbol{\omega})$ and its corresponding vortex-stretching vector $(\boldsymbol{W}^\omega)$. On the right the sketch of the corresponding vortical structure gathered when high alignment between these two vectors happen. Here, S^* is the normalized enstrophy production term associated with the vortex-stretching effects $\left(S^* = \boldsymbol{\omega}\cdot\boldsymbol{S}\cdot\boldsymbol{\omega}/(\nu/\eta^2)^3\right)$.*

The typical alignment between the vorticity $(\boldsymbol{\omega})$ and its corresponding vortex-stretching vector $(\boldsymbol{W}^\omega)$, is presented in Fig. 4.8. Such alignment is relevant to vortex-stretching mechanisms, i.e., enstrophy production $(||\ S^*\ ||\uparrow)$. It is noteworthy that the self-amplification phenomena diminishes due to the fairly large curvature of the vorticity lines, in such a way that these vortex-tubes become "passive structures", i.e., such vortex-worms does not interact back any more with the strain mechanisms. This suggests that regions with concentrated vorticity are the result/consequence rather than the dominating factor on the turbulence dynamics [104].

4.2 Large scale fluctuations

By the inspection of the modified Lumley triangle [61, 60, 16], a significant increase of turbulence anisotropy (in the gas phase) is confirmed as the level-set G approaches zero, i.e., in the vicinity of the liquid interface.

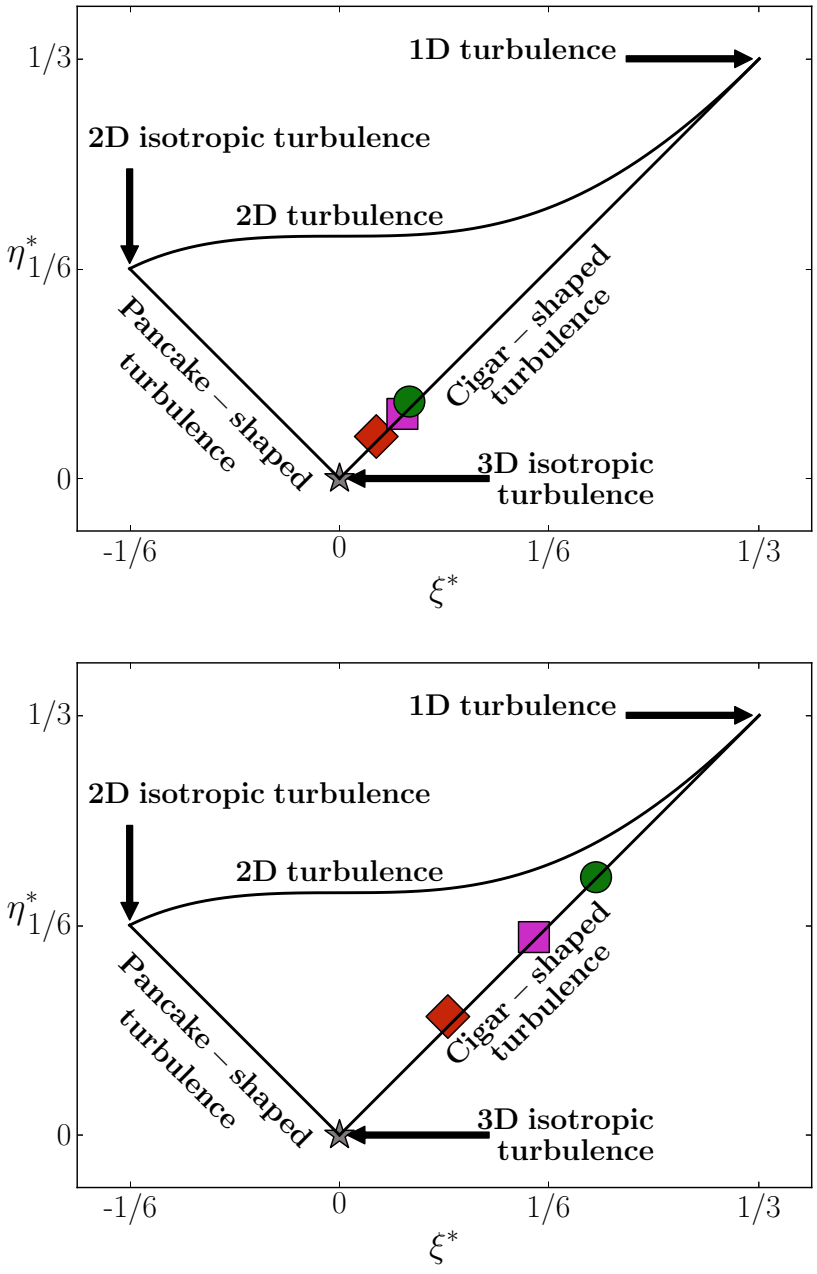

Figure 4.9. *Turbulence anisotropy as depicted in the modified Lumley triangle for* $\phi_\ell = 0.05$ *(top) and* $\phi_\ell = 0.10$ *(bottom). The symbols [*♦, ■, *and* ● *] correspond to the averaged behaviors observed in the far, intermediate, and near field regions from the liquid-gas interface, respectively. The symbol [*★*] corresponds to a reference HIT case in gaseous conditions. The invariants are defined as follows :* $6\left(\eta^*\right)^2 = b_{ij}b_{ji}$ *and* $6\left(\xi^*\right)^3 = b_{ij}b_{jk}b_{ki}$.

Thus, in Fig. 4.9 are reported the corresponding results for $\phi_\ell = 0.05$ at the top and $\phi_\ell = 0.10$ at the bottom (at $t^* = 6.0$ for both databases), together with the three-dimensional HIT reference case (symbol [★]). In the far region, the turbulent flow remains almost three-dimensional and isotropic ($\xi^* = \eta^* = 0$) for both cases $\phi_\ell = 0.05$ and $\phi_\ell = 0.10$. However, as the liquid-gas interface is approached, the couples of invariants (ξ^*, η^*) depart from the HIT region of the modified Lumley triangle and evolves towards the one-component state ($\xi^* = \eta^* = 1/3$), which is associated to axi-symmetric cigar-shaped turbulence, i.e., one-dimensional turbulence. Nonetheless, it seems worth to point out that the case with $\phi_\ell = 0.10$ display a larger departure than the one observed for $\phi_\ell = 0.05$. In regard to this, a similar behavior is reported in other flow configurations where other kind of interfaces are studied, such as : in the direct vicinity (downstream) of a shock wave in supersonic flow (Boukharfane et al. [8]), or in premixed flame front of flame kernel growth in weak turbulence (Zhao et al. [115]), in such a way that the standard HIT in the fresh reactants is modified and evolves towards one-dimensional turbulence for increasing values of the progress variable.

4.3 Small scale mixing and dissipation

4.3.1 Topology analysis

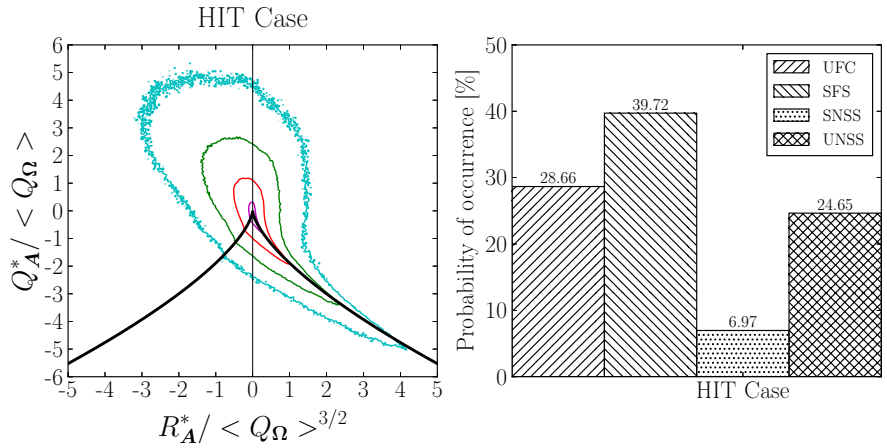

Figure 4.10. *JPDF of (R_A^*, Q_A^*) of the HIT reference case and their corresponding probability of occurrence of each flow topology quadrant. The four thin lines correspond to iso-contours of* $\log_{10}$ *(JPDF) equals to* -3, -2, -1, *and* 0. *Both invariants Q_A and R_A are normalized by the averaged value of the second invariant of the rotation tensor, i.e.,* $\langle Q_\Omega \rangle = \langle -\Omega_{ij}\Omega_{ji}/2 \rangle$.

Since the VGT is directly involved in the turbulence-scalar interaction (TSI), attention is turned to the flow topology of the small-scales of the velocity field. For this, the joint probability density function (JPDF) of the normalized second and third invariants of the velocity gradient tensor (i.e., Q_A^* and R_A^*) is inspected. Firstly the JPDF of the normalized second and third invariants of the VGT along with the probabilities of occurrence of each flow topology quadrant for the HIT reference case are scrutinized in Fig. 4.10. This JPDF shows a 'pear-like' shape, where most data points lie at the first, Q_1, and second, Q_2, quadrants of the (R_A^*, Q_A^*)-phase plane. This means that the flow have high probabilities to develop a local streamline topology that may produce or dissipate enstrophy due to vortex-stretching or vortex compressing mechanisms, respectively. It is also noteworthy that the probability of occurrence of the first, Q_1, and fourth, Q_4, quadrant are almost the same. The statistics of this latter quadrant have a remarkable tendency to embrace the right branch of the Vieillefosse discriminant line. This 'pear-like' shape is better known as the 'universal tear-drop' shape, simply because similar statistics have been already reported for a wide variety of flow configurations, e.g., plane mixing layer (Soria et al. [92]), turbulent boundary layer (Chong et al. [18]), etc. It has been also recovered far from different kind of interfaces or fronts, such as flames (Cifuentes et al., Wacks et al., Zhao et al. [19, 108, 115]) or shock waves (Ryu and Livescu, Boukharfane et al., Tian et al. [85, 8, 102]). Therefore this can be thought as a kind of universality of turbulence in the joint invariant (R_A^*, Q_A^*)-phase space.

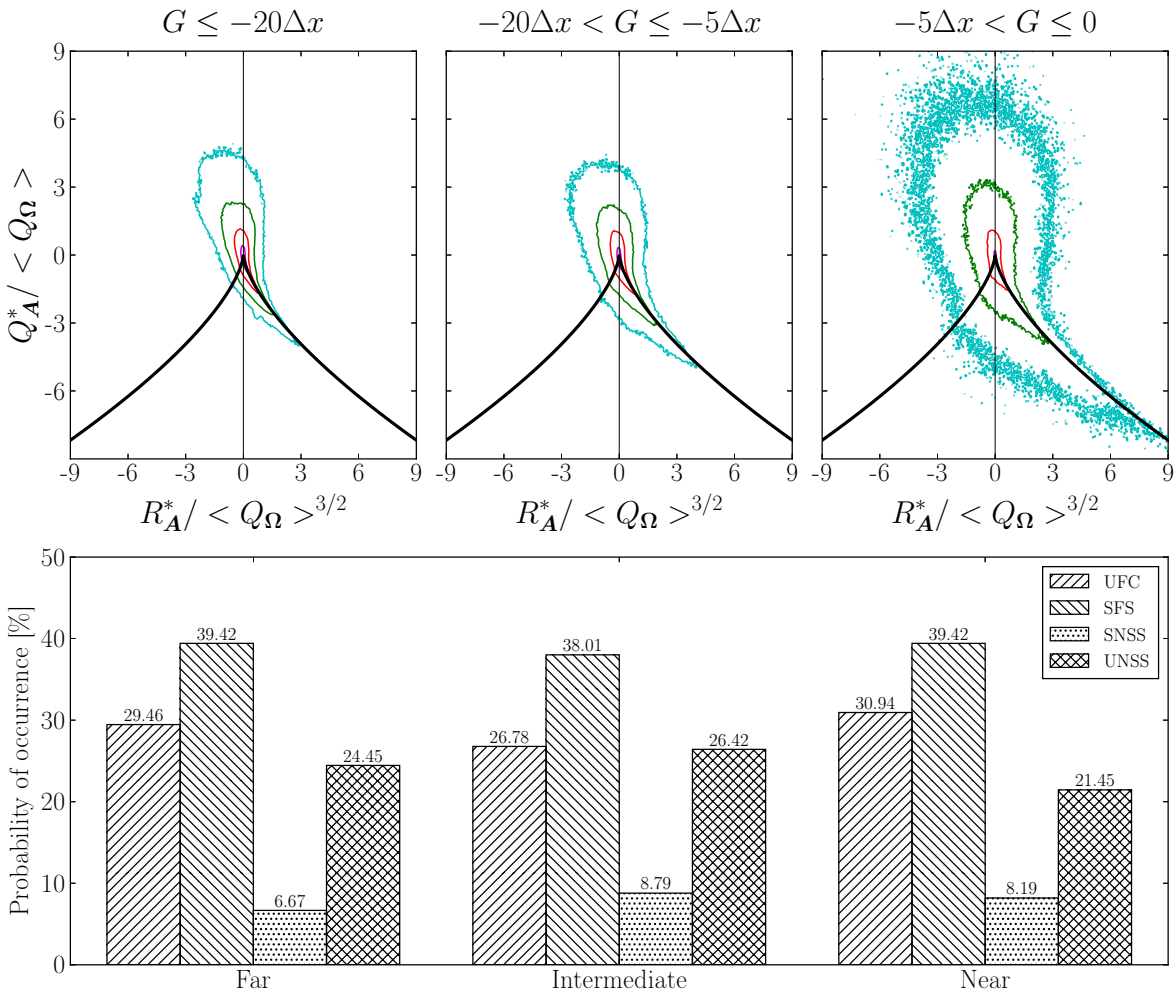

Figure 4.11. *JPDF of $(R^*_{\boldsymbol{A}}, Q^*_{\boldsymbol{A}})$ in the far (left), intermediate (center), and near (right) field regions together with the probability of occurrence of each streamline topology quadrant for $\phi_\ell = 0.05$. The four thin lines correspond to iso-contours of $\log_{10}$ (JPDF) equals to -3 -2, -1, and 0. Both invariants $Q^*_{\boldsymbol{A}}$ and $R^*_{\boldsymbol{A}}$ are normalized by the averaged value of the second invariant of the rotation tensor, i.e., $\langle Q_{\boldsymbol{\Omega}} \rangle = \langle -\boldsymbol{\Omega} \cdot \boldsymbol{\Omega} / 2 \rangle$.*

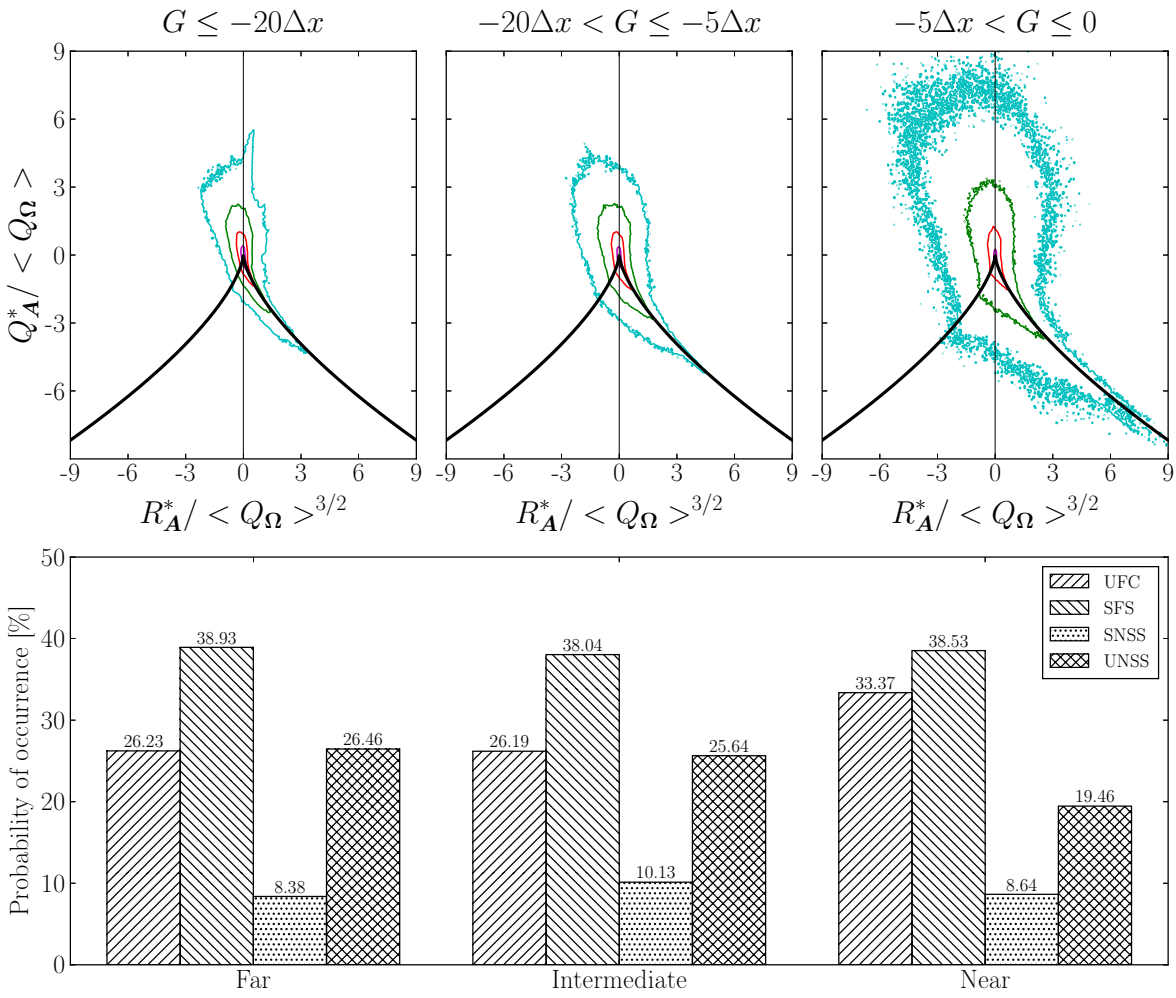

Figure 4.12. *JPDF of $(R^*_{\boldsymbol{A}}, Q^*_{\boldsymbol{A}})$ in the far (left), intermediate (center), and near (right) field regions together with the probability of occurrence of each streamline topology quadrant for $\phi_\ell = 0.10$. The four thin lines correspond to iso-contours of $\log_{10}$ (JPDF) equals to -3 -2, -1, and 0. Both invariants $Q^*_{\boldsymbol{A}}$ and $R^*_{\boldsymbol{A}}$ are normalized by the averaged value of the second invariant of the rotation tensor, i.e., $\langle Q_{\boldsymbol{\Omega}} \rangle = \langle -\boldsymbol{\Omega} \cdot \boldsymbol{\Omega}/2 \rangle$.*

Now, in order to shed light on the changes of the gaseous turbulence topology due to the presence of the liquid phase, the JPDF of the normalized second and third invariants of the VGT of the two-phase cases with $\phi_\ell = 0.05$ and $\phi_\ell = 0.10$ are considered in Figs. 4.11 and 4.12, respectively. In the same figures are also reported the probabilities of occurrence of each flow topology quadrant. In the far region, for both multi-phase cases, a 'tear-drop' shape quite similar to the one reported in Fig. 4.10 for the incompressible HIT case is conserved. Such tear-drop shape shows that the probability of occurrence, from the highest to the lowest, corresponds to the first, Q_1, second, Q_2, fourth, Q_4, and third Q_3 quadrants. There is a tendency, especially in the case with $\phi_\ell = 0.10$, to hug on the right branch of the Vieillefosse discriminant line. This suggests that, for the region under consideration, the flow-field topology is

barely impacted by the presence of liquid clusters and droplets. Nonetheless, as the liquid-gas interface is approached, the JPDF tend to become more symmetric with respect to the ordinate-axis. The corresponding histograms from Figs. 4.11 and 4.12 put into evidence that the more significant probability levels are associated to the SF/S topology region, which is relevant to enstrophy production via vortex-stretching mechanism, i.e., the first, Q_1 quadrant. Then, the next contributions are those that correspond to the first, Q_1, second, Q_2, quadrants. Their corresponding probability levels are significant and lie between 19.0% and 33.0%. The values of both quadrants are almost the same in the far region but become quite different as the interface is approached. Figures. 4.11 and 4.12 shows indeed that the volume fractions of each topology contribution gathered in the intermediate region contrast with those relevant to the far region. In particular, there is a significant increase of the probability levels associated to the third Q_3 quadrant, especially in the direct vicinity of the negative Vieillefosse discriminant line. This denotes a relevant increase of tube-like strain-dominated structures undergoing bi-axial compression. In the vicinity of the interface, the inspection of the volume fractions of each topology contribution shows, in comparison to the far region, a substantial increase of the probability levels of the first, Q_1 quadrant, and a decrease of the contribution of the fourth, Q_4 quadrant. Such behavior is more pronounced as the liquid volume fraction is increased from $\phi_\ell = 0.05$ to $\phi_\ell = 0.10$. Finally, in the region under consideration, the two dominant topologies correspond to the first, Q_1, and second, Q_2 quadrants, i.e., production and destruction of enstrophy due to vortex-stretching and vortex-compression mechanisms, respectively. They almost balance each other. This evolution goes together with an increased scatter of the corresponding data.

In order to analyze the straining processes, the JPDFs of (R_S, Q_S) are reported in Fig. 4.13 for the gaseous sub-regions. Far from the liquid-gas interface, for both volume of liquid fractions, a right-skewed joint statistics (i.e., $R_S > 0.0$) relevant to standard HIT is recovered [73]. This shape indicates that this region is mostly strain-dominated with sheet-like structures associated to axi-symmetric expansion (i.e., axial stretching). The JPDF gathered in the intermediate region presents a lower level of skewness, so the probability associated to a negative third invariant $(R_S < 0)$, relevant to strain-dominated flows with tube-like structures, is increased. This trend is enforced in near region : (i) for the case with $\phi_\ell = 0.05$ (top), there is an increase of the probability levels of bi-axial stretching, i.e., around the Vieillefosse discriminant-like line $(3:1:-4)$, and (ii) for the case with $\phi_\ell = 0.10$ (bottom), the same behavior is observed, together with a change of slope at $R_S = 0.0$: the flow-field tends to become two-dimensional in the vicinity of the interface.

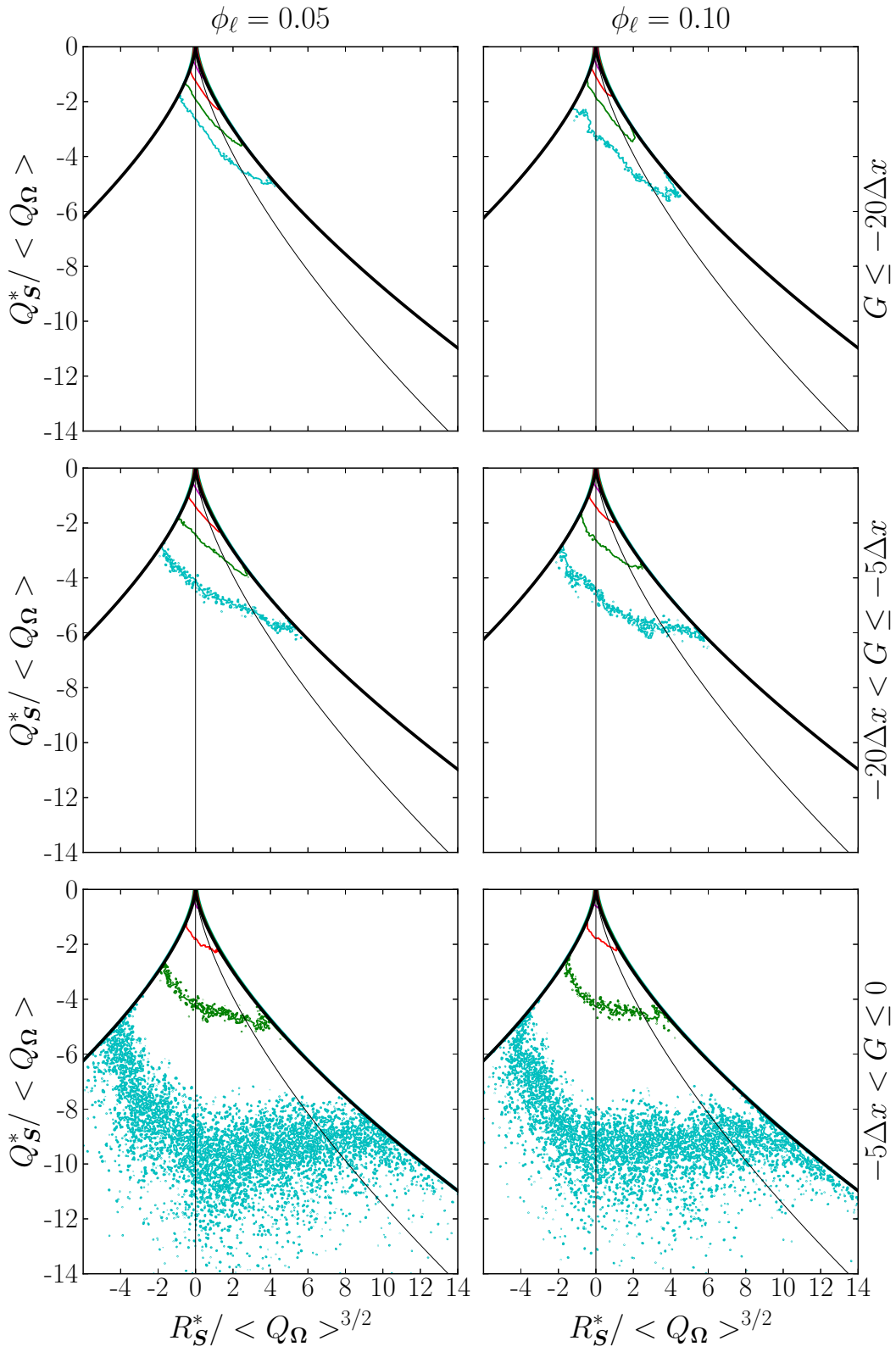

Figure 4.13. *JPDF of (R_S, Q_S) in the far (top row), intermediate (middle row), and near (bottom row) field regions for $\phi_\ell = 0.05$ (left column) and $\phi_\ell = 0.10$ (right column). The four thin lines correspond to iso-contours of $\log_{10}$ (JPDF) equals to -3 -2, -1, and 0. Both invariants R_S and Q_S are normalized by the averaged value of the second invariant of the rotation tensor, i.e., $\langle Q_\Omega \rangle = \langle -\mathbf{\Omega} \cdot \mathbf{\Omega}/2 \rangle$.*

The dissipative and vortical regions are studied in detail through the JPDFs of $(Q_\Omega, -Q_S)$, reported in Fig. 4.14. Far from the liquid-gas interface, for both cases $\phi_\ell = 0.05$ and $\phi_\ell = 0.10$, the right-skewed behavior of the standard HIT is recovered [73] $(Q_\Omega > -Q_S)$. The flow in this region resembles long-lived solid-body rotation, such topology is associated to structures featuring high values of enstrophy and little amounts of dissipation, i.e., vortex-tubes structures. The statistics gathered in the intermediate region loose this right-skewed tendency, such that Q_Ω and $-Q_S$ reach almost the same maximum values : vortex-tubes structures and irrotational dissipation display similar probability levels. Finally, in the vicinity of the interface, there is a significant increase in the magnitude of the invariants, in such a manner that enstrophy and dissipation rates increase as the interface is approached. Here, the probability iso-lines tend to cluster around the first bisecting line $(Q_\Omega = -Q_S)$, which is relevant to the prevalence of vortex-sheet structures. However, it is noteworthy that the statistics is top-skewed, thus emphasizing the predominance of dissipation over enstrophy in this region.

The dynamic of 'worms' formation is studied in Fig. 4.15 and Fig. 4.16. For both liquid volume fraction ($\phi_\ell = 0.05$ and $\phi_\ell = 0.10$), and for the three gaseous subregions, the joint statistics reported are associated to stretching processes, i.e., are right-skewed (positive values of Σ). This is in accordance with the behavior of the standard HIT [73]. Figures 4.15 and 4.16 also put into evidence that the largest values of Σ are associated to the lowest values of the corresponding abscissa-axis ($-Q_S$ and Q_Ω), which is related to little evidence of self-stretching by structures in the flow field which have large values of Q_Ω and $-Q_S$. For both statistics $(-Q_S, \Sigma)$ and (Q_Ω, Σ), the largest absolute values of Σ are associated to rather small or moderate values of $-Q_S$ and Q_Ω. Moreover, as the interface is approached, the distributions become narrower and more symmetric, with a reduced range of variation of Σ and an increased range of variation of both $-Q_S$ and Q_Ω.

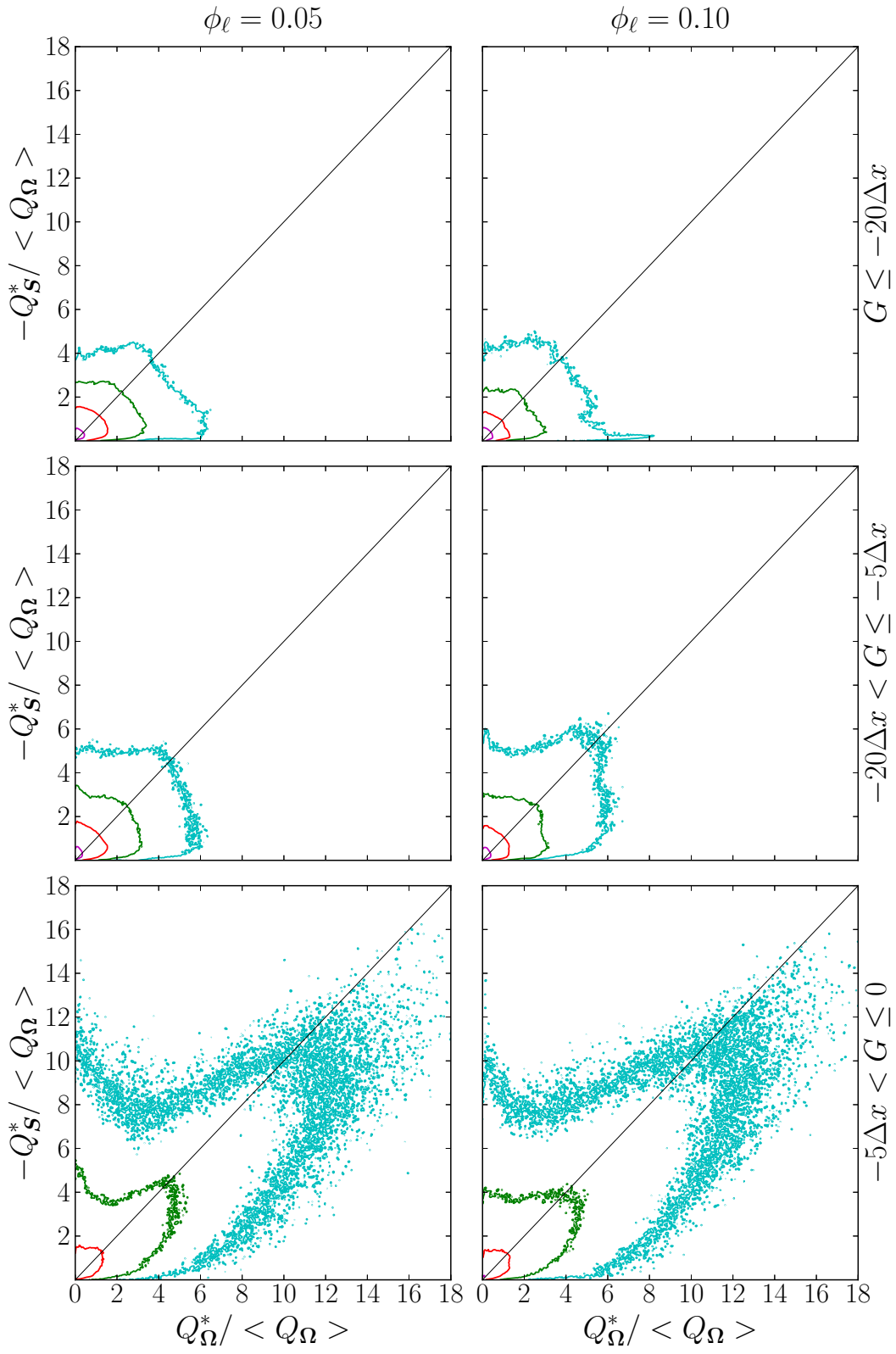

Figure 4.14. *Joint PDF* $(Q_\Omega, -Q_S)$ *in the far (top row), intermediate (middle row), and near (bottom row) field regions for* $\phi_\ell = 0.05$ *(left column) and* $\phi_\ell = 0.10$ *(right column). The four thin lines correspond to iso-contours of* $\log_{10}$ *(JPDF) equals to* -3 -2, -1, *and* 0. *Both invariants* Q_Ω *and* $-Q_S$ *are normalized by the averaged value of the second invariant of the rotation tensor, i.e.,* $\langle Q_\Omega \rangle = \langle -\mathbf{\Omega} \cdot \mathbf{\Omega}/2 \rangle$.

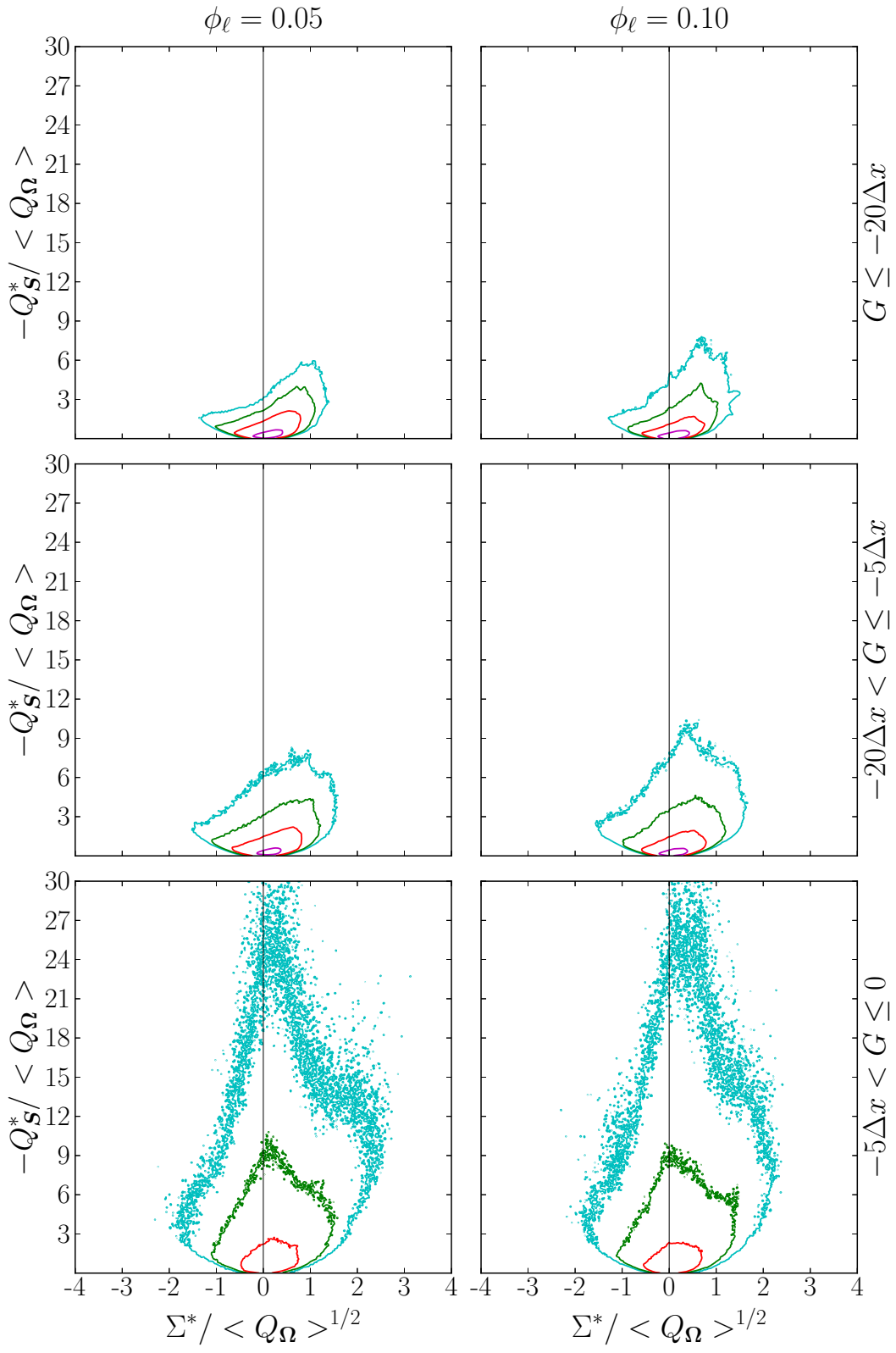

Figure 4.15. *Joint statistics of* $(\Sigma, -Q_S)$ *in the far (top row), intermediate (middle row), and near (bottom row) field regions for* $\phi_\ell = 0.05$ *(left column) and* $\phi_\ell = 0.10$ *(right column). The four thin lines correspond to iso-contours of* $\log_{10}$ *(JPDF) equals to* -3 -2, -1, *and* 0. *Both invariants* Σ *and* $-Q_S$ *are normalized by the averaged value of the second invariant of the rotation tensor, i.e.,* $\langle Q_\Omega \rangle = \langle -\mathbf{\Omega} \cdot \mathbf{\Omega}/2 \rangle$.

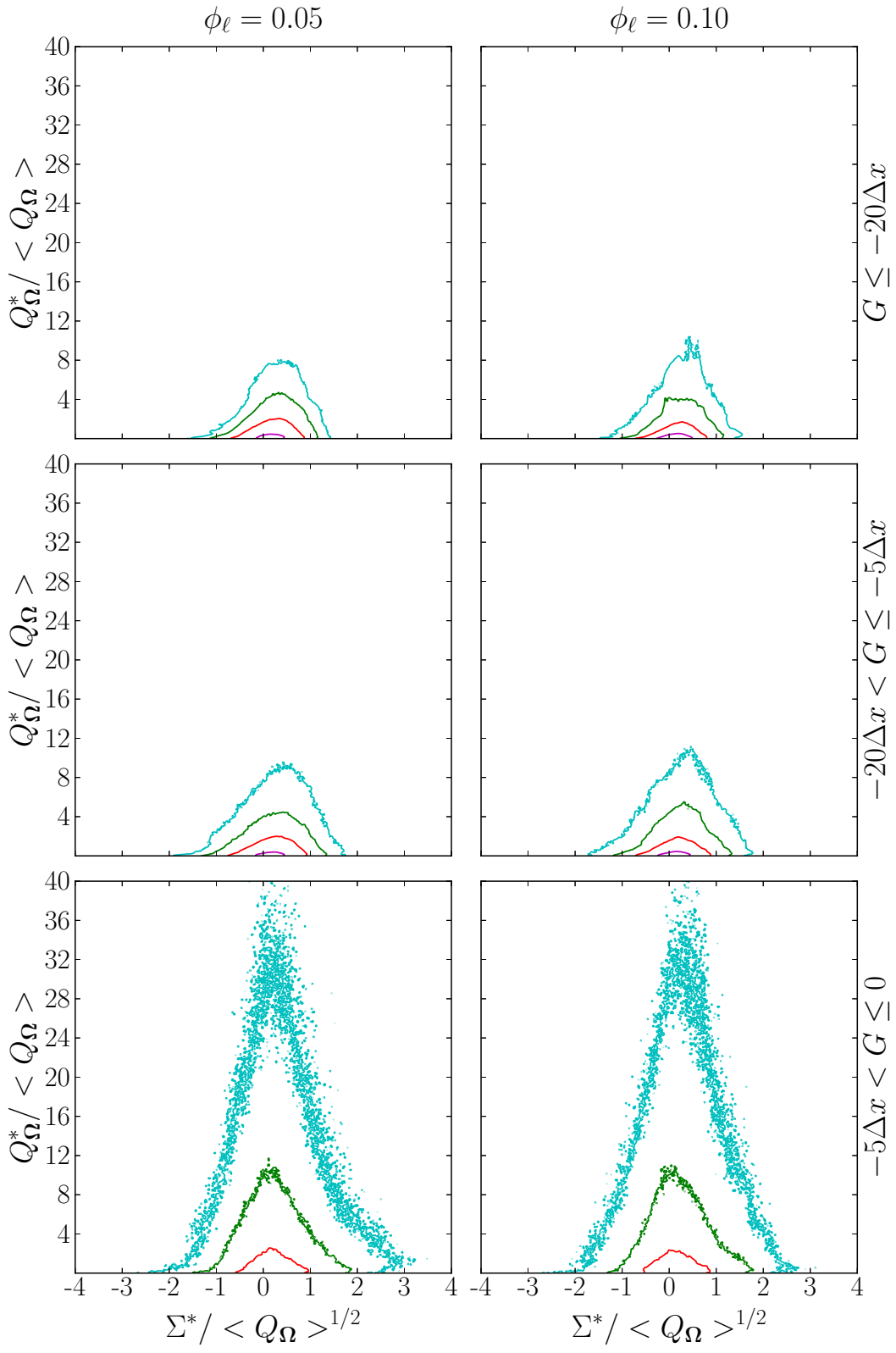

Figure 4.16. *Joint statistics of* (Σ, Q_Ω) *in the far (top row), intermediate (middle row), and near (bottom row) field regions for* $\phi_\ell = 0.05$ *(left column) and* $\phi_\ell = 0.10$ *(right column). The four thin lines correspond to iso-contours of* $\log_{10}$ *(JPDF) equals to* -3 -2, -1, *and* 0. *Both invariants* Σ *and* Q_Ω *are normalized by the averaged value of the second invariant of the rotation tensor,i.e.,* $\langle Q_\Omega \rangle = \langle -\mathbf{\Omega} \cdot \mathbf{\Omega}/2 \rangle$.

4.3.2 Geometrical analysis and alignment statistics

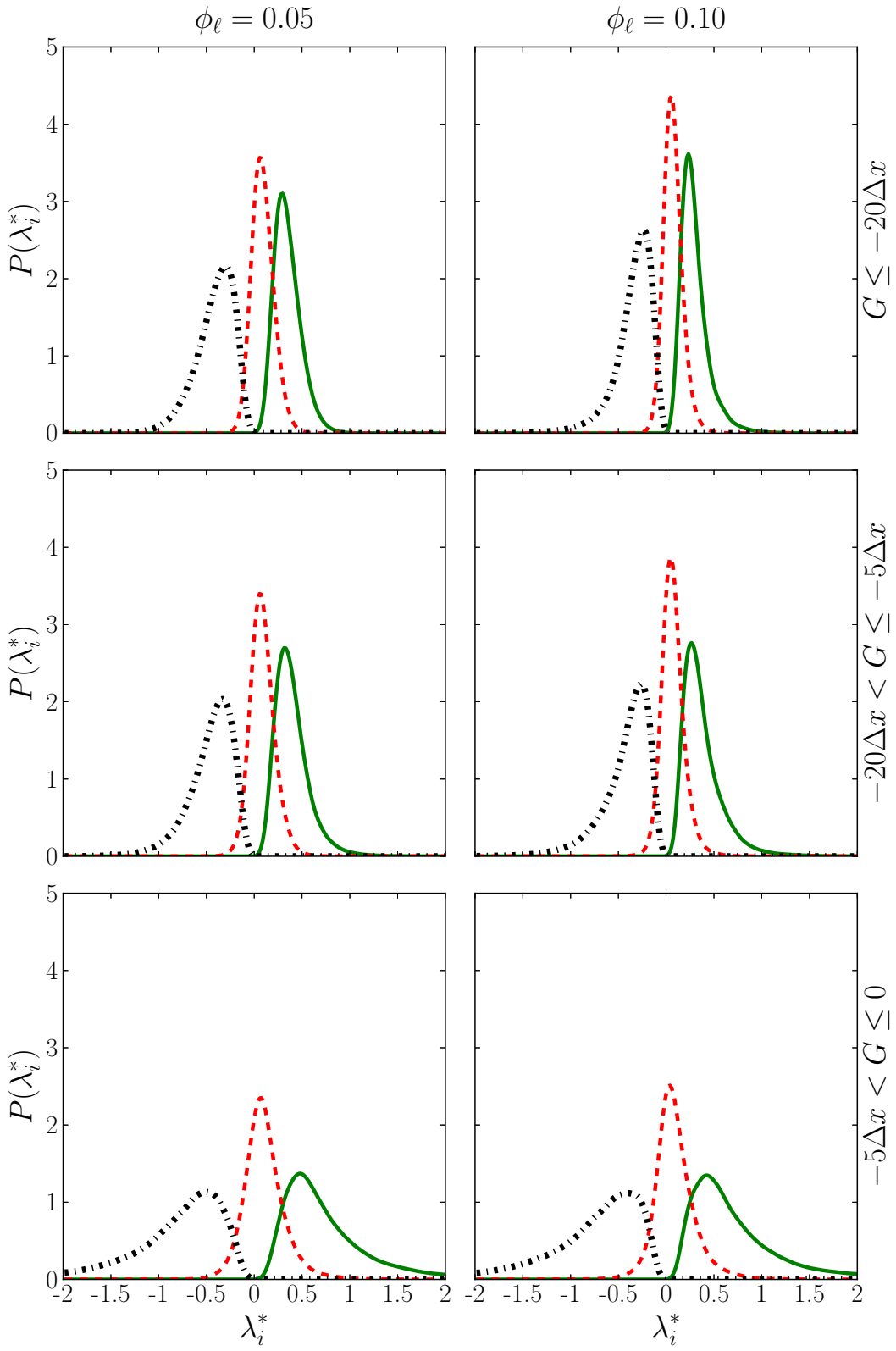

Figure 4.17. *PDF of the normalized eigenvalues :* λ_1^* (—), λ_2^* (- - -) *and* λ_3^* (-·-·) *; far (top row), intermediate (middle row), and near (bottom row) field regions for* $\phi_\ell = 0.05$ *(left column) and* $\phi_\ell = 0.10$ *(right column).*

The turbulence-scalar interaction (TSI) is a term that originates from the average of the first terms of the right hand side (RHS) of the scalar dissipation rate (SDR) equation, which is presented in chapter 5. In this section attention is focused on the TSI. Such interaction can be studied in the eigen-frame of the symmetric part $\boldsymbol{S}$ of the VGT $\boldsymbol{A}$. Since $\boldsymbol{S}$ is a second-rank symmetric tensor, the eigenvalues are real numbers that are defined in such a manner that $\lambda_1 > \lambda_2 > \lambda_3$. The eigenvalue $\lambda_1 > 0$ corresponds to the most extensive principal direction, λ_2 denotes the intermediate principal direction, and λ_3 is the most compressive principal direction. The incompressibility condition leads to $\lambda_1 + \lambda_2 + \lambda_3 = 0.0$. These quantities are essential for the analysis of the local structure and dynamics of the turbulent flow-field. The PDF of the normalized strain-rate tensor eigenvalues λ_i^* are reported in Fig. 4.17. They are non-dimensionalized by the Kolmogorov strain-rate $\nu\eta_K^{-2}$ with η_K the Kolmogorov length scale. From these statistics, it is found that the ranges of variations of the eigenvalues λ_i^* increases as the liquid-gas interface is approached. The distribution of λ_3^*, as expected, result in mostly negative values while the distribution of λ_1^* is mostly positive. Furthermore, the distributions of λ_1^* and λ_3^* are broader and flatter than the one of λ_2^*. Finally, the distribution of λ_2^* is positively skewed, which reflects the turbulent energy transfer [104].

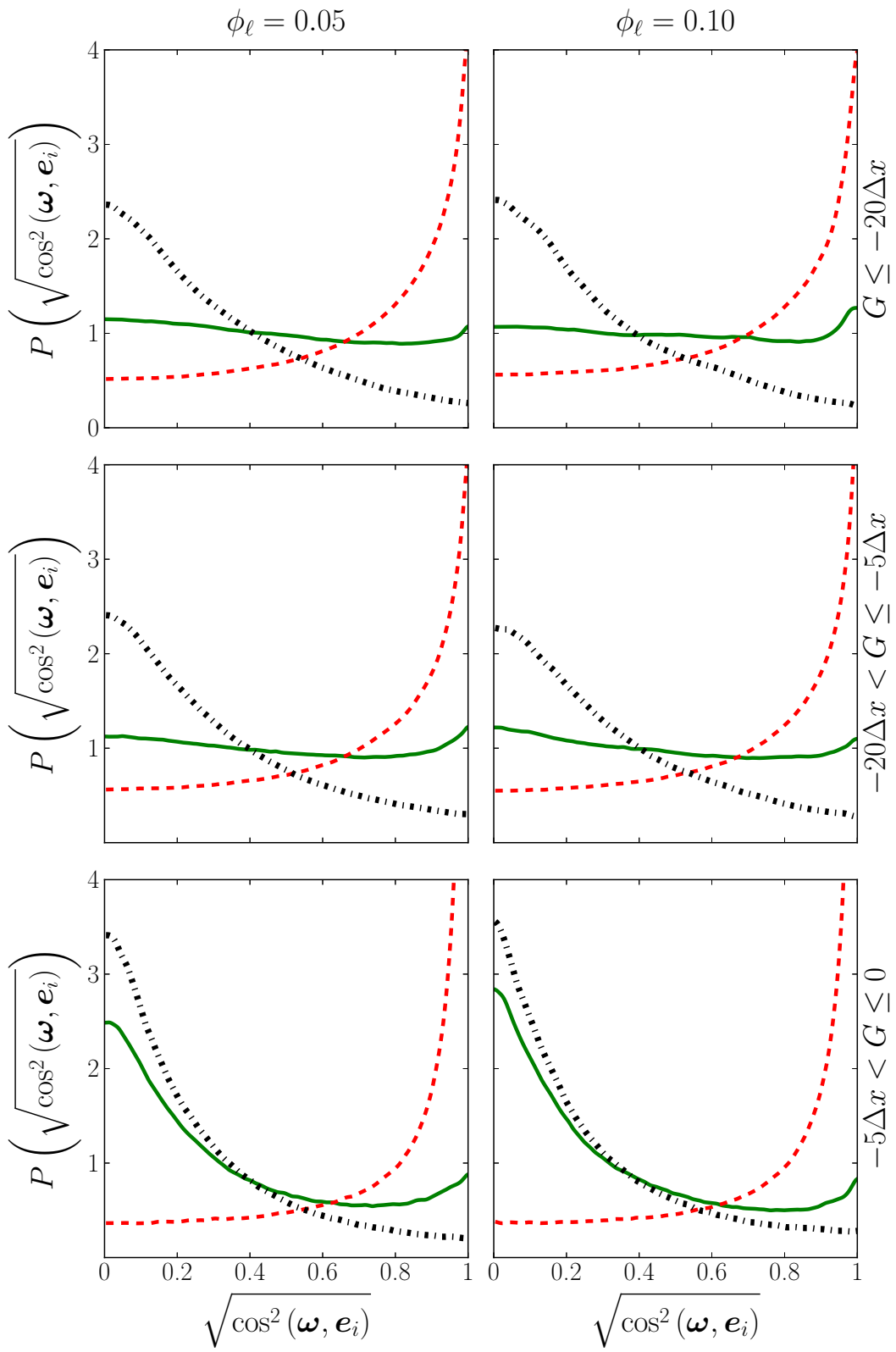

Figure 4.18. *The orientation between vorticity ($\boldsymbol{\omega}$) and strain-rate tensor principal directions ($\boldsymbol{e}_i$) : extension (——), intermediate (- - -), and compression (-·-·-); in the far (top row), intermediate (middle row), and near (bottom row) field regions for $\phi_\ell = 0.05$ (left column) and $\phi_\ell = 0.10$ (right column).*

It is known from previous analysis of incompressible HIT (see for instance Hamlington et al., Tsinober [45, 104]) that the PDF of the alignment between the vorticity vector $\boldsymbol{\omega}$ and the eigen-frame of the symmetric part of the VGT, i.e., $\boldsymbol{e}_i$, exhibits a preferential alignment with the eigenvector associated to the intermediate eigenvalue of the strain tensor $\boldsymbol{e}_2$. No special alignment of $\boldsymbol{\omega}$ with the most extensive principal direction given by $\boldsymbol{e}_1$ is found, and the vorticity vector $\boldsymbol{\omega}$ tends to be misaligned to the most compressive principal direction $\boldsymbol{e}_3$. Figure 4.18 confirms that these conclusions hold in the far and intermediate regions. However, as the liquid-gas interface is approached, there is a substantial increase in the probability levels associated with the transversality of the vorticity vector $\boldsymbol{\omega}$ with both the most extensive $(\boldsymbol{e}_1)$ and most compressive $(\boldsymbol{e}_3)$ principal directions. It is also noteworthy that the preferential alignment of the vorticity vector $\boldsymbol{\omega}$ with the intermediate principal direction $\boldsymbol{e}_2$ is significantly amplified in the vicinity of the interface, which reflects the enhancement of transfer and associated vortex-stretching processes.

The velocity evolution is now analyzed through the interaction between the vorticity-stretching vector, $\boldsymbol{W}^{\omega} = \boldsymbol{\omega} \cdot \boldsymbol{S}$ and the vorticity vector. This very interaction may be scrutinized through their product, i.e., $\boldsymbol{W}^{\omega} \cdot \boldsymbol{\omega} = || \boldsymbol{W}^{\omega} || \, || \boldsymbol{\omega} || \cos(\boldsymbol{W}^{\omega}, \boldsymbol{\omega})$, in such a manner that the sign of the cosine angle between these two vectors may indicate either enstrophy production or destruction, such that negative values are associated to vortex-stretching mechanisms, whereas positive values to vortex-compression mechanisms. Figure 4.19 puts into evidence the alignment between this two vectors, which is relevant to vortex-stretching predominance. This tendency is confirmed by the PDF of the normalized enstrophy production term displayed in Fig. 4.20, which shows a net (positive) enstrophy production, i.e., $\boldsymbol{\omega} \cdot \boldsymbol{S} \cdot \boldsymbol{\omega} > 0$ in all the analyzed gaseous sub-regions. The corresponding positively skewed PDF also shows that there is a significant increase of the levels of fluctuations as the interface is approached.

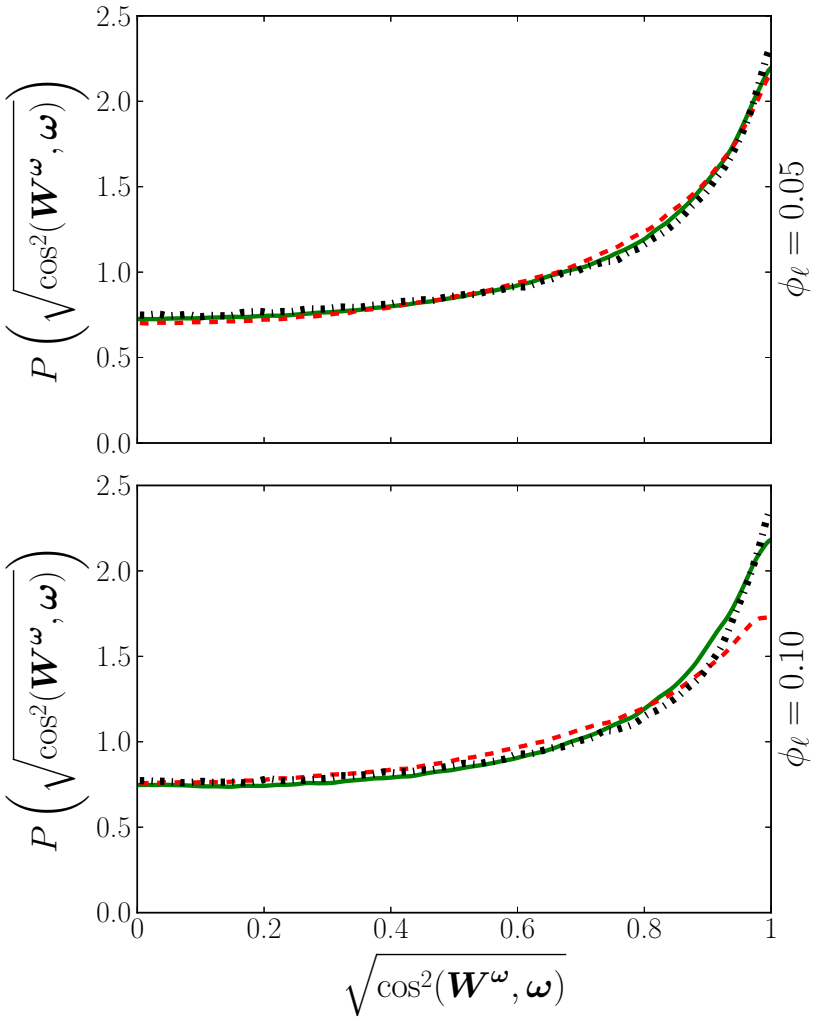

Figure 4.19. *Orientation between vortex-stretching vector (W^{ω}) and vorticity ($\boldsymbol{\omega}$) in the far (——), intermediate (- - -), and near (-·-·) field regions from the liquid-gas interface for $\phi_\ell = 0.05$ (top) and $\phi_\ell = 0.10$ (bottom).*

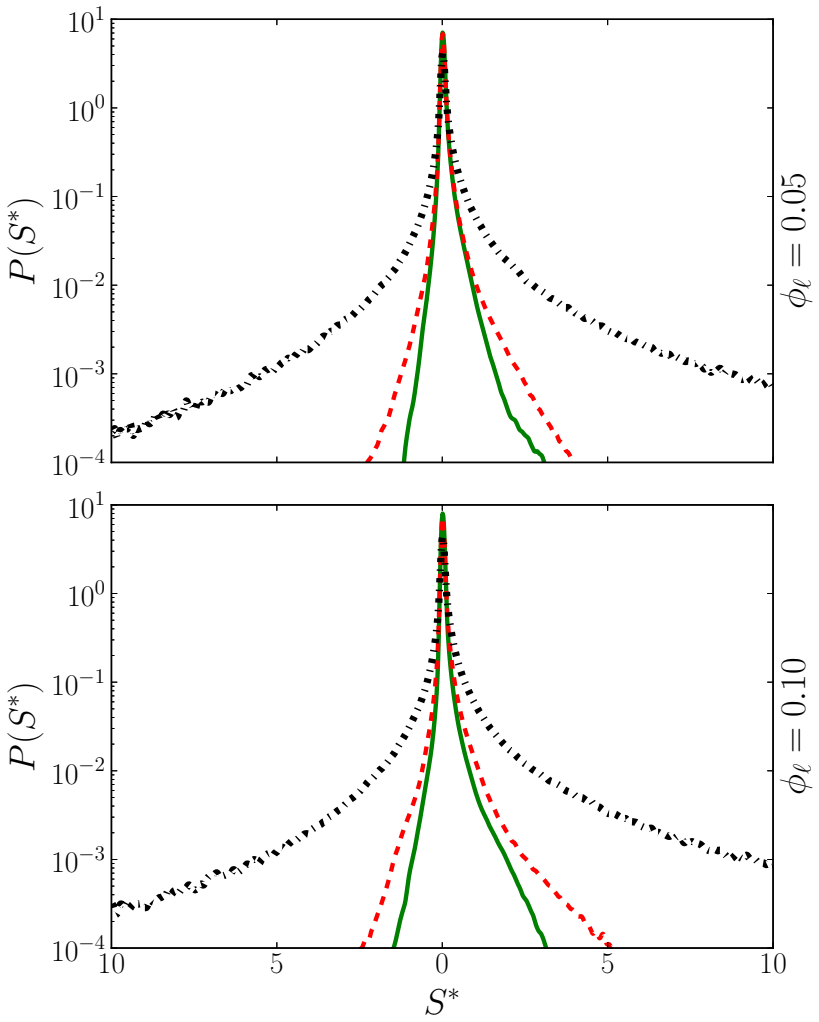

Figure 4.20. *PDF of the normalized enstrophy production term associated with the vortex-stretching effects* $\left(S^* = \boldsymbol{\omega} \cdot \boldsymbol{S} \cdot \boldsymbol{\omega} / (\nu/\eta^2)^3\right)$ *in the far (—), intermediate (- - -), and near (-·-) field regions from the liquid-gas interface for* $\phi_\ell = 0.05$ *(top) and* $\phi_\ell = 0.10$ *(bottom).*

The strain-enstrophy orientation angle, i.e., $\Gamma = \tan^{-1}\left((\boldsymbol{S} \cdot \boldsymbol{S}) / (\boldsymbol{\Omega} \cdot \boldsymbol{\Omega})\right)$ is now considered to conclude this chapter. This provides information about the possible predominance of strain ($\Gamma \gg 45°$ or rotation ($\Gamma \ll 45°$). Values approaching 45° are relevant to high levels of correlation between the two processes. Figure 4.21 shows that the PDF obtained in the far (—) and intermediate (- - -) regions are skewed towards values larger than 45°. As the liquid-gas interface is approached, a probability peak does appear,which is relevant to the highly correlated region, i.e., in the vicinity of $\Gamma = 45°$. It is also noteworthy that the PDF in the near field region (-·-) still exhibits a certain level of asymmetry at both tails, which puts into evidence that strain-dominated regions still prevail the over the rotation-dominated regions.

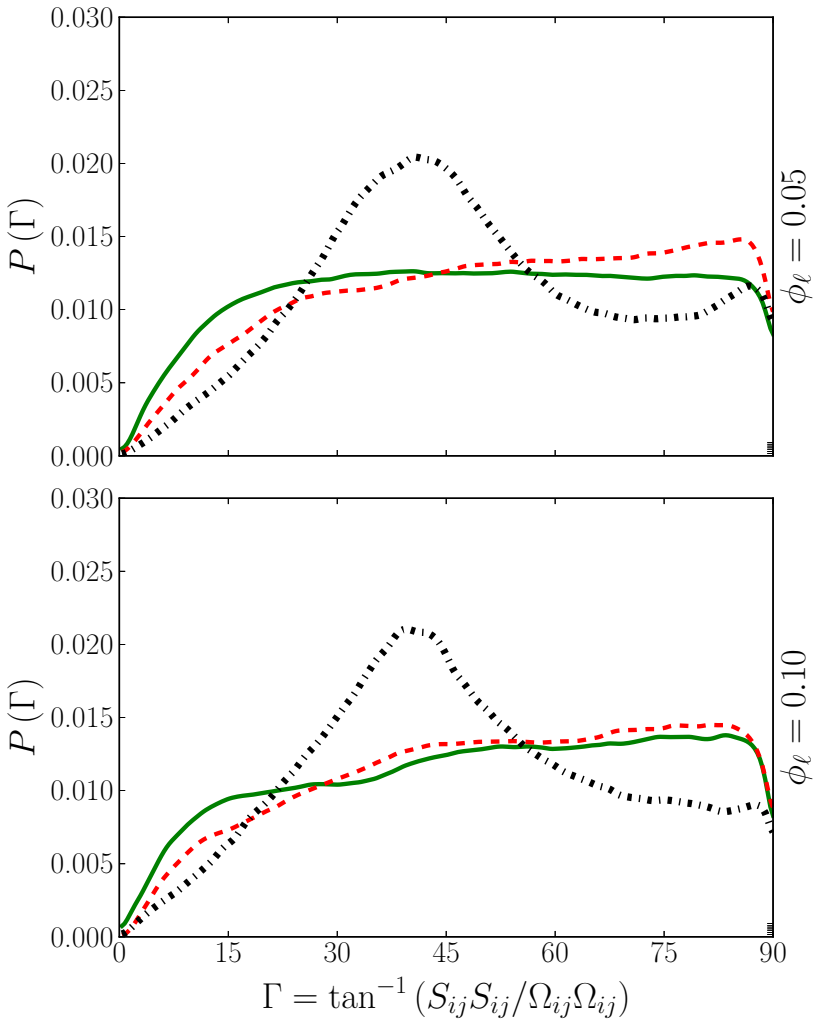

Figure 4.21. *PDF of the strain-enstrophy angle* $\mathbf{\Gamma}$ *in the far (—), intermediate (- - -), and near (-·-·) field regions for* $\phi_\ell = 0.05$ *(top) and* $\phi_\ell = 0.10$ *(bottom).*

4.4 Summary and conclusions

From a general viewpoint, such investigations of small-scale topologies in flows featuring fronts or interfaces remain rather uncommon in comparison to the amount of analyzes conducted in more standard incompressible turbulent flow conditions. Some analysis of this kind have been only very recently conducted for multi-species, variable-density shock-turbulence interaction (Tian et al. [101]), and droplet-laden decaying HIT configurations (Dodd and Jofre [23]). In this respect, it seems interesting to report analysis devoted to the dynamics of the smallest scales in turbulent evaporating two-phase flows. In this chapter attention is focused on the gaseous turbulent field, which is subdivided into different sub-regions depending on the level-set (G) values.

Firstly the evolution of the topology of the turbulent flow is inspected as the level-set value, G, tends to zero. The normalized invariants ξ^* and η^* of the traceless Reynolds stress anisotropy tensor $\boldsymbol{b}$ confirms that, as the liquid-gas interface is approached, the turbulence anisotropy is significantly increased, such that a progressive evolution takes place from the isotropic-turbulence state to the one-dimensional-turbulence state. Then, it is shown that the small-scale topology of the turbulent flow is also significantly altered in the vicinity of the liquid-gas interface, as is showed by the iso-lines of the (R_A^*, Q_A^*)-phase plane, where Q_A^* and R_A^* are, respectively, the second and third invariants of the velocity gradient tensor (VGT). In the far region, the classical tear-drop shape – associated to significant probability levels of the first, Q_1, and second, Q_2, quadrants of the (R_A^*, Q_A^*)-phase plane – is recovered. However, as the liquid-gas interface is approached, there is a significant increase of probability levels associated to the third, Q_3, quadrant, i.e., the SN/S/S topology. As a consequence, the probability levels of the first, Q_1, and second, Q_2, quadrants tend to become similar, and there is a decrease of the probability levels relevant to the fourth, Q_4, quadrant, which goes together with a larger scatter of the corresponding data. The statistics of the strain-rate $\boldsymbol{S}$ tensor and rotation tensor $\boldsymbol{\Omega}$ are subsequently studied to get further insights into the flow topology evolution as the liquid-gas interface is approached. The corresponding analysis puts into evidence the dominance of vortex sheet structures in the direct vicinity of the interface. This analysis is ended by a detailed inspection of geometrical features and alignment statistics. It shows that the preferential alignment of the vorticity vector with the intermediate principal direction $\boldsymbol{e}_2$ is significantly amplified in the vicinity of the interface, which reflects the enhancement of transfer and associated vortex-stretching processes. Finally, since the presence of the liquid may alter preferentially the component of the rotation and strain stress tensors in direction normal to the liquid-gas interface, one may expect an increase in the correlation between the two quantities, which is indeed unambiguously confirmed by the inspection of the strain-enstrophy angle Γ as the interface is approached.

5 Scalar field analysis of evaporative two-phase flows in HIT

Content of the chapter

The chapter presents the statistical characterization of the mixture fraction field of an evaporative multi-phase DNS simulation database set featuring two distinct values of the liquid volume fraction ϕ_ℓ. On the first part, results concerning the mixing scalar field are reported. Then attention is turned to the geometrical properties and alignment statistics of the scalar mixing and scalar dissipation. Such statistics are gathered at various distances from the interface, in such a manner that that the gas phase is divided into several sub-regions according to the values of the level-set G, i.e., the distance from the liquid-gas interface, as shown in Table 4.1.

5.1 Theoretical background

Scalar dissipation rate transport in evaporating two-phase flows

Before embarking on the detailed study of the computational data, it seems to be useful to provide a few words about the quantities that are central to the post-

processing and analyses of the present chapter. Such quantities are the scalar gradient and the scalar dissipation rate (SDR).

By taking the gradient of Eq. 2.7, the evolution of the scalar gradient $\boldsymbol{g}^{\xi} = \boldsymbol{\nabla}\xi$ is obtained :

$$\frac{D\boldsymbol{g}^{\xi}}{Dt} = -\boldsymbol{\nabla}\boldsymbol{u}\cdot\boldsymbol{g}^{\xi} + \boldsymbol{\nabla}\left(\boldsymbol{\nabla}\left(\mathcal{D}\boldsymbol{g}^{\xi}\right)\right) + \boldsymbol{\nabla}\dot{\boldsymbol{\omega}}_{\xi}, \tag{5.1}$$

which, once multiplied by $2\mathcal{D}\boldsymbol{g}^{\xi}$, leads to the SDR transport equation

$$\begin{aligned}\frac{DN_{\xi}}{Dt} =& 2\mathcal{D}\boldsymbol{g}^{\xi}\cdot\frac{D\boldsymbol{g}^{\xi}}{Dt}\\ =& \underbrace{-2\mathcal{D}\left(\boldsymbol{g}^{\xi}\right)^{T}\cdot\boldsymbol{S}\cdot\boldsymbol{g}^{\xi}}_{TSI} + \boldsymbol{\nabla}\left(\mathcal{D}\boldsymbol{\nabla}N_{\xi}\right) - 2\mathcal{D}^{2}\boldsymbol{\nabla}\boldsymbol{g}^{\xi}\boldsymbol{\nabla}\boldsymbol{g}^{\xi} + 2\mathcal{D}\boldsymbol{g}^{\xi}\boldsymbol{\nabla}\dot{\boldsymbol{\omega}}_{\xi}\end{aligned} \tag{5.2}$$

where $\boldsymbol{S} = (\boldsymbol{\nabla}\boldsymbol{u} + \boldsymbol{\nabla}\boldsymbol{u}^{T})/2$ denotes the symmetric part of the VGT, i.e., the strain-rate tensor. Indeed, it can be readily shown that there is no contribution of the anti-symmetric part $\boldsymbol{\Omega} = (\boldsymbol{\nabla}\boldsymbol{u} - \boldsymbol{\nabla}\boldsymbol{u}^{T})/2$ (i.e., rotation or vorticity) of the velocity gradient tensor $\boldsymbol{\nabla}\boldsymbol{u} = \boldsymbol{S} + \boldsymbol{\Omega}$ to the SDR evolution [9]. The RHS of the SDR contains four contributions. Two among them do involve the squared molecular diffusivity : (i) the second term in the RHS, which is a conservative contribution associated to the molecular fluxes of N_{ξ}, and (ii) the third term, which appears as a sink term : this is the SDR dissipation term. The fourth term appears as a possible production/destruction term associated to vaporization effects. Finally, the first term in the RHS of Eq. 5.2 is related to the so-called turbulence-scalar interaction (TSI) term that will be further analyzed below.

Provided that the turbulent Reynolds number is sufficiently large, the mean SDR $\overline{N}_{\xi}$ is approximately equal to the turbulent SDR $\overline{\varepsilon}_{\xi}$ which, under the present assumptions of constant density and constant diffusivity in the gaseous phase, writes $\overline{\varepsilon}_{\xi} = \mathcal{D}\overline{(\partial\xi'/\partial x_i)(\partial\xi'/\partial x_i)}$. The corresponding value of the mean SDR $\overline{N}_{\xi} = \mathcal{D}\overline{(\partial\xi/\partial x_i)(\partial\xi/\partial x_i)}$ can be deduced from the averaging of the above Eq. 5.2. One of the leading order terms of this transport equation is the TSI term, i.e., the average of the first contribution present in the RHS of Eq. 5.2. This term does involve the fluctuating velocity field, so the first step of the analysis of the corresponding scalar - velocity couplings at the smallest scales of the flow, is to characterize the turbulent velocity field. This has been done in detail in chapter 4. The second step is to characterize the scalar gradient and then the TSI term. This is the subject of the present chapter.

Scalar-scalar stretching vector alignment

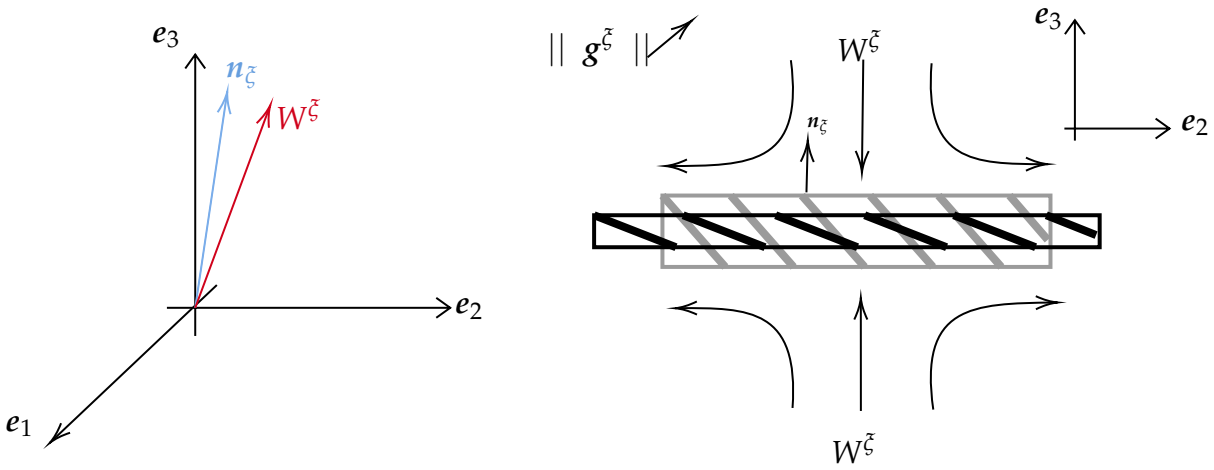

Figure 5.1. *On the left the eigen-space and the alignment between the normalized scalar gradient* $(\boldsymbol{n}_\xi)$ *and its corresponding scalar-stretching vector* $\left(\boldsymbol{W}^\xi\right)$*. On the right the two-dimensional sketch of the corresponding scalar structure gathered when high alignment between these two vectors happen. Here,* $\boldsymbol{n}_\xi = \boldsymbol{\nabla}\xi / \,||\, \boldsymbol{\nabla}\xi \,||= \boldsymbol{g}^\xi / \,||\, \boldsymbol{g}^\xi \,||$ *denotes the direction normal to the iso-contours of* ξ*, oriented towards the liquid.*

The typical alignment between the normalized scalar gradient $(\boldsymbol{n}_\xi)$ and its corresponding scalar-stretching vector $\left(\boldsymbol{W}^\xi\right)$ is presented in Fig. 5.1. Such alignment is relevant to the amplification of the scalar gradient $(||\, \boldsymbol{g}^\xi \,||\uparrow)$, which in turn is associated with predominance of compression [104], i.e., sheet-like structures.

Scalar-eigenframe alignments

The scalar structures gathered in isotropic homogeneous turbulence are presented in Fig.5.2. On the left is presented the compression of the scalar structure, whilst on the right the extension of the scalar structure. The normalized scalar gradient $(\boldsymbol{n}_\xi)$ presents the highest transversality with the intermediate direction $(\boldsymbol{e}_2)$, and a preferential alignment with the most compressive $(\boldsymbol{e}_3)$ eigenvector. When the scalar gradient is aligned with $\boldsymbol{e}_3$, the magnitude of the scalar gradient increases, otherwise when it is aligned with $\boldsymbol{e}_1$ or $\boldsymbol{e}_2$, the magnitude decreases. As both the most extensive and the intermediate directions of the strain eigen-frame are positive (in average), then the difference between the statistics presenting alignment with them relapse in the curvature of the generated scalar structures.

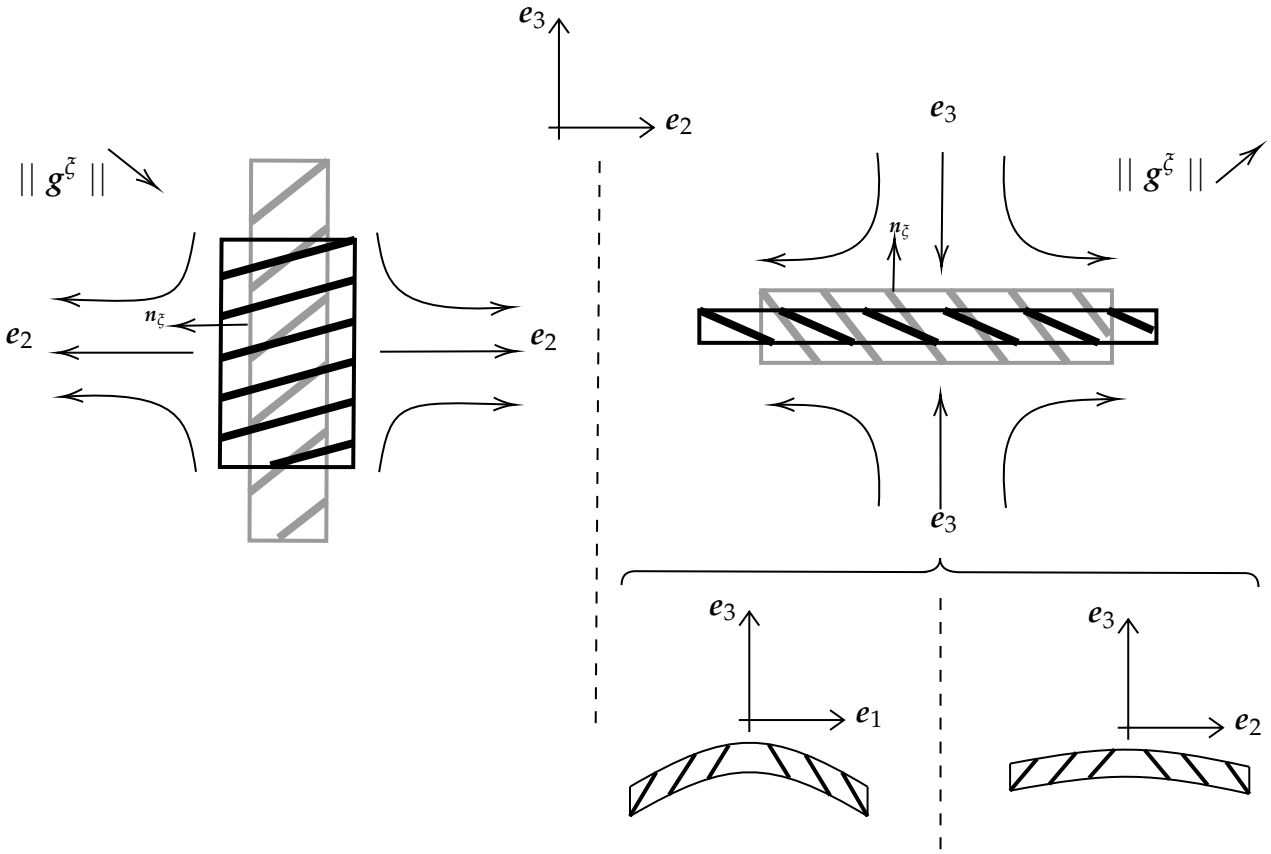

Figure 5.2. *Schematic of the two-dimensional scenarios of the alignment between the normalized scalar field* $(\boldsymbol{n}_\xi)$ *and the eigen-plane drawn by the intermediate* $(\boldsymbol{e}_2)$ *and most compressive* $(\boldsymbol{e}_3)$ *principal directions. The evolution in the diagrams is depicted from an initial state (in gray) to a current state (in black). On the left is presented the compression of the scalar structure, whilst on the right the extension of the scalar structure. Here,* $\boldsymbol{n}_\xi = \boldsymbol{\nabla}\xi / \,||\, \boldsymbol{\nabla}\xi \,||= \boldsymbol{g}^\xi / \,||\, \boldsymbol{g}^\xi \,||$ *denotes the direction normal to the iso-contours of* ξ*, oriented towards the liquid.*

5.2 Evolution of the mixing scalar field in the vicinity of the interface

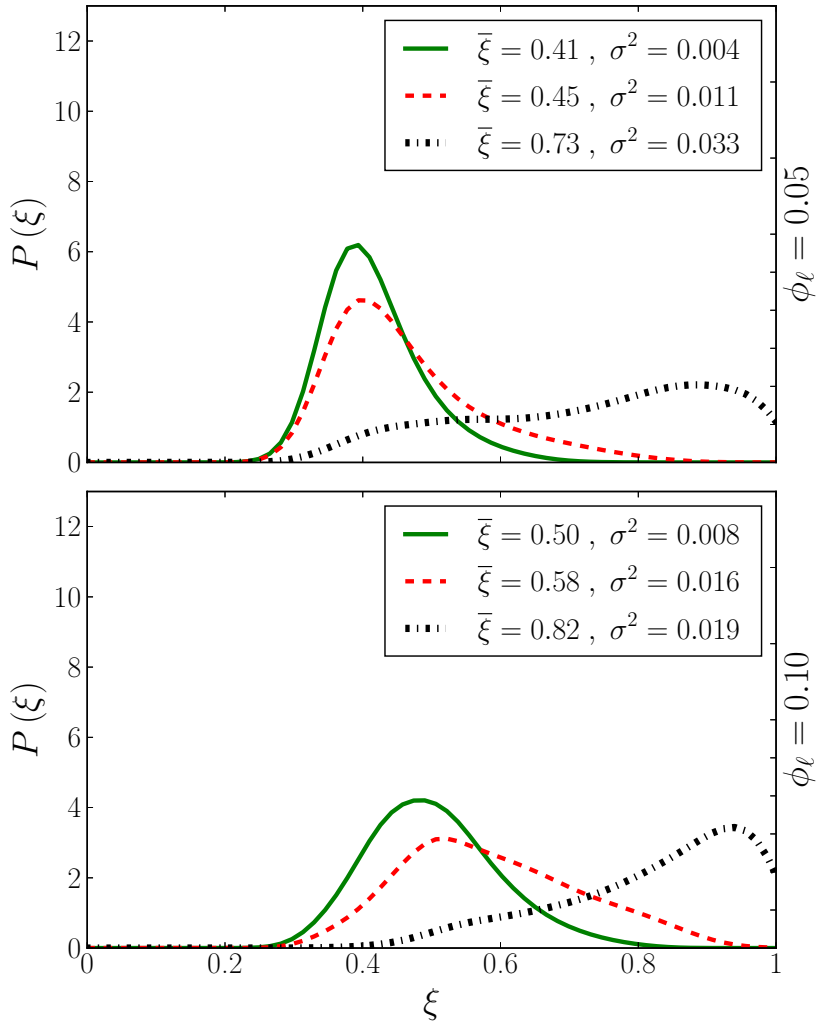

Figure 5.3. *PDF of the mixture fraction ξ in the far (—), intermediate (- - -), and near (-·-·) regions from the liquid-gas interface for $\phi_\ell = 0.05$ (top) and $\phi_\ell = 0.10$ (bottom). The corresponding mean and variance values are also reported for each condition and region.*

Mixture fraction probability density functions are displayed in Fig. 5.3. The statistics are collected in the far (—), intermediate (- - -), and near (-·-·) regions (see Table. 4.1, where the three sub-regions in the gas phase are defined as functions of the level-set value, G). For both cases, $\phi_\ell = 0.05$ and $\phi_\ell = 0.10$, the mean values $\left(\overline{\xi}\right)$ decrease as they are computed farther the liquid-gas interface. Moreover, the mean values for each region in the case with $\phi_\ell = 0.10$ are found to be larger than their counterparts obtained for $\phi_\ell = 0.05$. These PDF do also provide information on higher moments and, as regions farther from the interface are considered, the decay observed for the mixture fraction variance σ^2 is found to be larger for $\phi_\ell = 0.05$ than

for $\phi_\ell = 0.10$.

Then the PDF of the three components of the scalar gradient, $\boldsymbol{g}^\xi$, normalized by the Taylor length scale (λ_T), are presented in Fig. 5.4. There it is put into evidence that, as the interface is approached, an increase of the molecular mixing rate and SDR take place. Such a conclusion is obtained due to the increase of the amplitude of the variations of the scalar gradient components in the near region. However, the mean value of the three spatial derivatives is almost zero : despite the presence of the liquid phase, the small scale of the scalar field appears to be homogeneous in the standard frame of reference $\boldsymbol{R_X} = [\boldsymbol{R}_{X_1} \mid \boldsymbol{R}_{X_2} \mid \boldsymbol{R}_{X_3}] = [\partial\xi/\partial x \mid \partial\xi/\partial y \mid \partial\xi/\partial z]$. This apparent isotropy of the scalar gradient is related to the fact that the liquid phase is dispersed in the homogeneous isotropic turbulent (HIT) flow and a different behavior would have been observed in the presence of a large pool of liquid.

$$\boldsymbol{g}^\xi = \begin{bmatrix} g_1^\xi \\ g_2^\xi \\ g_3^\xi \end{bmatrix} = \boldsymbol{g}^\xi \cdot \boldsymbol{R_X}^T = \begin{bmatrix} \boldsymbol{g}^\xi \cdot \boldsymbol{R}_{X_1} \\ \boldsymbol{g}^\xi \cdot \boldsymbol{R}_{X_2} \\ \boldsymbol{g}^\xi \cdot \boldsymbol{R}_{X_3} \end{bmatrix} = \begin{bmatrix} \partial\xi/\partial x \\ \partial\xi/\partial y \\ \partial\xi/\partial z \end{bmatrix}$$

Therefore, it seems necessary to analyze in further detail the scalar gradient, but considering a local frame of reference which is *attached* to the liquid-gas interface. Such a set of coordinates is defined at each point of the computational domain by making use of the level-set function. A unit vector normal to the liquid-gas interface is defined from :

$$\boldsymbol{n} = \boldsymbol{\nabla} G / \left(\boldsymbol{\nabla} G \cdot \boldsymbol{\nabla} G\right)^{1/2}$$

From this normal unit vector definition, two tangential unit vectors $\boldsymbol{\tau}_1$ and $\boldsymbol{\tau}_2$ can be obtained as follows :

$$\boldsymbol{\tau}_1 = \boldsymbol{I} \times \boldsymbol{n} \quad \text{and} \quad \boldsymbol{\tau}_2 = \boldsymbol{\tau}_1 \times \boldsymbol{n}$$

These three vectors lead to a local frame of reference based on the level-set $\boldsymbol{R_G} = \left[\boldsymbol{R}_{G_1} \mid \boldsymbol{R}_{G_2} \mid \boldsymbol{R}_{G_3}\right] = [\boldsymbol{n} \mid \boldsymbol{\tau}_1 \mid \boldsymbol{\tau}_2]$. The scalar gradient $\boldsymbol{g}^\xi$ is now analyzed in this local frame of reference $\boldsymbol{R_G}$, *i.e.*, we study the projection of $\boldsymbol{g}^\xi$ onto each of the

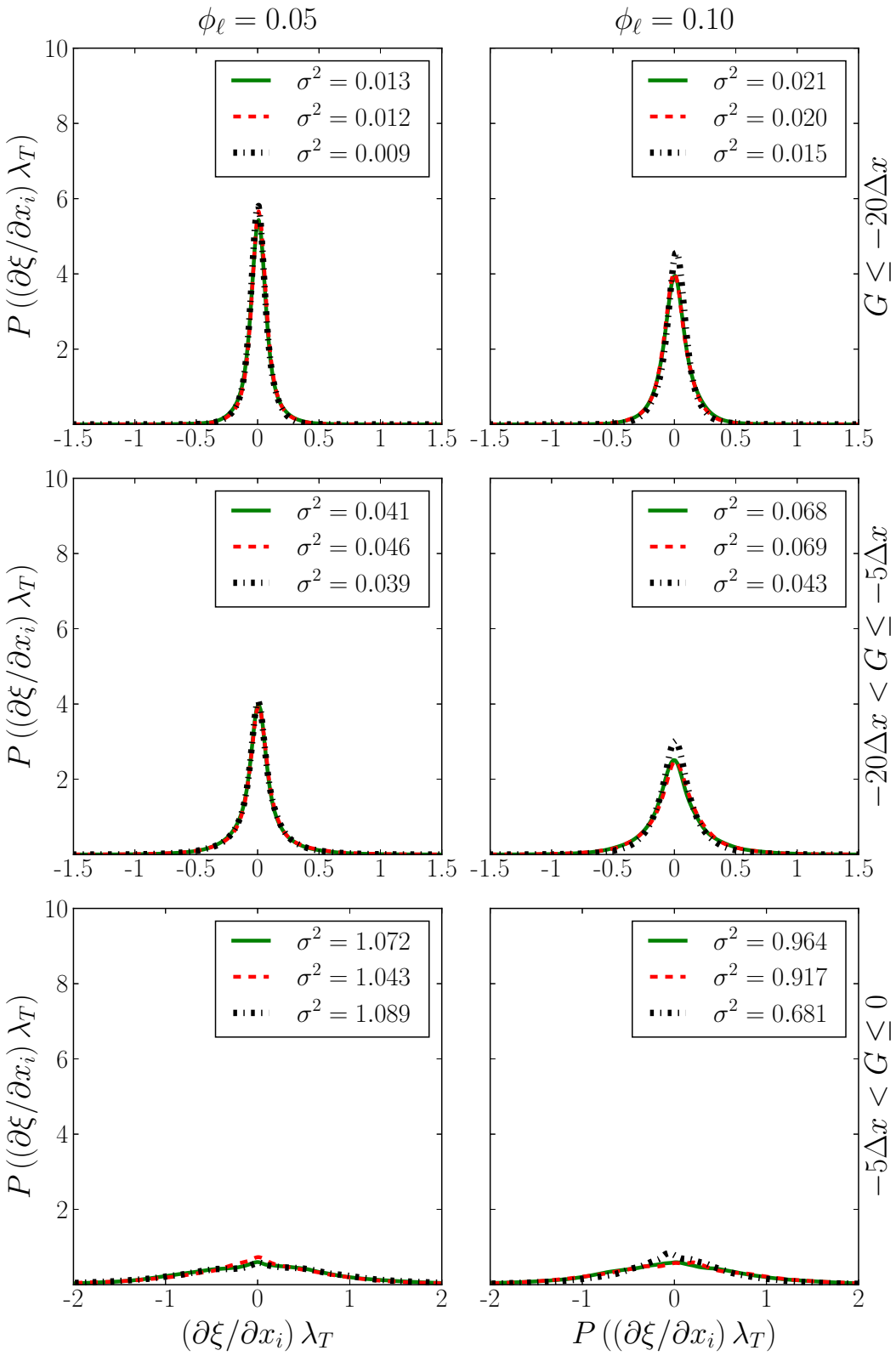

Figure 5.4. *Marginal PDF of the three components of scalar gradient : g_1^ξ (—), g_2^ξ (- - -), and g_3^ξ (-·-·), in the far (top row), intermediate (middle row), and near (bottom row) regions from the liquid-gas interface for $\phi_\ell = 0.05$ (left) and $\phi_\ell = 0.10$ (right). The corresponding mean and standard deviation values are also reported for each condition and region. Values are normalized by the Taylor length scale λ_T.*

corresponding unit vectors $\boldsymbol{n}$, $\boldsymbol{\tau}_1$, and $\boldsymbol{\tau}_2$:

$$\hat{\boldsymbol{g}}^{\xi} = \begin{bmatrix} \hat{g}_1^{\xi} \\ \hat{g}_2^{\xi} \\ \hat{g}_3^{\xi} \end{bmatrix} = \boldsymbol{g}^{\xi} \cdot \boldsymbol{R_G}^T = \begin{bmatrix} \boldsymbol{g}^{\xi} \cdot \boldsymbol{R}_{G_1} \\ \boldsymbol{g}^{\xi} \cdot \boldsymbol{R}_{G_2} \\ \boldsymbol{g}^{\xi} \cdot \boldsymbol{R}_{G_3} \end{bmatrix} = \begin{bmatrix} \boldsymbol{g}^{\xi} \cdot \boldsymbol{n} \\ \boldsymbol{g}^{\xi} \cdot \boldsymbol{\tau}_1 \\ \boldsymbol{g}^{\xi} \cdot \boldsymbol{\tau}_2 \end{bmatrix}$$

For both values of the liquid volume fraction i.e., $\phi_\ell = 0.05$ (left) and $\phi_\ell = 0.10$ (right), in the far field (top row of Fig. 5.5), the averaged values of the components of the scalar gradient projection onto the level-set frame of reference $\boldsymbol{R_G}$ are almost zero and the corresponding variance levels reported remain moderate. This confirms that in the far region the mixture fraction field is, effectively, almost homogeneous. In the intermediate region (middle row of Fig. 5.5), the statistics associated to the component of $\boldsymbol{g}^{\xi}$ projected onto the vector $\boldsymbol{n}$ pointing towards the interface, (*i.e.*, the normal component), becomes positively skewed. Finally, in the direct vicinity of the interface (bottom row Fig. 5.6), the normalized scalar gradient $\boldsymbol{n}_{\xi} = \boldsymbol{g}_{\xi} \,/\, || \, \boldsymbol{g}_{\xi} \, ||$ displays a preferential alignment with the direction normal to the interface $\boldsymbol{n} = \boldsymbol{\nabla} G \,/\, || \, \boldsymbol{\nabla} G \, ||$. This is fully consistent with the PDF reported in Fig. 5.5, i.e., $\hat{g}_1^{\xi}$ (—). Such alignment features more than ninety-nine percent positive values, thus confirming that this region is relevant to the mixture fraction diffusive layer established in the direct vicinity of the interface.

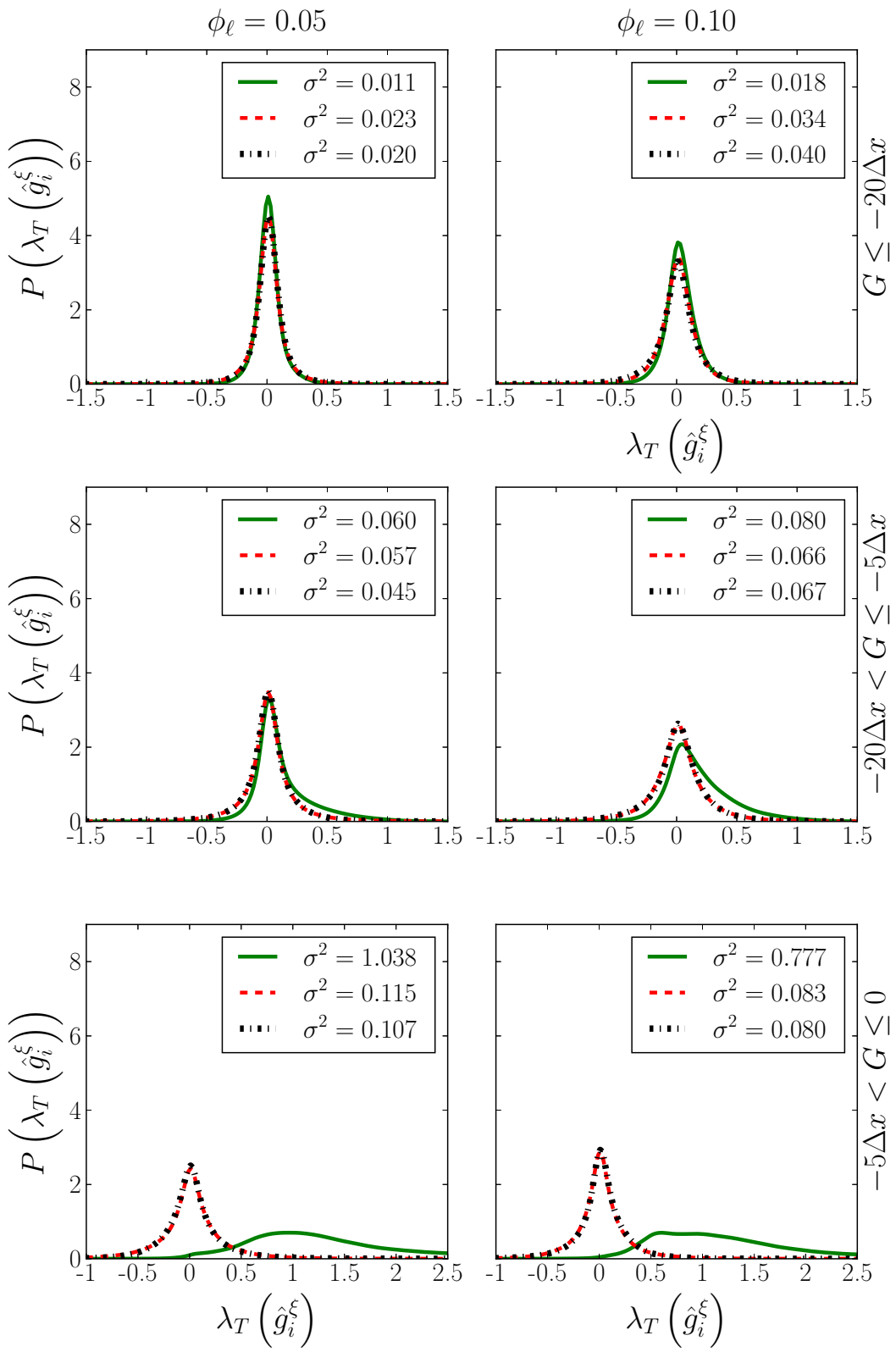

Figure 5.5. *PDF of the three components of the scalar gradient projected onto the local frame of reference attached to the level-set $\hat{g}_i^\xi$. (—) : projection onto the normal direction $\boldsymbol{n}$, (- - -) : projection onto the first tangential direction $\boldsymbol{\tau}_1$, and (-·-·-) : projection onto the second tangential direction $\boldsymbol{\tau}_2$. Results are gathered in the far (top row), intermediate (middle row), and near (bottom row) regions from the liquid-gas interface and for $\phi_\ell = 0.05$ (left) and $\phi_\ell = 0.10$ (right). Values are normalized by the Taylor length scale λ_T.*

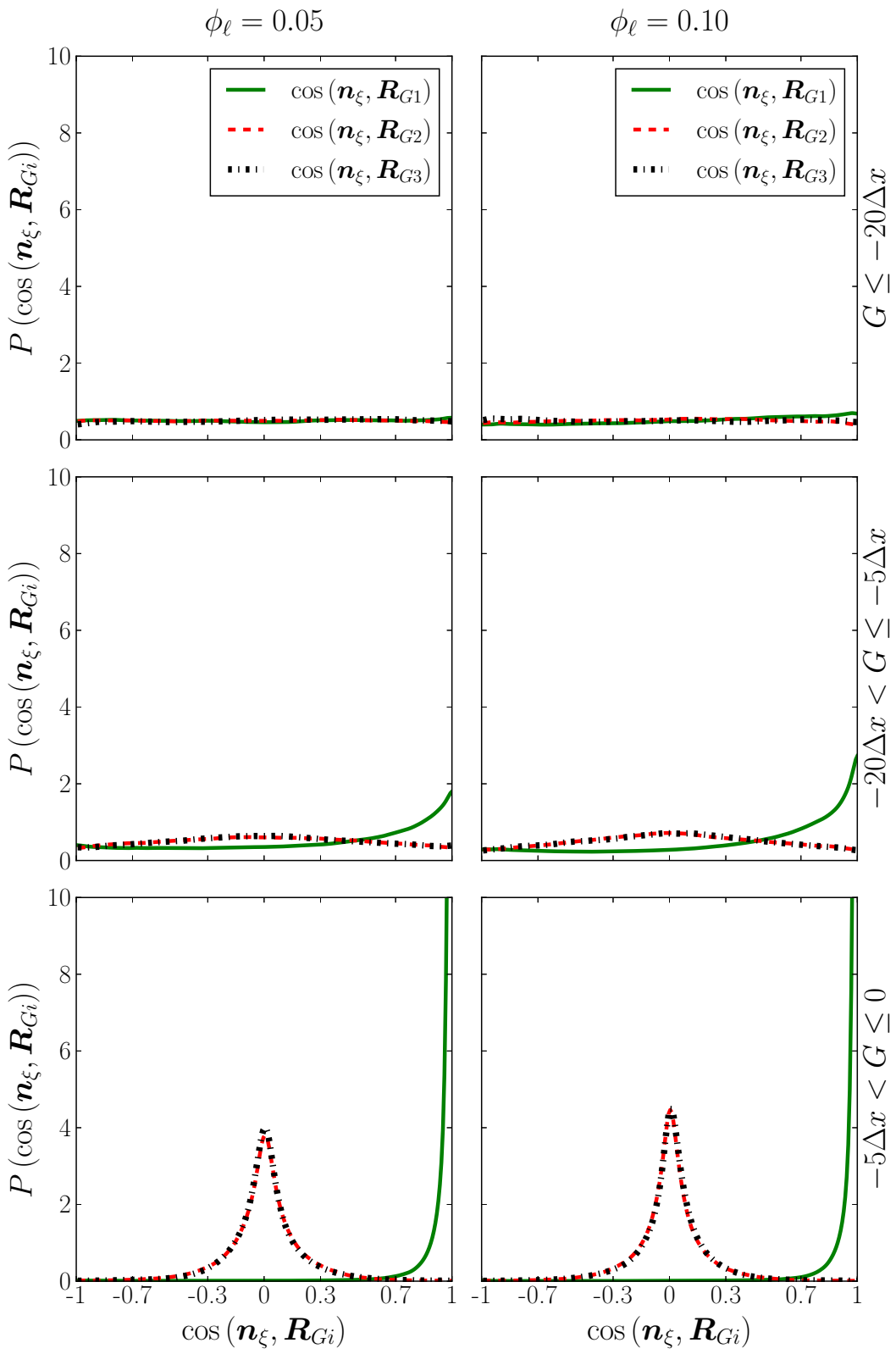

Figure 5.6. *Orientation between scalar gradient $\boldsymbol{n}_\xi$ and the unit vectors $\boldsymbol{R}_{G,i}$ relevant to the local frame of reference :* $\cos(\boldsymbol{n}_\xi, \boldsymbol{n})$ *(—),* $\cos(\boldsymbol{n}_\xi, \boldsymbol{\tau}_1)$ *(- - -), and* $\cos(\boldsymbol{n}_\xi, \boldsymbol{\tau}_1)$ *(-·-); in the far (top row), intermediate (middle row), and near (bottom row) regions from the liquid-gas interface for $\phi_\ell = 0.05$ (left) and $\phi_\ell = 0.10$ (right).*

Further information can be gathered from the statistical moments of the SDR, $N_{\tilde{\xi}}$, which are reported in Table 5.1, and from the PDF of its logarithm, $X = \left(\ln\left(N_{\tilde{\xi}}\right) - \ln\left(\overline{N_{\tilde{\xi}}}\right)\right) / \ln\left(\sigma_{N_{\tilde{\xi}}}\right)$, displayed in Fig. 5.7. It is worth mentioning that such statistical aspects of the scalar field not directly inherited from the turbulent velocity field, but instead are originated in the mixing process [36, 14]. In this sense, turbulence plays the role of enhancing mixing mechanism by means of stirring (turbulent convection). Stirring may be defined as the mechanism that distorts and increases the surface 'area' of the scalar field interface i.e., gradients of the mixing process will increase meanwhile the scalar length scale diminish [27]. In general, this process promotes a fast mixing rate, and at the same time, locally it also amplifies the spatio-temporal concentration gradient variations. This may induce large and intermittent fluctuations of the scalar field, which are quantified by departures of the PDF of the scalar field from a reference Gaussian behavior [95, 35, 96].

In the following description, the PDF is considered positive-skewed if the median value is smaller than the mean, and negative-skewed if the median value is greater than the mean. Moreover the characteristic kurtosis value is three for Gaussian distribution, and six for exponential distribution (according to Pearson's definition), such that the PDF can be classified as : mesokurtic if the kurtosis value is three, (zero excess kurtosis), leptokurtic if the kurtosis value is greater than three (positive excess kurtosis), and platykurtic if the kurtosis value is smaller than three (negative excess kurtosis).

As the liquid-gas interface is approached, for both values of the liquid volume fraction, the skewness of the SDR, $S_{N_{\tilde{\xi}}}$ exhibits an intermittent behavior, in such a manner that its value decreases from the far to the intermediate region, but it grows up again from the intermediate to the near region, retaining in the vicinity of the interface its largest value. Nonetheless, the skewness of its logarithm, S_X, displays a completely different behavior, this one becomes smaller as the liquid-gas interface is approached, all the reported PDF being always negatively skewed, as is shown in Fig. 5.7. In regard to the kurtosis of both the SDR and it logarithm ($E_{N_{\tilde{\xi}}}$ and E_X respectively), for both multi-phase cases, their values show the same intermittent evolution as the one presented by the skewness of $N_{\tilde{\xi}}$, in such a manner that all the PDF's are leptokurtic, excepting those of the standardized PDF of X in the far and and intermediate regions for the case of $\phi_\ell = 0.05$, which are platykurtic. The exponential tails that appear in Fig. 5.7 or Fig. 5.7 are due to rare and large-amplitude fluctuations and they increase as the liquid-gas interface is approached [109].

	Statistical Moments	Far	Intermediate	Near
$\phi_\ell = 0.05$	S_{N_ξ}	0.34	0.34	0.14
	E_{N_ξ}	-1.72	-1.73	-1.71
	S_X	-0.90	-0.90	-0.67
	E_X	0.15	0.07	-0.46
$\phi_\ell = 0.10$	S_{N_ξ}	0.23	0.42	3.16
	E_{N_ξ}	-1.87	-1.58	9.41
	S_X	-0.90	-0.65	-0.67
	E_X	0.39	-0.81	-0.60

Table 5.1 – *Statistical moments involving the scalar dissipation rate* $\left(N_{\tilde{\xi}}\right)$*, and the standardized SDR* $X = \left(\ln\left(N_{\tilde{\xi}}\right) - \ln\left(\overline{N_{\tilde{\xi}}}\right)\right) / \ln\left(\sigma_{N_{\tilde{\xi}}}\right)$*. The statistics presented correspond to the skewness* $S = \mu_3(\cdot) / \left(\mu_2(\cdot)\right)^{3/2}$*, and flatness* $E = \left(\mu_4(\cdot) / \left(\mu_2(\cdot)\right)^2\right) - 3$*. The symbols* $\mu_2(\cdot)$*,* $\mu_3(\cdot)$*, and* $\mu_4(\cdot)$ *denote the second, third and fourth central moments (respectively) of the corresponding quantities.*

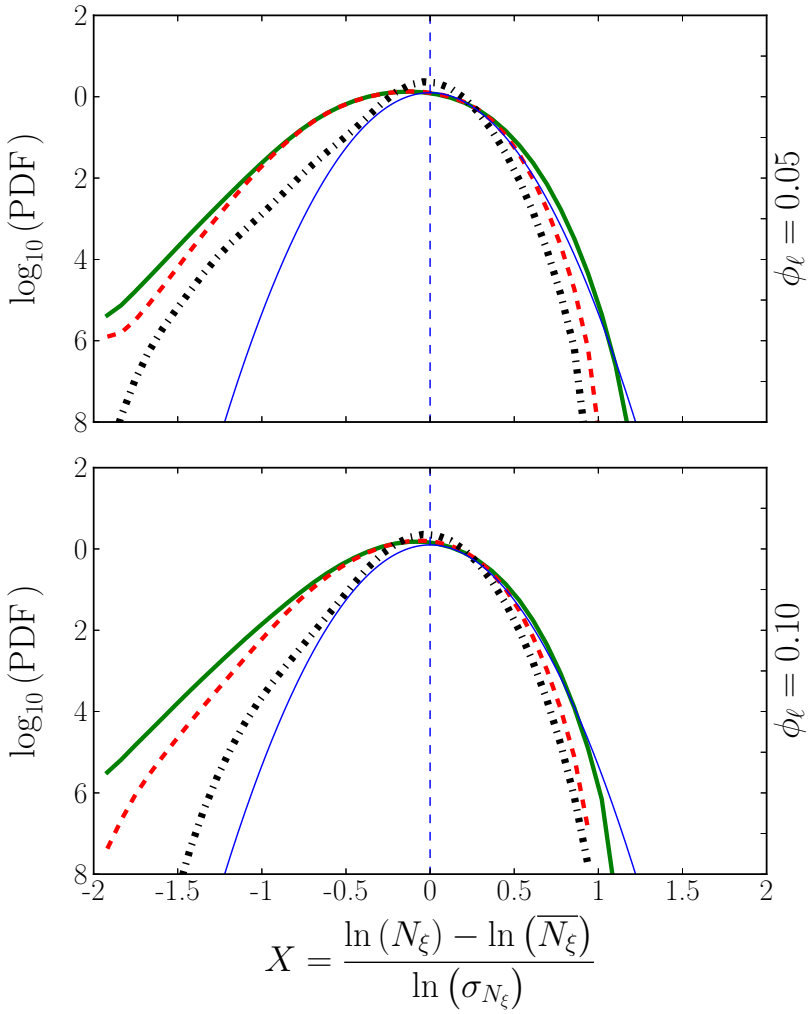

Figure 5.7. *Standardized PDF of* $X = \left(\ln\left(N_\xi\right) - \ln\left(\overline{N_\xi}\right)\right) / \ln\left(\sigma_{N_\xi}\right)$*, in the far (—), intermediate (- - -), and near (-·-·) regions from the liquid-gas interface for* $\phi_\ell = 0.05$ *(top) and* $\phi_\ell = 0.10$ *(bottom). The thin blue curve (—) represents a log-normal Gaussian distribution.*

5.3 Geometrical properties and alignment statistics of scalar mixing and dissipation

The statistical behavior of the TSI term, as given by Eq. 5.3, is now analyzed by considering the statistics of the alignment angles between $\boldsymbol{n}_\xi = \boldsymbol{g}_\xi / \,||\, \boldsymbol{g}_\xi \,||$ and the three eigenvectors $\boldsymbol{e}_i$ of the strain-rate tensor $\boldsymbol{S}$, see Fig. 5.8 :

$$\mathrm{TSI} = -2D\overline{\boldsymbol{g}_\xi \cdot \boldsymbol{S} \cdot \boldsymbol{g}_\xi} = -2N_\xi \overline{\sum_{i=1}^{i=3} \lambda_i \cos^2\left(\boldsymbol{n}_\xi, \boldsymbol{e}_i\right)} \tag{5.3}$$

The tendency of the scalar gradient to align with the most compressive direction $\boldsymbol{e}_3$ is recovered in the far region (top row of Fig. 5.8), for both volume of fluid ($\phi_\ell = 0.05$ and $\phi_\ell = 0.10$). Since the corresponding eigenvalue is negative, this leads to the positivity of the TSI term : turbulence produces scalar gradients by bringing iso-surfaces together [1]. The TSI term thus recovers its standard behavior, which contributes to SDR production. In the intermediate region is reduced the amplitude of scalar gradient production by the TSI term. This is due to a progressive transition of the alignment tendency from a preferential alignment of the scalar gradient with the compressive principal direction towards an orientation where it lies between the extensive and compressive directions. However, the highest probability levels of alignment of the scalar gradient remain associated to the most compressive principal direction, $\boldsymbol{e}_3$. In comparison to the far and intermediate regions, in the direct vicinity of the interface, the preferential alignment with the compressive principal direction becomes less marked. Here there are significant probability levels for a scalar gradient orientation featuring an angle of approximately forty-five degrees with the principal directions of compression and extension. The highest levels of probability however remain associated to a scalar gradient mostly aligned with the compressive principal direction $\boldsymbol{e}_3$. Compared to the far and the intermediate regions, the preferential alignment with the compressive principal direction is less marked in the near region. In this region, there are significant probability levels for a scalar gradient orientation featuring an angle of approximately forty-five degrees with the principal directions of compression and extension. In this respect, it is also noteworthy that the sign of the associated eigenvalues are opposite. However, their corresponding contributions to the TSI do not perfectly cancel out and there is some persistence of a preferential alignment with the compressive direction. So the most significant modification in the near region is an increased probability for the scalar gradient to be perpendicular to the intermediate direction $\boldsymbol{e}_2$, which is itself preferentially aligned with the vorticity vector.

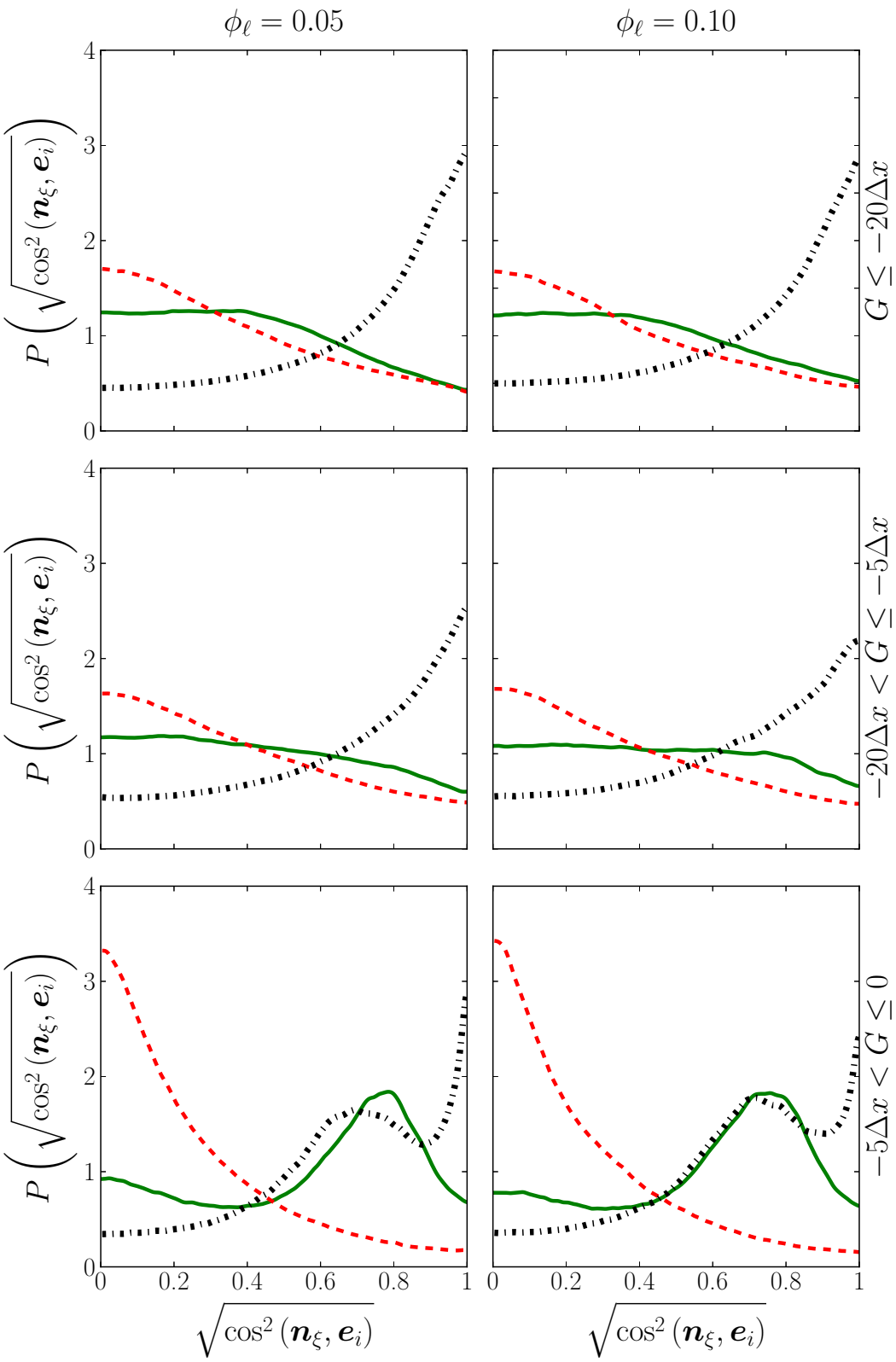

Figure 5.8. *Orientation between scalar gradient ($\boldsymbol{n}_\xi$) and strain-rate tensor principal directions ($\boldsymbol{e}_i$) : extension (——), intermediate (- - -) and compression (-·-·-); in the far (top row), intermediate (middle row), and near (bottom row) regions from the liquid-gas interface for $\phi_\ell = 0.05$ (left) and $\phi_\ell = 0.10$ (right).*

The corresponding instantaneous level-set iso-surfaces for the upper thresholds of the far (left) and near (right) regions are depicted in Fig. 5.9 for the case with $\phi_\ell = 0.05$, and Fig. 5.10 for the case with $\phi_\ell = 0.10$. Such level-set iso-surfaces are colored by the normalized scalar gradient orientation with respect to the extensive $\boldsymbol{e}_1$ (top row), intermediate, $\boldsymbol{e}_2$ (middle row), and compressive, $\boldsymbol{e}_3$ (bottom row), directions. In the far field, there is a remarkable predominance of the alignment with the compressive direction over the extensive and intermediate direction. This reflects an increase of the probability that $\boldsymbol{n}_\xi$ is perpendicular to $\boldsymbol{e}_2$, i.e., the value of $P\left(\sqrt{\cos^2\left(\boldsymbol{n}_\xi, \boldsymbol{e}_2\right)}\right)$ is approaching zero (see top row of Fig. 5.8). The results gathered in the near region confirm that the misalignment between $\boldsymbol{n}_\xi$ and $\boldsymbol{e}_2$ (blue color) increases as the liquid-gas interface is approached. A significant level of alignment of $\boldsymbol{n}_\xi$ with the most compressive principal direction $\boldsymbol{e}_3$ (red color) is maintained as the interface is approached.

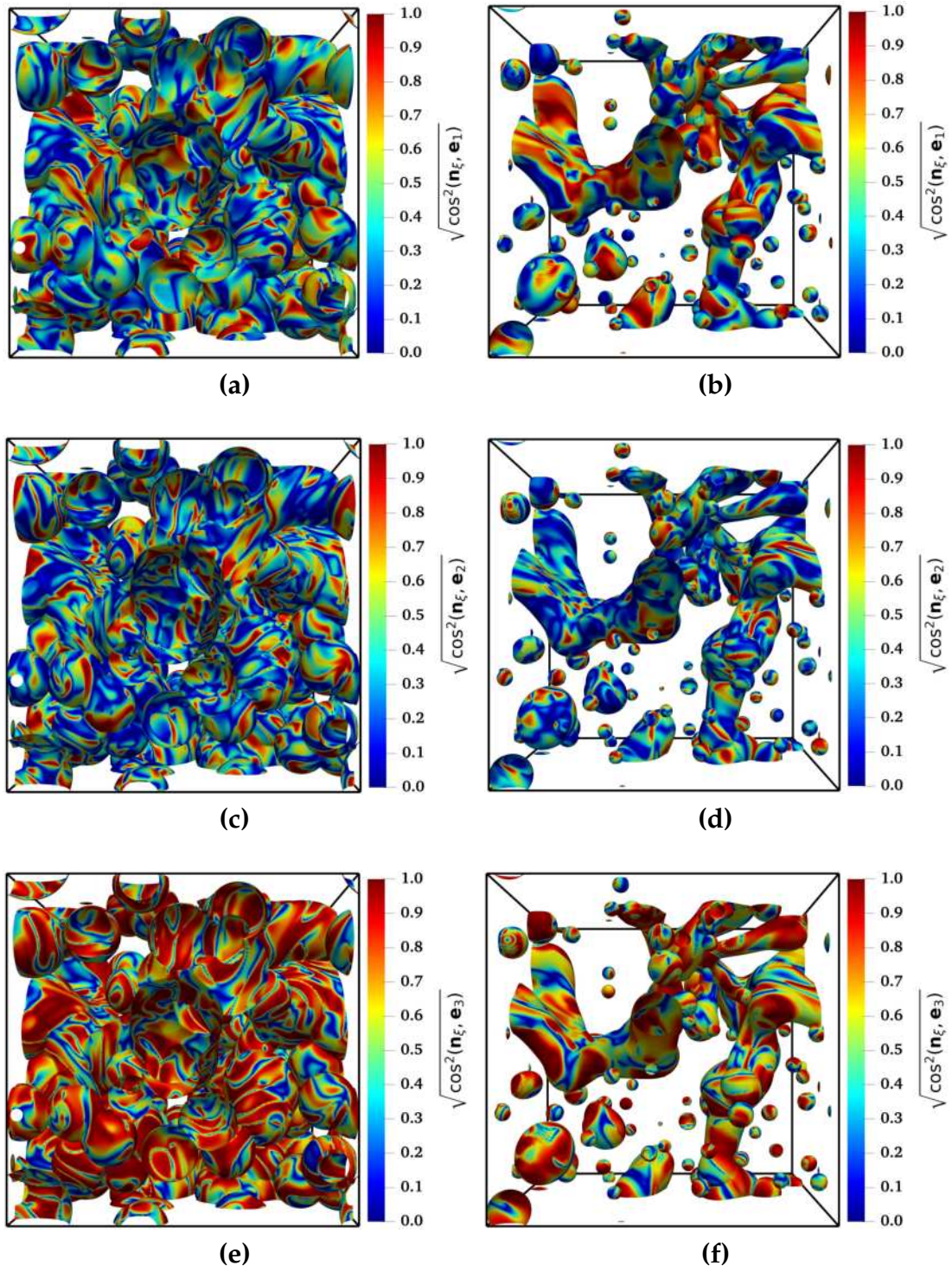

Figure 5.9. *View of an instantaneous level-set iso-surface for $\phi = 0.05$, of the far field (left) and near field (right) colored by the orientation between the scalar gradient and a principal direction, i.e., $\sqrt{\cos^2(\boldsymbol{n}_\xi, \boldsymbol{e}_i)}$ (with $i = 1$ at the top, $i = 2$ in the middle, and $i = 3$ at the bottom). (a) $\sqrt{\cos^2(\boldsymbol{n}_\xi, \boldsymbol{e}_1)}$, for the far field. (b) $\sqrt{\cos^2(\boldsymbol{n}_\xi, \boldsymbol{e}_1)}$, for the near field. (c) $\sqrt{\cos^2(\boldsymbol{n}_\xi, \boldsymbol{e}_2)}$, for the far field. (d) $\sqrt{\cos^2(\boldsymbol{n}_\xi, \boldsymbol{e}_2)}$, for the near field. (e) $\sqrt{\cos^2(\boldsymbol{n}_\xi, \boldsymbol{e}_3)}$, for the far field. (f) $\sqrt{\cos^2(\boldsymbol{n}_\xi, \boldsymbol{e}_3)}$, for the near field.*

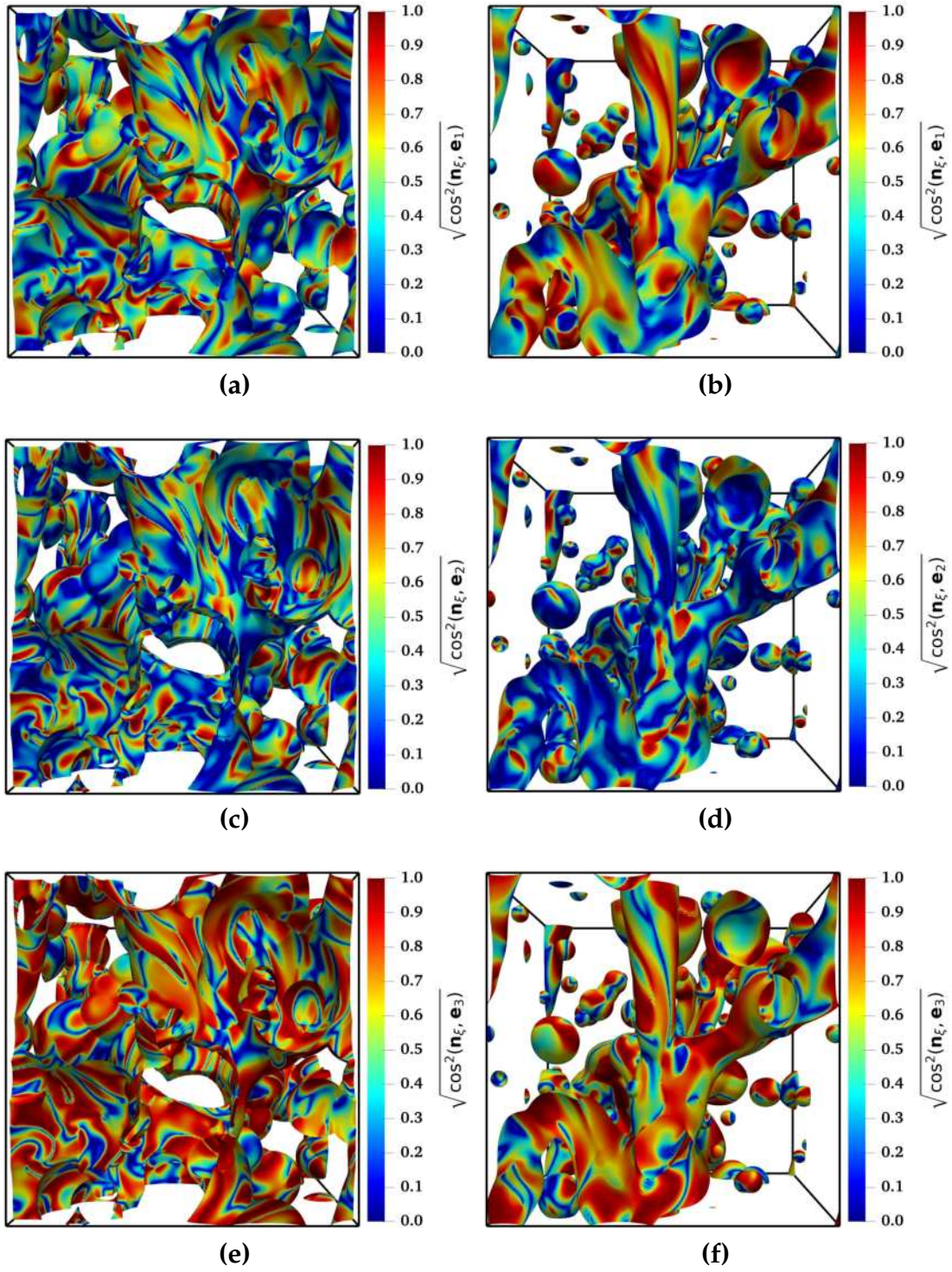

Figure 5.10. *View of an instantaneous level-set iso-surface for $\phi = 0.10$, of the far field (left) and near field (right) colored by the orientation between the scalar gradient and a principal direction, i.e., $\sqrt{\cos^2(\boldsymbol{n}_\xi, \boldsymbol{e}_i)}$ (with $i = 1$ at the top, $i = 2$ in the middle, and $i = 3$ at the bottom). (a) $\sqrt{\cos^2(\boldsymbol{n}_\xi, \boldsymbol{e}_1)}$, for the far field. (b) $\sqrt{\cos^2(\boldsymbol{n}_\xi, \boldsymbol{e}_1)}$, for the near field. (c) $\sqrt{\cos^2(\boldsymbol{n}_\xi, \boldsymbol{e}_2)}$, for the far field. (d) $\sqrt{\cos^2(\boldsymbol{n}_\xi, \boldsymbol{e}_2)}$, for the near field. (e) $\sqrt{\cos^2(\boldsymbol{n}_\xi, \boldsymbol{e}_3)}$, for the far field. (f) $\sqrt{\cos^2(\boldsymbol{n}_\xi, \boldsymbol{e}_3)}$, for the near field.*

In order to put in to better evidence the role played by each contribution to the TSI (i.e., $\lambda_i^* \cos^2\left(\boldsymbol{n}_{\tilde{\xi}}, \boldsymbol{e}_i\right)$, with $i = 1$, 2, and 3), now are considered the product between the squared orientation cosines and the eigenvalues, λ_i^* (normalized by the Kolmogorov strain-rate $\nu\eta_K^{-2}$). Figure 5.11 depict the PDF of such contribution to the TSI : extension (—), intermediate (- - -), and compression (-·-·-). For both phase cases, the highest probability levels are associated to the statistics of the extension and intermediate eigenvalue, which indicates that, in the whole gaseous phase, the TSI term is a production term (i.e., TSI $\gg 0$). This tendency, as the interface is approached, the fluctuations of these contributions, and especially those associated to extension and compression, are significantly increased. Figure 5.12 shows the normalized (also by the Kolmogorov strain-rate) semi-logarithmic scalar production term associated with stretching effects, which may continuously amplify the SDR due to stretching mechanisms which, in turn, may be balanced (to a certain level) by the dissipation of the scalar gradient itself. For both multi-phase cases, the PDF of the scalar production presents a positive net stretching, which is an universal property of any 'random' fluid. For a passive scalar such as the mixture fraction, the positiveness of its production, $B^* = -\left(\boldsymbol{g}^{\tilde{\xi}} \cdot \boldsymbol{S} \cdot \boldsymbol{g}^{\tilde{\xi}}\right)$, is associated with the production of curvature due to the concomitant processes of tilting and folding [104].

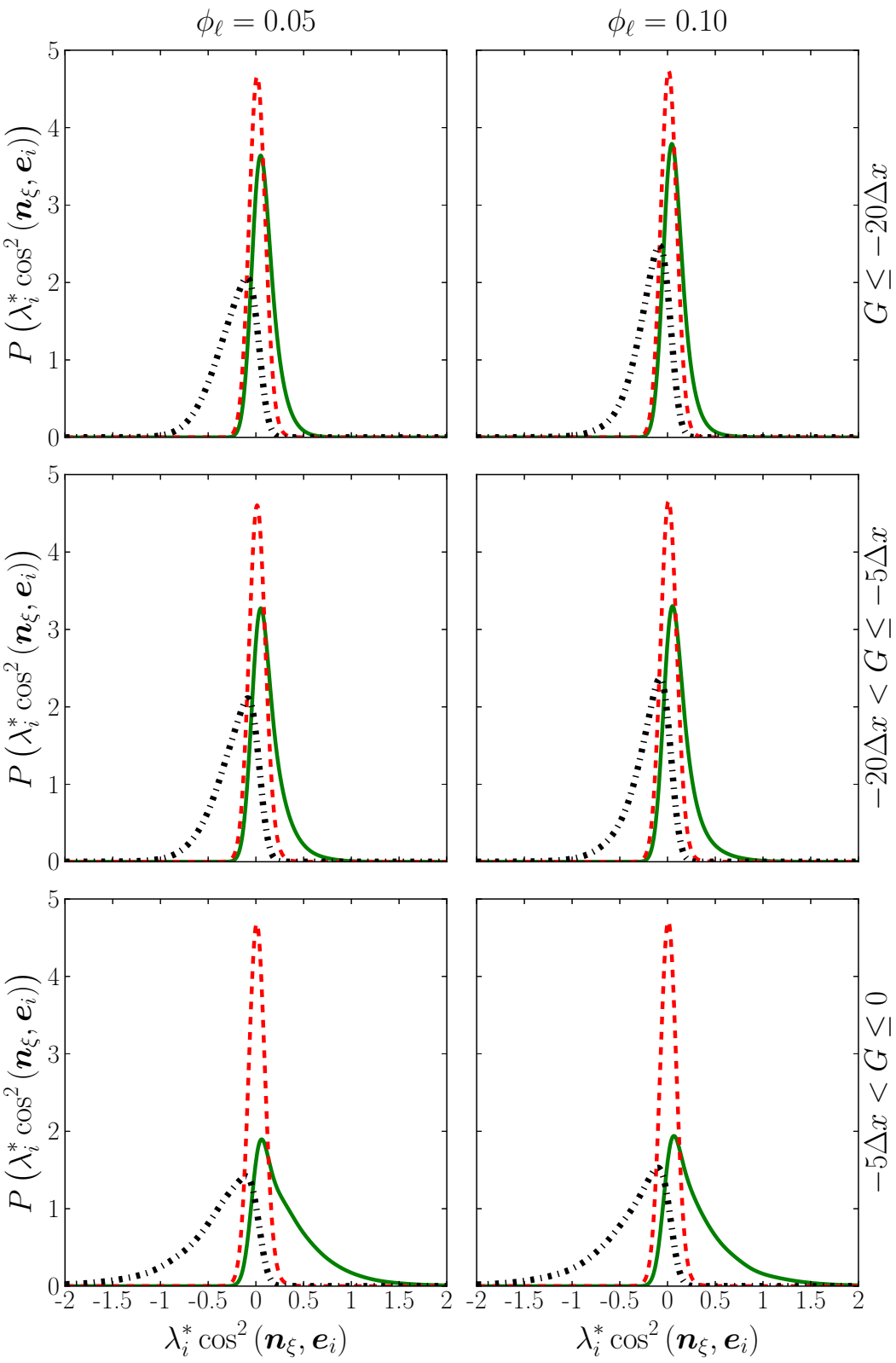

Figure 5.11. *PDFs of each principal contribution to the TSI :* $\lambda_1^* \cos^2(\boldsymbol{n}_\xi, \boldsymbol{e}_1)$ *[extension, —],* $\lambda_2^* \cos^2(\boldsymbol{n}_\xi, \boldsymbol{e}_2)$ *[intermediate, - - -], and* $\lambda_3^* \cos^2(\boldsymbol{n}_\xi, \boldsymbol{e}_3)$ *[compression, -·-·]; in the far (top row), intermediate (middle row), and near (bottom row) regions for* $\phi_\ell = 0.05$ *(left) and* $\phi_\ell = 0.10$ *(right).*

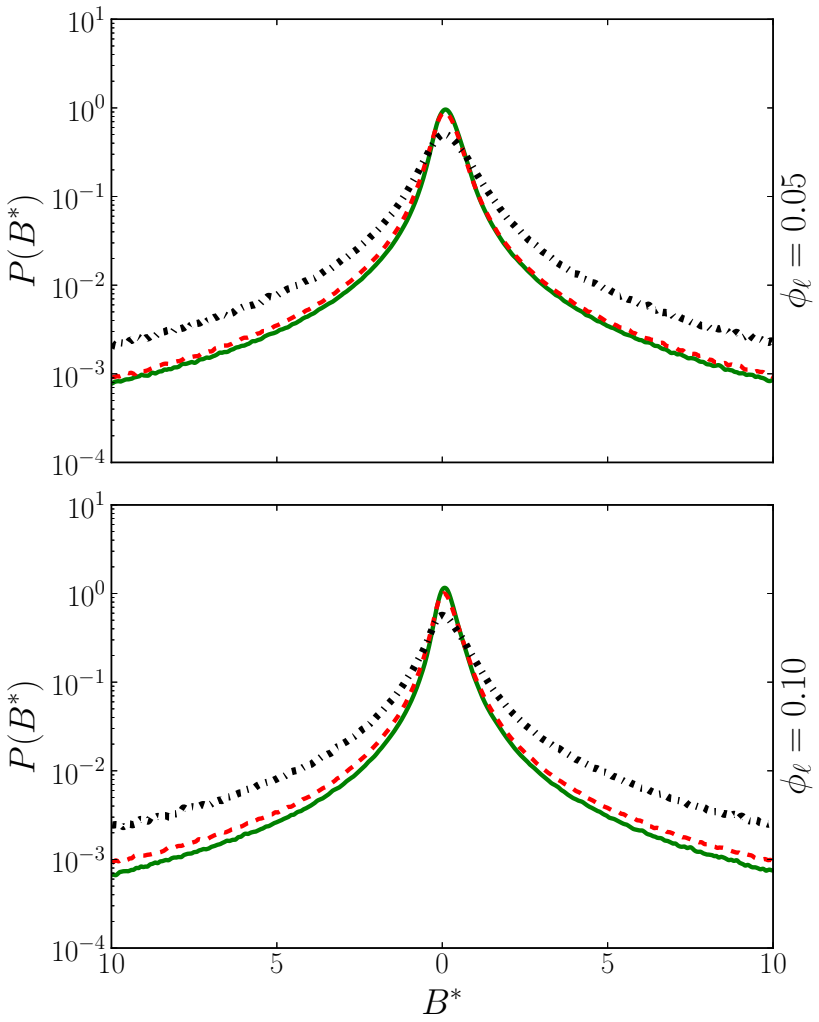

Figure 5.12. *PDF of the normalized scalar production term associated with the scalar stretching effects* $\left(B^* = -\left(\boldsymbol{g}^\xi \cdot \boldsymbol{S} \cdot \boldsymbol{g}^\xi\right) / \left(\left(\boldsymbol{g}^\xi\right)^2 \nu/\eta^2\right)\right)$ *in the far (—), intermediate (- - -), and near (-·-) regions from the liquid-gas interface for* $\phi_\ell = 0.05$ *(top) and* $\phi_\ell = 0.10$ *(bottom).*

At this level, it seems also interesting to scrutinize the interaction between the scalar gradient, $\boldsymbol{n}_\xi = \boldsymbol{g}^\xi / \mid\mid \boldsymbol{g}^\xi \mid\mid$, and the vorticity vector, $\boldsymbol{\omega}$. The corresponding alignments, displayed in Fig. 5.13, show that the two vectors are preferentially perpendicular to each other, and such tendency is enforced as the liquid-gas interface is approached. This result is consistent with our previous observations regarding the preferential alignments of vectors $\boldsymbol{n}_\xi$ and $\boldsymbol{\omega}$ with the principal directions $\boldsymbol{e}_3$ and $\boldsymbol{e}_2$, respectively.

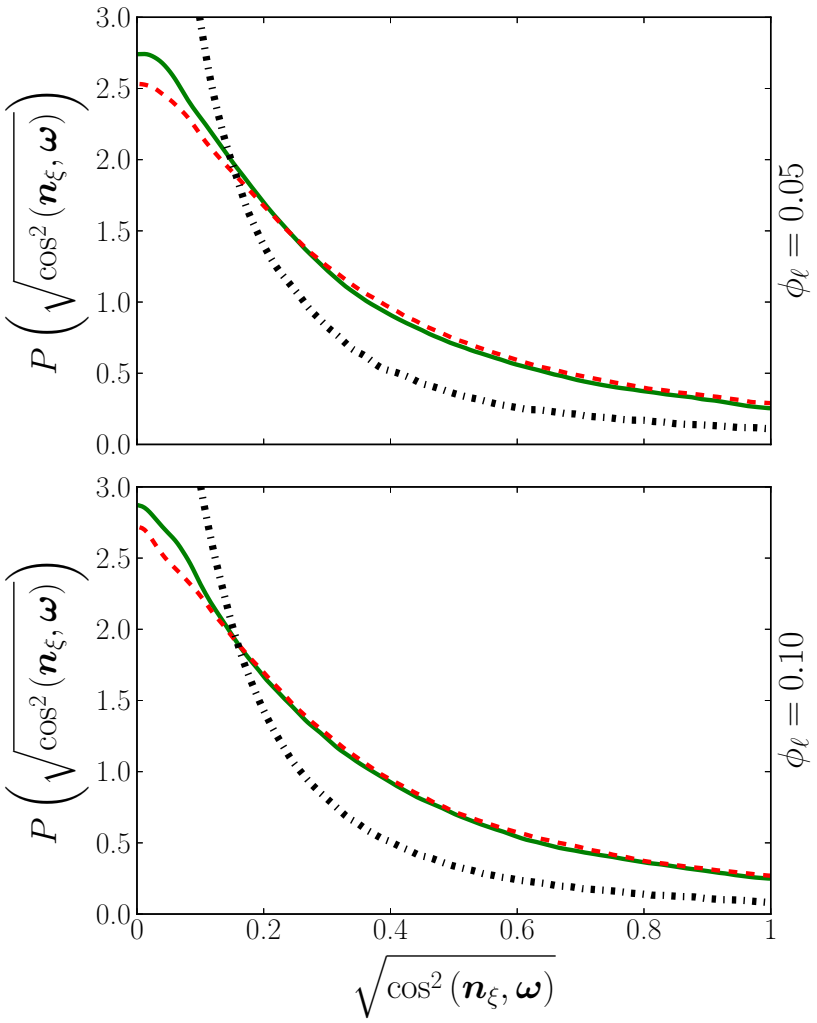

Figure 5.13. *The orientation between scalar gradient ($\boldsymbol{n}_\xi$) and vorticity ($\boldsymbol{\omega}$) in the far (—), intermediate (- - -), and near (-·-·) regions from the liquid-gas interface for $\phi_\ell = 0.05$ (top) and $\phi_\ell = 0.10$ (bottom).*

The role of the VGT in the scalar gradient evolution can be inspected in further details. In this respect, as previously highlighted by Pumir (1994) [82], the Vieillefosse lines of the (R_A, Q_A)-phase plane , i.e., the VGT characteristic polynomial discriminant equals to zero $\left(D_A = (27/4)R_A^2 + Q_A = 0\right)$, delineate two degenerative topologies : stable-star-node saddle-saddle (SsN/S/S) [negative Vieillefosse curve], and unstable-star-node saddle-saddle (UsN/S/S) [positive Vieillefosse curve], which are respectively associated to elliptic and hyperbolic flow regions. In elliptic flow regions the growth of the norm of the gradient, resulting from Eq. 5.3, cannot be very strong since the alignment of $\boldsymbol{n}_\xi$ with the eigenvector $\boldsymbol{e}_3$ is periodically destroyed. Conversely, in hyperbolic regions, where this alignment is enforced, high scalar gradients can develop as previously shown by Holzer and Siggia (1994) [48] for either scalar gradient or vorticity vector. Therefore, to get further insights, Fig. 5.14

considers the joint statistics of the amplitudes of these quantities, normalized by their corresponding RMS i.e., $P\left(||\,\boldsymbol{\omega}\,||^*, ||\,\boldsymbol{g}^\xi\,||^*\right)$. The shape of these JPDF suggests that these two quantities are statistically independent, especially in the vicinity of the liquid-gas interface.

The consideration of the alignment between the scalar stretching vector $\boldsymbol{W}^\xi \equiv -\boldsymbol{g}^\xi \cdot \boldsymbol{\nabla u}$ and the scalar gradient $\boldsymbol{g}^\xi$ is an alternative mean to foreground the intensification of the scalar dissipation. Figure 5.15 shows that, as the liquid-gas interface is approached, the alignment between these two vectors decreases, i.e., the far and intermediate regions depict higher levels of alignment between the two vectors. Such tendency is more pronounced for an increased value of ϕ_ℓ.

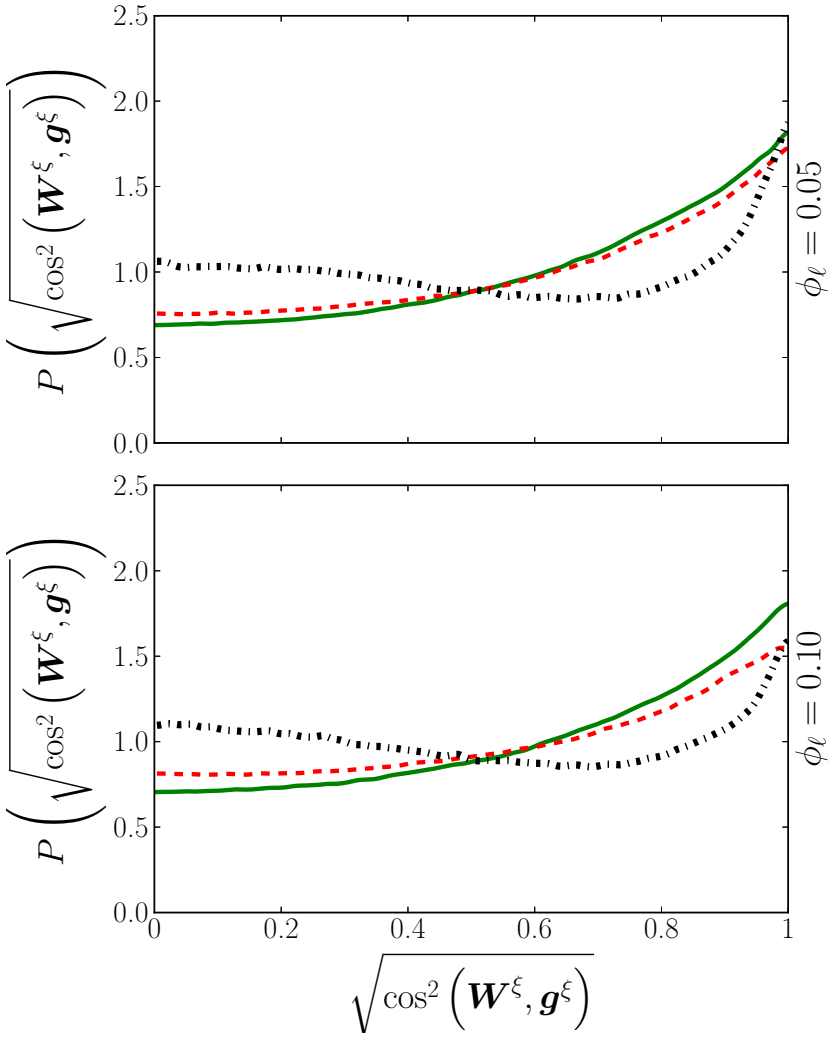

Figure 5.15. *Orientation between scalar stretching vector $\boldsymbol{W}^\xi$ and scalar gradient $\boldsymbol{g}^\xi$ in the far (—), intermediate (- - -), and near (-·-·) regions for $\phi_\ell = 0.05$ (top) and $\phi_\ell = 0.10$ (bottom).*

It is relevant to point out that the scalar stretching vector may be decomposed as

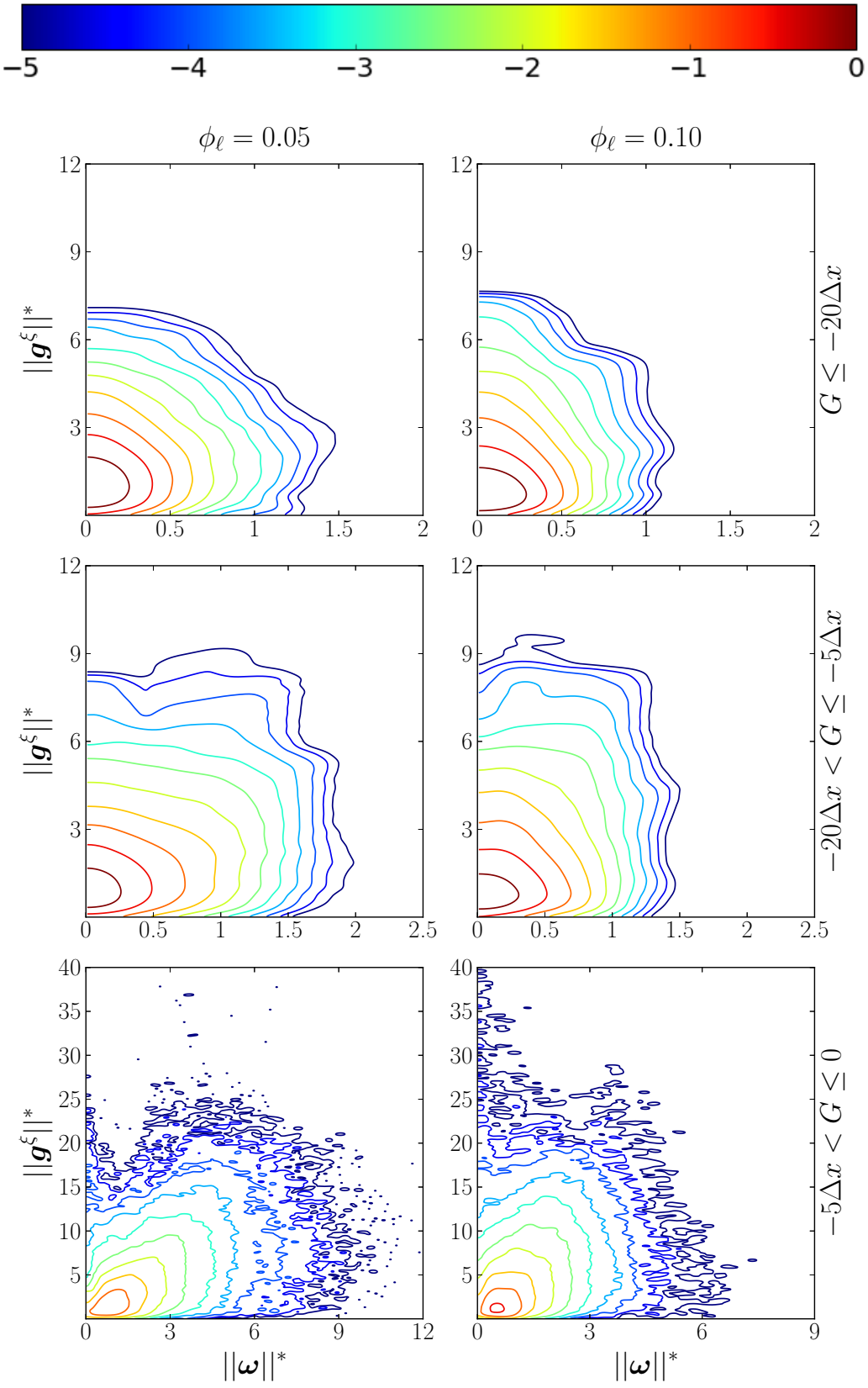

Figure 5.14. *JPDFs of the magnitudes (in log scale) normalized by their RMS values of vorticity* ($|| \boldsymbol{\omega}_k ||^*$) *and scalar gradient* ($|| \boldsymbol{g}^\xi ||^*$) *in the far (top row), intermediate (middle row), and near (bottom row) regions from the liquid-gas interface for* $\phi_\ell = 0.05$ *(left) and* $\phi_\ell = 0.10$ *(right).*

follows :

$$\boldsymbol{W}^{\xi} = \boldsymbol{W}^{\xi s} + \boldsymbol{W}^{\xi \Omega}$$

$$\boldsymbol{W}^{\xi} = -\boldsymbol{g}^{\xi} \cdot \boldsymbol{S} - \boldsymbol{g}^{\xi} \cdot \boldsymbol{\Omega}$$

with the anti-symmetric part, $\boldsymbol{\Omega}$, being related to the vorticity vector $\boldsymbol{\omega} = \boldsymbol{\nabla} \times \boldsymbol{u}$. The components of the anti-symmetric tensor, $\boldsymbol{\Omega}$, can readily be deduce from $2\Omega_{ij} = \varepsilon_{ijk}\omega_k$, where ε_{ijk} represents the Levi-Civita permutation tensor. So in Eq. 5.4, the two distinct contributions of the scalar stretching vector are presented in their vectorial form :

$$\boldsymbol{W}^{\xi} = -\boldsymbol{g}^{\xi} \cdot \boldsymbol{S} - \frac{1}{2}\boldsymbol{g}^{\xi} \times \boldsymbol{\omega} \tag{5.4}$$

with the first associated to the production/destruction of the scalar gradient norm (i.e., increase or decrease of $|| \boldsymbol{g}^{\xi} ||$), while the second is associated to the rotation or tilting of the gradient vector $\boldsymbol{g}^{\xi}$ without any influence on its norm (or its squared value, i.e., the SDR). Attention is therefore focused on the first contribution $\boldsymbol{W}^{\xi s} = -\boldsymbol{g}^{\xi} \cdot \boldsymbol{S}$, which is reported in Fig. 5.15. The corresponding PDF confirms, without any doubt, that the statistics of the alignment between $\boldsymbol{W}^{\xi s}$ and $\boldsymbol{g}^{\xi}$ is exactly the same as the one between $\boldsymbol{W}^{\xi}$ and $\boldsymbol{g}^{\xi}$.

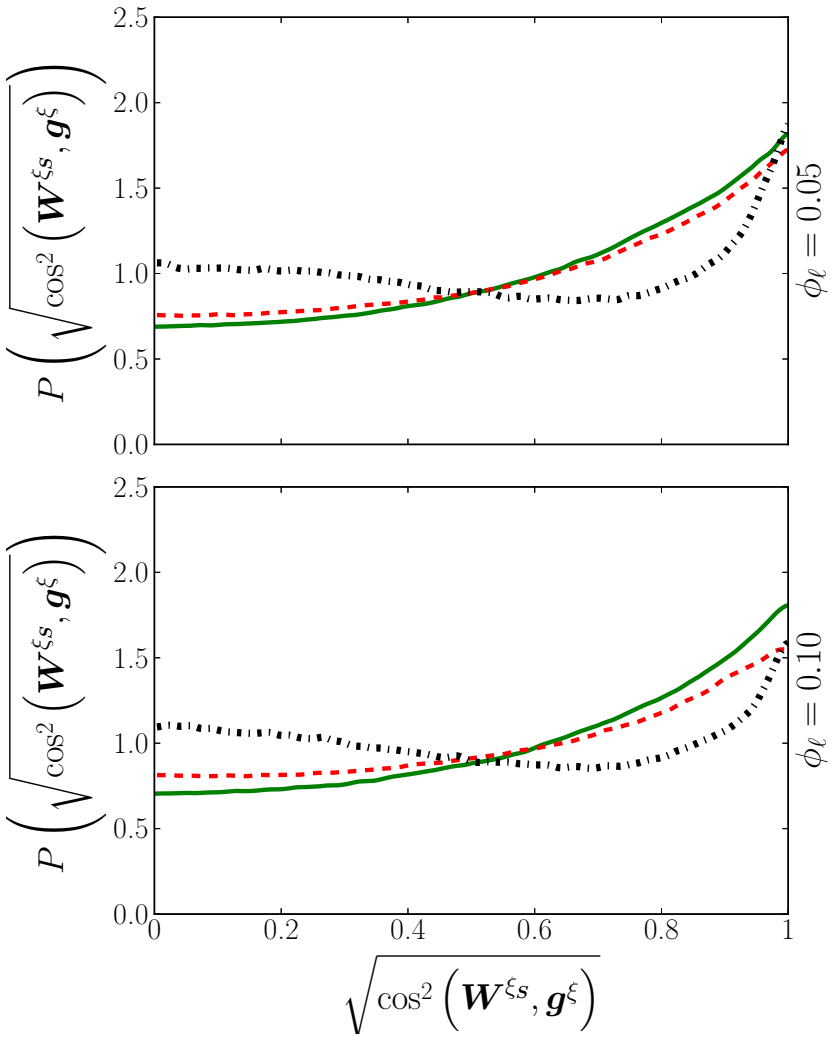

Figure 5.16. *Orientation between scalar stretching vector component $\boldsymbol{W}^{\xi s}$ and scalar gradient $\boldsymbol{g}^{\xi}$ in the far (—), intermediate (- - -), and near (-·-·) regions for $\phi_\ell = 0.05$ (top) and $\phi_\ell = 0.10$ (bottom).*

Now the strain-enstrophy orientation angle, Γ (previously reported in Fig. 4.21), is considered again, but this time their statistics are conditioned for various thresholds of the ratio $|| \boldsymbol{g}^{\xi} || / \overline{|| \boldsymbol{g}^{\xi} ||}$ equal to 0.25(—), 0.5(- - -), 1.0(-·-·), and 1.5(·····). The obtained PDFs showed in Fig. 5.17 exhibit an important difference between the far and intermediate regions associated to $G \ll -5\Delta x$, where regions of intense scalar mixing coincide with strain dominance regions ($\Gamma \gg 45°$), and the direct vicinity of the interface. Indeed, the corresponding behavior is no longer observed as the interface is approached (i.e., for values of G close to zero). In the vicinity of the interface, the various conditional PDF do not exhibit any remarkable difference and, in this region, the values of Γ are gathered around $\Gamma = 45°$: there is a strong correlation between strain and rotation.

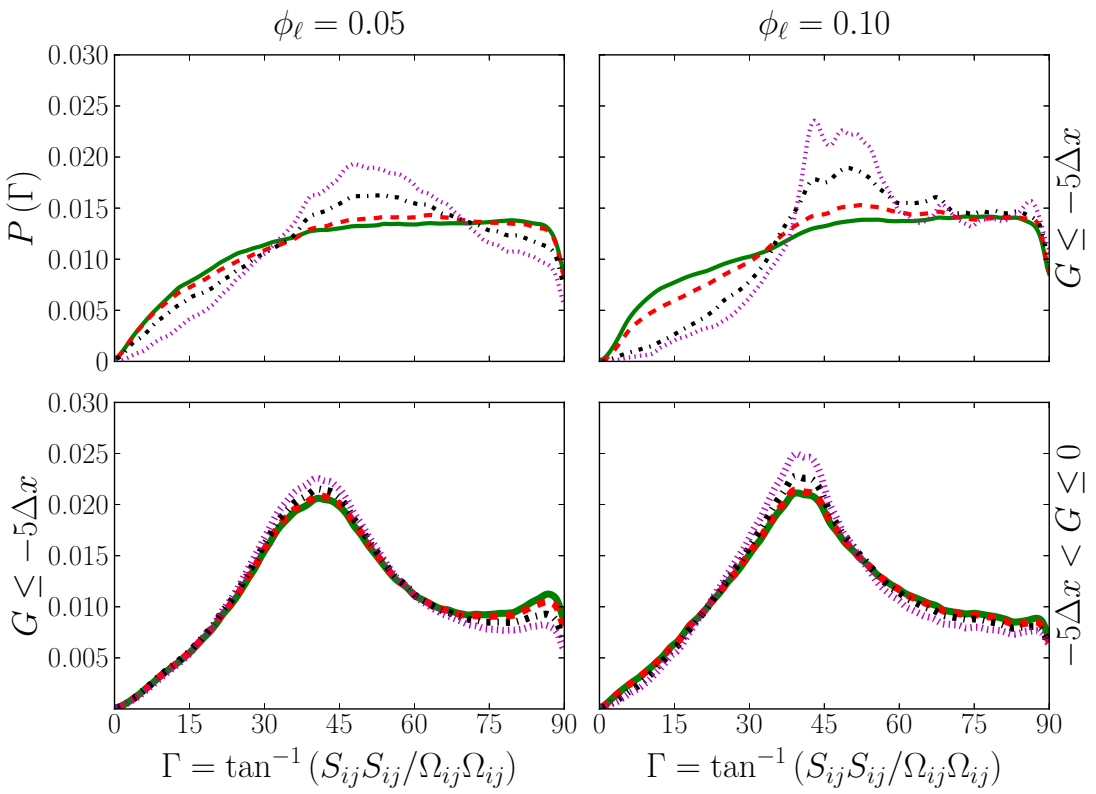

Figure 5.17. *PDF of the strain-enstrophy angle* Γ *conditioned for four threshold values :* $0.25\overline{||\, g^\xi \,||}$ *(—),* $0.5\overline{||\, g^\xi \,||}$ *(- - -),* $1.0\overline{||\, g^\xi \,||}$ *(-·-·),* *and* $1.5\overline{||\, g^\xi \,||}$ *(·····); in the* $G \leq -5\Delta x$ *(far+intermediate, top), and near (bottom) regions from the liquid-gas interface for* $\phi_\ell = 0.05$ *(left) and* $\phi_\ell = 0.10$ *(right).*

The influence of the liquid phase on scalar mixing is studied in further detail by taking into account the intensity of turbulent transfer. Such interaction is reflected in the statistics of the normalized intermediate strain $\mathbf{\Lambda}_2 = \sqrt{6}\lambda_2 / \sqrt{\lambda_1^2 + \lambda_2^2 + \lambda_3^2}$ [1]. The joint PDF between $\mathbf{\Lambda}_2$ and the normalized magnitude of the scalar gradient $||\, g^\xi \,||^*$ is also found to be sensitive to the proximity of the liquid-gas interface. A first remarkable point is that, in both the far and intermediate regions (for $\phi_\ell = 0.05$ and $\phi_\ell = 0.10$), the probability of $\mathbf{\Lambda}_2$ peaks around a value $\mathbf{\Lambda}_2^{max} = 0.2$. This behavior change in the vicinity of the interface, where $\mathbf{\Lambda}_2^{max} = 0.2$ is approaching unity. This figure also shows that regions of intense mixing rate (i.e., large values of $||\, g^\xi \,||^*$) are mostly associated to positive values of $\mathbf{\Lambda}_2$, which imply that regions featuring intense SDR are associated with a sheet-forming strain field [8]. Previous analyses of instantaneous iso-surfaces of the principal intermediate strain rate indeed concluded that sheet-forming strain field (i.e., $\mathbf{\Lambda}_2 \gg 0$) are themselves organized in the form of sheets, whereas line-forming strain fields ($\mathbf{\Lambda}_2 \ll 0$) are organized into smaller spotty structures. Intense vortex structures are in the form of elongated tubes (worms), while iso-surfaces of intense dissipation show that the most dissipative structures are in the

form of sheets.

The relationships between intermediate strain and scalar gradient magnitude (or the SDR) can be further investigated by computing conditional PDF such as those reported in Fig. 5.17, i.e., considering several thresholds of $|| \boldsymbol{g}^{\xi} || / \overline{|| \boldsymbol{g}^{\xi} ||}$ equal to 0.25(—), 0.5(- - -), 1.0(-·-), and 1.5(·····); but this time for the normalized intermediate strain-rate eigenvalue $\boldsymbol{\Lambda}_2$. Figure 5.19 displays the conditional statistics obtained in the far field exhibit significant differences between them. This figure shows that, in the far field, intense scalar mixing (·····) mostly corresponds to large values of Λ_2, a behavior that is attenuated as the liquid-gas interface is approached.

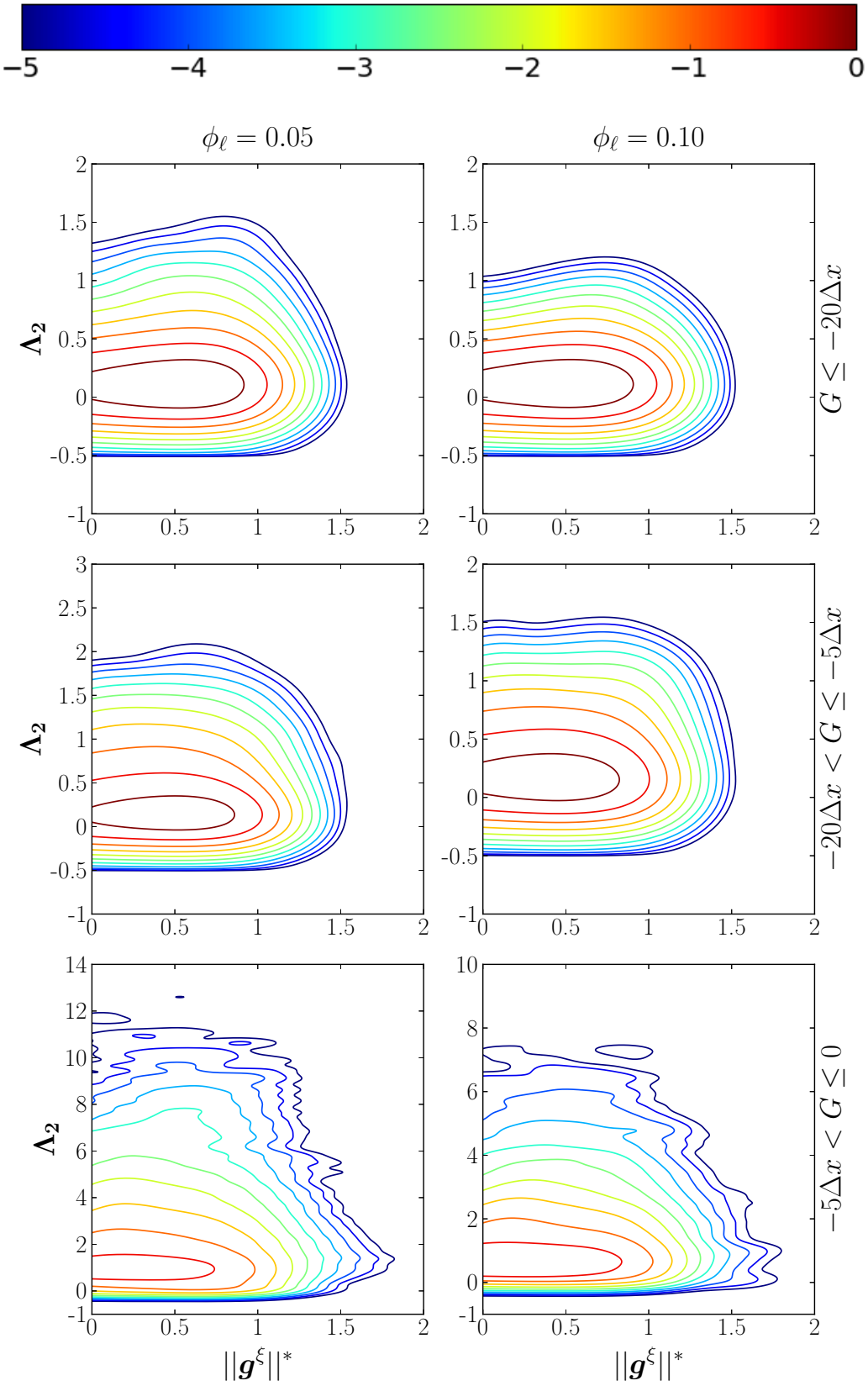

Figure 5.18. *JPDF of the magnitudes (in log scale) of the scalar gradient normalized by its RMS and the normalized intermediate strain-rate eigenvalue* $\mathbf{\Lambda}_2 = \sqrt{6}\lambda_2 / \sqrt{\lambda_1^2 + \lambda_2^2 + \lambda_3^2}$ *and in the far (top row), intermediate (middle row), and near (bottom row) regions from the liquid-gas interface for* $\phi_\ell = 0.05$ *(left) and* $\phi_\ell = 0.10$ *(right).*

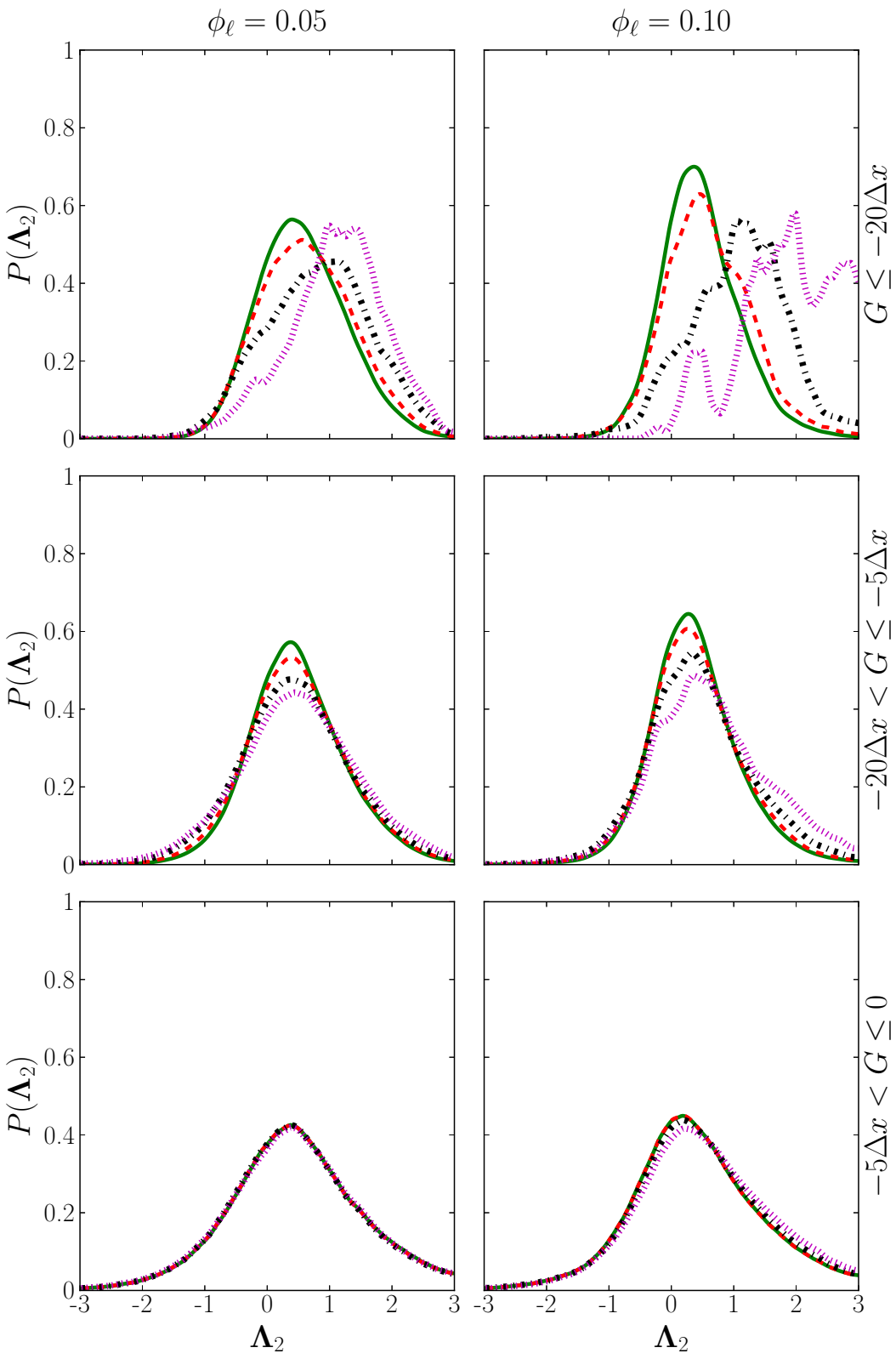

Figure 5.19. *PDF of the normalized intermediate strain-rate eigenvalue* $\Lambda_2 = \sqrt{6}\lambda_2/\sqrt{\lambda_1^2+\lambda_2^2+\lambda_3^2}$ $0.25\overline{||\, g^\xi \,||}$ (—), $0.5\overline{||\, g^\xi \,||}$ (- - -), $1.0\overline{||\, g^\xi \,||}$ (-·-·), *and* $1.5\overline{||\, g^\xi \,||}$ (·····); *in the far (top row), intermediate (middle row), and near (bottom row) regions for* $\phi_\ell = 0.05$ *(left) and* $\phi_\ell = 0.10$ *(right).*

5.4 Summary and conclusions

The mixture fraction field is exhaustively scrutinized from a set of evaporative multi-phase DNS databases featuring two distinct values of the liquid volume fraction ϕ_ℓ. In a fist step the scalar field, as well as its gradient and dissipation rate, are inspected on the basis of some geometrical properties and alignment statistics of the scalar field. The mean mixture fraction concentration, $\overline{\xi}$, and the corresponding variance levels are smaller as regions farther from the liquid-gas interface are considered. The components of the scalar gradient, $\boldsymbol{g}^{\xi}$, are studied in two different frames of reference : i) the standard one, i.e., $\boldsymbol{R_x}$, and ii) another one *attached* to the liquid-gas interface $\boldsymbol{R_G}$. In the first frame of reference, there is put into evidence that the molecular mixing rate and the SDR increase as the interface is approached, and under the second there is confirmed that in the far region the mixture fraction is almost homogeneous, but as the interface is approached, the variance levels grows, especially the one corresponding to the orientation with the unitary normal vector, $\boldsymbol{n}$. Such orientation becomes positively skewed in the vicinity of the interface. In this region the orientation of the scalar gradient is strongly aligned with $\boldsymbol{n}$. On the one hand, the skewness, $S_{N_{\tilde{\xi}}}$, and kurtosis, $E_{N_{\tilde{\xi}}}$, of the SDR display an intermittent behavior with their corresponding maximum value in the vicinity of the interface and, at the same time, positive excess of kurtosis. On the other hand, the standardized logarithmic of the SDR, X, presents PDF's that are always negatively skewed and which values decrease as the liquid-gas interface is approached, meanwhile negative excess of kurtosis is presented in the far and and intermediate regions for the case of 5% of liquid volume fraction, and leptokurtic kurtosis everywhere else. Then attention is focused on the TSI terms, their contributions, and some other statistics relevant for the mixture fraction field. The orientation between scalar gradient, $\boldsymbol{n}_{\tilde{\xi}}$, and strain-rate tensor principal directions, $\boldsymbol{e}_i$, exhibit a transition from being preferentially aligned with the eigenvector that contributes to SDR production in the far region, to being preferentially aligned with both eigenvectors that produce and dissipate the SDR and broadly misaligned with the intermediate eigenvector, in the vicinity of the liquid-gas interface. In this respect, the product between the squared orientation cosines and the normalized eigenvalues, $\lambda_i^* \cos^2\left(\boldsymbol{n}_{\tilde{\xi}}, \boldsymbol{e}_i\right)$, confirms that the TSI term is a production term in all the gaseous phase. Their corresponding normalized scalar production term, B^*, shows that due to the stretching mechanisms, the TSI continuously amplifies the SDR. The orientation between scalar gradient and vorticity, $\boldsymbol{\omega}$, displays a predilection of misalignment between them that increases as the interface is approached. The JPDF of the normalized magnitudes of vorticity, $||\ \boldsymbol{\omega}\ ||$, and scalar gradient, $||\ \boldsymbol{g}^{\tilde{\xi}}\ ||$, confirms that they are statistically independent. The orientation between the scalar gradient and the scalar

stretching vector, $\boldsymbol{W}^{\tilde{\zeta}}$, as well as between the scalar stretching vector contribution associated to the production/destruction of the scalar gradient norm, $\boldsymbol{W}^{\tilde{\zeta}s}$, unveil exactly the same behavior of decreasing the alignments as a region closer to the liquid-gas interface is considered. The strain-enstrophy angle, Γ, shows that intense scalar mixing coincides with strain dominance regions in all the gaseous domain excepting near the interface, where instead strong correlation between strain and rotation are found. The JPDF between normalized magnitude of the scalar gradient, and normalized intermediate strain-rate eigenvalue, $\boldsymbol{\Lambda}_2$, shows that regions featuring intense SDR are associated with a sheet-forming strain field. Finally, the conditional PDF of the normalized intermediate strain-rate eigenvalue puts into evidence that intense scalar mixing is correlated to large values of normalized intermediate eigenvalue, such behavior is attenuated as the liquid-gas interface is approached.

6 Lagrangian evolution equations analysis

Content of the chapter

This chapter enclosed the Lagrangian-statistical characterization of the turbulent velocity field. First the mathematical formalisms of the Lagrangian evolution equations and conditional mean trajectories (CMT) are presented. This is followed by a detailed description of the methodology used to gather such CMT. This methodology includes a novel consideration, which allows, for the first time, to scrutinize not only the direction, but also the magnitude of the trajectories computed from the terms of the LEE. Then a detailed inspection of the Lagrangian dynamics of the HIT reference case is presented. Finally the analysis concerning to the multi-phase cases featuring evaporation with different levels of volume of fluids, $\phi_\ell = 0.05$ and $\phi_\ell = 0.10$ is reported. The acquisition of the statistics is gathered at various distances from the interface, in such a manner that the gaseous phase is divided into several sub-regions according to the values of the level-set G, i.e., the distance from the liquid/gas interface, as shown in Table 6.1. It is noteworthy to remember that, in the gaseous phase, the distance to the interface is defined in such a manner that the level-set value, G, is negative.

Gaseous phase regions	Level-set intervals
Far	$G \leq -20\Delta x$
Intermediate	$-20\Delta x < G \leq -7\Delta x$
Near	$-7\Delta x < G \leq -2\Delta x$

Table 6.1 – *Definition of three sub-regions in the gaseous phase based on the level-set value G.*

6.1 Theoretical background

Mathematical formalism of the Lagrangian evolution equations (LEE)

In order to understand and model the dynamics of the turbulent structures of the VGT tensor, it is necessary to refine the study of the Lagrangian physical mechanisms of the local flow topologies of such invariants ($P_{\boldsymbol{A}}$, $Q_{\boldsymbol{A}}$ and $R_{\boldsymbol{A}}$). To do so, the first step consists into obtaining the time evolution of $\boldsymbol{A}$ in a Lagrangian frame of reference by taking the gradient of the Navier–Stokes equations [11] :

$$\begin{aligned} \dot{A}_{ij} &\equiv \frac{DA_{ij}}{Dt} \\ &= \frac{\partial A_{ij}}{\partial t} + u_k \frac{\partial A_{ij}}{\partial x_k} = \underbrace{-\frac{\partial u_i}{\partial x_k}\frac{\partial u_k}{\partial x_j}}_{A_{ik}A_{kj}} - \mathcal{H}^p_{ij} - \mathcal{H}^b_{ij} + \mathcal{T}_{ij} \end{aligned} \tag{6.1}$$

where D/Dt denotes the substantial (or total) derivative. The first term of the right-hand side describes the interaction between the invariants of the VGT. The second and third terms correspond to pressure Hessian and baroclinic effects, $\mathcal{H}^p_{ij}$ and $\mathcal{H}^b_{ij}$, respectively [41]. Finally the fourth term stands for the viscous contribution, $\mathcal{T}_{ij} \equiv \frac{\partial}{\partial x_j}\left(\frac{1}{\rho}\frac{\partial \sigma_{ik}}{\partial x_k}\right)$, with $\sigma_{ij} = 2\mu S^*_{ij}$ being the viscous stress tensor, where S^*_{ij} is the anisotropic part of the strain-rate tensor, i.e., $S^*_{ij} = S_{ij} - \frac{1}{3}S_{kk}\delta_{ij}$.

The two components of the pressure, i.e., pressure Hessian and baroclinic contribution terms, are defined as follows

$$\mathcal{H}_{ij} \equiv \frac{\partial}{\partial x_j}\left(\frac{1}{\rho}\frac{\partial p}{\partial x_i}\right) = \frac{1}{\rho}\frac{\partial^2 p}{\partial x_i \partial x_j} + \left(-\frac{1}{\rho^2}\frac{\partial \rho}{\partial x_j}\frac{\partial p}{\partial x_i}\right) \equiv \mathcal{H}^p_{ij} + \mathcal{H}^b_{ij}\,, \tag{6.2}$$

The pressure Hessian contribution can be related to the spatial distribution of the VGT [70, 21, 72, 62, 71], therefore it seems convenient to decomposed it into isotropic and anisotropic contributions, which drive the local and non-local effects, respectively. The isotropic part is purely local and can be defined as follows :

$$\mathcal{H}_{ij}^{p^{loc}} = -\operatorname{tr}\left(A^2\right)\frac{\delta_{ij}}{3} \tag{6.3}$$

thus, the deviatoric part, or non-local effect, may be deduced from the following difference :

$$\mathcal{H}_{ij}^{p^{non-loc}} = \mathcal{H}_{ij}^{p} - \mathcal{H}_{ij}^{p^{loc}} \tag{6.4}$$

At this level, it must be emphasized that a step-by-step derivation of the LEE is shown in Appendix A. Besides similar LEE can be readily derived for the invariants of the traceless VGT $\boldsymbol{A}^*$, as it is shown in Appendix B. The traceless VGT is indeed often considered to analyze turbulent flows featuring compressibility and/or dilatational effects [79, 85, 8, 101, 115, 64]. So the variable-density form of the transport equations for the second products Eq. 6.5 and triple products Eq. 6.6 are :

$$\begin{aligned}\frac{D\left(A_{in}A_{nj}\right)}{Dt} + 2A_{in}A_{nk}A_{kj} = &- A_{in}\mathcal{H}_{nj}^{p} - \mathcal{H}_{in}^{p}A_{nj} \\ &- A_{in}\mathcal{H}_{nj}^{b} - \mathcal{H}_{in}^{b}A_{nj} + A_{in}\mathcal{T}_{nj} + \mathcal{T}_{in}A_{nj}\end{aligned} \tag{6.5}$$

$$\begin{aligned}\frac{D\left(A_{in}A_{nk}A_{kj}\right)}{Dt} + 3A_{in}A_{nk}A_{kr}A_{rj} = &- A_{in}A_{nk}\mathcal{H}_{kj}^{p} - A_{in}\mathcal{H}_{nk}^{p}A_{kj} - \mathcal{H}_{in}^{p}A_{nk}A_{kj} \\ &- A_{in}A_{nk}\mathcal{H}_{kj}^{b} - A_{in}\mathcal{H}_{nk}^{b}A_{kj} - \mathcal{H}_{in}^{b}A_{nk}A_{kj} \\ &- A_{in}A_{nk}\mathcal{T}_{kj} - A_{in}\mathcal{T}_{nk}A_{kj} - \mathcal{T}_{in}A_{nk}A_{kj}\end{aligned} \tag{6.6}$$

It is known that the eigenvalues of A_{ij} satisfy the characteristic equation Eq. 6.7 :

$$\lambda^3 + P\lambda^2 + Q\lambda + R = 0 \tag{6.7}$$

therefore the tensor A_{ij} satisfies Eq. 6.8 :

$$A_{in}A_{nk}A_{kj} + PA_{ik}A_{kj} + QA_{ij} + R\delta_{ij} = 0 \tag{6.8}$$

For variable-density flows, the invariant of A_{ij} are :

$$P = -A_{kk} \tag{6.9a}$$
$$Q = \frac{1}{2}\left(P^2 - A_{ij}A_{ji}\right) \tag{6.9b}$$
$$R = \frac{1}{3}\left(-P^3 + 3PQ - A_{ij}A_{jk}A_{ki}\right) \tag{6.9c}$$

Taking the trace of Eq. 6.1 leads to the transport equation of the first invariant, P_A Eq. 6.10 :

$$\dot{P}_A \equiv \frac{DP_A}{Dt} = \underbrace{\left(P_A^2 - 2Q_A\right)}_{\mathcal{I}_{P_A}} + \underbrace{\mathcal{H}^p_{ii}}_{\mathcal{II}^p_{P_A}} + \underbrace{\mathcal{H}^b_{ii}}_{\mathcal{II}^b_{P_A}} + \underbrace{(-\mathcal{T}_{ii})}_{\mathcal{III}_{P_A}} \tag{6.10}$$

Taking the trace of Eq. 6.5 leads to the transport equation of the second invariant, Q_A :

$$\begin{aligned}\dot{Q}_A \equiv \frac{DQ_A}{Dt} = &\underbrace{(P_AQ_A - 3R_A)}_{\mathcal{I}_{Q_A}} + \underbrace{\left(P_A\mathcal{H}^p_{ii} + A_{in}\mathcal{H}^p_{ni}\right)}_{\mathcal{II}^p_{Q_A}} \\ &+ \underbrace{\left(P_A\mathcal{H}^b_{ii} + A_{in}\mathcal{H}^b_{ni}\right)}_{\mathcal{II}^b_{Q_A}} + \underbrace{(-P_A\mathcal{T}_{ii} - A_{in}\mathcal{T}_{ni})}_{\mathcal{III}_{Q_A}}\end{aligned} \tag{6.11}$$

Taking the trace of Eq. 6.6 leads to the transport equation of the third invariant, R_A :

$$\dot{R}_{\boldsymbol{A}} \equiv \frac{DR_A}{Dt} = \underbrace{(P_A R_A)}_{\mathcal{I}_{R_A}} + \underbrace{\left(Q_A \mathcal{H}^p_{ii} + P_A A_{in} \mathcal{H}^p_{ni} + A_{in} A_{nk} \mathcal{H}^p_{ki}\right)}_{\mathcal{II}^p_{R_A}} + \underbrace{\left(Q_A \mathcal{H}^b_{ii} + P_A A_{in} \mathcal{H}^b_{ni} + A_{in} A_{nk} \mathcal{H}^b_{ki}\right)}_{\mathcal{II}^b_{R_A}} + \underbrace{\left(-Q_A \mathcal{T}_{ii} - P_A A_{in} \mathcal{T}_{ni} - A_{in} A_{nk} \mathcal{T}_{ki}\right)}_{\mathcal{III}_{R_A}} \tag{6.12}$$

At this level, it seems noteworthy to make clear that the baroclinic pressure contribution, i.e., $\mathcal{II}^b_{\left(\dot{R}^*_{\boldsymbol{A}}, \dot{Q}^*_{\boldsymbol{A}}\right)}$, is not considered to gather the statistical analysis presented hereafter, simply because the flow configuration of the data-set correspond to incompressible constant-density flows, which implies this contribution is zero. Thus the pressure Hessian contribution will be the only pressure term taken into account and, in the following discussion of the results, it may be addressed just as $\mathcal{II}_{\left(\dot{R}^*_{\boldsymbol{A}}, \dot{Q}^*_{\boldsymbol{A}}\right)}$.

Mathematical formalism of the conditional mean trajectories (CMT)

The conditional mean trajectories (CMT) are used to study the Lagrangian physical evolution of local flow topologies of the invariants of $\boldsymbol{A}$. Such trajectories may be obtained considering a mean temporal rate of change of the invariants of A_{ij} using a conditional average technique similar to the one retained by Ooi et al. (1999) [73] :

$$\dot{X}(X,Y) \equiv \left\langle \frac{DX}{Dt} \middle| (X = X_0, Y = Y_0) \right\rangle = \frac{1}{N_{XY}} \sum_{X_0 - \Delta X/2}^{X_0 + \Delta X/2} \sum_{Y_0 - \Delta Y/2}^{Y_0 + \Delta Y/2} \frac{DX}{Dt}(X,Y) \tag{6.13a}$$

$$\dot{Y}(X,Y) \equiv \left\langle \frac{DY}{Dt} \middle| (X = X_0, Y = Y_0) \right\rangle = \frac{1}{N_{XY}} \sum_{X_0 - \Delta X/2}^{X_0 + \Delta X/2} \sum_{Y_0 - \Delta Y/2}^{Y_0 + \Delta Y/2} \frac{DY}{Dt}(X,Y) \tag{6.13b}$$

where ΔX and ΔY are the widths of the bins along the X and Y variables respectively, N_{XY} the number of samples in the domain $[X_0 - \Delta X/2 < X < X_0 + \Delta X/2]$ and $[Y_0 - \Delta Y/2 < Y < Y_0 + \Delta Y/2]$, and the brakes $\langle \cdot \rangle$ are the ensemble mean of DX/Dt or DY/Dt at $(X = X_0, Y = Y_0)$.

In order to calculate the averaged values of $DR_{\boldsymbol{A}}/Dt$ and $DQ_{\boldsymbol{A}}/Dt$ conditioned

upon R_A and Q_A, the (Q_A, R_A)-phase plane is firstly divided into $N_R \times N_Q$ equally sized bins, where N_R is the number of bins along the R_A coordinate and N_Q is the number of bins along the Q_A coordinate. The averaged values of DQ_A/Dt and DR_A/Dt are then computed at every bin in the (Q_A, R_A)-phase plane using Eq. 6.11 and Eq. 6.12, with R_A standing for X and Q_A standing for Y. The conditional mean values of DQ_A/Dt and DR_A/Dt are thus known for every bin in the (R_A^*, Q_A^*)-phase plane and represent a conditional mean vector field $\left[\dot{Q}_A(Q_A, R_A), \dot{R}_A(Q_A, R_A)\right]$ in the (R_A^*, Q_A^*)-phase plane.
The CMT's are computed using the conditional mean vector field :

$$\left\langle \frac{1}{Q_\Omega}\frac{DQ_A}{Dt} \middle| \frac{R_A}{Q_\Omega^{3/2}}, \frac{Q_A}{Q_\Omega} \right\rangle = \left\langle \frac{\mathcal{I}_Q}{Q_\Omega} + \frac{\mathcal{II}_Q}{Q_\Omega} + \frac{\mathcal{II}_Q^b}{Q_\Omega} + \frac{\mathcal{III}_Q}{Q_\Omega} \middle| \frac{R_A}{Q_\Omega^{3/2}}, \frac{Q_A}{Q_\Omega} \right\rangle \tag{6.14a}$$

$$\left\langle \frac{1}{Q_\Omega^{3/2}}\frac{DR_A}{Dt} \middle| \frac{R_A}{Q_\Omega^{3/2}}, \frac{Q_A}{Q_\Omega} \right\rangle = \left\langle \frac{\mathcal{I}_R}{Q_\Omega^{3/2}} + \frac{\mathcal{II}_R}{Q_\Omega^{3/2}} + \frac{\mathcal{II}_R^b}{Q_\Omega^{3/2}} + \frac{\mathcal{III}_R}{Q_\Omega^{3/2}} \middle| \frac{R_A}{Q_\Omega^{3/2}}, \frac{Q_A}{Q_\Omega} \right\rangle \tag{6.14b}$$

The minimal level of convergence to compute the conditional mean trajectories presented below is set-up to a minimum of 300 samples per bin different from zero. This is in accordance with Ooi et al. (1999) [73].

6.2 Lagrangian dynamics of the VGT

Before embarking in the detailed analysis of the CMT, it seems convenient to explain the setting procedure of the reference scale of each (R_A^*, Q_A^*)-phase plane presented in Figs. 6.1, 6.2, 6.7 - 6.10. The scale is represented by the horizontal arrow printed at the top of the first quadrant, Q_1, of the (R_A^*, Q_A^*)-phase planes. Previously, in the literature, it seems that such a scale had been chosen in a rather "arbitrary" manner, just to allow a proper visualization of the vector fields [73, 112, 102]. This contrast with the scales of the CMT presented hereafter, which have been computed considering statistical properties of each term of the budget, as the mean vector length, $\overline{X}_{\langle \dot{R}_A^*, \dot{Q}_A^* \rangle} = \left|\left| \sqrt{\left(\dot{R}_A^*\right)^2 + \left(\dot{Q}_A^*\right)^2} \right|\right|$, and its corresponding standard deviation, $\sigma_{\langle \dot{R}_A^*, \dot{Q}_A^* \rangle}$. The exact vector scale is computed by adding to the mean vector length three times the scalar deviation, $\zeta_{term} = \overline{X}_{\langle \dot{R}_A^*, \dot{Q}_A^* \rangle} + 3\sigma_{\langle \dot{R}_A^*, \dot{Q}_A^* \rangle}$. Then the exact vector scale, ζ_{term}, is rounded up if the decimal fraction is equal or higher to 0.50, $\Sigma_{term} = \lceil \zeta_{term} \rceil$, or rounded down if the decimal fraction is lower than 0.50, $\Sigma_{term} = \lfloor \zeta_{term} \rfloor$. In this

manner, the scale of the CMT of each term, Σ_{term}, only count on significant digits before the decimal point. The scale-computation methodology proposed in this work allows to compare, for the first time, not only the orientation, but also the magnitude of all the terms between them. The exact, ζ_{term}, and rounded, Σ_{term}, vector scale values of the CMT's of the LEE are summarized in Tables 6.2 and 6.3 for the HIT reference case and the two-phase flow cases featuring evaporation, respectively.

6.2.1 HIT reference case

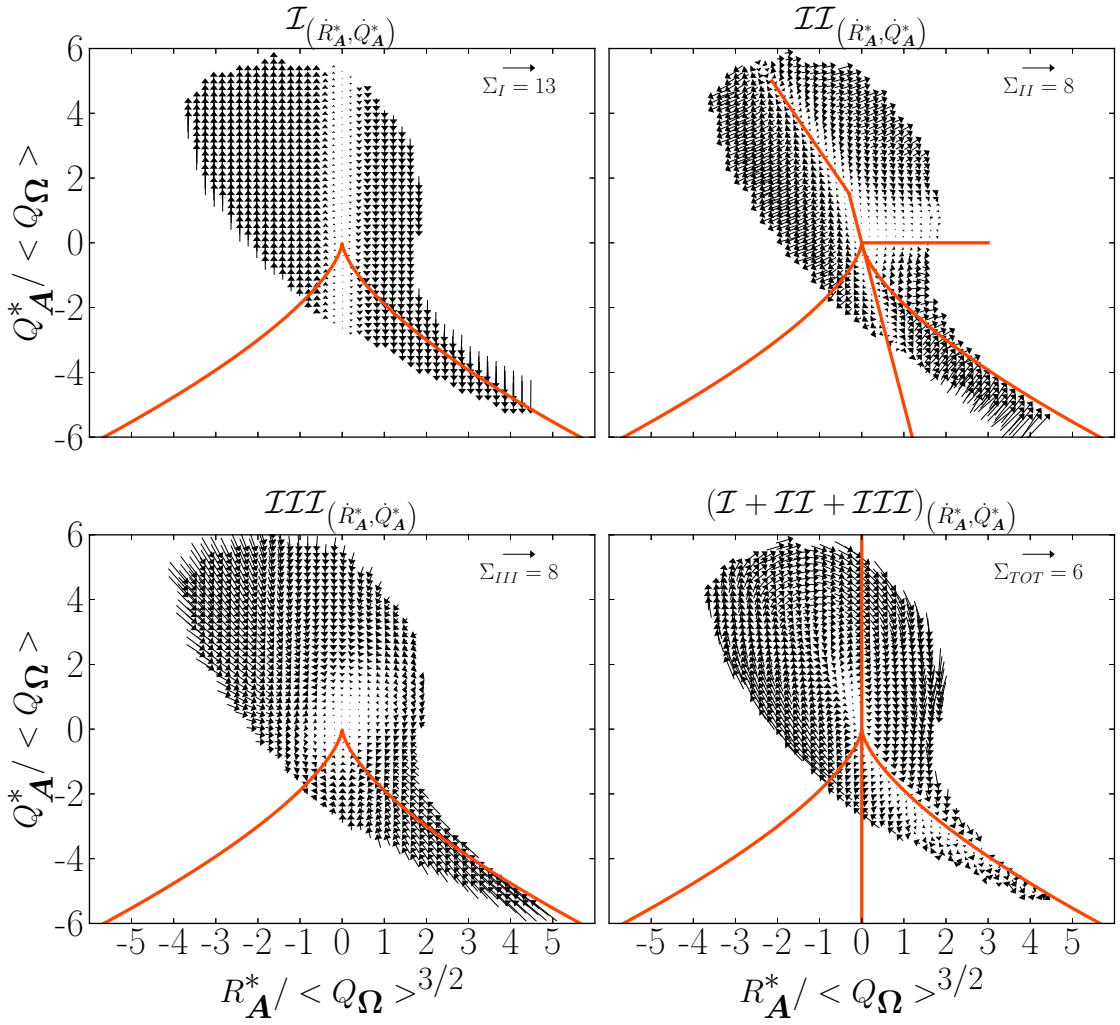

Figure 6.1. *CMT's of the LEE of the HIT reference case of the (R^*_A, Q^*_A)-phase plane. The terms of the evolution equations presented here correspond to $\mathcal{I}_{(R^*_A,Q^*_A)}$: interaction between the velocity invariants; $\mathcal{II}_{(R^*_A,Q^*_A)}$: pressure contribution; $\mathcal{III}_{(R^*_A,Q^*_A)}$: viscous contribution; and $(\mathcal{I}+\mathcal{II}+\mathcal{III})_{(R^*_A,Q^*_A)}$: total contribution. The scale of the vector of each term is computed as function of the mean vector length $\left(\overline{X}_{\langle \dot{R}^*_A,\dot{Q}^*_A\rangle} = \left|\left| \sqrt{(\dot{R}^*_A)^2 + (\dot{Q}^*_A)^2} \right|\right|\right)$ and its corresponding standard deviation $\left(\sigma_{\langle \dot{R}^*,\dot{Q}^*\rangle}\right)$ as follows : $\Sigma term = \overline{X}_{\langle \dot{R}^*_A,\dot{Q}^*_A\rangle} + 3\sigma_{\langle \dot{R}^*_A,\dot{Q}^*_A\rangle}$.*

$term_{(\dot{R}_A^*,\dot{Q}_A^*)}$:	I	II	III	$I+II+III$	II^{local}	$II^{nonlocal}$
ζ_{term}	12.72	7.86	7.78	5.67	3.93	6.69
Σ_{term}	13	8	8	6	4	7

Table 6.2 – *Vector scale values of the CMT's for the LEE of the HIT reference case. Terms $\mathcal{I}$, $\mathcal{II}$, $\mathcal{III}$, and their corresponding sum, $\mathcal{I}+\mathcal{II}+\mathcal{III}$, are presented in Fig. 6.1. Terms $\mathcal{II}^{local}$, and $\mathcal{II}^{nonlocal}$, are presented in Fig. 6.2.*

The mutual interaction between the invariants, i.e., $\mathcal{I}_{(\dot{R}_A^*,\dot{Q}_A^*)}$, is displayed at the top left of Fig. 6.1. The local flow topology dynamics shows vectors that increase in the enstrophy-production-dominated region $[\Delta^* > 0, R_A^* < 0]$ which indicates that tube-like-strain-dominated structures enhance enstrophy production due to vortex stretching mechanisms, whereas "decreasing" trajectories are obtained in the enstrophy-dissipation-dominated region $[\Delta^* > 0, R_A^* > 0]$ which allows self-amplification of the strain-rate tensor, so sheet-like-strain-dominated structures, are formed due to vortex compressing mechanisms. In regard to the magnitude of the vectors, they remain almost constant along the ordinate axis, and only change with the abscissa axis, so, near the value of $R_A^* = 0$, the magnitudes are very small but they rise as the vectors are computed farther from the origin, i.e., $R_A^* < 0$ and $R_A^* > 0$. However, it is important to point out that the positive and negative values are likely to cancel each other owing that the first traceless invariant of the VGT P_A^* is zero, which means the mutual effects on R_A^* are small.

The pressure Hessian contribution, i.e., $\mathcal{II}_{(\dot{R}_A^*,\dot{Q}_A^*)}$, is displayed at the top right of Fig. 6.1. The local flow topology dynamics shows vectors that move away from an asymptote line which is approached by two segments of tilted-lines, the first with a negative slope of $m = -5$ that crosses from the quadrant Q_2 to the quadrant Q_4 passing through the origin of the (R_A^*, Q_A^*)-phase plane, and the second a smaller line segment with a negative slope of $m = -2$ which lies in the second quadrant Q_2; in such a manner that the enstrophy-production-dominated region lies on the left side of the negative-tilted-lines, and the enstrophy-dissipation-dominated region on its right side. In this region, where the unstable topology dynamics happens, vectors depict a change in direction (clockwise) once the right Vieillefosse discriminant line is crossed. The magnitude of the vectors are very small in the vicinity of the asymptote and along the positive abscissa axis $R_A^* > 0$, but as the vectors are computed farther, their magnitude increases.

The viscous contribution, i.e., $\mathcal{III}_{(\dot{R}_A^*,\dot{Q}_A^*)}$, is displayed at the bottom left of Fig. 6.1.

The local flow topology dynamics in both, enstrophy-production- and enstrophy-dissipation-dominated regions, shows vectors that point toward the origin of the (R_A^*, Q_A^*)-phase plane. Such behavior is linked to the fact that trajectories are dominated by viscous effects instead of inertial effects, i.e., very low turbulent Reynolds number (Re_t). The magnitude of the vectors decrease as they are computed closer to the origin.

The total mean temporal rate of change, i.e., $(\mathcal{I}+\mathcal{II}+\mathcal{III})_{(\dot{R}_A^*, \dot{Q}_A^*)}$, is displayed at the bottom right of Fig. 6.1. The local flow topology dynamics shows "rotative" vectors in clockwise direction from UF/C to UN/S/S, SN/S/S and SF/S topology, with the origin of the (R_A^*, Q_A^*)-phase plane as the center of rotation. In regard to the magnitude of the vectors, which is proportional to the magnitude of the mean rate of change of the VGT invariants, that is very small in the vicinity of the origin and keeps like that along the positive Vieillefosse discriminant line, i.e., $\Delta^* > 0$, which indicates that the temporal mean rates of change $\left\langle \frac{DQ_A}{Dt} \right\rangle$ and $\left\langle \frac{DR_A}{Dt} \right\rangle$ are pretty small in flow regions with small gradients, nonetheless, the magnitude increases as the vectors are computed farther. Such behavior represents the Lagrangian dynamics in fully developed turbulence that maintains the tear-drop shape of the (R_A^*, Q_A^*) distribution showed in Fig. 4.10.

In general, by comparing the magnitudes, orientations and directions of the local flow topology dynamics of all the contributions, ($\mathcal{I}$, $\mathcal{II}$, and $\mathcal{III}$)$_{(\dot{R}_A^*, \dot{Q}_A^*)}$; it can be inferred that the rotational trajectories in clockwise direction mainly comes from the mutual interaction of the invariants and the pressure Hessian, i.e., $\mathcal{I}_{(\dot{R}_A^*, \dot{Q}_A^*)}$ and $\mathcal{II}_{(\dot{R}_A^*, \dot{Q}_A^*)}$ respectively. Such conclusion has been already pointed out for a wide variety of flow configurations, as for incompressible isotropic turbulence by Martin et al. (1998) [63] and Ooi et al. (1999) [73]; compressible isotropic turbulence by Pirozzoli and Grasso (2004) [79], buffer and logarithmic regions of compressible turbulent boundary layers by You-Biao and Xi-Yun (2013) [112] and Bechlars and Sandberg (2017) [4] respectively. Nonetheless, in the literature there are only scarce efforts to analyze into the dynamics of the pressure Hessian contribution. Therefore it seems worthwhile to proceed in a more detailed analysis of the local, $\mathcal{II}^{local}$, and non-local, $\mathcal{II}^{nonlocal}$, contributions of such pressure Hessian tensor.

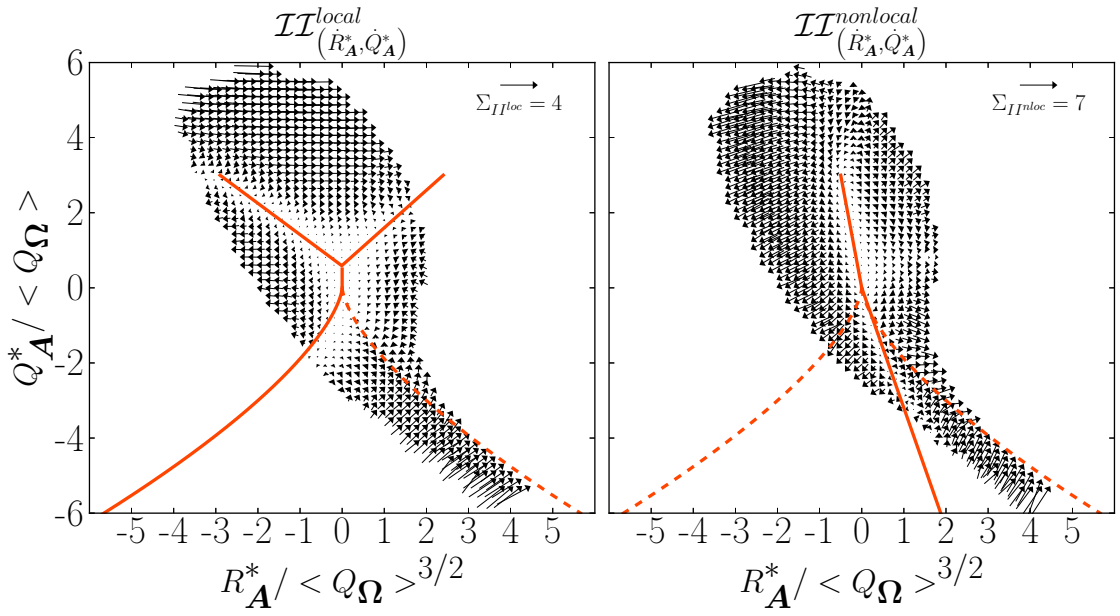

Figure 6.2. *CMT's of the LEE of the HIT reference case of the* (R^*_A, Q^*_A)*-phase plane. The terms of the evolution equations presented here correspond to* $\mathcal{II}^{local}$ *: local contribution of pressure Hessian; and* $\mathcal{II}^{nonlocal}$ *: non-local contribution of the Hessian pressure. The scale of the vector of each term is computed as function of the mean vector length* $\left(\overline{X}_{\langle \dot{R}^*_A, \dot{Q}^*_A \rangle} = \left|\left| \sqrt{\left(\dot{R}^*_A\right)^2 + \left(\dot{Q}^*_A\right)^2} \right|\right|\right)$ *and its corresponding standard deviation* $\left(\sigma_{\langle \dot{R}^*, \dot{Q}^* \rangle}\right)$ *as follows :* $\Sigma term = \overline{X}_{\langle \dot{R}^*_A, \dot{Q}^*_A \rangle} + 3\sigma_{\langle \dot{R}^*_A, \dot{Q}^*_A \rangle}$.

In Fig. 6.2 the local and non-local contributions to the pressure Hessian term are presented. On the one hand the local pressure Hessian contribution displays three regions with different local flow topology dynamics, which are bounded by the left Vieillefosse discriminant line, $\Delta^* < 0$, a positive segment of the ordinate axis that departs from the (R^*_A, Q^*_A)-phase plane origin until the point $[R^*_A = 0, Q^*_A = 0.5]$, and two asymptotes lines which are approached by two different tilted-lines that depart from the point where the ordinate axis segment ends. So the first line crosses the quadrant Q_2 and the second the quadrant Q_1, in such a manner that these tilted lines have a slope of $m = \pm 0.8$ respectively. The local flow topology dynamics of the first region, bounded by the left Vieillefosse discriminant line $(\Delta^* < 0)$ and the asymptote that crosses the quadrant Q_2, corresponds to vectors driven by purely vortex stretching mechanisms that only amplify the third VGT invariant, R^*_A, in the enstrophy-production-dominated region. The magnitude of the corresponding vectors increases as they are computed farther from the origin of the (R^*_A, Q^*_A)-phase plane. In the second region, the local flow topology dynamics, bounded by the two asymptotes, is associated to vectors that are driven by both vortex stretching and vortex compressing mechanisms, in such a manner that only the third VGT

invariant, R_A^*, is amplified; but this time, from the enstrophy-production-, to the enstrophy-dissipation-dominated region. The magnitude of the vectors increases as they are computed closer to the point $R_A^* = 0$. Finally the local flow topology dynamics of the third region, bounded by the tilted-line that crosses the quadrant Q_1 and the left Vieillefosse discriminant line ($\Delta^* < 0$), display vectors that rotate in counter-clockwise direction from SN/S/S to UN/S/S and UF/C topology, with the origin of the (R_A^*, Q_A^*)-phase plane as the center of rotation. The vectors computed where the tube-like-strain-dominated structures are generated, (quadrant Q_3), are just a few and feature small magnitude; while the vectors corresponding to sheet-like-strain-dominated structures depict well-defined trajectories towards the right Vieillefosse discriminant line, $\Delta^* > 0$, and once the vectors are computed in the enstrophy-dissipation-dominated region, their trajectories spin rapidly as the value of the ordinate grows, i.e., $Q_A^* > 0$, until they reach the point where vortex compressing mechanisms drive the values of both VGT invariants, R_A^*, and Q_A^*, to zero, as the vectors sketch trajectories towards the asymptote that cross the quadrant, Q_1, and towards the (R_A^*, Q_A^*)-phase plane origin. The magnitude of these vectors increases as they are computed farther from the origin of the (R_A^*, Q_A^*)-phase plane.

On the other hand the non-local pressure Hessian contribution display vectors that move away from asymptote bounds and that are similar to those described for the total pressure Hessian but here, the tilted-line that approached the asymptote departing from the (R_A^*, Q_A^*)-phase plane origin (and crossing the quadrant Q_4), has a negative slope ($m = -3.5$), and the tilted-line that approached the asymptote that crosses the quadrant Q_2 has a slope $m = 6$ (almost aligned to the positive ordinate axis). Together, both tilted-lines separate the enstrophy-production-dominated region at their left side, and the enstrophy-dissipation-dominated region at their right side. Such asymptotic behavior vanishes for Q_A^* approximately equal to 3 and then, above this value but in the vicinity of the asymptote, are plotted vectors with small magnitude that clearly move away from both regions, i.e., the one dominated by enstrophy production and the other one dominated by enstrophy dissipation. The magnitude of these vectors are very small in the vicinity of the asymptote and along the positive abscissa axis $R_A^* > 0$ and, as the vectors are computed farther from them, the magnitude increases.

By comparing the magnitude, orientation and direction of the local flow topology dynamics of the vectors of the local and non-local pressure Hessian contributions, it is evident that, in the present case, the local flow topology dynamics of the total pressure Hessian vectors comes mainly from the non-local pressure Hessian contribution.

6.2.2 HIT in two-phase flow cases

Once the HIT reference case has been addressed, attention is turn to the two-phase flow cases featuring two different volume of liquid, $\phi_\ell = 0.05$ and $\phi_\ell = 0.10$. The non-dimensional time retained to perform the analysis of both data-bases is $t^* = 6.0$, the same non-dimensional time as the one considered in chapter 4.

Figure 6.3 depicts the focal and non-focal streamline topologies of the (R_A^*, Q_A^*)-phase plane, by assigning a specific color to each one : Q_1 (UF/C — ●), Q_2 (SF/S — ●), Q_3 (SN/S/S — ●), and Q_4 (UN/S/S — ●).

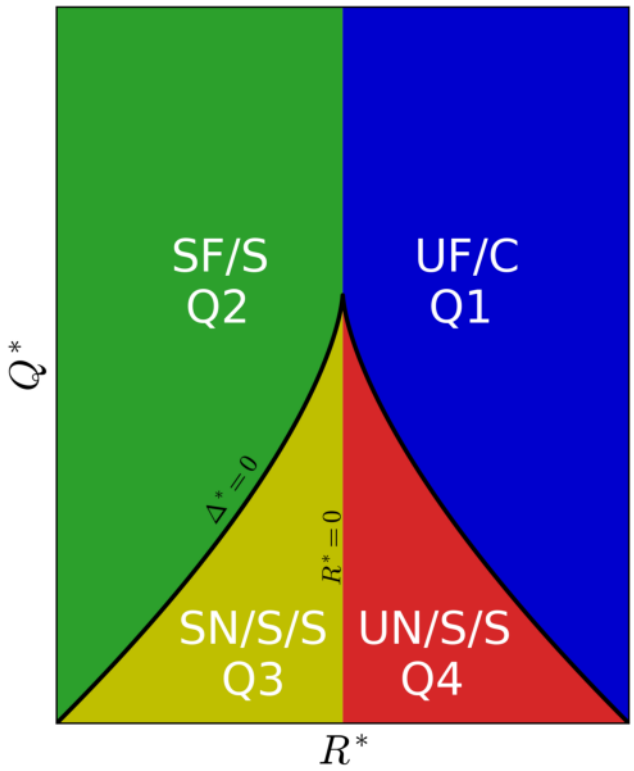

Figure 6.3. *Classification of streamline topology in the (R_A^*, Q_A^*)-phase plane : Q_1 (UF/C — ●), Q_2 (SF/S — ●), Q_3 (SN/S/S — ●), and Q_4 (UN/S/S — ●)*

Figures 6.4 and 6.5 display an illustration of the flow topology obtained in median cut-planes along x-, y-, and z-directions for $\phi_\ell = 0.05$ and $\phi_\ell = 0.10$, respectively. They show that, in the vicinity of the liquid-gas interface, the probability level of the first quadrant, Q_1 (UF/C — ●), increases compared to its level in the far region, meanwhile the second quadrant, Q_2 (SF/S — ●), remains practically constant in all the gaseous sub-regions. The third quadrant, Q_3 (SN/S/S — ●) does not experience any important change as the liquid-gas interface is approached, keeping always the smallest probability level of the four possible topologies. Finally, the fourth quadrant,

Q_4 (UN/S/S — ●), displays a decrease of its probability level in the near region. These conclusions are quantitatively assessed in Fig. 6.6, where the probabilities of occurrence for each flow topology quadrant are reported for $\phi_\ell = 0.05$ (top) and for $\phi_\ell = 0.10$ (bottom), obtained in the far, intermediate, and near regions from the liquid-gas interface.

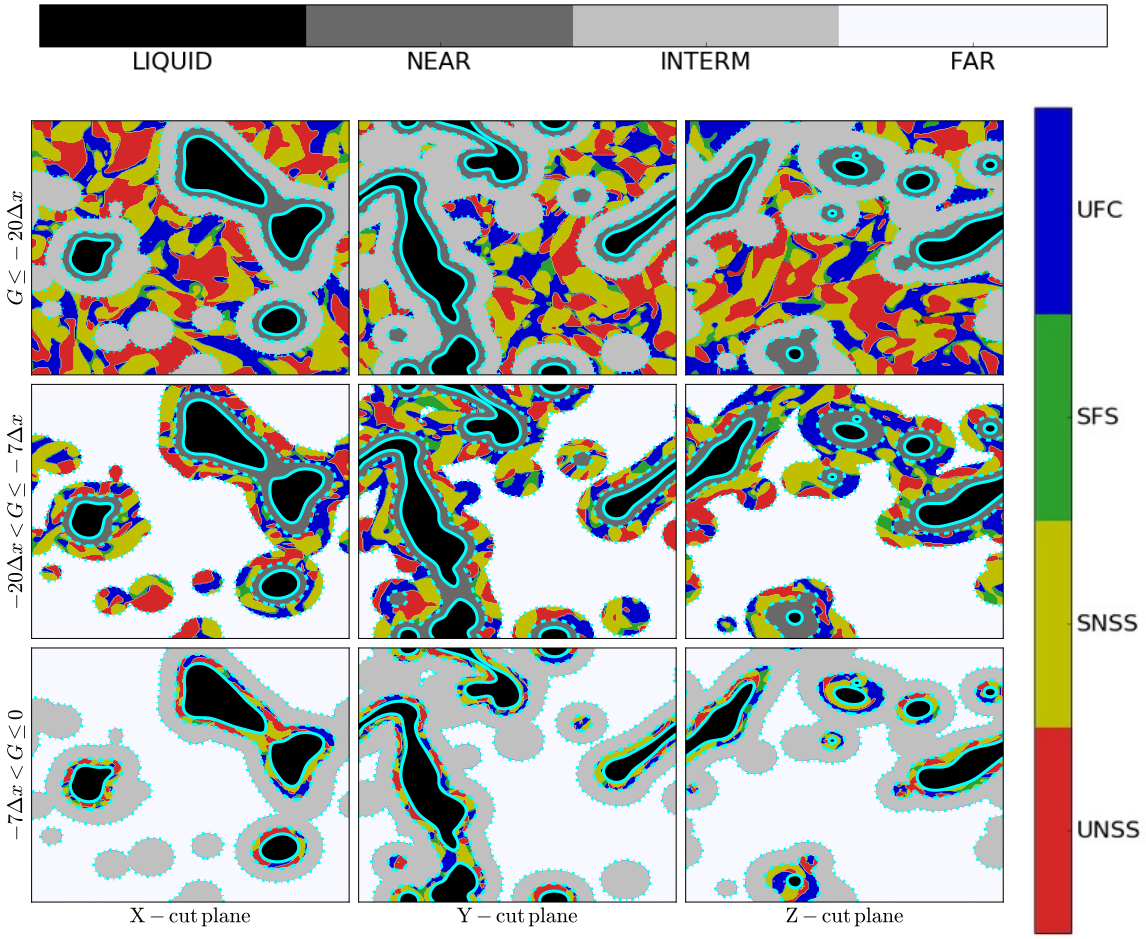

Figure 6.4. *Median cut-planes along x-, y-, and z-directions for $\phi_\ell = 0.05$, delineating three level-set iso-contours : solid cyan line $(G = 0)$, dashed cyan line : $(G = -7\Delta x)$, and dot-dashed cyan line : $(G = -20\Delta x)$. The cut-planes present the far (transparent), intermediate (silver), near (gray), and liquid (black) regions, and the scalar field colored by the four different non-degenerative flow fields topological regions.* UF/C : UN/S/S : SN/S/S : SF/S = *unstable-focus compressing : unstable-node saddle-saddle : stable-node saddle-saddle : stable-focus stretching. The field and topological regions are over-imposed in such a manner that the topological regions are shown only over the corresponding transparent level-set regions : far (top row), intermediate (medium row), and near (bottom row).*

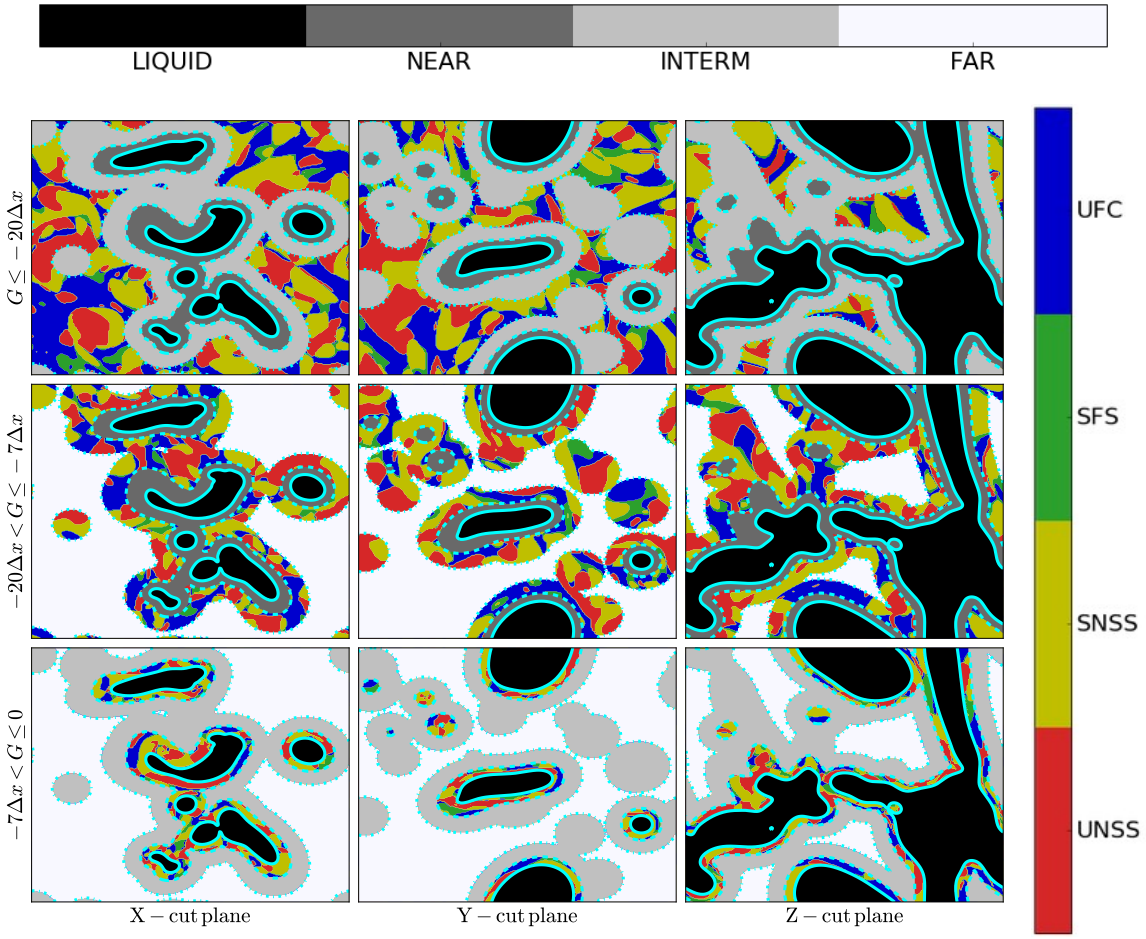

Figure 6.5. *Median cut-planes along x-, y-, and z-directions for* $\phi_\ell = 0.10$*, delineating three level-set iso-contours : solid cyan line* $(G = 0)$*, dashed cyan line :* $(G = -7\Delta x)$*, and dot-dashed cyan line :* $(G = -20\Delta x)$*. The cut-planes present the far (white), intermediate (silver), near (gray), and liquid (black) regions, and the scalar field colored by the four different non-degenerative flow fields topological regions.* UF/C : UN/S/S : SN/S/S : SF/S = *unstable-focus compressing : unstable-node saddle-saddle : stable-node saddle-saddle : stable-focus stretching. The field and topological regions are over-imposed in such a manner that the topological regions are shown only over the corresponding transparent level-set regions : far (top row), intermediate (medium row), and near (bottom row).*

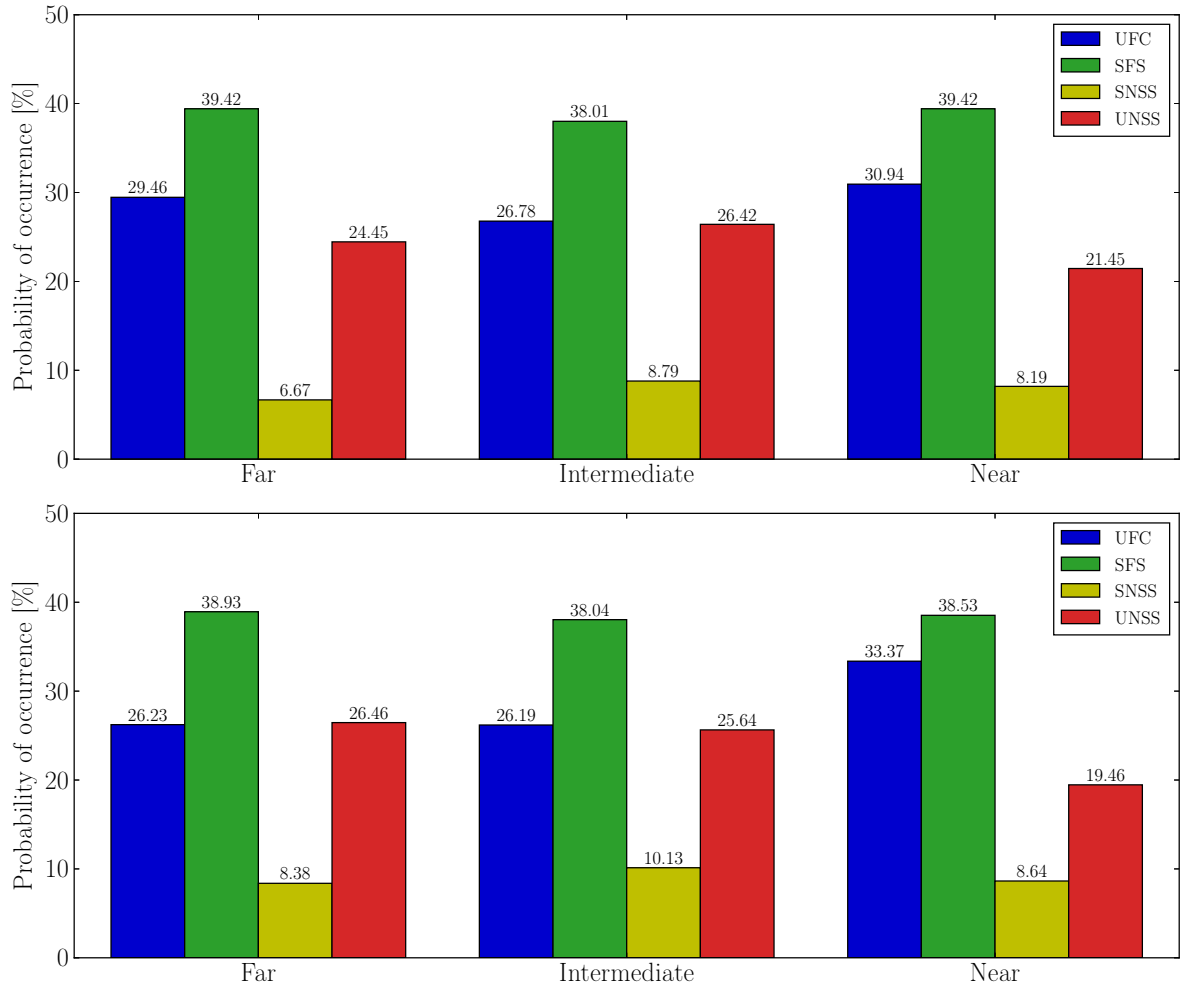

Figure 6.6. *Probability of occurrence of each streamline topology quadrant in the far (left), intermediate (center), and near (right) field regions $\phi_\ell = 0.05$ (top) and for $\phi_\ell = 0.10$ (bottom).*

In regard to the results gathered for the budget of the VGT Eqs. 6.11 and 6.12, ($\mathcal{I}$, $\mathcal{II}$, and $\mathcal{III}$)$_{(\dot{R}^*_A,\dot{Q}^*_A)}$, as well as the split of the pressure Hessian term into its local, $\mathcal{II}^{local}$, and non-local, $\mathcal{II}^{nonlocal}$, contributions; will be presented and scrutinized for the far, intermediate, and near regions from the liquid-gas interface in Figs. 6.7 - 6.10. Their corresponding exact, ζ_{term}, and rounded, Σ_{term}, vector scale values are summarized in Table 6.3.

Field regions	$term_{\left(\dot{R}_A^*,\dot{Q}_A^*\right)}$:	I	II	III	I+II+III	II^{local}	$II^{nonlocal}$
Far	ζ_{term}	7.02	4.15	3.81	2.84	2.54	3.53
	Σ_{term}	7	4	4	3	3	4
Interm	ζ_{term}	7.10	5.19	4.05	4.58	1.59	4.34
	Σ_{term}	7	5	4	5	2	4
Near	ζ_{term}	7.84	10.54	11.99	6.26	1.84	9.89
	Σ_{term}	8	11	12	6	2	10

Table 6.3 – *Vector scale values retained for the displayed CMT. Terms $\mathcal{I}$, $\mathcal{II}$, $\mathcal{III}$, $\mathcal{I}+\mathcal{II}+\mathcal{III}$, and the corresponding pressure Hessian decomposition, $\mathcal{II}^{local}$, and $\mathcal{II}^{nonlocal}$, are presented in Figs. 6.7 - 6.10 for both the multi-phase cases with $\phi_\ell = 0.05$ and $\phi_\ell = 0.10$.*

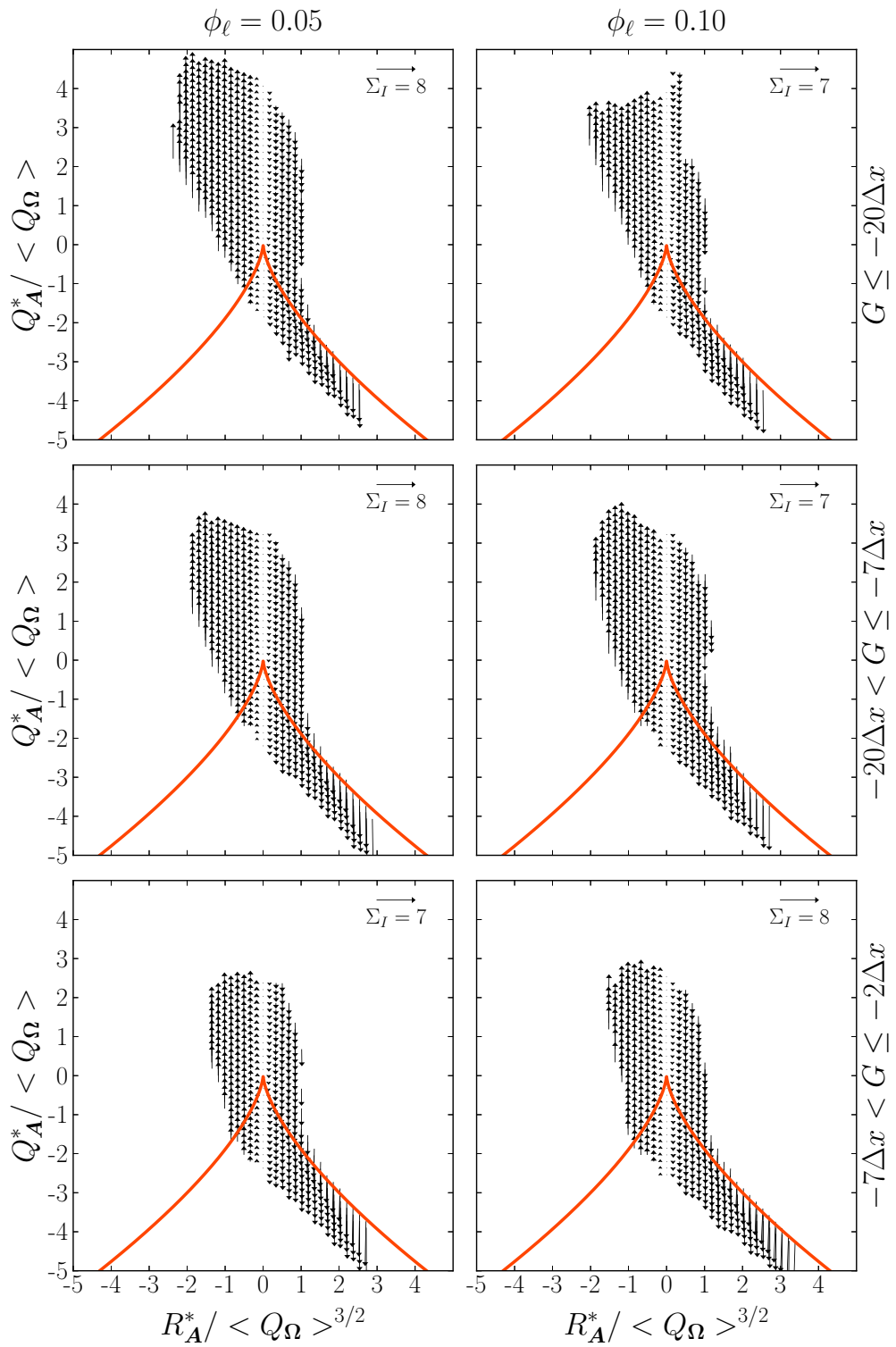

Figure 6.7. *CMT's of the LEE of the far (top row), intermediate (middle row) and near (bottom row) region of the (R^*_A, Q^*_A)-phase plane for the multi-phase case with $\phi_\ell = 0.05$ (left column) and $\phi_\ell = 0.10$ (right column). The term of the evolution equations presented correspond to $\mathcal{I}_{(R^*_A, Q^*_A)}$: interaction between the velocity invariants. The scale of the vector of each term is computed as function of the mean vector length $\left(\overline{X}_{\langle \dot{R}^*_A, \dot{Q}^*_A \rangle} = \left|\left| \sqrt{\left(\dot{R}^*_A\right)^2 + \left(\dot{Q}^*_A\right)^2} \right|\right|\right)$ and its corresponding standard deviation $\left(\sigma_{\langle \dot{R}^*_A, \dot{Q}^*_A \rangle}\right)$ as follows : $\Sigma term = \overline{X}_{\langle \dot{R}^*_A, \dot{Q}^*_A \rangle} + 3\sigma_{\langle \dot{R}^*_A, \dot{Q}^*_A \rangle}$.*

The mutual interactions between the invariants, i.e., $\mathcal{I}_{\left(\dot{R}_A^*,\dot{Q}_A^*\right)}$, are displayed in Fig. 6.7 for the far, intermediate, and near regions from the liquid-gas interface in the top, middle and bottom row, respectively, for the multi-phase case with $\phi_\ell = 0.05$ (left column), and $\phi_\ell = 0.10$ (right column). In general, the local flow topology dynamics shows the same behavior, even in the vicinity of the liquid-gas interface, where increasing vectors are obtained in the enstrophy-production-dominated region (vortex stretching mechanisms) $[\Delta^* < 0, R_A^* < 0]$, whereas decreasing trajectories are formed in the enstrophy-dissipation-dominated region where sheet-like-strain-dominated structures $[\Delta^* < 0, R_A^* > 0]$ are generated by vortex compressing mechanisms $[\Delta^* > 0, R_A^* > 0]$. In regard to the magnitude of these vectors, for the three regions, they remain almost constant along the ordinate axis, and only change along the abscissa axis, so, near the abscissa value of $R_A^* = 0$, the magnitudes are very small but they rise as the vectors are computed farther from the origin. The scale of the vector $\Sigma_{\mathcal{I}_{\left(\dot{R}_A^*,\dot{Q}_A^*\right)}}$ increases slightly as the liquid-gas interface is approached.

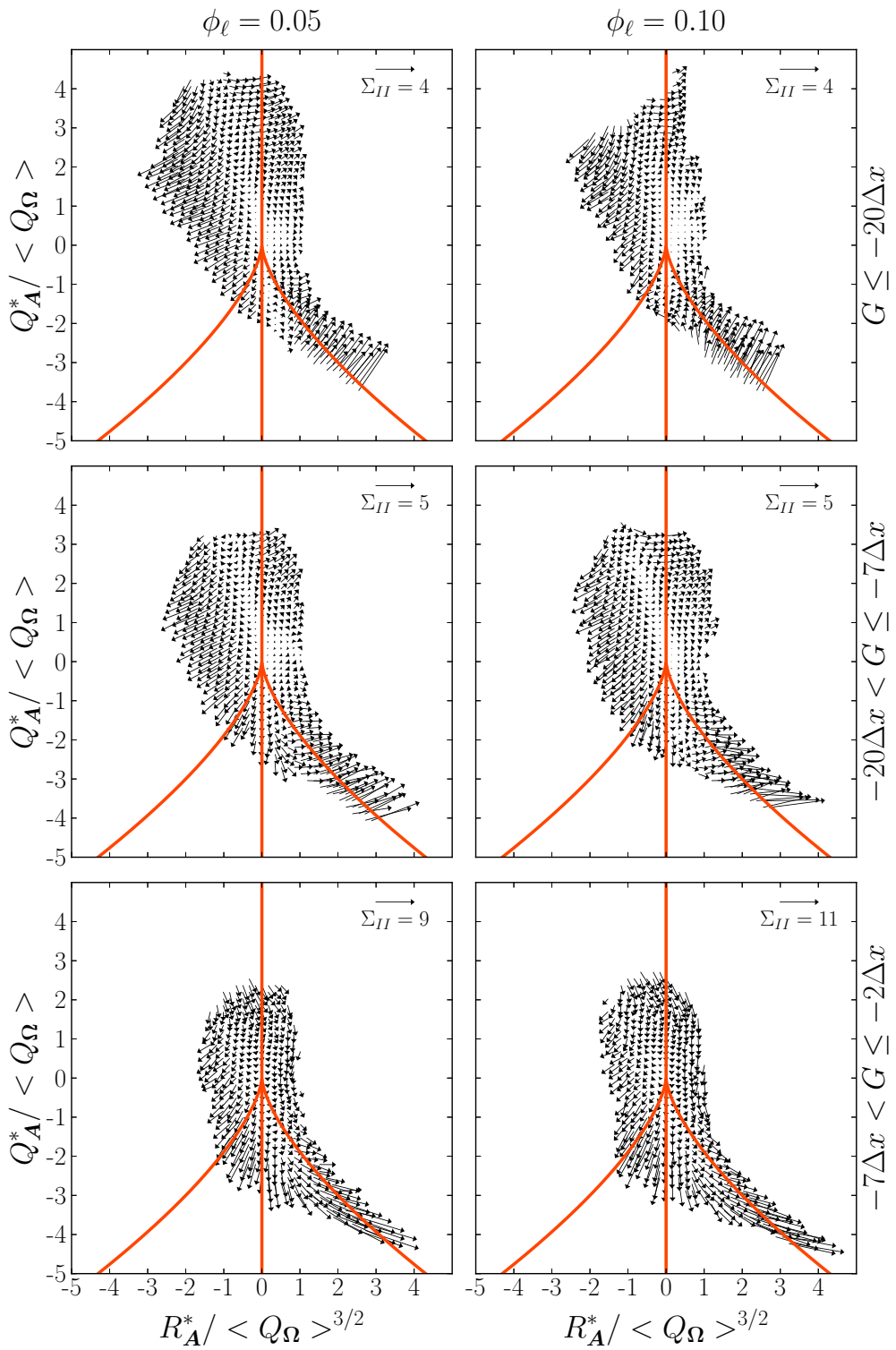

Figure 6.8. *CMT's of the LEE of the far (top row), intermediate (middle row) and near (bottom row) region of the (R^*_A, Q^*_A)-phase plane for the multi-phase case with $\phi_\ell = 0.05$ (left column) and $\phi_\ell = 0.10$ (right column). The term of the evolution equations presented correspond to $\mathcal{II}_{(R^*_A, Q^*_A)}$: pressure Hessian contribution. The scale of the vector of each term is computed as function of the mean vector length $\left(\overline{X}_{\langle \dot{R}^*_A, \dot{Q}^*_A \rangle} = \left|\left| \sqrt{\left(\dot{R}^*_A\right)^2 + \left(\dot{Q}^*_A\right)^2} \right|\right|\right)$ and its corresponding standard deviation $\left(\sigma_{\langle \dot{R}^*_A, \dot{Q}^*_A \rangle}\right)$ as follows : $\Sigma term = \overline{X}_{\langle \dot{R}^*_A, \dot{Q}^*_A \rangle} + 3\sigma_{\langle \dot{R}^*_A, \dot{Q}^*_A \rangle}$.*

The pressure Hessian term, i.e., $\mathcal{II}_{(\dot{R}_A^*,\dot{Q}_A^*)}$, is presented in Fig. 6.8 for the far, intermediate, and near regions from the liquid-gas interface in the top, middle and bottom row, respectively, for the multi-phase case with $\phi_\ell = 0.05$ (left column), and $\phi_\ell = 0.10$ (right column). This time the three regions depict local flow topology dynamics that departs from the behavior reported at the HIT reference case (top-right of Fig. 6.1). For the sake of clarity, the dynamics of the pressure Hessian contribution are scrutinized quadrant by quadrant and compared between the various gaseous sub-regions as follows :

- the local flow topology dynamics in the first quadrant, Q_1, i.e., the region dominated by enstrophy-dissipation, delineates vectors that move farther from the (R_A^*, Q_A^*)-phase plane origin in such a manner that in the far and intermediate regions, for positive values along the ordinate axis, the second, Q_A^*, but especially the third, R_A^*, VGT invariants are amplified due to vortex compressing mechanisms, in such a manner that the vectors magnitude becomes weaker as the (R_A^*, Q_A^*)-phase plane origin is approached from both, the positive values along the ordinate axis and the right Vieillefosse discriminant line, $\Delta^* > 0$. Conversely, in the near region, the second VGT invariant, Q_A^*, is mainly amplified. It has a magnitude that also becomes weaker as the (R_A^*, Q_A^*)-phase plane origin is approached from both, the positive values along the ordinate axis and the right Vieillefosse discriminant line, $\Delta^* > 0$.
- the local flow topology dynamics in the second quadrant, Q_2, i.e., the region dominated by enstrophy-production, display vectors that move farther from the (R_A^*, Q_A^*)-phase plane origin in such a manner that in the far, intermediate, and near regions, both VGT invariants are amplified due to vortex stretching mechanisms. In the far region, for large positive values along the ordinate axis, the vectors show a clockwise rotational behavior as the vectors are computed farther from the abscissa value $R_A^* = 0$; such tendency vanishes as the liquid-gas interface is approached.
- the local flow topology dynamics in the third quadrant, Q_3, i.e., the region dominated by tube-like-strain structures, depicts vectors in the far region that depart towards the left Vieillefosse discriminant line $\Delta^* < 0$ in such a manner that the invariants Q_A^* and R_A^* of the VGT are amplified as the vectors are computed farther from the (R_A^*, Q_A^*)-phase plane origin and closer to the negative Vieillefosse line, especially around the ordinate axis value of $Q_A^* \sim 1.6$ (for both multi-phase cases), where only the amplification of the third invariant R_A^* diminishes drastically. The intermediate and near regions delineate vectors that mainly amplify the second VGT invariant, Q_A^*, such that the strain toughly

enhances the tube-like structures even in the vicinity of the left Vieillefosse discriminant line $\Delta^* < 0$; this enhancement grows as the vectors are computed farther from the (R_A^*, Q_A^*)-phase plane origin.

- the local flow topology dynamics in the fourth quadrant, Q_4, i.e., the region dominated by sheet-like-strain structures, is associated to vectors that point towards the positive Vieillefosse discriminant line $\Delta^* > 0$ in the far, intermediate, and near regions from the liquid-gas interface, but the trajectories display different rotative behaviors as the vectors are computed closer to the right Vieillefosse line $\Delta^* > 0$, such that in the far and intermediate regions the dynamics is in clockwise sense, whereas it retakes counter-clockwise in the near region. The amplification of both Q_A^* and R_A^* VGT invariants take place in the far region, whilst in the intermediate and near regions the third VGT invariant, R_A^* is mainly amplified. Nonetheless such invariant amplification enhances in all three regions the vortex compressing mechanisms which is responsible for the enstrophy dissipation, so being stronger as the vectors are computed farther from the (R_A^*, Q_A^*)-phase plane origin and closer to the discriminant line $\Delta^* > 0$.

The scale of the vector $\Sigma_{\mathcal{II}_{\left(\dot{R}_A^*, \dot{Q}_A^*\right)}}$ strongly increases in the vicinity of the liquid-gas interface. The value in the near region being more than two times the one in the intermediate or far regions.

At this point, it seems suitable to scrutinize the local and non-local pressure Hessian dynamics, given that the pressure Hessian is one of the leading order term of Eqs. 6.11 and 6.12. Thereby, in the one hand, Figure 6.9 presents the local pressure Hessian contribution, which displays three regions with different local flow topology dynamics of vectors. The corresponding vectors are bounded by the left Vieillefosse discriminant line, $\Delta^* < 0$, a positive segment of the ordinate axis that departs from the (R_A^*, Q_A^*)-phase plane origin until the point $[R_A^* = 0, Q_A^* = 0.5]$, and two asymptotes lines which are approached by two different tilted-lines departing from the point where the ordinate axis segment ends. In the far and near regions both tilted-lines placed in the quadrants Q_1 and Q_2, do cross all the vector cloud. The corresponding slopes of the lines are $m = \pm 0.8$ in the far region, and in the near region the slope $m = 1.2$ corresponds to the line placed in the quadrant Q_1, and the slope $m = -1.0$ corresponds to the line that lies in the second quadrant Q_2. In the intermediate region the tilted-lines drawn in the first, Q_1, and second, Q_2, quadrants have a slope of $m = \pm 0.8$. However, these lines do not cross entirely the vector cloud. The local flow topology dynamics of the three regions, in comparison to the HIT reference case (left (R_A^*, Q_A^*)-phase plane of Fig. 6.2), do not present any drastic change in their vectors, so only the evolution in function of the level-set function will be detailed out

as follow :

- the local flow topology dynamics of the (R_A^*, Q_A^*)-phase plane region bounded by the left Vieillefosse discriminant line $(\Delta^* < 0)$ and the asymptote that crosses the quadrant Q_2, delineates vectors where vortex stretching mechanisms mainly amplify the third VGT invariant, R_A^*, such that the enstrophy production is enhanced. The amount of computed vectors grows as the liquid-gas interface is approached and in regard to their magnitude, it increases as they are computed farther from the negative Vieillefosse discriminant line $(\Delta^* < 0)$ and the asymptote that crosses the quadrant Q_2. The corresponding increase is larger in the intermediate and near regions.
- the local flow topology dynamics of the (R_A^*, Q_A^*)-phase plane region bounded by the two asymptotes displays vectors which are driven by stretching and compressing vortex mechanisms, such that the third VGT invariant, R_A^*, is mainly amplified from the enstrophy-production- to the enstrophy-dissipation-dominated region. The number of vectors computed diminishes as the liquid-gas interface is approached. In the vicinity of the asymptotes the magnitude of the vectors increase as they are computed closer to the point $R_A^* = 0$, but these vectors computed farther from the ordinate axis $(Q_A^* > 2)$, increases their magnitude as they are computed farther from such value of Q_A^*.
- the local flow topology dynamics of the (R_A^*, Q_A^*)-phase plane region bounded by the tilted-line that crosses the quadrant Q_1 and the left Vieillefosse discriminant line $(\Delta^* < 0)$, exhibits vectors that rotate in counter-clockwise direction from SN/S/S to UN/S/S and UF/C topology, with the origin of the (R_A^*, Q_A^*)-phase plane as the center of rotation. The vectors computed where the tube-like-strain-dominated structures are generated (quadrant Q_3) are just a few in the far region, but their number increases a bit as the liquid-gas interface is approached. In any case, in the three regions they have small magnitude. The vectors corresponding to sheet-like-strain-dominated structures display well defined trajectories towards the right Vieillefosse discriminant line, $\Delta^* > 0$, and once the vectors are computed in the enstrophy-dissipation-dominated region, their trajectories spin rapidly as the value of the ordinate grows, i.e., $Q_A^* > 0$, until vortex compressing mechanisms drive the values of both VGT invariants, R_A^*, and Q_A^*, to zero, as the vectors sketch trajectories towards the asymptote that crosses the quadrant, Q_1, and towards the (R_A^*, Q_A^*)-phase plane origin. Such behavior is magnified as the liquid-gas interface is approached. The magnitude of such vectors increases as they are computed farther from the origin of the (R_A^*, Q_A^*)-phase plane.

The scale of the local contribution ($\Sigma_{II^{loc}}$) remains small in the three regions displaying small variations.

On the other hand, the non-local pressure Hessian contribution is reported in Figure. 6.10. The corresponding topology dynamics seems to be the same as the one of the total pressure Hessian contribution (see Fig. 6.8), displaying only some slight differences in the far and intermediate regions. This can be easily glimpsed by looking at the scale of the non-local contribution ($\Sigma_{II^{nloc}}$), which increases nearly three times as the liquid-gas interface is approached. Comparing the magnitude of both local ($\Sigma_{II^{loc}}$) and non-local ($\Sigma_{II^{nloc}}$) pressure Hessian contributions in the same field region, it is evident that the non-local component is always the leading order term that drives the topological dynamics of the pressure Hessian.

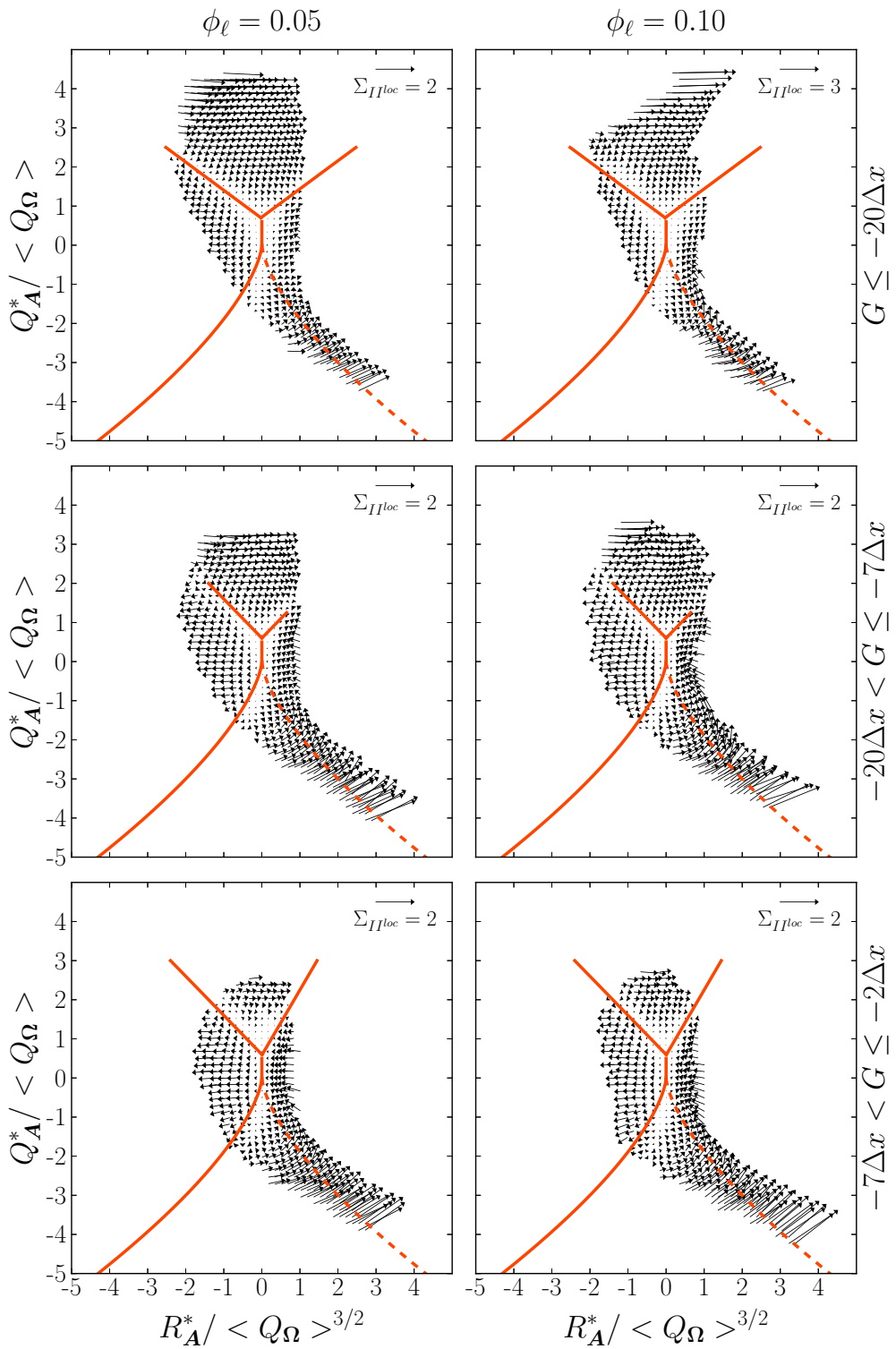

Figure 6.9. *CMT's of the LEE of the far (top row), intermediate (middle row) and near (bottom row) region of the (R^*_A, Q^*_A)-phase plane for the multi-phase case with $\phi_\ell = 0.05$ (left column) and $\phi_\ell = 0.10$ (right column). The term of the evolution equations presented correspond to $\mathcal{II}^{local}$: local pressure Hessian contribution. The scale of the vector of each term is computed as function of the mean vector length $\left(\overline{X}_{\langle \dot{R}^*_A, \dot{Q}^*_A \rangle} = \left|\left| \sqrt{\left(\dot{R}^*_A\right)^2 + \left(\dot{Q}^*_A\right)^2} \right|\right|\right)$ and its corresponding standard deviation $\left(\sigma_{\langle \dot{R}^*, \dot{Q}^* \rangle}\right)$ as follows : $\Sigma term = \overline{X}_{\langle \dot{R}^*_A, \dot{Q}^*_A \rangle} + 3\sigma_{\langle \dot{R}^*_A, \dot{Q}^*_A \rangle}$.*

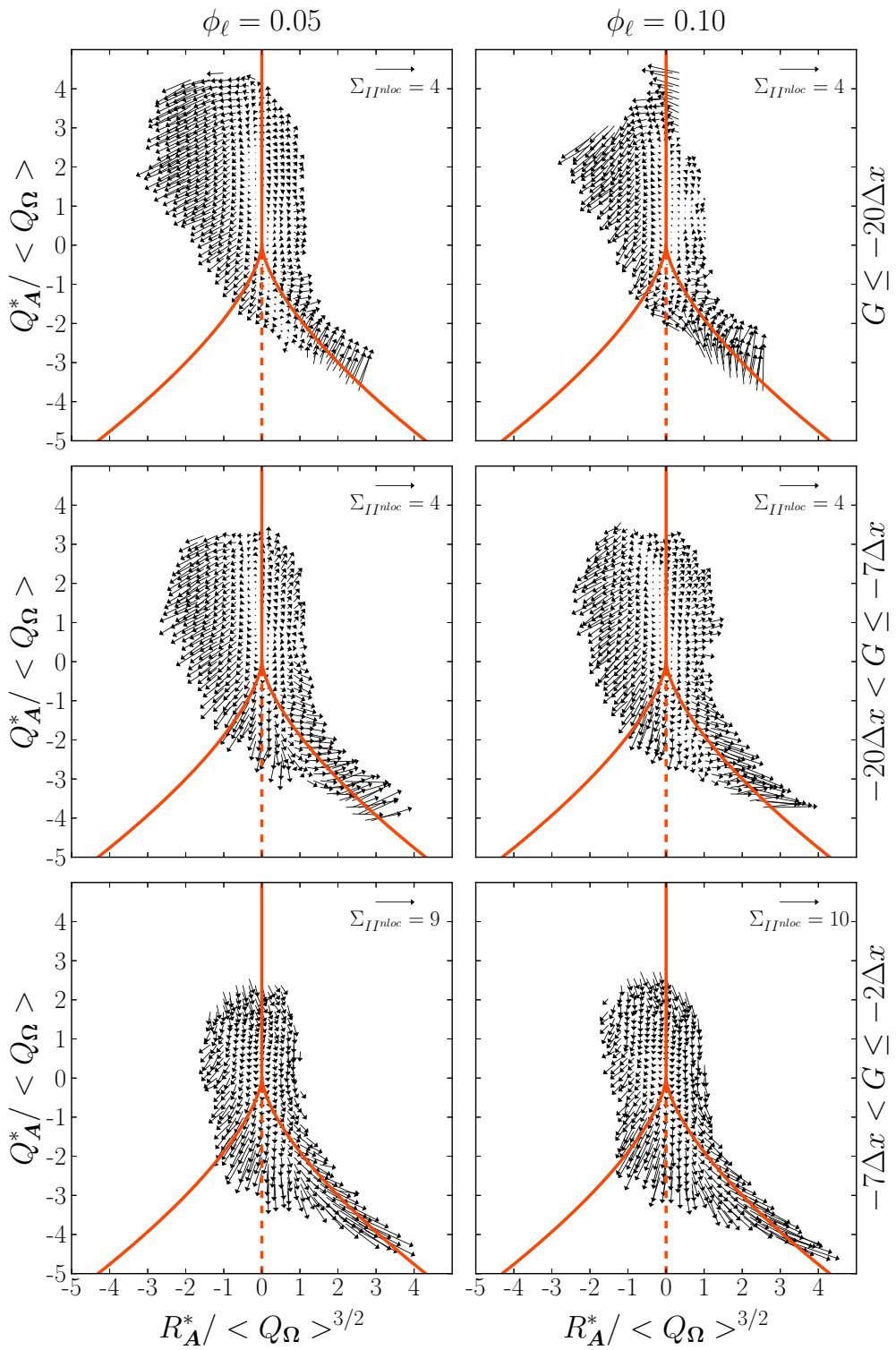

Figure 6.10. *CMT's of the LEE of the far (top row), intermediate (middle row) and near (bottom row) region of the (R^*_A, Q^*_A)-phase plane for the multi-phase case with $\phi_\ell = 0.05$ (left column) and $\phi_\ell = 0.10$ (right column). The term of the evolution equations presented correspond to $\mathcal{II}^{nonlocal}$: non-local pressure Hessian contribution. The scale of the vector of each term is computed as function of the mean vector length $\left(\overline{X}_{\langle \dot{R}^*_A, \dot{Q}^*_A \rangle} = \left|\left| \sqrt{\left(\dot{R}^*_A\right)^2 + \left(\dot{Q}^*_A\right)^2} \right|\right|\right)$ and its corresponding standard deviation $\left(\sigma_{\langle \dot{R}^*, \dot{Q}^* \rangle}\right)$ as follows : $\Sigma term = \overline{X}_{\langle \dot{R}^*_A, \dot{Q}^*_A \rangle} + 3\sigma_{\langle \dot{R}^*_A, \dot{Q}^*_A \rangle}$.*

The viscous contribution, i.e., $\mathcal{III}_{\left(\dot{R}_A^*,\dot{Q}_A^*\right)}$, is shown in Fig. 6.11 for the far, intermediate, and near regions from the liquid-gas interface in the top, middle and bottom row, respectively, for the multi-phase case with $\phi_\ell = 0.05$ (left column), and $\phi_\ell = 0.10$ (right column). The local flow topology dynamics shows that for the far and intermediate regions, the vectors of the four (R_A^*, Q_A^*)-phase plane quadrants, Q_1, Q_2, Q_3, and Q_4, point towards the center of the invariant space, but in the near region the topology dynamics of the enstrophy-production and enstrophy-dissipation-dominated regions change in such a manner that their vectors, for the negative values along the ordinate axis, move parallel to their respective Vieillefosse discriminant lines until they approach zero, then the vectors rotate and display trajectories that mainly amplifies the second VGT invariant, Q_A^*. Then, when the vectors are computed for $Q_A^* \sim> 2$, they rotate again pointing towards the vertical line drawn at the constant ordinate value $R_A^* = 0$. In this region the viscous effects are enhanced by the presence of the liquid-gas interface, which seems to play an important role since the scale of the vector $\Sigma_{\mathcal{III}_{\left(\dot{R}_A^*,\dot{Q}_A^*\right)}}$ strongly increases as the liquid-gas interface is approached, being the value in the near region more than the double than the one obtained in the intermediate or far regions, as it happens for the vector magnitude of the pressure Hessian contribution $\Sigma_{\mathcal{III}_{\left(\dot{R}_A^*,\dot{Q}_A^*\right)}}$.

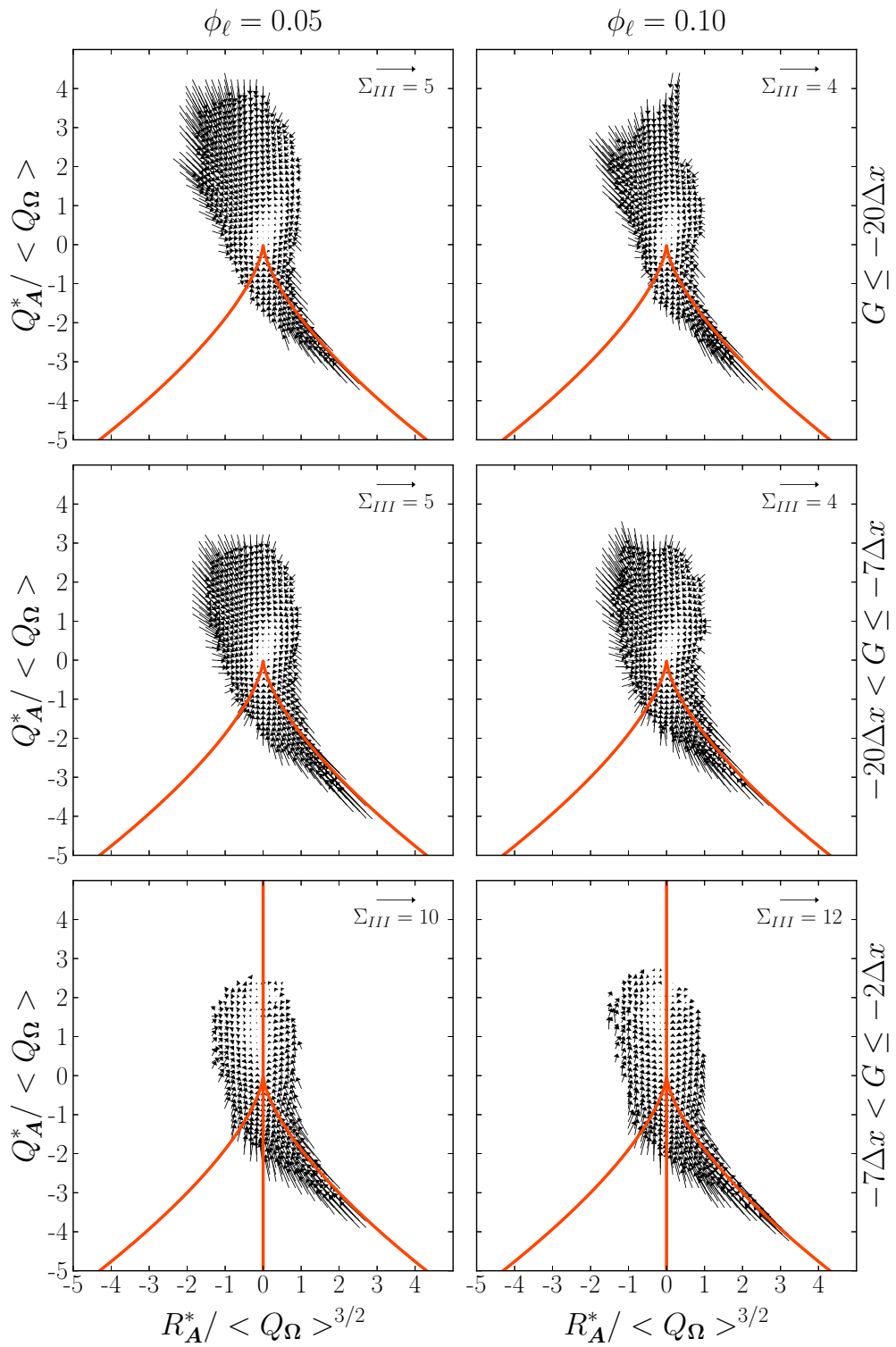

Figure 6.11. *CMT's of the LEE of the far (top row), intermediate (middle row) and near (bottom row) region of the (R^*_A, Q^*_A)-phase plane for the multi-phase case with $\phi_\ell = 0.05$ (left column) and $\phi_\ell = 0.10$ (right column). The term of the evolution equations presented correspond to $\mathcal{III}_{(R^*_A, Q^*_A)}$: viscous contribution. The scale of the vector of each term is computed as function of the mean vector length $\left(\overline{X}_{\langle \dot{R}^*_A, \dot{Q}^*_A \rangle} = \left|\left| \sqrt{\left(\dot{R}^*_A\right)^2 + \left(\dot{Q}^*_A\right)^2} \right|\right|\right)$ and its corresponding standard deviation $\left(\sigma_{\langle \dot{R}^*_A, \dot{Q}^*_A \rangle}\right)$ as follows : $\Sigma term = \overline{X}_{\langle \dot{R}^*_A, \dot{Q}^*_A \rangle} + 3\sigma_{\langle \dot{R}^*_A, \dot{Q}^*_A \rangle}$.*

Finally the mean total rate of change, i.e., $(\mathcal{I}+\mathcal{II}+\mathcal{III})_{(\dot{R}^*_A,\dot{Q}^*_A)}$, is displayed in Figure 6.12, for the far, intermediate, and near regions from the liquid-gas interface in the top, middle and bottom row, respectively, for the multi-phase case with $\phi_\ell = 0.05$ (left column), and $\phi_\ell = 0.10$ (right column). The local flow topology dynamics displays rotative vectors in clockwise direction from UF/C to UN/S/S, SN/S/S and SF/S topology, with the (R^*_A, Q^*_A)-phase plane origin, as the center of rotation. Nonetheless the classical tear-drop shape is not maintained : so the focal topologies (first and second quadrants, Q_1 and Q_2), and non-focal topologies (third and fourth quadrants, Q_3 and Q_4), exhibit significant differences in comparison to the reference HIT case :

- the local flow topology dynamics in the quadrant Q_1, i.e., enstrophy-dissipation-dominated region, delineates decreasing vectors that, in the three regions, rotate in such a way that mainly the second VGT invariant, Q^*_A, is amplified so the magnitude of the vectors increases as they are computed farther from the value of the ordinate axis $R^*_A = 0$. In the far and near regions, for the ordinate axis values between 0 and -1, the computed vectors start to point towards the positive Vieillefosse discriminant line, and below the ordinate axis value of -1, the vectors becomes weaker and without any defined direction. Instead in the intermediate region, the vectors computed below the ordinate value of -1, show a clear behavior related to amplification of both VGT invariants Q^*_A and R^*_A along the positive Vieillefosse discriminant line, such that the magnitude of the vectors increases as they are computed farther from the (R^*_A, Q^*_A)-phase plane origin.
- the local flow topology dynamics in the quadrant Q_2, i.e., enstrophy-production-dominated region, displays increasing vectors that move in such a manner that in the far region the second VGT invariant, Q^*_A, is mainly amplified, but as the liquid-gas interface is approached, the amplification of the third VGT invariant, R^*_A, grows. Such evolution of the orientation shows clearly that the trajectories of the vectors computed in the vicinity of the left Vieillefosse discriminant line $\Delta^* < 0$ departs from the rotative clockwise tendency as the liquid-gas interface is approached, especially in the near region. In regard to the magnitude of the vectors, they grows as are computed farther from the (R^*_A, Q^*_A)-phase plane origin, and also the magnitudes in this quadrant become larger as the liquid-gas interface is approached.
- the local flow topology dynamics in the quadrant Q_3, i.e., tube-like-strain-dominated structures, depicts vectors that, in the far region, depart towards the left Vieillefosse discriminant line $\Delta^* < 0$ in such a manner that the invariants Q^*_A and R^*_A of the VGT are amplified as the vectors are computed farther from

the (R_A^*, Q_A^*)-phase plane origin and closer to the negative Vieillefosse line. In the intermediate region the vectors do not show any clear tendency and their magnitude are, in average, the weakest of all the (R_A^*, Q_A^*)-phase plane. In the near region the vectors mainly depart towards the negative Vieillefosse discriminant line and mainly amplify the third VGT invariant, R_A^*, such that the magnitude of the vectors grows as they are computed farther from the (R_A^*, Q_A^*)-phase plane origin.

- the local flow topology dynamics in the quadrant Q_4, i.e., sheet-like-strain-dominated structures, is associated to vectors that point towards the third quadrant Q_3, i.e., tube-like-strain-dominated structures, in such a way that both VGT invariants Q_A^* and R_A^* are amplified and their magnitude increases as the vectors are computed farther from the positive Vieillefosse discriminant line and closer to the SN/S/S topology. Conversely, in the intermediate region, the vectors amplify both VGT invariants Q_A^* and R_A^* but along the positive Vieillefosse discriminant line, with a larger magnitude as they are computed closer to the discriminant line $\Delta^* > 0$. Nonetheless, the vectors computed farther from this line display no clear trajectories and weak magnitude. In the near region, the vectors show an abrupt change of direction around the abscissa value $R_A^* \sim 1.5$, such that the vectors computed at $R_A^* < 1.5$ mainly point towards the third quadrant Q_3 weakly amplifying both VGT invariants, and those computed at $R_A^* > 1.5$ enhance the sheet-like-strain-dominated structures amplifying both VGT invariants. Thus, the magnitude of the vectors are greater as they are computed closer to the right Vieillefosse discriminant line; most of the vectors computed farther from the right discriminant line, around $R_A^* \sim 1.5$, show none of the dynamic tendencies just described.

The scale of the vector Σ_{TOT} strongly increases as the liquid-gas interface is approached, being the value in the near region almost three times larger than the value obtained in the far region.

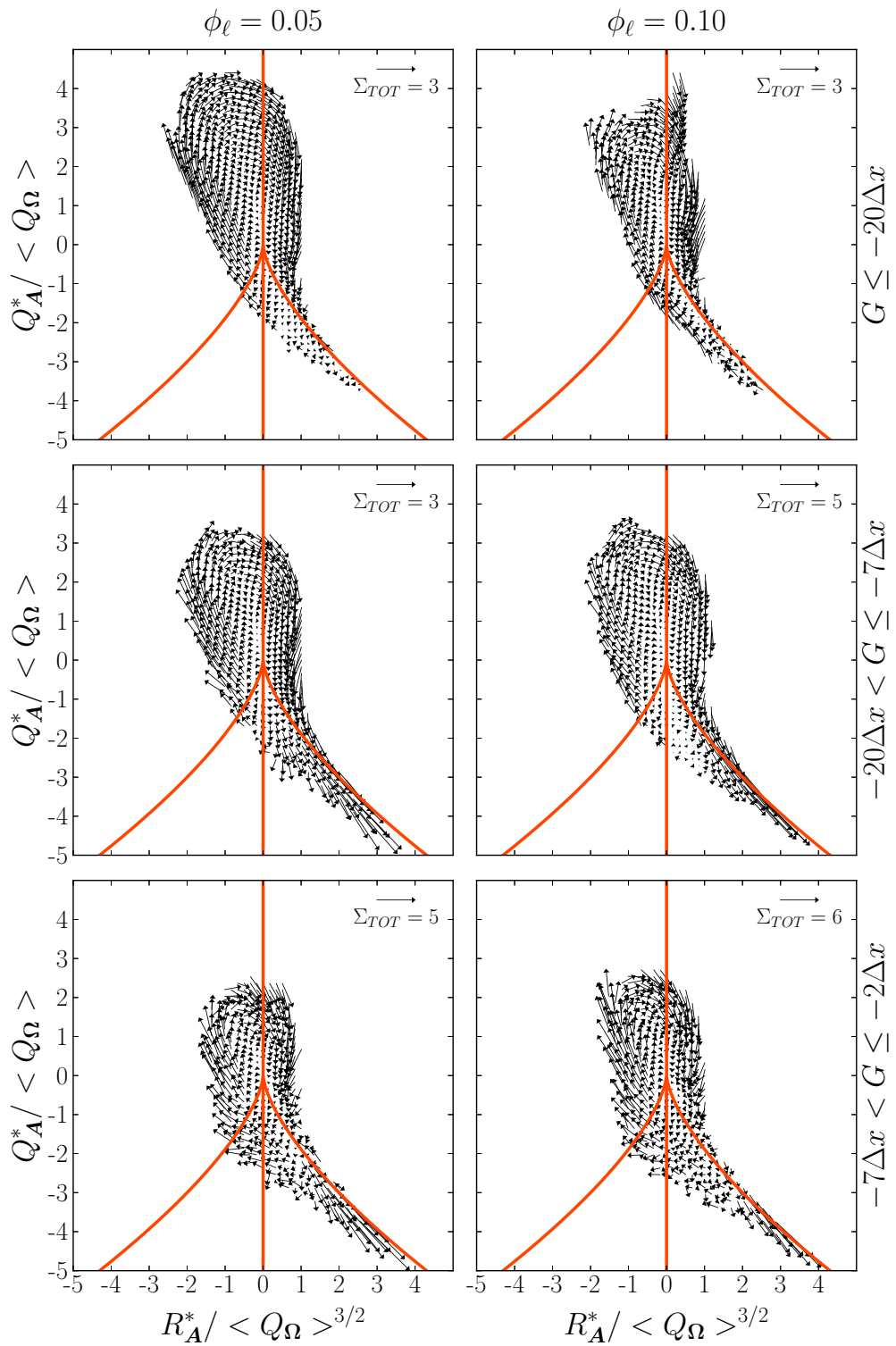

Figure 6.12. *CMT's of the LEE of the far (top row), intermediate (middle row) and near (bottom row) region of the (R^*_A, Q^*_A)-phase plane for the multi-phase case with $\phi_\ell = 0.05$ (left column) and $\phi_\ell = 0.10$ (right column). The term of the evolution equations presented correspond to $(\mathcal{I}+\mathcal{II}+\mathcal{III})_{(R^*_A,Q^*_A)}$: total contribution. The scale of the vector of each term is computed as function of the mean vector length $\left(\overline{X}_{\langle \dot{R}^*_A,\dot{Q}^*_A\rangle} = \left|\left| \sqrt{\left(\dot{R}^*_A\right)^2 + \left(\dot{Q}^*_A\right)^2} \right|\right|\right)$ and its corresponding standard deviation $\left(\sigma_{\langle \dot{R}^*_A,\dot{Q}^*_A\rangle}\right)$ as follows : $\Sigma term = \overline{X}_{\langle \dot{R}^*_A,\dot{Q}^*_A\rangle} + 3\sigma_{\langle \dot{R}^*_A,\dot{Q}^*_A\rangle}$.*

6.3 Summary and conclusions

The evolution of turbulent local flow topology dynamics is scrutinized on the basis of DNS of vaporizing two-phase flows in different sub-regions (described in function of the level-set variable). The analysis is based on the Lagrangian evolution equations (LEE) of the velocity gradient tensor (VGT) invariants. In a first step are briefly addressed the mathematical formalisms of both, the LEE – in their variable-density form –, and the conditional mean trajectories (CMT). It is followed by the explanation of the scale-computation methodology proposed in this work that allows, for the first time, to compare not only the orientation and direction, but also the magnitude of all the terms of the LEE between them. Then a detailed analysis of the HIT reference case is presented, in which the interaction between the velocity invariants $\left(\mathcal{I}_{\left(R_A^*,Q_A^*\right)}\right)$, the pressure Hessian contribution $\left(\mathcal{II}_{\left(R_A^*,Q_A^*\right)}\right)$, the viscous contribution $\left(\mathcal{III}_{\left(R_A^*,Q_A^*\right)}\right)$, the total contribution $\left((\mathcal{I}+\mathcal{II}+\mathcal{III})_{\left(R_A^*,Q_A^*\right)}\right)$ are scrutinized. The comparison performed between the magnitudes, orientations and directions of the local flow topology dynamics of all contributions, ($\mathcal{I}$, $\mathcal{II}$, and $\mathcal{III}$)$_{\left(\dot{R}_A^*,\dot{Q}_A^*\right)}$, puts into evidence that the rotational trajectories in clockwise direction mainly comes from the mutual interaction of the invariants $\left(\mathcal{I}_{\left(R_A^*,Q_A^*\right)}\right)$, and the pressure Hessian contribution $\left(\mathcal{II}_{\left(R_A^*,Q_A^*\right)}\right)$, therefore the pressure Hessian contribution is then scrutinized in more detail by splitting it into its isotropic and anisotropic parts, which drive the local $\left(\mathcal{II}^{local}\right)$ and non-local $\left(\mathcal{II}^{nonlocal}\right)$ effects, respectively. Such decomposition allows to notice that it is the contribution of the non-local pressure Hessian that mainly drives the total pressure Hessian dynamics. Then, the HIT two-phase cases featuring evaporation with different levels of volume of fluids, $\phi_\ell = 0.05$ and $\phi_\ell = 0.10$, are analyzed. The statistics of such cases are gathered at various distances, by dividing the gaseous phase into several sub-regions according to the values of the level-set G. The statistics of these HIT two-phase flow cases are meticulously scrutinized by analyzing the various terms of the LEE in each gaseous sub-region. In regard to the interaction between the velocity invariants $\left(\mathcal{I}_{\left(R_A^*,Q_A^*\right)}\right)$, the local flow topology dynamics shows the same behavior, even in the vicinity of the liquid-gas interface and the scale of the vector $\Sigma_{\mathcal{I}_{\left(\dot{R}_A^*,\dot{Q}_A^*\right)}}$ increases slightly as the interface is approached. The pressure Hessian contribution $\left(\mathcal{II}_{\left(R_A^*,Q_A^*\right)}\right)$ displays large variations in its local flow topology dynamics as the liquid-gas interface is approached, as well as a large increment in its scale vector $\Sigma_{\mathcal{II}_{\left(\dot{R}_A^*,\dot{Q}_A^*\right)}}$. The non-local pressure Hessian contribution $\left(\mathcal{II}^{nonlocal}\right)$ remains the one that drives the dynamics of the total pressure Hessian contribution. The viscous contribution $\left(\mathcal{III}_{\left(R_A^*,Q_A^*\right)}\right)$ shows a large increase of its scale $\Sigma_{\mathcal{III}_{\left(\dot{R}_A^*,\dot{Q}_A^*\right)}}$ as the liquid-gas interface is approached. The value in the near region becomes more

than two times larger than its value in the intermediate or far regions. Finally, the total contribution $\left((\mathcal{I}+\mathcal{II}+\mathcal{III})_{\left(R_A^*,Q_A^*\right)}\right)$ is presented, where it is put into evidence that the pressure Hessian contribution increases its influence on the total local flow topology dynamics in the vicinity of the liquid-gas interface.

7 Conclusions and perspectives

This thesis work has been undertaken at Institut Pprime UPR 3346 CNRS - ENSMA, and it has been financially supported by **CONACyT-MX** through the scholarship No. 622998. The generation of the numerical data-bases was made possible thanks to the granted access to the HPC resources from GENCI-[CCRT|CINES|OCCIGEN] under the allocation DARI A0052B07456. This work aims at bringing a deeper understanding of the physics of turbulent mixing in vaporizing two-phase flows, with improvement of combustion performance as the targeted objective.

At first, a brief introduction of fluid mechanics and combustion science was presented. Then a general presentation of the computational fluid dynamics (CFD) was made. The focus is on the actual challenges of the direct numerical simulations (DNS) of multi-phase turbulent mixing. Such challenges consider the accurate simulation of : jet breakup, atomization (dense, dilute and very dilute regimes) and subsequent mixing of vapor. This is followed by a short report on recent numerical works devoted to the scalar dissipation rate (SDR) modeling, and especially the efforts made in the study of the turbulent-scalar interaction (TSI) term.

The massively parallel solver employed to gather the DNS data-bases was ARCHER, (which stands for *Academic Research Code for Hydrodynamic Equations Resolution*). ARCHER solves the three-dimensional incompressible form of the Navier-Stokes equations by using the *coupled level-set/volume-of-fluid (CLSVOF) method* in conjunction with an incompressible flow projection algorithm. The spatial derivatives for convective terms are evaluated using the *fifth-order precision WENO scheme*, whereas the viscous and molecular diffusion terms are computed using a *second-order central finite difference scheme*. The temporal integration is performed by using a *third-order precision Runge-Kutta scheme*. At the center of the cells are defined the scalar variables, such as pressure. The

preconditioning of the conjugate gradient method in the Poisson equation is settled by a *first-order multi-grid projection algorithm*, and at the liquid-gas interface, the jump conditions are imposed through the *ghost fluid (GF) method*. In regard to the interface tracking, a *coupled level-set/volume-of-fluid (CLSVOF) method* is used, in order to take advantage of both level-set and VOF strategies : mass loss is limited through the use of the VOF method and a detailed description of interface is ensured within the level-set framework. The turbulence is maintained by a linear forcing method. The choice of linear forcing was made for its simplicity and because of the lack of extensive studies dedicated to two-phase flow DNS forcing methods. The mixture fraction is defined by assuming local thermodynamic equilibrium, so mass fraction of fuel evaporated at the liquid-gas interface can be determined from the Clausius-Clapeyron law. The evolution of the mixture fraction field is performed using the same numerical schemes as these used to solve the momentum equation, but at the vicinity of the interface the evaluation of the spatial derivatives are based on ghost values deduced from the *Aslam extension method*.

The numerical set-up corresponds to two-phase flows in a three-dimensional homogeneous isotropic turbulence (HIT) cube featuring periodic boundaries and forced turbulence with a value of the turbulent kinetic energy maintained at low constant level of 3.6 $m^2 \cdot s^{-2}$. There were considered two different volume fractions of liquid, $\phi_\ell = 0.05$ and $\phi_\ell = 0.10$. The simulations were performed on regular meshes featuring a resolution of $256 \times 256 \times 256$ computational points. The characterization of the turbulent and scalar fields of the HIT reference case, in the evaporative and non-evaporative multi-phase flow cases, were presented, in order to confirms the ability of `ARCHER` to accurately simulate this kind of flows.

The statistical characterization of the turbulent velocity field was reported by dividing the gaseous phase into sub-regions as functions of the level-set. Firstly were addressing the topology evolution of the energetic scales of the turbulent flow, through the normalized invariants ξ^* and η^* of the Reynolds stress anisotropy tensor $\boldsymbol{b}$. Then a detailed analysis of the small-scale topology of the turbulent flow was reported. Such analysis consist into scrutinizing the velocity gradient tensor (VGT), by inspecting its local flow topologies in the invariant-phase planes. The analysis of the turbulent velocity field is closed by reporting a detailed inspection of geometrical features and alignment statistics for relevant turbulent quantities, such as the vorticity vector and strain-enstrophy angle.

The statistical characterization of the mixture fraction field gathers the inspection of some geometrical properties and alignment statistics of the scalar field, as well as its gradient and dissipation rate. Then attention is focused on the TSI terms, their

contributions, and some other statistics relevant to the mixture fraction field, such as the orientation between scalar gradient and strain-rate tensor principal directions or vorticity vector, as well as their corresponding JPDF (normalized magnitudes of vorticity and scalar gradient, and normalized magnitude of the scalar gradient, and normalized intermediate strain-rate eigenvalue).

The last chapter reports the Lagrangian-statistical characterization of the turbulent velocity field. Firstly are briefly addressed the mathematical formalisms of both, the Lagrangian evolution equations (LEE) – in their variable-density form –, and the conditional mean trajectories (CMT). Then the HIT reference case is reported and compared with some Lagrangian studies gathered for a variety of flow configurations. Finally the two HIT two-phase flow cases were meticulously scrutinized by analyzing the various terms of the LEE in each gaseous sub-region.

Perspectives and future works related to the present study may consist into generate some other data-sets, the first one gathering another HIT two-phase flows, but considering a higher level of resolution, which is appropriate for the study of micro-scale properties of scalar and turbulence fields at the boundary layer of the droplets featuring evaporation. The second DNS databases may correspond to a different configuration, which is more representative of practical applications : it is the temporal development of two-phase flow mixing layers. Then the development of a complete model for the scalar fluctuations in the presence of evaporation may be considered. The design of such a model is essential for the description of turbulent two-phase flow combustion, which requires the fluctuating mixture fraction field. The corresponding mixture fraction variance and associated level of dissipation rate thus require a specific closure to be settled. The corresponding mixture fraction variance level indeed appears as a standard input to estimate the unresolved fluctuations of the equivalence ratio within either the RANS or the LES framework. This clearly emphasizes the relevance of the present study with respect to process engineering or combustion applications. In a first step of this analysis the derivation of instantaneous SDR transport equation will be revisited. It should be indeed emphasized that, if some derivations have been already presented in the literature, the strict - in the mathematical sense - derivation of this transport is far from being an obvious task and requires some special care. Once this preliminary but essential issue has been addressed, we will proceed with a detailed (i.e., term by term) analysis of the corresponding transport equation. In comparison with the situation of reference, i.e., passive scalar in incompressible turbulence, some equilibrium displacements are expected : in the presence of evaporation (and depending on its intensity), the dominant terms of the transport equation are not expected to remain associated

to the same physical phenomena. The possibility to derive an algebraic closure for the mean scalar dissipation rate will be investigated. Such algebraic closures are often retained to proceed with the numerical simulation of two-phase flows but the evaporation processes are expected to influence the mixing frequency, which is an essential ingredient in such representations. In a second step of this analysis, a complete closure of the mean SDR transport equation, more versatile than algebraic closures, will be attempted.

A

Lagrangian evolution equations for the invariants of the VGT tensor

In this annex, the step-by-step deduction of the transport equations of the invariants of the VGT A_{ij}, i.e., Eqs (6.10)-(6.12), is presented.

Firstly the Navier–Stokes equations are presented in Einstein notation in Eq. A.1 :

$$\frac{Du_i}{Dt} = \frac{\partial u_i}{\partial t} + u_k \frac{\partial u_i}{\partial x_k} = \frac{1}{\rho}\left(-\frac{\partial p}{\partial x_i} + \frac{\partial \sigma_{ik}}{\partial x_k}\right) \tag{A.1}$$

To obtain the time evolution of the VGT A_{ij} in a Lagrangian frame, the gradient of Eq. A.1 with respect to x_j is taken :

$$\frac{\partial}{\partial x_j}\left(\frac{Du_i}{Dt}\right) = \frac{\partial}{\partial x_j}\left(\frac{\partial u_i}{\partial t}\right) + \frac{\partial}{\partial x_j}\left(u_k \frac{\partial u_i}{\partial x_k}\right) = \frac{\partial}{\partial x_j}\left(\frac{1}{\rho}\left(-\frac{\partial p}{\partial x_i}\right)\right) + \frac{\partial}{\partial x_j}\left(\frac{1}{\rho}\left(\frac{\partial \sigma_{ik}}{\partial x_k}\right)\right)$$

Where the terms of the right-hand side represent : Hessian pressure $\left(\mathcal{H}^p_{ij}\right)$, baroclinic pressure $\left(\mathcal{H}^b_{ij}\right)$, and viscous term $\left(\mathcal{T}_{ij}\right)$:

$$\mathcal{H}^p_{ij} = \frac{1}{\rho}\frac{\partial^2 P}{\partial x_i \partial x_j} \qquad \mathcal{H}^b_{ij} = -\frac{1}{\rho^2}\frac{\partial \rho}{\partial x_j}\frac{\partial P}{\partial x_i} \qquad \mathcal{T}_{ij} = \frac{\partial}{\partial x_j}\left(\frac{1}{\rho}\frac{\partial \sigma_{ik}}{\partial x_k}\right) ; \sigma_{ij} = 2\mu S^*_{ij}$$

$$\underbrace{\frac{\partial A_{ij}}{\partial t} + u_k \frac{\partial A_{ij}}{\partial x_k}}_{\frac{DA_{ij}}{Dt}} + \underbrace{\frac{\partial u_i}{\partial x_k}\frac{\partial u_k}{\partial x_j}}_{A_{ik}A_{kj}} = -\mathcal{H}^p_{ij} - \mathcal{H}^b_{ij} + \mathcal{T}_{ij}$$

$$\boxed{\dot{A}_{ij} \equiv \frac{DA_{ij}}{Dt} = -A_{ik}A_{kj} - \mathcal{H}^p_{ij} - \mathcal{H}^b_{ij} + \mathcal{T}_{ij}} \tag{A.2}$$

The evolution equations of the A_{ij} invariants are obtained by forming appropriate products with Eq. A.2 and taking the trace. So the compressible transport equations for the second products Eq. A.3 and triple products Eq. A.4 are :

$$\begin{aligned}\frac{D\left(A_{in}A_{nj}\right)}{Dt} + 2A_{in}A_{nk}A_{kj} = &- A_{in}\mathcal{H}^{p}_{nj} - \mathcal{H}^{p}_{in}A_{nj} \\ &- A_{in}\mathcal{H}^{b}_{nj} - \mathcal{H}^{b}_{in}A_{nj} + A_{in}\mathcal{T}_{nj} + \mathcal{T}_{in}A_{nj}\end{aligned} \tag{A.3}$$

$$\begin{aligned}\frac{D\left(A_{in}A_{nk}A_{kj}\right)}{Dt} + 3A_{in}A_{nk}A_{kr}A_{rj} = &- A_{in}A_{nk}\mathcal{H}^{p}_{kj} - A_{in}\mathcal{H}^{p}_{nk}A_{kj} - \mathcal{H}^{p}_{in}A_{nk}A_{kj} \\ &- A_{in}A_{nk}\mathcal{H}^{b}_{kj} - A_{in}\mathcal{H}^{b}_{nk}A_{kj} - \mathcal{H}^{b}_{in}A_{nk}A_{kj} \\ &+ A_{in}A_{nk}\mathcal{T}_{kj} + A_{in}\mathcal{T}_{nk}A_{kj} + \mathcal{T}_{in}A_{nk}A_{kj}\end{aligned} \tag{A.4}$$

It is known that the eigenvalues of A_{ij} satisfy the characteristic equation Eq. A.5 ; therefore the tensor A_{ij} satisfies Eq. A.6 :

$$\lambda^3 + P_A\lambda^2 + Q_A\lambda + R_A = 0 \tag{A.5}$$

$$A_{in}A_{nk}A_{kj} + P_A A_{ik}A_{kj} + Q_A A_{ij} + R_A\delta_{ij} = 0 \tag{A.6}$$

For compressible flow, the invariant of the VGT A_{ij} are :

$$P_A = -A_{kk} \tag{A.7a}$$

$$Q_A = \frac{1}{2}\left(P^2 - A_{ij}A_{ji}\right) \tag{A.7b}$$

$$R_A = \frac{1}{3}\left(-P^3 + 3PQ - A_{ij}A_{jk}A_{ki}\right) \tag{A.7c}$$

It is important to keep in mind :

$$\begin{aligned}A_{kk} &= -P_A \\ A_{ij}A_{ji} &= P_A^2 - 2Q_A \\ A_{ij}A_{jk}A_{ki} &= -P_A^3 + 3P_AQ_A - 3R_A\end{aligned}$$

Taking the trace of Eq. A.2 and substituting the invariants :

$$trc\left(A_{ij}\right) = A_{ii} \qquad trc\left(\mathcal{H}^{p}_{ij}\right) = \mathcal{H}^{p}_{ii}$$
$$trc\left(A_{ik}A_{kj}\right) = A_{ij}A_{ji} \qquad trc\left(\mathcal{H}^{b}_{ij}\right) = \mathcal{H}^{b}_{ii}$$

$$\frac{D\left(A_{ii}\right)}{Dt} = -A_{ij}A_{ji} - \mathcal{H}^{p}_{ii} - \mathcal{H}^{b}_{ii} + \mathcal{T}_{ii}$$

$$\frac{D(\cancel{-A_{ii}})}{Dt}^{P_A} = A_{ij}A_{ji} + \mathcal{H}^{p}_{ii} + \mathcal{H}^{b}_{ii} - \mathcal{T}_{ii}$$

$$A_{kk} = -P_A \quad ; \quad A_{ij}A_{ji} = P_A^2 - 2Q_A \quad \therefore$$

$$\boxed{\dot{P}_A \equiv \frac{DP_A}{Dt} = \underbrace{\left(P_A^2 - 2Q_A\right)}_{I_{P_A}} + \underbrace{\mathcal{H}^{p}_{ii}}_{II^{p}_{P_A}} + \underbrace{\mathcal{H}^{b}_{ii}}_{II^{b}_{P_A}} + \underbrace{\left(-\mathcal{T}_{ii}\right)}_{III_{P_A}}} \tag{A.8}$$

Taking the trace of Eq. A.3 and substituting the invariants :

$$trc\left(A_{in}A_{nj}\right) = A_{in}A_{ni} \qquad trc\left(A_{in}\mathcal{H}^{p}_{nj}\right) = A_{in}\mathcal{H}^{p}_{ni}$$
$$trc\left(A_{in}A_{nk}A_{kj}\right) = A_{in}A_{nk}A_{ki} \qquad trc\left(A_{in}\mathcal{H}^{b}_{nj}\right) = A_{in}\mathcal{H}^{b}_{ni}$$

$$\frac{D\left(A_{in}A_{ni}\right)}{Dt} + 2A_{in}A_{nk}A_{ki} = -A_{in}\mathcal{H}^{p}_{ni} - \mathcal{H}^{p}_{in}A_{ni} - A_{in}\mathcal{H}^{b}_{ni} - \mathcal{H}^{b}_{in}A_{ni} + A_{in}\mathcal{T}_{ni} + \mathcal{T}_{in}A_{ni}$$

$$\frac{D\left(A_{in}A_{ni}\right)}{Dt} + 2A_{in}A_{nk}A_{ki} = -2A_{in}\mathcal{H}^{p}_{ni} - 2A_{in}\mathcal{H}^{b}_{ni} + 2A_{in}\mathcal{T}_{ni}$$

$$A_{in}A_{ni} = P_A^2 - 2Q_A \quad ; \quad A_{in}A_{nk}A_{ki} = -P_A^3 + 3\left(P_AQ_A - R_A\right) \quad \therefore$$

$$\frac{D\left(P_A^2 - 2Q_A\right)}{Dt} - 2P_A^3 + 6\left(P_AQ_A - R_A\right) = -2A_{in}\mathcal{H}^{p}_{ni} - 2A_{in}\mathcal{H}^{b}_{ni} + 2A_{in}\mathcal{T}_{ni}$$

$$\frac{D\left(P_A^2 - 2Q_A\right)}{Dt} - 2P_A^3 + 6P_AQ_A - 6R_A = -2A_{in}\mathcal{H}^p_{ni} - 2A_{in}\mathcal{H}^b_{ni} + 2A_{in}\mathcal{T}_{ni}$$

$$\frac{D\left(P_A^2 - 2Q_A\right)}{Dt} = 2P_A^3 - 6P_AQ_A + 6R_A - 2A_{in}\mathcal{H}^p_{ni} - 2A_{in}\mathcal{H}^b_{ni} + 2A_{in}\mathcal{T}_{ni}$$

Using the Chain Rule :

$$\begin{aligned}\frac{D\left(P_A^2 - 2Q_A\right)}{Dt} &= \frac{D\left(P_A^2 - 2Q_A\right)}{DP_A}\frac{DP_A}{Dt} + \frac{D\left(P_A^2 - 2Q_A\right)}{DQ_A}\frac{DQ_A}{Dt} \\ &= 2P_A\frac{DP_A}{Dt} - 2\frac{DQ_A}{Dt} \quad ; \\ \frac{D\left(P_A^2 - 2Q_A\right)}{Dt} &= 2\frac{DP_A^2}{Dt} - 2\frac{DQ_A}{Dt}\end{aligned}$$

It is necessary to deduce the transport equation of P_A^2, so Eq. A.8 is multiplying by P_A as follows :

$$P_A\left(\frac{DP_A}{Dt} = \left(P_A^2 - 2Q_A\right) + \mathcal{H}^p_{ii} + \mathcal{H}^b_{ii} - \mathcal{T}_{ii}\right)$$

$$\frac{D\left(P_A^2\right)}{Dt} = P_A\left(P_A^2 - 2Q_A\right) + P_A\mathcal{H}^p_{ii} + P_A\mathcal{H}^b_{ii} - P_A\mathcal{T}_{ii}$$

$$\frac{D\left(P_A^2\right)}{Dt} = P_A^3 - 2P_AQ_A + P_A\mathcal{H}^p_{ii} + P_A\mathcal{H}^b_{ii} - P_A\mathcal{T}_{ii} \quad \therefore$$

$$2\frac{DP_A^2}{Dt} - 2\frac{DQ_A}{Dt} = 2P_A^3 - 6P_AQ_A + 6R_A - 2A_{in}\mathcal{H}^p_{ni} - 2A_{in}\mathcal{H}^b_{ni} + 2A_{in}\mathcal{T}_{ni}$$

$$-2\frac{DQ_A}{Dt} = -2\frac{DP_A^2}{Dt} + 2P_A^3 - 6P_AQ_A + 6R_A - 2A_{in}\mathcal{H}^p_{ni} - 2A_{in}\mathcal{H}^b_{ni} + 2A_{in}\mathcal{T}_{ni}$$

$$-2\frac{DQ_A}{Dt} = -2\left(P_A^3 - 2P_AQ_A + P_A\mathcal{H}_{ii}^p + P_A\mathcal{H}_{ii}^b - P_A\mathcal{T}_{ii}\right) + 2P_A^3 - 6P_AQ_A + 6R_A - 2A_{in}\mathcal{H}_{ni}^p - 2A_{in}\mathcal{H}_{ni}^b + 2A_{in}\mathcal{T}_{ni}$$

$$-2\frac{DQ_A}{Dt} = -2P_A^3 + 4P_AQ_A - 2P_A\mathcal{H}_{ii}^p - 2P_A\mathcal{H}_{ii}^b + 2P_A\mathcal{T}_{ii} + 2P_A^3 - 6P_AQ_A + 6R_A - 2A_{in}\mathcal{H}_{ni}^p - 2A_{in}\mathcal{H}_{ni}^b + 2A_{in}\mathcal{T}_{ni}$$

$$-2\frac{DQ_A}{Dt} = -2P_AQ_A + 6R_A - 2P_A\mathcal{H}_{ii}^p - 2P_A\mathcal{H}_{ii}^b + 2P_A\mathcal{T}_{ii} - 2A_{in}\mathcal{H}_{ni}^p - 2A_{in}\mathcal{H}_{ni}^b + 2A_{in}\mathcal{T}_{ni}$$

$$\boxed{\dot{Q}_A \equiv \frac{DQ_A}{Dt} = \underbrace{(P_AQ_A - 3R_A)}_{I_{Q_A}} + \underbrace{\left(P_A\mathcal{H}_{ii}^p + A_{in}\mathcal{H}_{ni}^p\right)}_{II_{Q_A}^p} + \underbrace{\left(P_A\mathcal{H}_{ii}^b + A_{in}\mathcal{H}_{ni}^b\right)}_{II_{Q_A}^b} + \underbrace{(-P_A\mathcal{T}_{ii} - A_{in}\mathcal{T}_{ni})}_{III_{Q_A}}} \tag{A.9}$$

Taking the trace of Eq. A.4 and substituting the invariants :

$$trc\left(A_{in}A_{nj}\right) = A_{in}A_{ni} \qquad trc\left(A_{in}A_{nk}\mathcal{H}_{kj}\right) = A_{in}A_{nk}\mathcal{H}_{ki}$$
$$trc\left(A_{in}A_{nk}A_{kj}\right) = A_{in}A_{nk}A_{ki} \qquad trc\left(A_{in}\mathcal{H}_{nk}A_{kj}\right) = A_{in}\mathcal{H}_{nk}A_{ki}$$
$$trc\left(A_{in}A_{nk}A_{kr}A_{rj}\right) = A_{in}A_{nk}A_{kj}A_{ji} \qquad trc\left(\mathcal{H}_{in}A_{nk}A_{kj}\right) = \mathcal{H}_{in}A_{nk}A_{ki}$$

$$\frac{D\left(A_{in}A_{nk}A_{ki}\right)}{Dt} + 3A_{in}A_{nk}A_{kj}A_{ji} = -A_{in}A_{nk}\mathcal{H}_{ki}^p - A_{in}\mathcal{H}_{nk}^pA_{ki} - \mathcal{H}_{in}^pA_{nk}A_{ki} - A_{in}A_{nk}\mathcal{H}_{ki}^b - A_{in}\mathcal{H}_{nk}^bA_{ki} - \mathcal{H}_{in}^bA_{nk}A_{ki} + A_{in}A_{nk}\mathcal{T}_{ki} + A_{in}\mathcal{T}_{nk}A_{ki} + \mathcal{T}_{in}A_{nk}A_{ki}$$

$$\frac{D\left(A_{in}A_{nk}A_{ki}\right)}{Dt} + 3A_{in}A_{nk}A_{kj}A_{ji} = -3A_{in}A_{nk}\mathcal{H}_{ki}^p - 3A_{in}A_{nk}\mathcal{H}_{ki}^b + 3A_{in}A_{nk}\mathcal{T}_{ki}$$

$$A_{in}A_{nk}A_{ki} = -P_{\boldsymbol{A}}^3 + 3\left(P_{\boldsymbol{A}}Q_{\boldsymbol{A}} - R_{\boldsymbol{A}}\right) \quad ; \quad A_{in}A_{nk}A_{kj}A_{ji} =? \quad \therefore$$

$$\begin{aligned}\frac{D\left(-P_{\boldsymbol{A}}^3 + 3P_{\boldsymbol{A}}Q_{\boldsymbol{A}} - 3R_{\boldsymbol{A}}\right)}{Dt} = &-3A_{in}A_{nk}A_{kj}A_{ji} - 3A_{in}A_{nk}\mathcal{H}_{ki}^{p} \\ &- 3A_{in}A_{nk}\mathcal{H}_{ki}^{b} + 3A_{in}A_{nk}\mathcal{T}_{ki}\end{aligned}$$

The Caley-Hamilton Theorem states that «*Every square matrix satisfies its own characteristic equation*», so Eq. A.6 is recalled and multiplied by A_{ij}, and then take the trace :

$$A_{nr}\left(A_{im}A_{mk}A_{kj} + P_{\boldsymbol{A}}A_{ik}A_{kj} + Q_{\boldsymbol{A}}A_{ij} + R_{\boldsymbol{A}}\delta_{ij} = 0\right)$$

$$A_{in}A_{nk}A_{kr}A_{rj} + P_{\boldsymbol{A}}A_{in}A_{nk}A_{kj} + Q_{\boldsymbol{A}}A_{in}A_{nj} + R_{\boldsymbol{A}}A_{ij} = 0$$

$$A_{in}A_{nk}A_{kj}A_{ji} + P_{\boldsymbol{A}}A_{in}A_{nk}A_{ki} + Q_{\boldsymbol{A}}A_{in}A_{ni} + R_{\boldsymbol{A}}A_{ii} = 0$$

$$\begin{gathered}A_{kk} = -P_{\boldsymbol{A}} \quad ; \quad A_{ij}A_{ji} = P_{\boldsymbol{A}}^2 - 2Q_{\boldsymbol{A}} \quad ; \quad A_{ij}A_{jk}A_{ki} = -P_{\boldsymbol{A}}^3 + 3P_{\boldsymbol{A}}Q_{\boldsymbol{A}} - 3R_{\boldsymbol{A}} \quad ; \\ A_{in}A_{nk}A_{kj}A_{ji} = -P_{\boldsymbol{A}}\left(-P_{\boldsymbol{A}}^3 + 3P_{\boldsymbol{A}}Q_{\boldsymbol{A}} - 3R_{\boldsymbol{A}}\right) - Q_{\boldsymbol{A}}\left(P_{\boldsymbol{A}}^2 - 2Q_{\boldsymbol{A}}\right) - R_{\boldsymbol{A}}\left(-P_{\boldsymbol{A}}\right) \quad \therefore\end{gathered}$$

$$A_{in}A_{nk}A_{kj}A_{ji} = -3P_{\boldsymbol{A}}^2Q_{\boldsymbol{A}} + 3P_{\boldsymbol{A}}R_{\boldsymbol{A}} + P_{\boldsymbol{A}}^4 - P_{\boldsymbol{A}}^2Q_{\boldsymbol{A}} + 2Q_{\boldsymbol{A}}^2 + P_{\boldsymbol{A}}R_{\boldsymbol{A}}$$

$$-3\left(A_{in}A_{nk}A_{kj}A_{ji} = -3P_{\boldsymbol{A}}^2Q_{\boldsymbol{A}} + 3P_{\boldsymbol{A}}R_{\boldsymbol{A}} + P_{\boldsymbol{A}}^4 - P_{\boldsymbol{A}}^2Q_{\boldsymbol{A}} + 2Q_{\boldsymbol{A}}^2 + P_{\boldsymbol{A}}R_{\boldsymbol{A}}\right)$$

$$\begin{aligned}-3A_{in}A_{nk}A_{kj}A_{ji} = &\,9P_{\boldsymbol{A}}^2Q_{\boldsymbol{A}} - 9P_{\boldsymbol{A}}R_{\boldsymbol{A}} - 3P_{\boldsymbol{A}}^4 \\ &+ 3P_{\boldsymbol{A}}^2Q_{\boldsymbol{A}} - 6Q_{\boldsymbol{A}}^2 - 3P_{\boldsymbol{A}}R_{\boldsymbol{A}}\end{aligned}$$

$$-3A_{in}A_{nk}A_{kj}A_{ji} = -3P_{\boldsymbol{A}}^4 + 12P_{\boldsymbol{A}}^2Q_{\boldsymbol{A}} - 6Q_{\boldsymbol{A}}^2 - 12P_{\boldsymbol{A}}R_{\boldsymbol{A}}$$

Using the Chain Rule :

$$\begin{aligned}\frac{D\left(-P_A^3+3P_AQ_A-3R_A\right)}{Dt} &= \frac{d\left(-P_A^3+3P_AQ_A-3R_A\right)}{dP_A}\frac{dP_A}{dt}\\ &+\frac{d\left(-P_A^3+3P_AQ_A-3R_A\right)}{dQ_A}\frac{dQ_A}{dt}\\ &+\frac{d\left(-P_A^3+3P_AQ_A-3R_A\right)}{dR_A}\frac{dR_A}{dt} \quad ;\\ \frac{D\left(-P_A^3+3P_AQ_A-3R_A\right)}{Dt} &= \left(3Q_A-3P_A^2\right)\frac{dP_A}{dt}+\left(3P_A\right)\frac{dQ_A}{dt}+\left(-3\right)\frac{dR_A}{dt} \qquad \therefore\end{aligned}$$

$$\begin{aligned}\frac{D\left(-P_A^3+3P_AQ_A-3R_A\right)}{Dt} &= -3A_{in}A_{nk}A_{kj}A_{ji}-3A_{in}A_{nk}\mathcal{H}^p_{ki}-3A_{in}A_{nk}\mathcal{H}^b_{ki}+3A_{in}A_{nk}\mathcal{T}_{ki}\\ &= \underbrace{\boxed{\left(3Q_A-3P_A^2\right)\left[\left(P_A^2-2Q_A\right)+\mathcal{H}^p_{ii}+\mathcal{H}^b_{ii}-\mathcal{T}_{ii}\right]}}_{(a)}\\ &+\underbrace{\boxed{\left(3P_A\right)\left[\left(P_AQ_A-3R_A\right)+P_A\mathcal{H}^p_{ii}+A_{in}\mathcal{H}^p_{ni}+P_A\mathcal{H}^b_{ii}+A_{in}\mathcal{H}^b_{ni}-P_A\mathcal{T}_{ii}-A_{in}\mathcal{T}_{ni}\right]}}_{(b)}\\ &+\underbrace{\boxed{\left(-3\right)\frac{dR_A}{dt}}}_{(c)}\end{aligned}$$

Developing term (a) :

$$\begin{aligned}\left(3Q_A-3P_A^2\right)\left[\left(P_A^2-2Q_A\right)+\mathcal{H}^p_{ii}+\mathcal{H}^b_{ii}-\mathcal{T}_{ii}\right] &=\\ &+3P_A^2Q_A-6Q_A^2+3Q_A\mathcal{H}^p_{ii}+3Q_A\mathcal{H}^b_{ii}-3Q_A\mathcal{T}_{ii}\\ &-3P_A^4+6P_A^2Q_A-3P_A^2\mathcal{H}^p_{ii}-3P_A^2\mathcal{H}^b_{ii}+3P_A^2\mathcal{T}_{ii}\\ &=-3P_A^4+9P_A^2Q_A-6Q_A^2+3Q_A\mathcal{H}^p_{ii}-3P_A^2\mathcal{H}^p_{ii}+3Q_A\mathcal{H}^b_{ii}\\ &\quad-3Q_A\mathcal{T}_{ii}-3P_A^2\mathcal{H}^b_{ii}+3P_A^2\mathcal{T}_{ii}\end{aligned}$$

Developing term (b) :

$$\left(3P_A\right)\left[\left(P_AQ_A-3R_A\right)+P_A\mathcal{H}^p_{ii}+A_{in}\mathcal{H}^p_{ni}+P_A\mathcal{H}^b_{ii}+A_{in}\mathcal{H}^b_{ni}-P_A\mathcal{T}_{ii}-A_{in}\mathcal{T}_{ni}\right]=$$
$$3P_A^2Q_A-9P_AR_A+3P_A^2\mathcal{H}^p_{ii}+3P_AA_{in}\mathcal{H}^p_{ni}+3P_A^2\mathcal{H}^b_{ii}+3P_AA_{in}\mathcal{H}^b_{ni}-3P_A^2\mathcal{T}_{ii}-3P_AA_{in}\mathcal{T}_{ni}$$

Then, the developed terms (a) and (b) are sum together :

$$\begin{aligned}(a+b) = &-3P_A^4 + 12P_A^2 Q_A - 9P_A R_A \\ &+ \cancelto{0}{3P_A^2 \mathcal{H}^p_{ii} - 3P_A^2 \mathcal{H}^p_{ii}} + 3Q_A \mathcal{H}^p_{ii} + 3P_A A_{in} \mathcal{H}^p_{ni} \\ &+ \cancelto{0}{3P_A^2 \mathcal{H}^b_{ii} - 3P_A^2 \mathcal{H}^b_{ii}} + 3Q_A \mathcal{H}^b_{ii} + 3P_A A_{in} \mathcal{H}^b_{ni} \\ &+ \cancelto{0}{3P_A^2 \mathcal{T}_{ii} - 3P_A^2 \mathcal{T}_{ii}} - 3Q_A \mathcal{T}_{ii} - 3P_A A_{in} \mathcal{T}_{ni}\end{aligned}$$

$$\begin{aligned}(a+b) = &-3P_A^4 + 12P_A^2 Q_A - 9P_A R_A \\ &+ 3Q_A \mathcal{H}^p_{ii} + 3P_A A_{in} \mathcal{H}^p_{ni} \\ &+ 3Q_A \mathcal{H}^b_{ii} + 3P_A A_{in} \mathcal{H}^b_{ni} \\ &- 3Q_A \mathcal{T}_{ii} - 3P_A A_{in} \mathcal{T}_{ni} \qquad \therefore\end{aligned}$$

$$\begin{aligned}-3\frac{dR_A}{dt} = &-(a+b) - 3P_A^4 + 12P_A^2 Q_A - 6Q_A^2 - 12P_A R_A \\ &- 3A_{in}A_{nk}\mathcal{H}^p_{ki} - 3A_{in}A_{nk}\mathcal{H}^b_{ki} + 3A_{in}A_{nk}\mathcal{T}_{ki}\end{aligned}$$

$$\begin{aligned}-3\frac{dR_A}{dt} = &\cancelto{0}{+3P_A^4 - 3P_A^4} \cancelto{0}{+12P_A^2 Q_A - 12P_A^2 Q_A} \cancelto{0}{+6Q_A^2 - 6Q_A^2} \\ &+ 9P_A R_A - 12P_A R_A \\ &- 3Q_A \mathcal{H}^p_{ii} - 3P_A A_{in} \mathcal{H}^p_{ni} - 3A_{in}A_{nk}\mathcal{H}^p_{ki} \\ &- 3Q_A \mathcal{H}^b_{ii} - 3P_A A_{in} \mathcal{H}^b_{ni} - 3A_{in}A_{nk}\mathcal{H}^b_{ki} \\ &+ 3Q_A \mathcal{T}_{ii} + 3P_A A_{in} \mathcal{T}_{ni} + 3A_{in}A_{nk}\mathcal{T}_{ki}\end{aligned}$$

$$\begin{aligned}-3\frac{dR_A}{dt} = &-3P_A R_A - 3Q_A \mathcal{H}^p_{ii} - 3P_A A_{in} \mathcal{H}^p_{ni} - 3A_{in}A_{nk}\mathcal{H}^p_{ki} \\ &- 3Q_A \mathcal{H}^b_{ii} - 3P_A A_{in} \mathcal{H}^b_{ni} - 3A_{in}A_{nk}\mathcal{H}^b_{ki} \\ &+ 3Q_A \mathcal{T}_{ii} + 3P_A A_{in} \mathcal{T}_{ni} + 3A_{in}A_{nk}\mathcal{T}_{ki}\end{aligned}$$

$$\dot{R}_{\boldsymbol{A}} \equiv \frac{DR_{\boldsymbol{A}}}{Dt} = \underbrace{(P_{\boldsymbol{A}} R_{\boldsymbol{A}})}_{I_{R_{\boldsymbol{A}}}} + \underbrace{\left(Q_{\boldsymbol{A}} \mathcal{H}^{p}_{ii} + P_{\boldsymbol{A}} A_{in} \mathcal{H}^{p}_{ni} + A_{in} A_{nk} \mathcal{H}^{p}_{ki}\right)}_{II^{p}_{R_{\boldsymbol{A}}}} + \underbrace{\left(Q_{\boldsymbol{A}} \mathcal{H}^{b}_{ii} + P_{\boldsymbol{A}} A_{in} \mathcal{H}^{b}_{ni} + A_{in} A_{nk} \mathcal{H}^{b}_{ki}\right)}_{II^{b}_{R_{\boldsymbol{A}}}} + \underbrace{\left(-Q_{\boldsymbol{A}} \mathcal{T}_{ii} - P_{\boldsymbol{A}} A_{in} \mathcal{T}_{ni} - A_{in} A_{nk} \mathcal{T}_{ki}\right)}_{III_{R_{\boldsymbol{A}}}} \tag{A.10}$$

B

Lagrangian evolution equations for the traceless invariants of the VGT tensor

From Eqs. (A.8)-(A.10), it is possible to deduce the transport equations for the invariants of the deviatoric, i.e., traceless, VGT $\boldsymbol{A}^*$. Indeed, as the tensor $\boldsymbol{A}^*\boldsymbol{A}^*$ and $\boldsymbol{A}^*\boldsymbol{A}^*\boldsymbol{A}^*$ can be written as follows :

$$\begin{aligned}(A^*A^*)_{ij} &= A^*_{ik}A^*_{kj} = (A_{ik} + \frac{\delta_{ik}}{3}P)(A_{kj} + \frac{\delta_{kj}}{3}P) \\ &= (AA)_{ij} + \frac{2P}{3}A_{ij} + \frac{1}{9}\delta_{ij}P^2 \,, \end{aligned} \tag{B.1a}$$

$$\begin{aligned}(A^*A^*A^*)_{ij} &= (A^*A^*)_{ik}A^*_{kj} = ((AA)_{ik} + \frac{2P}{3}A_{ik} + \frac{1}{9}\delta_{ik}P^2)(A_{kj} + \frac{\delta_{kj}}{3}P) \\ &= (AAA)_{ij} + \frac{P}{3}(AA)_{ij} + \frac{2P}{3}(AA)_{ij} + \frac{2P^2}{9}A_{ij} + \frac{P^3}{9} + \frac{P^2}{9}A_{ij} + \frac{1}{27}\delta_{ij}P^3 \\ &= (AAA)_{ij} + P\ (AA)_{ij} + \frac{P^2}{3}A_{ij} + \frac{1}{27}\delta_{ij}P^3 \,, \end{aligned} \tag{B.1b}$$

the invariants of $\boldsymbol{A}^*$ can be expressed using P, Q, and R,

$$\begin{aligned}Q^* &= -\frac{1}{2}(A^*A^*)_{ii} = -\frac{1}{2}\left[(AA)_{ii} + \frac{2P}{3}A_{ii} + \frac{1}{3}P^2\right] \\ &= -\frac{1}{2}\left[(AA)_{ii} - \frac{P^2}{3}\right] = -\frac{1}{2}\left[P^2 - 2Q - \frac{P^2}{3}\right] \\ &= Q - \frac{1}{3}P^2 \end{aligned} \tag{B.2a}$$

$$\begin{aligned}R^* &= -\frac{1}{3}(A^*A^*A^*)_{ii} = -\frac{1}{3}\left[(AAA)_{ii} + P\ (AA)_{ii} + \frac{P^2}{3}A_{ii} + \frac{1}{9}P^3\right] \\ &= -\frac{1}{3}\left[(AAA)_{ii} + P\ (AA)_{ii} - \frac{P^3}{3} + \frac{1}{9}P^3\right] \end{aligned}$$

$$= -\frac{1}{3}\left[\left(3PQ - P^3 - 3R\right) + P\left(P^2 - 2Q\right) - \frac{2P^3}{9}\right]$$
$$= R - \frac{1}{3}PQ + \frac{2}{27}P^3 \tag{B.2b}$$

Applying the chain-rule of differential operations to the above equations leads to the transport equations for P^*, Q^*, and R^* that can be written as

$$\frac{DP^*}{Dt} = 0 \tag{B.3a}$$
$$\frac{DQ^*}{Dt} = \frac{DQ}{Dt} - \frac{2P}{3}\frac{DP}{Dt}$$
$$= \mathrm{I}_{Q^*} + \mathrm{II}_{Q^*} + \mathrm{III}_{Q^*} + \mathrm{IV}_{Q^*} \tag{B.3b}$$
$$\frac{DR^*}{Dt} = \frac{DR}{Dt} - \frac{1}{3}(P\frac{DQ}{Dt} + Q\frac{DP}{Dt}) + \frac{2P^2}{9}\frac{DP}{Dt}$$
$$= \mathrm{I}_{R^*} + \mathrm{II}_{R^*} + \mathrm{III}_{R^*} + \mathrm{IV}_{R^*} \tag{B.3c}$$

where the various terms present in the RHS are given by

$$\mathrm{I}_{Q^*} = \mathrm{I}_Q - \frac{2P}{3}\mathrm{I}_P = -\frac{2}{3}P^3 + \frac{7}{3}PQ - 3R \tag{B.4a}$$
$$\mathrm{II}_{Q^*} = \frac{1}{3}P\mathcal{H}^p_{ii} + A_{ij}\mathcal{H}^p_{ji} \tag{B.4b}$$
$$\mathrm{III}_{Q^*} = \frac{1}{3}P\mathcal{H}^b_{ii} + A_{ij}\mathcal{H}^b_{ji} \tag{B.4c}$$
$$\mathrm{IV}_{Q^*} = -\frac{1}{3}P\mathcal{T}_{ii} - A_{ij}\mathcal{T}_{ji} \tag{B.4d}$$

and

$$\mathrm{I}_{R^*} = \mathrm{I}_R - \frac{1}{3}(P\mathrm{I}_Q + Q\mathrm{I}_P) + \frac{2P^2}{9}\mathrm{I}_P = \frac{2}{9}P^4 - \frac{10}{9}P^2Q + \frac{2}{3}Q^2 + 2PR \tag{B.5a}$$
$$\mathrm{II}_{R^*} = \frac{6Q - P^2}{9}\mathcal{H}^p_{ii} + \frac{2P}{3}A_{ij}\mathcal{H}^p_{ji} + A_{ik}A_{kj}\mathcal{H}^p_{ki} \tag{B.5b}$$
$$\mathrm{III}_{R^*} = \frac{6Q - P^2}{9}\mathcal{H}^b_{ii} + \frac{2P}{3}A_{ij}\mathcal{H}^b_{ji} + A_{ik}A_{kj}\mathcal{H}^b_{ki} \tag{B.5c}$$
$$\mathrm{IV}_{R^*} = -\frac{6Q - P^2}{9}\mathcal{T}_{ii} - \frac{2P}{3}A_{ij}\mathcal{T}_{ji} - A_{ik}A_{kj}\mathcal{T}_{ki} \tag{B.5d}$$

C

Résumé de la thèse de l'école doctorale SIMME

Contribution à l'étude numérique des interactions turbulence - transfert de masse dans les écoulements diphasiques en évaporation

Chapitre 1. Introduction

La mécanique des fluides et la science de la combustion ont joué un rôle central dans la vie humaine depuis les plus anciennes civilisations *"fleuve"* comme la Mésopotamie, l'Égypte, la Chine, pour n'en citer que quelques-unes. D'une part, la mécanique des fluides est la branche de la physique qui s'intéresse à l'étude du comportement des fluides en mouvement stable, transitionnel et totalement instable. Certains des scientifiques et philosophes les plus éminents de la Grèce antique ont été les premiers à tenter de conceptualiser formellement certaines caractéristiques des fluides et leurs mouvements (Tokaty [103]), ainsi par exemple Aristote a utilisé pour la première fois le *«principe de continuité»* et a proposé une distinction entre le mouvement naturel et forcé, Archimède a basé la statique des fluides réelle, et Hérons d'Alexandria a inventé le *"Herons Reactive Motor"*, qui est considéré comme le père des moteurs à réaction, des fusées et des turbines. Quelques siècles plus tard, l'un des scientifiques italiens les plus éminents de la Renaissance, Léonard de Vinci, a donné la base mathématique et physique du concept de continuité et a été le premier à faire une distinction entre le concept physique et mathématique

du point. Plus tard, le mathématicien suisse Leonhard Paul Euler a introduit les concepts de base de la mécanique des fluides moderne en développant le concept de particule fluide, et a proposé : i) l'équation différentielle de la ligne de courant, ii) la loi de conservation de la masse, et iii) les équations différentielles de continuité et de mouvement fluide pour les écoulements potentiels (non visqueux). Ensuite, la première tentative pour décrire mathématiquement le mouvement des fluides visqueux a été faite par l'ingénieur et physicien français Claude-Louis Navier et le physicien et mathématicien anglo-irlandais George Gabriel Stokes. Conjointement avec la déduction des équations de Navier-Stokes et les contributions de l'ingénieur et physicien irlandais Osborne Reynolds, voir Fig. C.1 : i) le nombre dimensionnel de Reynolds (Re), et ii) la découverte des modes d'écoulement laminaire et turbulent des fluides ; le domaine de recherche sur la turbulence a été formellement créé.

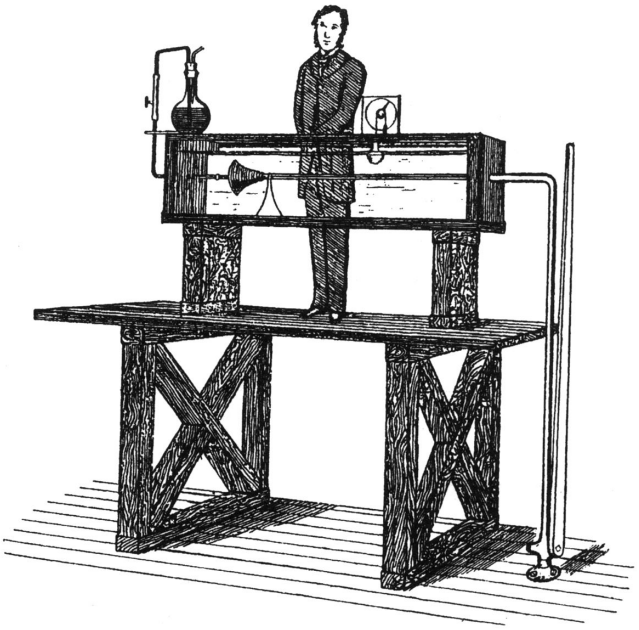

Figure C.1. *Croquis d'Osborne Reynolds et de son expérience de turbulence fluide de 1883*

D'un autre côté, en ce qui concerne la science de la combustion, la première tentative scientifique pour définir le concept de *"combustion"* a probablement été faite par le physicien et alchimiste flamand Johannes Baptista van Helmont, car il a compris qu'il existe des gaz de différents la nature à partir de l'air atmosphérique alors qu'il étudiait le processus de combustion du charbon de bois et observait l'interaction entre le combustible, le comburant (atmosphère) et la flamme/la chaleur ; il a donc déclaré que la combustion implique la fuite d'un "esprit sauvage" (spiritus silvestre), c'est-à-dire de la fumée/suie provenant de l'interaction combustible-oxydant (Harris [46]). Avec cette expérience, il découvrit le dioxyde de carbone (CO_2) et introduisit le mot *gaz* dans le langage scientifique. Néanmoins, la science moderne de la combustion a été fondée par le chimiste français Antoine Laurent Lavoisier, lorsqu'il a étudié : i)

la production d'acide phosphorique, et ii) la calcination des sulfates ; qui à la fin du processus prennent du poids en raison de l'absorption de dioxyde de carbone. Cette découverte lui a également valu le titre de *"père de la chimie moderne"* (Kohler [56]). Même si la science de la combustion a joué un rôle important dans les civilisations humaines, sa recherche et son développement ont été fortement encouragés au cours du 19^{th} siècle en raison de différents faits : i) la demande d'énergie émise pour la révolution industrielle, ii) les scientifiques ont commencé pour comprendre les concepts clés sur lesquels le moteur à combustion interne a été construit, et iii) le carburant nécessaire pour alimenter le moteur devenait disponible en grandes quantités.

En 1862, l'inventeur belge Jean-Joseph Etienne Lenoir a inventé la première automobile au monde qui utilise un moteur inventé par lui-même. Puis en 1876, l'ingénieur allemand Nicolaus August Otto, après plusieurs années d'expérimentation avec le moteur Lenoir, inventa le premier moteur "Otto" à quatre temps fonctionnant au gaz de pétrole et utilisant un allumage par bougie. Depuis des contributions d'Otto, le prochain défi était d'utiliser des carburants liquides, dans ce contexte, les procédés de pulvérisation et de vaporisation deviennent des sujets d'étude centraux pour les ingénieurs. À la fin du 19^{th} siècle, trois procédés différents ont été inventés pour accomplir cette tâche : i) carburateur, ii) vaporisation à bulbe chaud et iii) injection directe, voir Fig. C.2 ; ce dernier fut introduit en 1897 par l'ingénieur allemand Rudolf Christian Karl Diesel (Sass [86]).

Figure C.2. *Schéma d'un moteur Diesel à combustion*

Depuis les contributions de Leonhard Paul Euler et jusqu'à la seconde moitié du XXe siècle, les approches expérimentales et théoriques étaient les seules approches possibles pour aborder les problèmes posés par la mécanique des fluides. Le premier calcul d'un écoulement turbulent pratique a été réalisé par Prandtl (1925) [80], lorsque

le concept de longueur de mélange a été introduit, et avec lequel la viscosité turbulente a été déterminée avec succès ; mais l'émergence dans les années 1960_s de la mécanique des fluides numériques (CFD) a révolutionné le domaine. Cette troisième approche relativement nouvelle de l'étude et du développement de la mécanique des fluides a été rendue possible grâce à la fusion des améliorations de la capacité de mémoire et de la vitesse de calcul des ordinateurs réalisées á partir des années 1950_s (voir Fig. C.3 [1] [2]), ainsi que le développement de méthodes numériques et algorithmes, la CFD consiste donc à tirer parti de la quantité importante de calculs que les ordinateurs peuvent effectuer dans un temps relativement court, en y implémentant plusieurs algorithmes numériques sous forme de programmes, afin de pouvoir ensemble résoudre les problèmes d'écoulement des fluides. Les premiers solveurs CFD appropriés ont été présentés à la conférence de Stanford de 1968 sur le calcul des couches limites turbulentes [20], et au symposium de la NASA sur les couches limites turbulentes compressibles de 1968 organisé au centre de recherche Langley [68]. Les solveurs présentés lors de ces conférences été basés sur l'approche RANS (Reynolds-Average Navier-Stokes), cependant dans le contexte du recherche, les solutions des équations moyennes manquait d'informations sur les caractéristiques instables de l'écoulement, c'est-à-dire que les phénomènes réels de transition et de turbulence ne peuvent pas être étudiés en détail par ce moyen. Néanmoins, des approches "avancées" de modélisation CFD ont été développés pour surmonter les limitations que présente l'approche RANS : où les mouvements à grande échelle (grands tourbillons) de l'écoulement turbulent sont calculés directement et seuls les mouvements à l'échelle du sous-maille (SGS) sont modélisés, et ii) des simulations numériques directes (DNS), dont les bases ont été posées par Douglas and Douglas (1972) [24] (recherches du National Center for Atmospheric Research), où aucun modèle de turbulence n'est pris en compte, ce qui signifie que toute la gamme des échelles spatiales et temporelles de la turbulence doit être résolue. LES et DNS ont ouvert de nouvelles opportunités pour simuler des écoulements de fluides avec une plus grande fidélité. Elles ont permis d'étudier des nombreux phénomènes physiques, présents dans des écoulements complexes, qui sont très difficiles à obtenir et/ou à mesurer en laboratoire, tels que : pulvérisation, atomisation, évaporation et combustion.

En ce qui concerne la science de la combustion, au cours de la première moitié du 20^{th} siècle, avec les avancées théoriques et expérimentales, de grands progrès concernant l'amélioration des moteurs Otto et Diesel ont été réalisés. En outre, le premier moteur à réaction a été introduit en 1936 par le physicien allemand Joachim Pabst

1. Par Jitze Couperus-Flickr : Supercalculateur-Les débuts, CC BY 2.0, https://commons.wikimedia.org/w/index.php?curid=19382150
2. Par Penalva-Own work, CC BY-SA 4.0, https://commons.wikimedia.org/w/index.php?curid=47918630


Figure C.3. *A gauche le supercalculateur CDC* 6600 *avec sa console, lancé en* 1964*, et à droite le supercalculateur Occigen installé par GENCI au CINES, à Montpellier ; avec lesquelles les bases de données présentées dans cette thèse ont été obtenues.*

von Ohain, lorsqu'il a conçu le premier avion à réaction opérationnel – le **Heinkel He** 178 – et seulement huit ans après, à la fin de la 2^{eme} guerre mondiale, la deutsche Luftwaffe a mis en service le premier avion de chasse à réaction, le **Messerschmitt Me** 262. Même si l'amélioration et/ou la création de nouveaux moteurs à combustion interne plus efficaces et plus fiables ont fortement stimulé le domaine de la recherche en sciences de la combustion, il est primordial de souligner qu'il n'était pas possible d'utiliser des outils CFD-DNS pour effectuer des travaux de recherche dans le domaine de la combustion jusqu'aux 1990_s ; ceci est dû au fait que dans tout processus de combustion, plusieurs phénomènes se déroulent simultanément et interagissent entre eux de manière complexe : i) cinétique chimique, ii) thermochimie, iii) transport (coefficients de diffusion moléculaire des espèces et diffusivité de la chaleur), et iv) mécanique des fluides. Ce qui – numériquement parlant – est très difficile à prendre en compte tous ensemble, donc les codes CFD qui simulent la combustion sont assez différents de ceux utilisés pour étudier les écoulements inertes.

De nos jours, pour donner la priorité à un stockage sûr et à des conditions de fonctionnement sûres, la plupart des systèmes sont basés sur une combustion diphasique non prémélangées ou partiellement prémélangées. Dans de tels cas, lorsque des régimes turbulents doivent être pris en compte, il peut être nécessaire de prendre en compte la fonction de densité de probabilité (PDF) de composition du mélange. Cependant, pour des raisons pratiques, la composition du mélange peut être caractérisée grâce à un ensemble réduit de grandeurs scalaires incluant une variable de fraction de mélange, ou traceur d'entrée de carburant ξ, dont la PDF marginale est présumée à partir de la connaissance de ses deux premiers moments en utilisant une fonction bêta. Ainsi, il semble nécessaire d'envisager une modélisation supplémentaire spécifique des équations de transport pour la variance, $\widetilde{\xi}_v = \widetilde{\xi^2} - \widetilde{\xi}^2 = \widetilde{\xi''^2}$, et la moyenne, $\widetilde{\xi}$ de la fraction de mélange, afin d'obtenir une fermeture plus fiable permettant de

mieux résoudre la combustion turbulente dans un écoulement diphasique. La quantité $\widetilde{q} = \overline{\rho q}/\overline{\rho}$ désigne la valeur de Favre ou moyenne en masse de q, tandis que $\overline{q}$ est sa moyenne d'ensemble (moyenne de Reynolds). L'équation de transport de la variance scalaire qui caractérise l'énergie des fluctuations de composition nécessite qu'une fermeture spécifique soit proposée pour la contribution du taux de dissipation scalaire turbulente (SDR), tandis que la fermeture de l'équation de transport pour la valeur moyenne de la fraction de mélange $\widetilde{\xi}$ ne pose pas de difficulté de modélisation particulière. Le SDR est défini par $\widetilde{\varepsilon}_{\xi} = \overline{\rho \mathcal{D} (\partial \xi'' / \partial x_i)(\partial \xi'' / \partial x_i)} / \overline{\rho}$ avec $\mathcal{D}$ étant la diffusivité moléculaire. Dans des conditions gazeuses standard, cette quantité est souvent représentée par une fermeture algébrique simplifiée, ce qui implique la relaxation linéaire des fluctuations scalaires $\widetilde{\varepsilon}_{\xi} = \widetilde{\xi}_v / (C_{\xi} \tau_T)$ avec τ_T une échelle de temps caractéristique de la turbulence et C_{ξ} une constante de modélisation (Gomet et al. [40]). Sa pertinence a été étudiée pour une grande variété d'écoulements gazeux, y compris les conditions associées aux écoulements à grande vitesse (Buttay et al. [9]). L'utilisation d'un tel modèle de relaxation linéaire (LRM) est assez intéressante car elle évite la considération d'une équation de transport modélisée supplémentaire pour la moyenne SDR (Gomet et al. [40]). Cependant, il est légitime de remettre en cause sa validité pour des configurations moins standard, telles que les configurations diphasiques avec transfert de masse présentées dans le manuscrit. Une telle question est légitime lorsque l'attention est tournée vers le comportement des termes d'ordre supérieur présents dans l'équation de transport du SDR, y compris le terme d'interaction turbulence-scalaire (TSI). L'analyse du terme TSI concentre déjà beaucoup d'efforts dans des conditions de turbulence incompressible, e.g., Gibson (1968) [38], Ashurst et al. (1987) [1], Ruetsch and Maxey (1991) [84], et Tsinober (2009) [104]. Il a été récemment étendu aux écoulements compressibles par Buttay et al. (2016) [9] et Boukharfane et al. (2018) [8] ; et il faut également souligner qu'il a reçu une attention considérable pour les conditions de combustion prémélangée au cours des dix dernières années, e.g., Swaminathan and Chakraborty (2007) [99], Mura et al. (2008) [65] et Chakraborty et al. (2011) [12]. Ceci contraste avec le cas des écoulements diphasiques avec transfert de masse pour lesquels l'équation de transport SDR et le terme TSI associé ont été plus rarement analysés (Bouali et al., Zhao et al. (2016, 2020) [6, 116]).

Cette thèse est composée de sept (7) chapitres et de trois (3) annexes. Il est organisé comme suit :

§2«Présentation du solveur ARCHER» ce chapitre rappelle brièvement les équations régissant les écoulements des fluides incompressibles, visqueux et évaporatifs ; ainsi que la présentation des approches numériques utilisées par le solveur

ARCHER.

§3«Initialisation et paramétrage des simulations DNS» ce chapitre présente la configuration numérique du cas de référence DNS THI et des cas d'écoulement diphasique DNS THI, suivi de la caractérisation correspondante des champs de fraction turbulente et de mélange.

§4«Analyse du champ de vitesse dans un contexte diphasique avec évaporation» ce chapitre présente la caractérisation statistique du champ de vitesse associé à l'écoulement turbulente. Dans un premier temps sont abordés les résultats concernant les fluctuations de vitesse, par exemple l'énergie cinétique turbulente ou le tenseur de contraintes de Reynolds associé, qui caractérisent les échelles énergétiques. Ensuite, l'attention est tournée vers le tenseur de gradient de vitesse (VGT), qui est pertinent pour les échelles dissipatives. Il convient de rappeler que le tenseur de gradient de vitesse $\boldsymbol{A} = \boldsymbol{\nabla} \otimes \boldsymbol{u}$ contient des informations clés sur les taux de déformation des lignes, surfaces et volumes [63]. L'évolution des caractéristiques de la turbulence est scrutée à différentes distances de l'interface, de telle sorte que la phase gazeuse soit divisée en plusieurs sous-régions selon les valeurs de la level-set G, c'est-à-dire la distance de la interface liquide-gaz. L'acquisition des statistiques procède de cette manière parce que l'interface liquide-gaz ne modifie pas seulement l'isotropie des fluctuations de vitesse mais aussi la structure dissipative (c'est-à-dire à petite échelle) du champ d'écoulement turbulent. Il est à souligner qu'en phase gazeuse, la distance à l'interface est définie de telle sorte que la valeur de level-set, G, soit négative.

§5«Analyse du champ scalaire dans un contexte diphasique avec évaporation» ce chapitre présente la caractérisation statistique du champ de fraction de mélange d'un ensemble de bases de données de simulation DNS diphasique avec transfert de masse comportant deux valeurs distinctes de la fraction volumique du liquide ϕ_ℓ. Dans la première partie, les résultats concernant le champ de mélange scalaire sont rapportés. Ensuite, l'attention est tournée vers les propriétés géométriques et les statistiques d'alignement du mélange scalaire et de la dissipation scalaire. De telles statistiques sont recueillies à différentes distances de l'interface.

§6«Analyse des équations d'évolution Lagrangienne» ce chapitre incluait la caractérisation statistique lagrangienne du champ de vitesse associé à l'écoulement turbulente. Dans un premier temps, les formalismes mathématiques des équations d'évolution Lagrangienne (LEE) et des trajectoires moyennes conditionnelles (CMT) sont présentés. Ceci est suivi d'une description détaillée de la méthodologie utilisée pour rassembler ces CMT. Cette méthodologie comprend une nouvelle considération, qui permet, pour la première fois, de scruter non seulement la direction, mais aussi l'amplitude des trajectoires calculées à partir des

termes de la LEE. Ensuite, une analyse détaillée de la dynamique lagrangienne du cas de référence THI est présentée. Enfin, l'analyse concernant les cas diphasiques THI considérant un changement de phase avec différents niveaux de fraction volumique de liquide, $\phi_\ell = 0.05$ et $\phi_\ell = 0.10$ est rapportée. L'acquisition des statistiques est regroupée à différentes distances de l'interface.

Chapitre 2. Présentation du solveur ARCHER

Le solveur massivement parallèle ARCHER[3] (qui signifie *Academic Research Code for Hydrodynamic Equations Resolution*), a été développé au laboratoire CORIA dans le but d'étudier les phénomènes impliqués dans les écoulements diphasiques, laminaires ou turbulents, incompressibles ou compressibles et avec ou sans des changements de phase. Pour mener cette recherche, ARCHER a été utilisé pour résoudre la forme incompressible tridimensionnelle des équations de Navier-Stokes. ARCHER utilise un *schéma WENO d'ordre cinq* pour les termes convectifs, un *schéma central aux différences finies d'ordre deux* pour évaluer les contributions visqueuses et de diffusion, et un *schéma de Runge-Kutta d'ordre trois* pour l'intégration temporelle. Un *algorithme multi-grille* est utilisé pour le préconditionnement de la méthode du gradient conjugué dans l'équation de Poisson. *La méthode ghost fluid (GF)* est utilisée pour les variables discontinues aux interfaces liquide/gaz et la *méthode couplée level-set/volume-of-fluid (CLSVOF)* est retenue pour assurer la conservation de la masse du système. Dans ce chapitre, les outils numériques utilisés pour générer l'ensemble de données d'écoulement diphasique avec évaporation ne sont que brièvement présentés car une présentation détaillée des méthodes et des équations résolues peut être trouvée dans les travaux de thèse de Tanguy (2004) [100], Ménard (2007) [66] et Duret (2013) [25].

La méthode couplage level-set/volume-of-fluid (CLSVOF)

L'objectif le plus important de la *méthode VOF*, pour la simulation d'écoulements diphasiques, est d'imposer la conservation de la masse. Cette méthode discrétise une

3. https://www.coria-cfd.fr/index.php/Archer

fraction volumique donnée (de gaz ou de liquide) sur le domaine de calcul, de telle sorte que la conservation de la fraction volumique est garantie lorsqu'elle est transportée par le champ de vitesse [57, 44, 81, 5]. Cependant, dans un formalisme eulérien (maillage fixe par exemple) l'approche *VOF* décrit mal la topologie de l'interface, il n'est donc pas le mieux adapté pour calculer des grandeurs caractéristiques de la surface telles que : les directions normale et tangente, comme ainsi que la courbure. De plus, les phénomènes physique mises en jeu dans un écoulement diphasique reposent sur la précision de la *méthode VOF*, tels que :

- la cassure et la coalescence induisent dans certaines régions du domaine la formation de gouttelettes ou de ligaments d'une épaisseur de l'ordre de quelques fois seulement la taille de maille typique, rendant ainsi difficile la description topologique de structures fines, et
- des sauts abrupts dans certains domaines (comme la densité ou la viscosité) peuvent empêcher le calcul dans la zone correspondante.

De plus, pour les simulations tridimensionnelles, le formalisme devient plus complexe et coûteux, puisqu'il est nécessaire d'effectuer une reconstruction de l'interface à partir de la fonction de fraction volumique, fonction scalaire discontinue utilisée pour suivre la phase liquide.

Au contraire, la *méthode level-set*, développée par Osher and Sethian (1988) [75], est basée sur une fonction scalaire continue, G, qui mesure la distance à l'interface que nous essayons d'utiliser pour décrire differentes zones dans le domaine du calcul. Une telle fonction, grâce à la résolution d'une équation de convection, permet de suivre la déformation de l'interface dans un champ de vitesse donné. Cependant, la mise en œuvre de la méthode level-set pour la simulation des écoulements diphasiques ne peut pas être directe, à cause :

- des pertes de masse qui résultent d'erreurs numériques dissipatives dans la résolution de l'équation de transport, et
- des changements importants des propriétés physiques induits par l'étalement ou le resserrement des iso-contours du champ G.

Considérant les avantages et les inconvénients offerts des deux approches *level-set* et *VOF* ; Sussman and Puckett (2000) [97] a introduit la *le couplage level-set/volume-of-fluid (CLSVOF)*, dont l'objectif principal est de profiter de la description géométrique précise de la *méthode level-set* (calcul précis de la direction normale et de la courbure) et, en même temps, de bénéficier de la conservation implicite de la masse offerte par la *méthode VOF*. Un tel couplage nécessite une procédure particulière pour recalculer la distance à l'interface à chaque pas de temps.

Méthode pondérée essentiellement non oscillant (WENO) d'ordre cinq

Comme cela a déjà été mentionné, la génération de petites gouttelettes et de ligaments minces pose un défi de discrétisation numérique, étant donné que leur description doit être optimale. Par conséquent, afin de garantir que ces régions seront bien résolues, une *méthode pondérée essentiellement non oscillant (WENO) d'ordre cinq*, proposée par Guang-Shan and Chi-Wang (1996) [43], est utilisée. La formulation *essentiellement non oscillant (ENO)* consiste à prendre en compte une combinaison des différentes approximations *ENO* possibles, de telle sorte que si l'une des approximations *ENO* est interpolée sur une discontinuité, sa contribution sera obtenir un poids minimum, puis minimiser les erreurs numériques résultantes.

Dans les différentes simulations rapportées dans cette thèse, deux types d'erreurs peuvent survenir dans le cadre de la résolution de petites gouttelettes et de ligaments minces, la première est liée à la *méthode level-set*, la seconde à la *méthode VOF* :

- la disparition de la structure d'où les pertes de masse deviennent non négligeables, et
- la fragmentation artificielle des ligaments en plusieurs filaments, avec cependant une bonne conservation de la masse.

Afin d'améliorer ces pertes de masse avec la *méthode level-set*, la procédure de lissage et de pondération est appliquée, non sur les dérivées, mais sur la variable à discrétiser puis la solution lissée est dérivée en utilisant un schéma centré. Cette forme modifiée du *schéma WENO de cinquième ordre* a été proposée par Estivalezes (2002) [30]. De telles améliorations sont également documentées dans la thèse de Tanguy (2004) [100].

Schéma de Runge-Kutta d'ordre trois

Les *méthodes de Runge-Kutta* sont une famille de méthodes itératives implicites et explicites utilisées pour la discrétisation temporelle afin d'approximer les solutions d'équations différentielles ordinaires. Ils sont largement utilisés en raison de leur bon compromis entre stabilité numérique et précision. L'ordre de la méthode donne le nombre d'étapes du schéma avec lesquelles plusieurs valeurs intermédiaires de la variable intégrée au sein d'un pas de temps seront évaluées. En augmentant le nombre de pas, la précision est également augmentée, mais cela va de pair avec un temps de calcul accru de chaque pas de temps. Dans le cadre de ce travail les simulations été réalises avec un *schéma de Runge-Kutta d'ordre trois*.

Méthode ghost fluid

Pour les simulations d'écoulements diphasiques incompressibles, la surface des discontinuités est introduite explicitement dans les équations, de sorte que le déplacement des interfaces des corps liquides est calculé au moyen de la *méthode level-set*, et les conditions de saut sont explicitement imposées en tant que contraintes supplémentaires qui dépendent des caractéristiques locales de l'interface. Grâce à cela, la *la méthode ghost fluid*, développée par Fedkiw et al. (1999) [33], permet d'étendre les variables discontinues par continuité au-delà de l'interface avant de procéder à la différentiation de celle-ci, ce qui permet à son tour d'imposer une condition de saut. Alors la dérivation de la variable étendue ne pose pas de problème puisqu'elle a été rendue différentiable grâce à l'extension par continuité.

Chapitre 3. Initialisation et paramétrage des simulations DNS

La configuration étudiée correspond à des écoulements 3D diphasiques turbulent homogène isotrope (THI) dans un domaine cubique, présentant des conditions limites périodiques. De telles simulations de l'écoulement ont été effectuées sur une maillage régulier présentant une résolution de $256 \times 256 \times 256$ points de calcul. Les propriétés physiques sont quasiment les mêmes que celles précédemment documentées dans les travaux de Duret et al. (2012) [26] et Bouali et al. (2016) [6] : la valeur de la tension superficielle est de $\sigma = 0{,}0108 kg \cdot s^{-2}$ alors que les viscosités gaz et liquide sont $\mu_g = 1.879 \times 10^{-5} kg \cdot m^{-1} \cdot s^{-1}$ et $\mu_\ell = 5.65 \times 10^{-4} kg \cdot m^{-1} \cdot s^{-1}$, respectivement. Le rapport de densité entre les deux phases ρ_ℓ / ρ_g est fixé à 30, et la fraction volumique de liquide est $\phi_\ell = V_\ell / V$, où V_{ell} désigne le volume de liquide et $V = V_\ell + V_g$ est le volume total, soit $V = L^3$ avec $L = 1.5 \times 10^{-4} m$ la longueur caractéristique du domaine de calcul. Dans la présente étude, deux valeurs différentes de la fraction volumique du liquide sont considérées : $\phi_\ell = 0.05$ et $\phi_\ell = 0.10$.

Il est à noter que la base de données générée dans le cadre de cette étude diffère de celle de Bouali et al. (2016) [6], qui considérée une turbulence décroissante. Ici les bases de données DNS correspondent à des turbulences forcées avec une valeur de l'énergie cinétique turbulente (TKE, κ) maintenue au niveau constant bas de $\kappa = 3{,}6$ $m^2 \cdot s^{-2}$. Le TKE est défini dans l'Eq. C.1.

$$\kappa = \frac{\overline{\boldsymbol{u}' \cdot \boldsymbol{u}'}}{2} \tag{C.1}$$

Les simulations actuelles ont été construites en deux étapes successives. La première consiste à générer les conditions de pulvérisation initiales à partir de simulations numériques THI statistiquement convergentes réalisées avec le même niveau de résolution mais sans aucune considération du transfert de masse. Ces simulations préliminaires d'écoulement diphasique THI sont exécutées jusqu'à ce que la convergence des moments de second ordre soit atteinte sur la base des valeurs de l'énergie cinétique turbulente normalisée ΔU, définie ci-dessous dans l'équation. C.2. Ceci est obtenu une fois que $t^+ = (t - t_0)/\tau_{T_0}$ atteint $t^+ = 12.0$ pour $\phi_\ell = 0.05$ et $t^+ = 9$ pour $\phi_\ell = 0.10$. L'évaporation est activée dans un deuxième temps et les données sont regroupées de $t^* = 0.0$ à $t^* = 6.0$ avec $t^* = (t - t_1)/\tau_{T_1}$. Dans l'expression ci-dessus, les échelles de temps turbulentes sont évaluées à partir de $\tau_{T_0} = \kappa_0/\varepsilon_0$ et $\tau_{T_1} = \kappa_1/\varepsilon_1$, respectivement, avec ε le taux de dissipation TKE. Les indices zéro et unité correspondent aux valeurs initiales et finales de la phase de convergence préliminaire, qui est conduite sans aucune considération des processus d'évaporation.

$$\Delta U = 100 \times \left(\frac{U(t) - U(t_1)}{U(t_1)} \right) \tag{C.2}$$

avec

$$U = \left(\frac{2\kappa}{3} \right)^{1/2} \tag{C.3}$$

Quelques détails techniques considérés pour mettre en place les simulations numériques sont présentés, et suivis d'analyse de la capacité du code ARCHER à simuler les écoulements diphasiques : THI, simulations d'écoulement diphasique avec ou sans évaporation. Les propriétés physiques des simulations, résumées dans le Tableau C.1 et le Tableau C.2, ont été choisisses pour se placer dans le régime de rupture secondaire d'un jet, où les interactions entre la turbulence (gaz-liquide, et liquide-liquide) – telles que la collision, la coalescence et la désintégration de grandes structures – ont lieu et peuvent être capturées avec précision. Il convient de souligner qu'un tel régime a un importance certain dans la perspective d'étude des dispositifs basée sur la combustion par pulvérisation.

La Figure C.4 montre des champs in instantanés de l'écoulement diphasique turbulent tridimensionnel avec $\phi_\ell = 10$. La surface affichée correspond à l'iso-contour $G = -2\Delta x$ de la level-set. Une telle valeur se situe dans la phase gazeuse au voisinage de l'interface liquide-gaz. L'iso-surface a été colorée par la valeur du second invariant normalisé Q_A/Q_Ω du VGT. Trois valeurs distinctes de temps normalisés

sont présentées : (a) $t^+ = 0.0$, (b) $t^* = 0.0$, et (c) $t^* = 6.0$. Nous pouvons observer que l'interface présente des niveaux importants de courbure et de plissement, qui peuvent inversement altérer le comportement du champ de turbulence, la fraction de mélange et le taux de dissipation scalaire (SDR) au voisinage de l'interface.

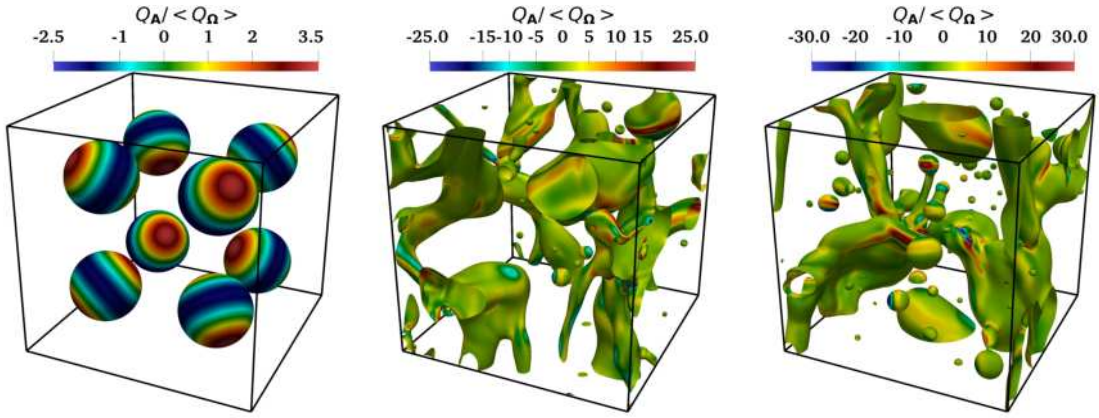

(a) $t^+ = 0.0$ **(b)** $t^+ = 0.0$ **(c)** $t^* = 6.0$

Figure C.4. *Image 3D instantanés du cas d'écoulement turbulent diphasique avec $\phi_\ell = 0.10$ à trois temps normalisés différents : (a) temps initial $(t^+ = 0.0\ right)$, (b) activation du module d'évaporation $(t^* = 0.0)$, et (c) pas de temps avec une concentration moyenne de vapeur de $\overline{\xi} = 0.56$ $(t^* = 6.0)$. Les contours affichés correspondent à la valeur level-set de $G = -2\Delta x$, qui sont colorés par le deuxième invariant Q_A normalisé par la valeur moyenne du deuxième invariant du tenseur de rotation, c'est-à-dire, $\langle Q_\Omega \rangle = \langle -\Omega_{ij}\Omega_{ji}/2 \rangle$.*

Cas	u_{RMS} (m/s)	ℓ_t (μm)	λ (μm)	η_K (μm)	Re_t (-)	Re_λ (-)	τ_{T_0} (μs)	τ_{T_1} (μs)
THI	1.55	16.71	11.03	1.18	309.2	22.7	44.6	-
$\phi_\ell = 0.05$	1.54	18.57	11.82	1.21	306.9	23.9	21.4	17.5
$\phi_\ell = 0.10$	1.47	23.30	14.26	1.33	293.0	26.1	30.8	19.9

Table C.1 – *Paramètres d'écoulement turbulent pour le cas THI de référence au temps non dimensionné $t^+ = 2.5$, et pour les deux cas évaporatifs multiphasiques avec $\phi_\ell = 0.05$ et $\phi_{ell} = 0.10$, au temps non dimensionné $t^* = 6.0$.*

Simulation	$\overline{\xi}$	We_g (-)	We_ℓ (-)	Re_ℓ (-)	Oh_ℓ (-)
$\phi_\ell = 0.05$	0.44	1.23	48.2	350	0.02
$\phi_\ell = 0.10$	0.56	1.12	72.7	430	0.02

Table C.2 – *Paramètres d'écoulement multiphasique au temps post-traité $t^* = 6.0$ pour les deux cas, $\phi_\ell = 0.05$ et $\phi_\ell = 0.10$.*

Chapitre 4. Analyse du champ de vitesse dans un contexte diphasique avec évaporation

Le chapitre présente la caractérisation statistique du champ de vitesse turbulente. Dans un premier temps sont abordés les résultats concernant les fluctuations de vitesse, par exemple l'énergie cinétique turbulente ou le tenseur de contraintes de Reynolds associé, qui caractérisent les échelles énergétiques. Ensuite, l'attention est portée sur le tenseur de gradient de vitesse (TGV), qui est pertinent pour les échelles dissipatives. Il convient de rappeler que le tenseur des gradients de vitesse $\boldsymbol{A} = \boldsymbol{\nabla} \otimes \boldsymbol{u}$ contient des informations clés sur les taux de déformation des lignes, surfaces et volumes infinitésimaux [63]. L'évolution des caractéristiques de la turbulence est analysée à différentes distances de l'interface, de telle sorte que la phase gazeuse soit divisée en plusieurs sous-régions selon les valeurs de la level-set G, c'est-à-dire la distance à l'interface liquide-gaz, comme indiqué dans le tableau C.3. L'acquisition des statistiques procède de cette manière parce que l'interface liquide-gaz modifie non seulement l'isotropie des fluctuations de vitesse, mais aussi les structures dissipatives (c'est-à-dire à petite échelle) du champ d'écoulement turbulent. Il est à souligner qu'en phase gazeuse, la distance à l'interface est définie de telle sorte que la valeur de level-set, G, soit négative.

région en phase gazeuse	plage de valeurs level-set
lointain [♦]	$G \leq -20\Delta x$
intermédiaire [■]	$-20\Delta x < G \leq -5\Delta x$
proche [●]	$-5\Delta x < G \leq 0.0$

Table C.3 – *Définition de trois sous-régions en phase gazeuse sur la base de la valeur level-set.*

D'un point de vue général, de telles investigations de topologies à petite échelle dans des écoulements comportant des fronts ou des interfaces restent plutôt rares par rapport à la quantité d'analyses menées dans des conditions d'écoulement turbulent incompressible plus standard. Certaines analyses de ce type n'ont été menées que très récemment pour les interactions choc-turbulence multi-espèces à densité variable (Tian et al. [101]) et les configurations THI en décroissance chargées de gouttelettes (Dodd and Jofre [23]). A cet égard, il semble intéressant de présenter une analyse consacrée à la dynamique des plus petites échelles dans les écoulements diphasiques turbulents s'évaporant. Dans ce chapitre, l'attention se concentre sur le champ turbulent gazeux, qui est subdivisé en différentes sous-régions en fonction des valeurs de niveau (G). Tout d'abord, dans la Figure C.5 l'évolution de la topologie de l'écoulement turbulent est inspectée lorsque la valeur de level-set, G, tend vers zéro. Les invariants normalisés

ξ^* et η^* du tenseur d'anisotropie des contraintes de Reynolds $\boldsymbol{b}$ confirment qu'à mesure que l'on s'approche de l'interface liquide-gaz, l'anisotropie de la turbulence est significativement augmentée, de sorte qu'une évolution progressive se produit depuis de l'état de turbulence isotrope à l'état de turbulence unidimensionnel.

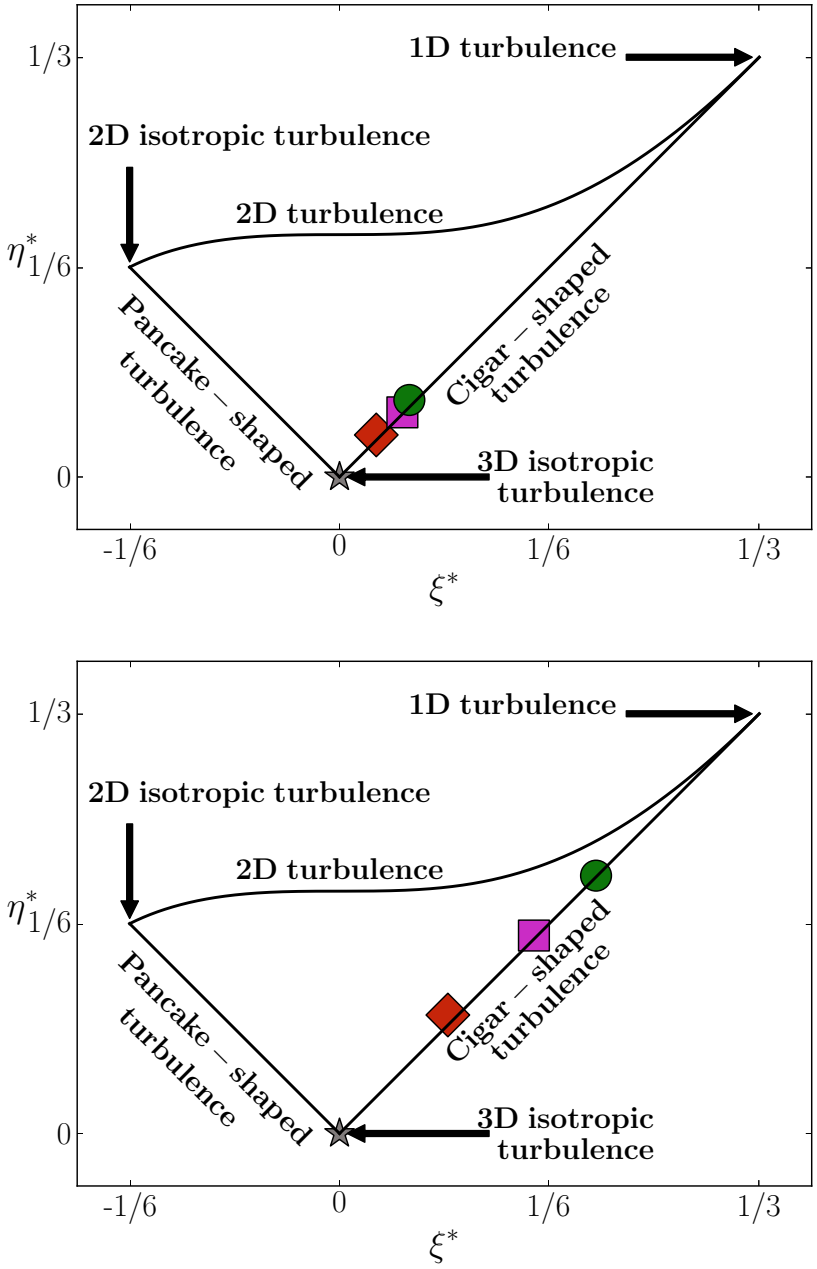

Figure C.5. *Anisotropie de la turbulence telle que représentée dans le triangle de Lumley pour $\phi_\ell = 0{,}05$ (en haut) et $\phi_\ell = 0{,}10$ (en bas). Les symboles [♦, ■, et ●] correspondent aux comportements moyennés observés dans les régions lointain, intermédiaire et proche de l'interface liquide-gaz, respectivement. Le symbole [★] correspond à un cas THI de référence en conditions gazeuses. Les invariants sont définis comme suit : $6\,(\eta^*)^2 = b_{ij}b_{ji}$ et $6\,(\xi^*)^3 = b_{ij}b_{jk}b_{ki}$.*

Ensuite, dans les Figures C.6 et C.7, il est montré que la topologie à petite échelle de l'écoulement turbulent est également significativement altérée au voisinage de l'interface liquide-gaz, comme le montrent les iso-lignes dans le plan du phase (R_A^*, Q_A^*), où Q_A^* et R_A^* sont respectivement les deuxième et troisième invariants du tenseur de gradient de vitesse (VGT). Dans la région éloignée, la forme classique de larme – à des niveaux de probabilité significatifs associée au le premier et du deuxième quadrants Q_1, et Q_2, du plan de phase (R_A^*, Q_A^*) – est retrouvée. Cependant, à mesure que l'on s'approche de l'interface liquide-gaz, il y a une augmentation significative des niveaux de probabilité associés au troisième quadrant Q_3, c'est-à-dire la topologie SN/S/S. En conséquence, les niveaux de probabilité du premier quadrant, Q_1, et du deuxième, Q_2, ont tendance à devenir similaires, et il y a une diminution des niveaux de probabilité relatifs au quatrième, Q_4, qui va de pair avec une plus grande dispersion des données correspondantes.

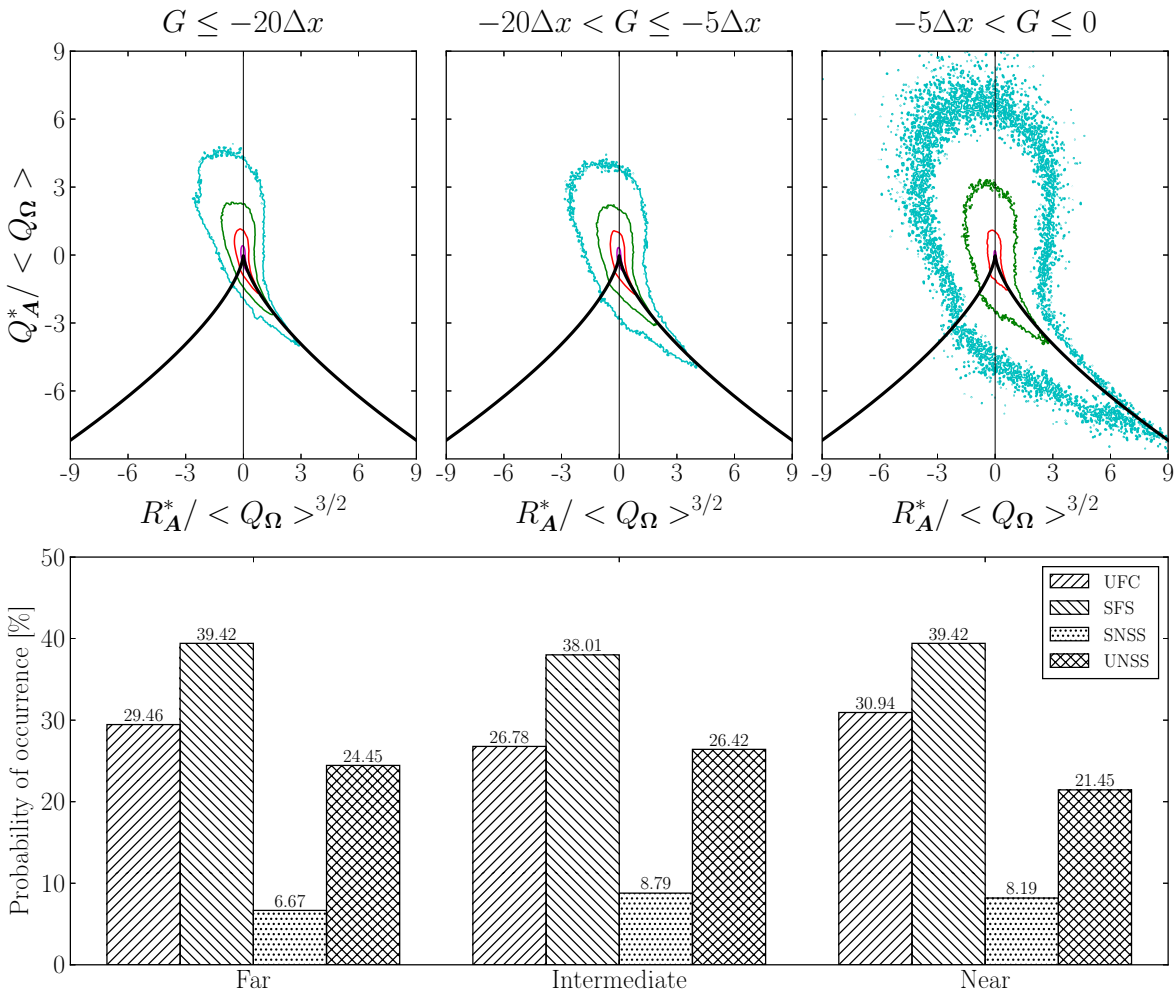

Figure C.6. *JPDF de (R^*_A, Q^*_A) dans les régions de champ lointain (gauche), intermédiaire (centre) et proche (droite) ainsi que la probabilité d'occurrence de chacun quadrant de topologie pour $\phi_\ell = 0.05$. Les quatre lignes fines correspondent aux iso-contours de $\log_{10}$ (JPDF) égaux à -3 -2, -1 et 0. Les deux invariants Q^*_A et R^*_A sont normalisés par la valeur moyenne du deuxième invariant du tenseur de rotation, soit $\langle Q_{Omega} \rangle = \langle -\mathbf{\Omega} \cdot \mathbf{\Omega}/2 \rangle$.*

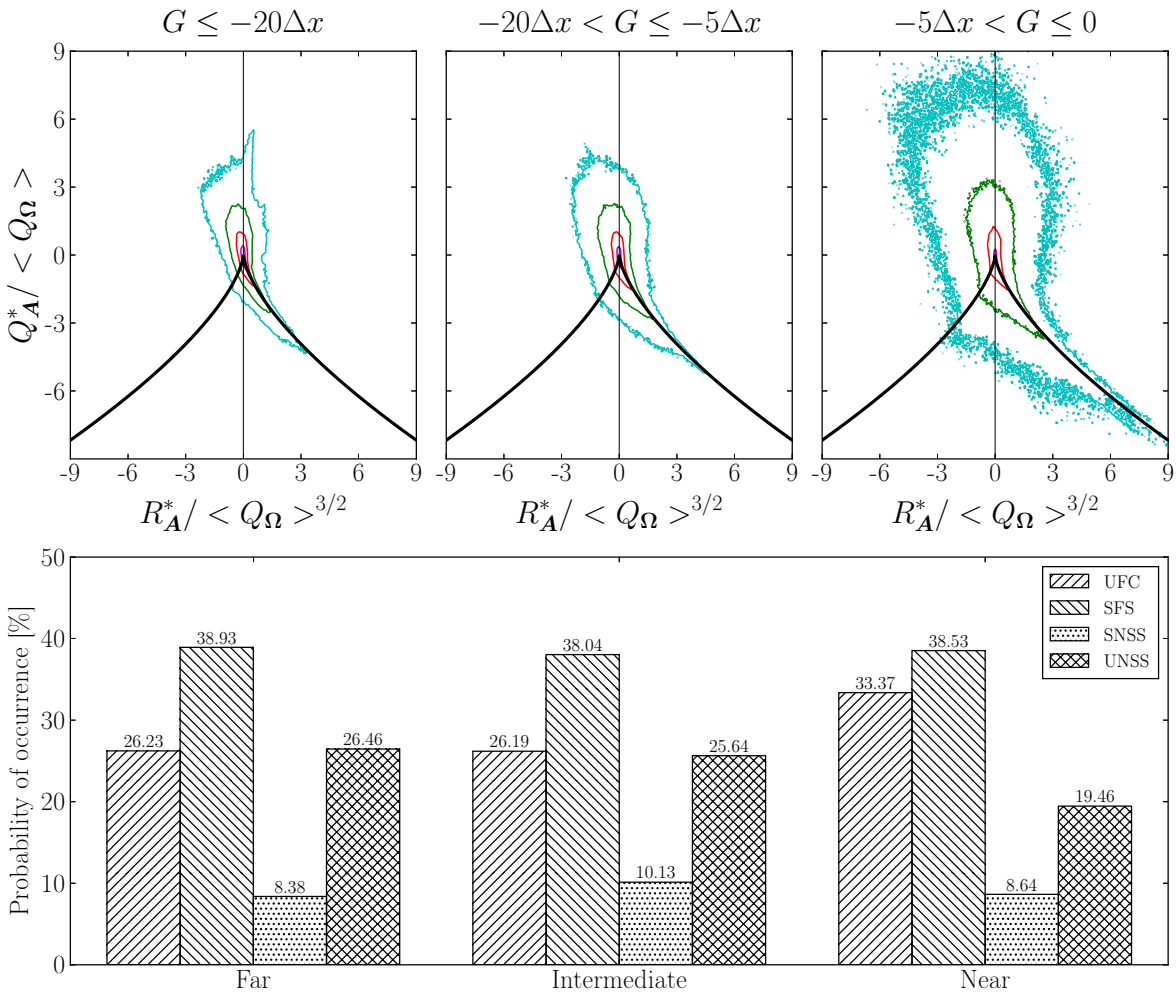

Figure C.7. *JPDF de (R^*_A, Q^*_A) dans les régions de champ lointain (gauche), intermédiaire (centre) et proche (droite) ainsi que la probabilité d'occurrence de chacun quadrant de topologie pour $\phi_\ell = 0.10$. Les quatre lignes fines correspondent aux iso-contours de* $\log_{10}$ *(JPDF) égaux à -3 -2, -1 et 0. Les deux invariants Q^*_A et R^*_A sont normalisés par la valeur moyenne du deuxième invariant du tenseur de rotation, soit $\langle Q_{Omega} \rangle = \langle -\mathbf{\Omega} \cdot \mathbf{\Omega}/2 \rangle$.*

Les statistiques du tenseur de vitesse de déformation $\boldsymbol{S}$ et du tenseur de rotation $\mathbf{\Omega}$ sont ensuite étudiées pour mieux comprendre l'évolution de la topologie de l'écoulement à mesure que l'interface liquide-gaz est approchée. L'analyse correspondante met en évidence la dominance des structures en nappes vortex au voisinage direct de l'interface. Cette analyse se termine par une inspection détaillée des caractéristiques géométriques et des statistiques d'alignement. Elle montre que l'alignement préférentiel du vecteur tourbillon avec la direction principale intermédiaire $\boldsymbol{e}_2$ est significativement amplifié au voisinage de l'interface, ce qui reflète l'amélioration du transfert et des processus d'étirement tourbillonnaire associés. Enfin, la présence du liquide pouvant altérer préférentiellement la composante des tenseurs de rotation et

de contrainte de déformation dans la direction normale à l'interface liquide-gaz, on peut s'attendre à une augmentation de la corrélation entre les deux grandeurs, ce qui est en effet confirmé sans ambiguïté par l'étude de l'angle déformation-enstrophie Γ à l'approche de l'interface.

Chapitre 5. Analyse du champ scalaire dans un contexte diphasique avec évaporation

Le chapitre présente la caractérisation statistique du champ de fraction de mélange à partir d'un ensemble de bases de données de simulation DNS multiphasique avec évaporation par deux valeurs distinctes de la fraction volumique du liquide ϕ_ℓ. Dans la première partie, les résultats concernant le champ scalaire de mélange sont présentés. Ensuite, l'attention se porte sur les propriétés géométriques et les statistiques d'alignement du mélange scalaire et de la dissipation scalaire. De telles statistiques sont recueillies à différentes distances de l'interface, de telle sorte que la phase gazeuse soit divisée en plusieurs sous-régions selon les valeurs de la level-set G, c'est-à-dire la distance de l'interface liquide-gaz, comme indiqué dans le tableau C.3.

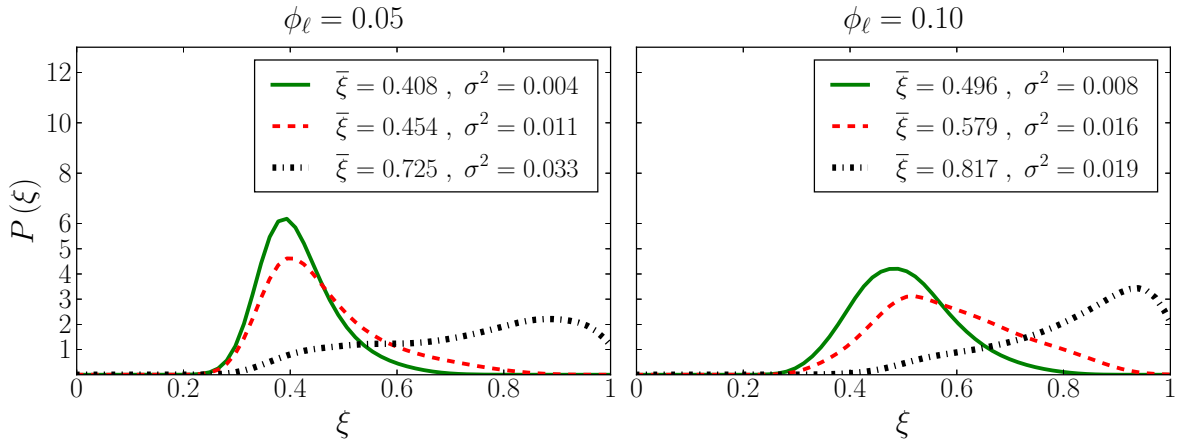

Figure C.8. *PDF de la fraction de mélange ξ dans les régions éloignées (——), intermédiaires (- - -) et proches (-·-·) de l'interface liquide-gaz pour $\phi_\ell = 0.05$ (gauche) et $\phi_\ell = 0.10$ (droite). Les valeurs de moyenne et de variance correspondantes sont également reportées pour chaque condition et région.*

Le champ de fraction de mélange est examiné de manière exhaustive. Dans une première étape, le champ scalaire, ainsi que son gradient et son taux de dissipation, sont inspectés sur la base de certaines propriétés géométriques et statistiques d'alignement du champ scalaire. La concentration moyenne de la fraction de mélange, $\overline{\xi}$, et les niveaux de variance correspondants sont plus petits à mesure que les régions plus

éloignées de l'interface liquide-gaz sont considérées (voir Fig. C.8). Les composantes du gradient scalaire, g^{ξ}, sont étudiées dans deux référentiels différents : i) le référentiel standard, c'est-à-dire $\boldsymbol{R_x}$, et ii) un autre *attaché* à l'interface liquide-gaz $\boldsymbol{R_G}$. Dans le premier repère de référence, il est mis en évidence que le taux de mélange moléculaire et le SDR augmentent à mesure que l'interface est approchée, et dans le second il est confirmé que dans la région éloignée la fraction de mélange est presque homogène, mais lorsque l'interface est approchée, les niveaux de variance croissent, notamment celui correspondant à l'orientation alignée avec le vecteur normal unitaire, $\boldsymbol{n}$ (voir Fig. C.8).

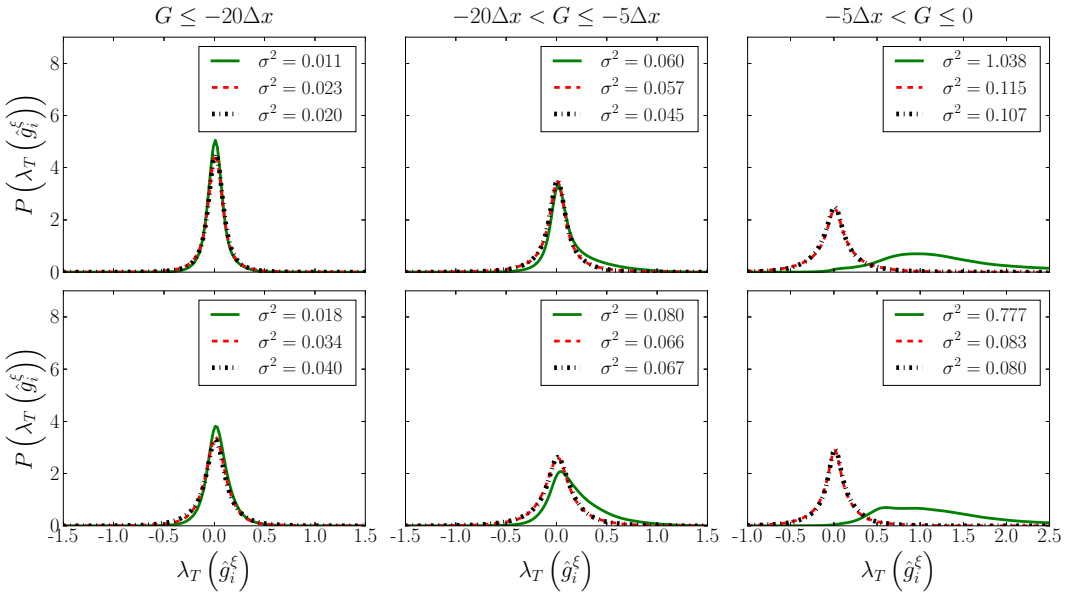

Figure C.9. *PDF des trois composantes du gradient scalaire projeté sur le référentiel local attaché à la level-set $\hat{g}_i^{\xi}$. (——) : projection suivant la direction normale $\boldsymbol{n}$, (- - -) : projection suivant la première direction tangentielle $\boldsymbol{\tau}_1$, et (-·-·-) : projection suivant la deuxième direction tangentielle $\boldsymbol{\tau}_2$. Les résultats sont rassemblés dans les régions éloignées (à gauche), intermédiaires (au centre) et proches (à droite) de l'interface liquide-gaz et pour $\phi_\ell = 0.05$ (en haut) et $\phi_\ell = 0.10$ (en bas). Les valeurs sont normalisées par l'échelle de longueur de Taylor λ_T.*

Une telle orientation devient asymétrique (positivement) au voisinage de l'interface. Dans cette région, l'orientation du gradient scalaire est préférentiellement alignée sur $\boldsymbol{n}$. D'une part, l'asymétrie, S_{N_ξ}, et le kurtosis, E_{N_ξ}, du SDR affichent un comportement intermittent avec leur valeur maximale correspondante au voisinage de l'interface et, en même temps, un excès positif d'aplatissement. D'autre part, la logarithmique standardisée du SDR, X, présente des PDF qui sont toujours négativement asymétriques et dont les valeurs diminuent à mesure que l'interface liquide-gaz est approchée, tandis qu'un excès négatif de kurtosis est présenté dans les régions éloignées et intermédiaires (pour le cas de 5% de fraction volumique de liquide), et

d'aplatissement leptokurtique partout ailleurs. Ensuite, l'attention se concentre sur les termes de la STI, leurs contributions et quelques autres statistiques pertinentes pour le domaine de la fraction de mélange. L'orientation entre le gradient scalaire, $\boldsymbol{n}_{\tilde{\xi}}$, et les directions principales du tenseur de vitesse de déformation, $\boldsymbol{e}_i$, présente une transition depuis l'alignement préférentiel avec le vecteur propre qui contribue à la production de SDR dans la région lointaine, en étant préférentiellement aligné avec les deux vecteurs propres qui produisent et dissipent le SDR, et largement désaligné avec le vecteur propre intermédiaire, au voisinage de l'interface liquide-gaz. A cet égard, le produit entre les cosinus d'orientation élevés au carré et les valeurs propres normalisées, $\lambda_i^* \cos^2\left(\boldsymbol{n}_{\tilde{\xi}}, \boldsymbol{e}_i\right)$, confirme que le terme TSI est un terme de production dans toute la phase gazeuse. Leur terme de production scalaire normalisé correspondant, B^*, montre qu'en raison des mécanismes d'étirement, le TSI amplifie continuellement le SDR. L'orientation entre gradient scalaire et tourbillon, $\boldsymbol{\omega}$, affiche une prédilection de désalignement entre eux qui augmente à mesure que l'on s'approche de l'interface. Le JPDF des magnitudes normalisées du tourbillon, $||\,\boldsymbol{\omega}\,||$, et du gradient scalaire, $||\,\boldsymbol{g}^{\tilde{\xi}}\,||$, confirme qu'ils sont statistiquement indépendants. L'orientation entre le gradient scalaire et le vecteur d'étirement scalaire, $\boldsymbol{W}^{\tilde{\xi}}$, ainsi qu'entre la contribution du vecteur d'étirement scalaire associée à la production/destruction de la norme du gradient scalaire, $\boldsymbol{W}^{\tilde{\xi}s}$, dévoilent exactement le même comportement de diminution des alignements qu'une région plus proche de l'interface liquide-gaz est considérée. L'angle déformation-enstrophie, Γ, montre qu'un mélange scalaire intense coïncide avec des régions de dominance de déformation dans tout le domaine gazeux sauf près de l'interface, où une forte corrélation entre déformation et rotation est trouvée (voir Fig. C.10).

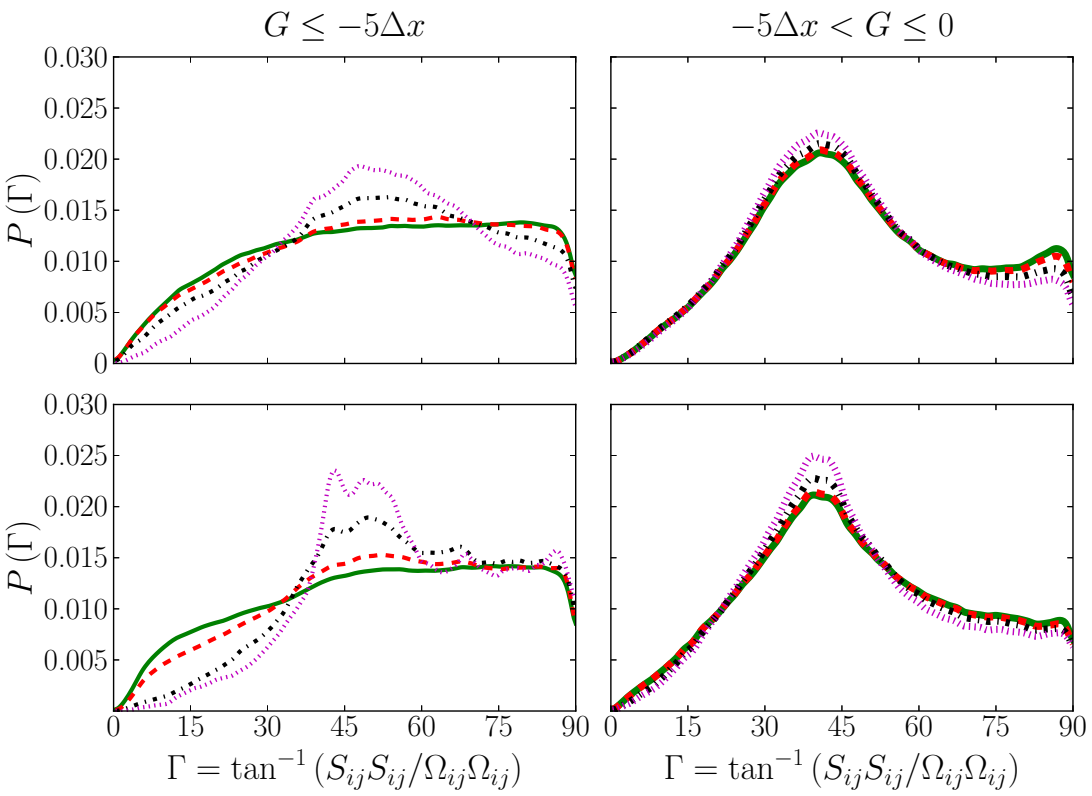

Figure C.10. *PDF de l'angle déformation-enstrophie* $\mathbf{\Gamma}$ *conditionné pour quatre valeurs seuils : 0,25* $\overline{||g^{\zeta}||}$ *(—), 0,5*$\overline{||g^{\zeta}||}$ *(- - -), 1.0*$\overline{||g^{\zeta}||}$ *(-·-·), et 1.5*$\overline{||g^{\zeta}||}$ *(·····); dans les régions* $G <\leq -5\Delta x$ *(loin+intermédiaire, gauche) et proche (droite) de l'interface liquide-gaz pour* $\phi_\ell = 0.05$ *(haut) et* $\phi_\ell = 0.10$ *(en bas).*

La JPDF entre l'amplitude normalisée du gradient scalaire et la valeur propre du taux de déformation intermédiaire normalisé, $\mathbf{\Lambda}_2$, montre que les régions présentant un SDR intense sont associées à un champ de déformation formant des feuillets. Enfin, la PDF conditionnelle de la valeur propre de vitesse de déformation intermédiaire normalisée met en évidence qu'un mélange scalaire intense est corrélé à de grandes valeurs de la valeur propre intermédiaire normalisée, un tel comportement est atténué à mesure que l'interface liquide-gaz est approchée.

Chapitre 6. Analyse des équations d'évolution Lagrangienne

Le chapitre comprends la caractérisation statistique lagrangienne du champ de vitesse turbulente. Tout d'abord, les formalismes mathématiques des équations d'évolution lagrangiennes et des trajectoires moyennes conditionnelles (CMT) sont présentés, suivis d'une explication détaillée de la méthodologie employée pour rassembler ces CMT. Cette méthodologie compte avec une nouvelle considération, qui permet

pour la première fois, d'étudier non seulement la direction, mais aussi l'ampleur des trajectoires calculées à partir des termes de la LEE. Ensuite, une inspection détaillée de la dynamique lagrangienne du cas de référence THI est présentée. Enfin, l'analyse concernant les cas multiphasiques présentant une évaporation avec différents niveaux de fraction volumique de liquide, $\phi_\ell = 0.05$ et $\phi_\ell = 0.10$ est rapportée. L'acquisition des statistiques est regroupée à différentes distances de l'interface, de sorte que la phase gazeuse est divisée en plusieurs sous-régions selon les valeurs de la level-set G, c'est-à-dire la distance au liquide/ interface de gaz, comme indiqué dans le tableau C.4. Il est à noter qu'en phase gazeuse, la distance à l'interface est définie de telle sorte que la valeur de level-set, G, soit négative.

région en phase gazeuse	plage de valeurs level-set
lointain	$G \leq -20\Delta x$
intermédiaire	$-20\Delta x < G \leq -7\Delta x$
proche	$-7\Delta x < G \leq -2\Delta x$

Table C.4 – *Définition de trois sous-régions en phase gazeuse à partir de la valeur level-set G.*

Par souci de concision et afin d'éviter de nombreuses répétitions, seulement l'étude du cas diphasique $\phi_\ell = 0.10$ est brièvement rapporté dans les Figures C.11 et C.12, qui sont brièvement décrits dans le paragraphe suivant.

L'évolution de la dynamique topologique locale turbulente est analysée dans les différentes sous-régions gazeuses du champ (décrites en fonction de la variable level-set), en rassemblant dans un post-process les équations d'évolution lagrangienne des invariants VGT. Dans une première étape sont brièvement abordés les formalismes mathématiques des équations d'évolution lagrangienne (LEE) – sous leur forme compressible – et des trajectoires moyennes conditionnelles (CMT). Ils sont suivis par l'explication de la méthodologie de calcul d'échelle proposée dans ce travail qui permet, pour la première fois, de comparer non seulement l'orientation, mais aussi l'ampleur de tous les termes de la LEE entre eux. Ensuite, une analyse détaillée du cas de référence THI est présentée, dans laquelle l'interaction entre les invariants de vitesse $\left(\mathcal{I}_{(R_A^*,Q_A^*)}\right)$, contribution du Hessien de pression $\left(\mathcal{II}_{(R_A^*,Q_A^*)}\right)$, la contribution visqueuse $\left(\mathcal{III}_{(R_A^*,Q_A^*)}\right)$, la contribution totale $\left((\mathcal{I}+\mathcal{II}+\mathcal{III})_{(R_A^*,Q_A^*)}\right)$ sont scrutés. La comparaison de la grandeur, de la direction et du sens de la dynamique topologique locale de toutes les contributions, $(\mathcal{I}$, $\mathcal{II}$, et $\mathcal{III})_{(\dot{R}_A^*,\dot{Q}_A^*)}$, met en évidence que les trajectoires de rotation dans le sens horaire provient principalement de l'interaction mutuelle des invariants $\left(\mathcal{I}_{(R_A^*,Q_A^*)}\right)$, et de la contribution Hessienne

de pression $\left(\mathcal{II}_{\left(R_A^*,Q_A^*\right)}\right)$, donc la contribution Hessienne de pression est ensuite examinée plus en détail en la divisant en ses parties isotrope et anisotrope, qui pilotent le $\left(\mathcal{II}^{local}\right)$ et les effets non locaux $\left(\mathcal{II}^{nonlocal}\right)$, respectivement. Une telle décomposition permet de remarquer que c'est la contribution de la pression non locale qui pilote principalement la dynamique. Enfin, les cas diphasiques THI présentant une évaporation, pour les deux fractions volumiques de liquide, $\phi_\ell = 0.05$ et $\phi_\ell = 0.10$, sont rapportés. Les statistiques de tels cas sont rassemblées à différentes distances, en divisant la phase gazeuse en plusieurs sous-régions selon les valeurs de la level-set G. Les statistiques de ces cas THI diphasiques sont minutieusement étudiés en analysant, les deux cas ensemble, et chacun des termes du LEE dans chaque sous-région gazeuse. En ce qui concerne l'interaction entre les invariants de vitesse $\left(\mathcal{I}_{\left(R_A^*,Q_A^*\right)}\right)$, la dynamique topologique locale montre le même comportement, même au voisinage de l'interface liquide-gaz. L'échelle du vecteur $\Sigma_{\mathcal{I}_{\left(\dot{R}_A^*,\dot{Q}_A^*\right)}}$ augmente légèrement à mesure que l'on s'approche de l'interface. La contribution du Hessienne de pression $\left(\mathcal{II}_{\left(R_A^*,Q_A^*\right)}\ right\right)$ affiche de grands changements dans sa dynamique topologique locale à mesure que l'on s'approche de l'interface liquide-gaz, ainsi qu'un grand incrément dans son vecteur d'échelle $\Sigma_{\mathcal{II}_{\left(\dot{R}_A^*,\dot{Q}_A^*\right)}}$. La contribution Hessienne de pression non locale $\left(\mathcal{II}^{nonlocal}\right)$ reste celle qui pilote la dynamique du Hessienne de pression. La contribution visqueuse $\left(\mathcal{III}_{\left(R_A^*,Q_A^*\right)}\right)$ montre une forte augmentation de son échelle du vecteur $\Sigma_{\mathcal{III}_{\left(\dot{R}_A^*,\dot{Q}_A^*\right)}}$ lorsque l'interface liquide-gaz est approchée : la valeur dans la région proche est plus du double de la valeur obtenue dans les régions de champ intermédiaire ou lointain. Enfin, la contribution totale $\left((\mathcal{I}+\mathcal{II}+\mathcal{III})_{\left(R_A^*,Q_A^*\right)}\right)$ est présentée, où il est mis en évidence que la contribution de la pression Hessienne augmente son influence sur la dynamique topologique locale totale au voisinage de liquide-interface gaz.

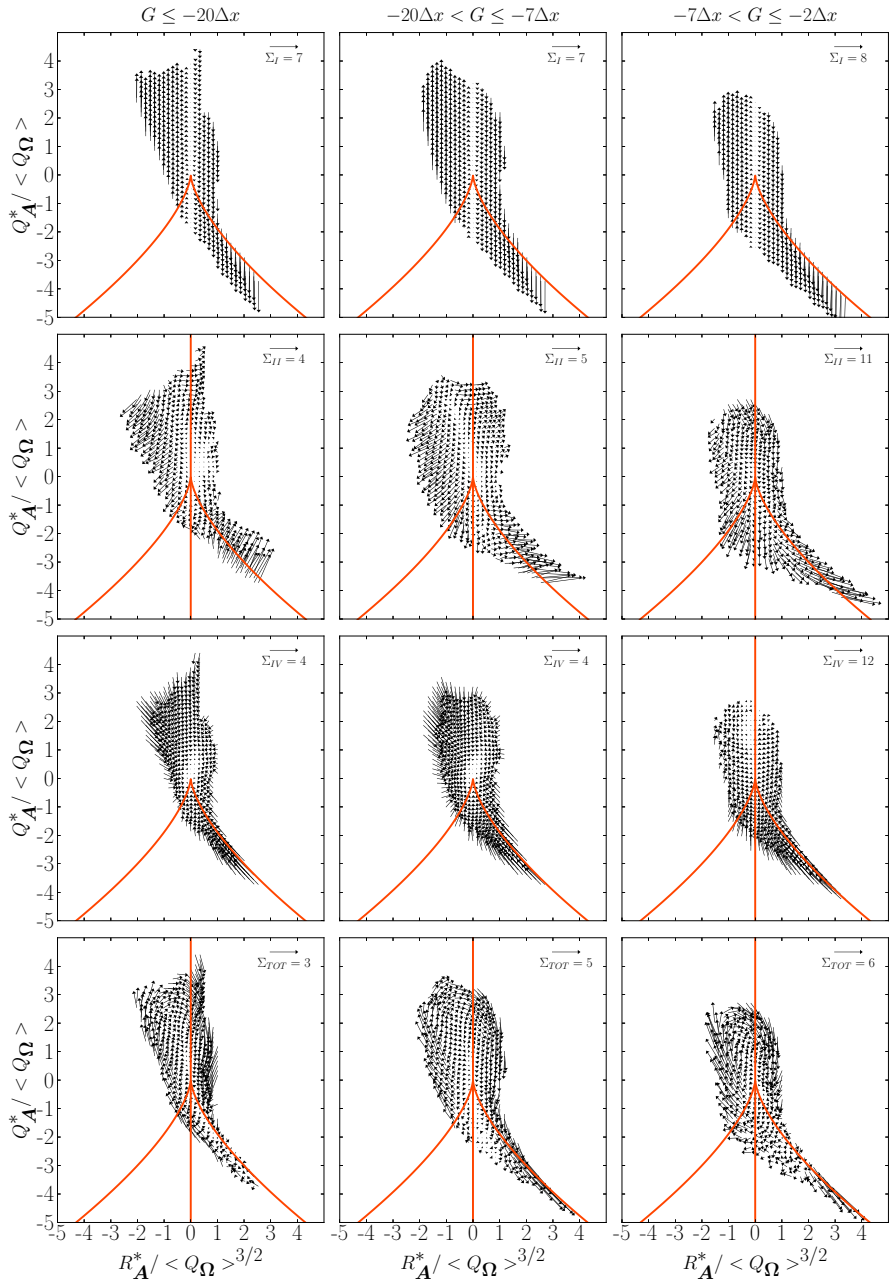

Figure C.11. *CMT du LEE dans la région éloignée (colonne de gauche), intermédiaire (colonne du milieu) et proche (colonne de gauche) dans le plan de phase* (R_A^*, Q_A^*) *pour le cas multiphasique avec* $\phi_\ell = 0.10$. *Les termes des équations d'évolution présentées correspondent à* $I_{(R_A^*, Q_A^*)}$ *: interaction entre les invariants de vitesse (première ligne);* $II_{(R_A^*, Q_A^*)}$ *: contribution de la pression (deuxième rangée);* $\mathrm{IV}_{(R_A^*, Q_A^*)}$ *: contribution visqueuse (troisième rangée); et* $(\mathrm{I} + \mathrm{II} + \mathrm{IV})_{(R_A^*, Q_A^* \text{ droite})}$ *: contribution totale (quatrième rangée). L'échelle du vecteur de chaque terme est calculée en fonction de la longueur moyenne du vecteur* $\left(\overline{X_{\langle \dot{R}^*, \dot{Q}^* \rangle}} = \left|\left| \sqrt{\left(\dot{R}_A^*\right)^2 + \left(\dot{Q}_A^*\right)^2} \right|\right|\right)$ *et son écart type correspondant* $\left(\sigma_{\langle \dot{R}^*, \dot{Q}^* \rangle}\right)$ *comme suit :* $\Sigma term = \overline{X_{\langle \dot{R}^*, \dot{Q}^* \rangle}} + 3\sigma_{\langle \dot{R}^*, \dot{Q}^* \rangle}$.

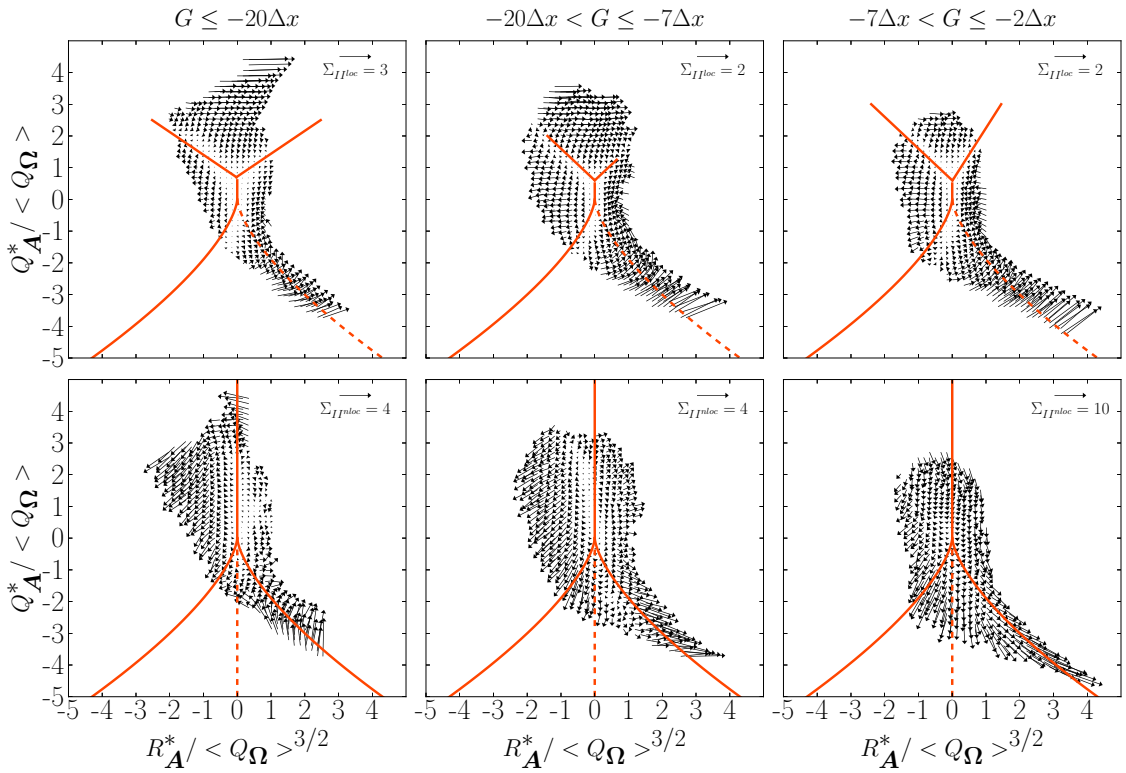

Figure C.12. *CMT du LEE dans la région éloignée (colonne de gauche), intermédiaire (colonne du milieu) et proche (colonne de gauche) dans le plan de phase* (R^*_A, Q^*_A) *pour le cas multiphasique avec* $\phi_\ell = 0.10$. *Les termes des équations d'évolution présentées correspondent à* Π^{local} *: pression locale contribution Hessienne (rangée du haut) ; et* $\Pi^{nonlocal}$ *: contribution Hessienne de pression non locale (rangée du bas). L'échelle du vecteur de chaque terme est calculée en fonction de la longueur moyenne du vecteur* $\left(\overline{X_{\langle \dot{R}^*, \dot{Q}^* \rangle}} = \left|\left| \sqrt{\left(\dot{R}^*_A\right)^2 + \left(\dot{Q}^*_A\right)^2} \right|\right|\right)$ *et son écart type correspondant* $\left(\sigma_{\langle \dot{R}^*, \dot{Q}^* \rangle}\right)$ *comme suit :* $\Sigma term = \overline{X_{\langle \dot{R}^*, \dot{Q}^* \rangle}} + 3\sigma_{\langle \dot{R}^*, \dot{Q}^* \rangle}$.

Chapitre 7. Conclusion et perspectives

Ce travail de thèse a été réalisé à l'Institut Pprime UPR 3346 CNRS - ENSMA, et il a été soutenu financièrement par le programme **CONACyT-Gouvernement Français** par le biais de la bourse n°622998. La réalisation des bases de données numériques a été rendue possible grâce à l'accès accordé aux ressources HPC de GENCI-[CCRT | CINES | OCCIGEN] sous l'allocation DARI A0052B07456. Ce travail vise à approfondir la compréhension de la physique sous-jacente du mélange turbulent dans des écoulements diphasiques en présence d'évaporation, afin d'améliorer les performances de combustion.

Dans un premier temps, un bref rappel de l'importance de la mécanique des fluides et de la science de la combustion dans le développement du genre humain a été fait.

Ensuite, une introduction générale à la dynamique des fluides numérique (CFD) a été présentée, afin de se concentrer sur les défis réels des simulations numériques directes (DNS) des écoulements de mélange turbulents multiphasiques. Ces défis nécessitent de prendre en compte la simulation précise de : la rupture du jet, l'atomisation (régimes dense, dilué et très dilué) et le mélange des vapeurs. Ceci est suivi d'un bref compte rendu des travaux numériques récents consacrés à la modélisation du taux de dissipation scalaire (SDR), et en particulier des efforts déployés dans l'étude du terme d'interaction turbulente-scalaire (TSI).

Le solveur massivement parallèle utilisé pour générer les bases de données DNS est ARCHER, (qui signifie *Academic Research Code for Hydrodynamic Equations Resolution*). ARCHER résout la forme incompressible tridimensionnelle des équations de Navier-Stokes en utilisant la méthode *coupled level-set/volume-of-fluid (CLSVOF)* combinée avec un algorithme de projection incompressible. Les dérivées spatiales des termes convectifs sont évaluées à l'aide du *schéma WENO précis au cinquième ordre*, tandis que les termes de flux moléculaires sont calculés à l'aide d'un *schéma centré aux différences finies de second ordre*. L'intégration temporelle est effectuée en utilisant un *schéma de Runge-Kutta d'ordre 3*. Au centre des cellules sont définies les variables scalaires, telle que la pression. Le préconditionnement de la méthode du gradient conjugué dans l'équation de Poisson est réglé par un *algorithme de projection multigrille du premier ordre*, et à l'interface liquide-gaz, les conditions de saut sont imposées par le *la méthode ghost fluid (GF)*. En ce qui concerne le suivi d'interface, une *méthode couplée level-set/volume-of-fluid (CLSVOF)* est utilisée, afin de profiter à la fois des stratégies level-set et VOF : la perte de masse est limitée par l'utilisation de la méthode VOF et une description détaillée de l'interface est assurée dans le cadre de la méthode level-set. La turbulence est maintenue par une méthode de forçage linéaire. Le choix du forçage linéaire a été fait pour sa simplicité et en raison du manque d'études approfondies dédiées aux méthodes de forçage DNS appliquées aux écoulements diphasiques. La fraction de mélange est définie en supposant un équilibre thermodynamique local, de sorte que la fraction massique de combustible évaporée à l'interface liquide-gaz peut être déterminée à partir de la loi de Clausius-Clapeyron. L'évolution du champ de fraction de mélange est rassemblée en employant les mêmes schémas numériques que ceux utilises pour résoudre l'équation de la quantité de mouvement, mais au voisinage de l'interface l'évaluation des dérivées spatiales est basée sur des valeurs fantômes déduites de la *Méthode d'extension Aslam*.

Les domaines de calcul retenus correspondent à des écoulements diphasiques se développant dans un cube de turbulence isotrope homogène (THI) tridimensionnel présentant des conditions aux limites périodiques et une turbulence forcée avec une

valeur de l'énergie cinétique turbulente fixé à 3.6 $m^2 \cdot s^{-2}$. On a considéré deux niveaux de fraction volumique de liquide différents, $\phi_\ell = 0.05$ et $\phi_\ell = 0.10$. Les simulations ont été effectuées sur des maillages réguliers présentant une résolution de $256 \times 256 \times 256$ points de calcul. Ensuite, la caractérisation des champs turbulents et scalaires du cas de référence THI, et les cas d'écoulement multiphasique avec ou sans évaporation, ont été présentés, afin de confirmer la capacité de ARCHER à simuler avec précision ce type de conditions.

La caractérisation statistique du champ de vitesse turbulent a été rapportée en divisant la phase gazeuse en sous-régions en fonction du level-set. Premièrement, nous avons abordé l'évolution de la topologie des échelles énergétiques de l'écoulement turbulent, à travers les invariants normalisés ξ^* et η^* du tenseur d'anisotropie des contraintes de Reynolds $\boldsymbol{b}$. Ensuite, une analyse détaillée de la topologie à petite échelle de l'écoulement turbulent a été rapportée. Une telle analyse associées dans le plan des invariants consiste à scruter le tenseur de gradient de vitesse, en inspectant les topologies locales. L'analyse du champ de vitesse turbulente se conduit par une inspection détaillée des caractéristiques géométriques et des statistiques d'alignement des quantités pertinentes de la turbulence, telles que le vecteur de tourbillon et l'angle déformation-enstrophie.

La caractérisation statistique du champ de fraction de mélange s'appuie sur l'analyse de certaines propriétés géométriques et statistiques d'alignement du champ scalaire, ainsi que son gradient et son taux de dissipation. Ensuite, l'attention est concentrée sur les termes TSI, leurs contributions et quelques autres statistiques pertinentes pour le champ de fraction de mélange, comme l'orientation entre les directions principales, du tenseur de vitesse de déformation du gradient scalaire et du vecteur vorticité, ainsi que les JPDF correspondantes (amplitudes normalisées du tourbillon et du gradient scalaire, et l'amplitude normalisée du gradient scalaire, et la valeur propre de la vitesse de déformation intermédiaire normalisée).

Le dernier chapitre est consacré à la caractérisation statistique lagrangienne du champ de vitesse turbulente. Tout d'abord sont brièvement abordés les formalismes mathématiques des équations d'évolution lagrangiennes (LEE) – sous leur forme à densité variable –, et des trajectoires moyennes conditionnelles (CMT). Ensuite, le cas de référence THI est rapporté et comparé à certaines études lagrangiennes rassemblées pour une variété de configurations d'écoulement. Enfin, les deux cas d'écoulement diphasique THI ont été minutieusement examinés en analysant les différents termes du LEE dans chaque sous-région gazeuse.

Les perspectives et les travaux futurs liés à la présente étude pourraient consister

à générer d'autres ensembles de données, le premier correspondant à nouveau à un écoulement diphasique THI, mais en considérant un niveau de résolution plus élevé, ce qui est approprié pour l'étude des propriétés à micro-échelle de champs scalaires et de turbulence en tenant compte de la couche limite au voisinage des gouttelettes touchées par l'évaporation. La seconde base de données DNS pourrait correspondre à une configuration différente, plus représentative des applications pratiques : il s'agit du développement temporel d'un couche de mélange diphasique. Ensuite, le développement d'un modèle complet pour les fluctuations scalaires en présence d'évaporation peut être envisagé. La conception d'un tel modèle est essentielle pour la description de la combustion en écoulement diphasique turbulent, qui nécessite de décrire le champ de fraction de mélange fluctuant. Les variations de fraction de mélange et le niveau de dissipation associé nécessitent donc une fermeture spécifique. Le niveau de variance de la fraction de mélange apparaît en effet comme une paramétré standard pour estimer les fluctuations non résolues de richesse dans le cadre RANS ou LES. Cela souligne clairement la pertinence de la présente sous-tâche en ce qui concerne les applications de génie des procédés ou de combustion. Dans une première étape, la dérivation de l'équation de transport instantanée du SDR sera revisitée. Il faut en effet souligner que, si certaines dérivations ont déjà été présentées dans la littérature, l'obtention stricte - au sens mathématique - de cette équation transport est loin d'être une tâche évidente et nécessite un soin particulier. Une fois cette question préliminaire mais essentielle résolue, nous procéderons à une analyse détaillée (c'est-à-dire terme par terme) de l'équation de transport correspondante. Par rapport à la situation de référence, c'est-à-dire celle d'un scalaire passif en turbulence incompressible, des déplacements d'équilibre sont attendus : en présence d'évaporation (et selon son intensité), les termes dominants de l'équation de transport ne devraient pas rester associés aux mêmes phénomènes physiques. La possibilité d'obtenir une fermeture algébrique pour le taux de dissipation scalaire moyen sera étudiée. De telles fermetures algébriques sont souvent retenues pour procéder à la simulation numérique des écoulements diphasiques mais les processus d'évaporation devraient influencer la fréquence de mélange, qui est un ingrédient essentiel dans de telles représentations. Dans une seconde étape de cette analyse, une modalisation plus complète de l'équation de transport du SDR moyen, plus générale que les fermetures algébriques, sera tentée.

References

[1] W.T. Ashurst, A.R. Kerstein, R.M. Kerr, and C.H. Gibson. Alignment of vorticity and scalar gradient with strain rate in simulated Navier-Stokes turbulence. *The Physics of Fluids*, 30(8) : 2343–2353, 1987. doi : https://10.1063/1.866513.

[2] T. Aslam. A partial differential equation approach to multidimensional extrapolation. *Journal of Computational Physics*, 193(1) :349 – 355, 2004. ISSN 0021-9991. doi : https://doi.org/10.1016/j.jcp.2003.08.001.

[3] S. Balachandar and J.K. Eaton. Turbulent dispersed multiphase flow. *Annual Review of Fluid Mechanics*, 42(1) :111–133, 2010. doi : 10.1146/annurev.fluid.010908.165243. URL https://doi.org/10.1146/annurev.fluid.010908.165243.

[4] P. Bechlars and R.D. Sandberg. Evolution of the velocity gradient tensor invariant dynamics in a turbulent boundary layer. *Journal of Fluid Mechanics*, 815 :223–242, 2017. doi : 10.1017/jfm.2017.40.

[5] A. Benkenida and J. Magnaudet. Une méthode de simulation d'écoulements diphasiques sans reconstruction d'interfaces. *Comptes Rendus de l'Académie des Sciences - Series IIB - Mechanics-Physics-Astronomy*, 328(1) :25–32, 2000. ISSN 1287-4620. doi : https://doi.org/10.1016/S1287-4620(00)88412-4. URL https://www.sciencedirect.com/science/article/pii/S1287462000884124.

[6] Z. Bouali, B. Duret, F.X. Demoulin, and A. Mura. DNS analysis of small-scale turbulence-scalar interactions in evaporating two-phase flows. *International Journal of Multiphase Flow*, 85 :326 – 335, 2016. doi : https://doi.org/10.1016/j.ijmultiphaseflow.2016.06.020.

[7] Z Bouali, A Mura, and J Reveillon. 8. liquid fuel combustion. *Advanced Turbulent Combustion Physics and Applications*, page 328, 2021.

[8] R. Boukharfane, Z. Bouali, and A. Mura. Evolution of scalar and velocity dynamics in planar shock-turbulence interaction. *Shock Waves*, 28(6) :1117–1141, 2018. ISSN 1432-2153. doi : 10.1007/s00193-017-0798-5.

[9] R. Buttay, G. Lehnasch, and A. Mura. Analysis of small-scale scalar mixing processes in highly under-expanded jets. *Shock Waves*, 26 :193–212, 2016. doi : 10.1007/s00193-015-0599-7.

[10] J.W. Cahn and J.E. Hilliard. Free energy of a nonuniform system. iii. nucleation in a two-component incompressible fluid. *The Journal of Chemical Physics*, 31(3) :688–699, 1959. doi : 10.1063/1.1730447. URL https://doi.org/10.1063/1.1730447.

[11] B.J. Cantwell. Exact solution of a restricted euler equation for the velocity gradient tensor. *The Physics of Fluids*, 4(4) :782–793, 1992. doi : 10.1063/1.858295. URL https://doi.org/10.1063/1.858295.

[12] N. Chakraborty, M. Champion, A. Mura, and N. Swaminathan. *Scalar dissipation rate approach*, pages 74–102. Cambridge University Press, Cambridge, 2011.

[13] R. Chein and J.N. Chung. Effects of vortex pairing on particle dispersion in turbulent shear flows. *International Journal of Multiphase Flow*, 13(6) :785–802, 1987. ISSN 0301-9322. doi : https://doi.org/10.1016/0301-9322(87)90066-8. URL https://www.sciencedirect.com/science/article/pii/0301932287900668.

[14] M. Chertkov, G. Falkovich, I. Kolokolov, and V. Lebedev. Statistics of a passive scalar advected by a large-scale two-dimensional velocity field : Analytic solution. *Physical Review E*, 51 : 5609–5627, Jun 1995. doi : 10.1103/PhysRevE.51.5609. URL https://link.aps.org/doi/10.1103/PhysRevE.51.5609.

[15] P.H. Chiu, R.K. Lin, and T.W.H. Sheu. A differentially interpolated direct forcing immersed boundary method for predicting incompressible Navier-Stokes equations in time-varying complex geometries. *Journal of Computational Physics*, 229(12) :4476 – 4500, 2010. ISSN 0021-9991. doi : https://doi.org/10.1016/j.jcp.2010.02.013.

[16] K.S. Choi and J.L. Lumley. The return to isotropy of homogeneous turbulence. *Journal of Fluid Mechanics*, 436 :59–84, 2001. doi : 10.1017/S002211200100386X.

[17] M.S. Chong, A.E. Perry, and B.J. Cantwell. A general classification of three-dimensional flow fields. *The Physics of Fluids*, 2 :765–777, 1990. doi : 10.1063/1.857730.

[18] M.S. Chong, J. Soria, A.E. Perry, J. Chacin, B.J. Cantwell, and Y. Na. Turbulence structures of wall-bounded shear flows found using DNS data. *Journal of Fluid Mechanics*, 357 :225–247, 1998.

[19] L. Cifuentes, C. Dopazo, J. Martin, and C. Jimenez. Local flow topologies and scalar structures in a turbulent premixed flame. *The Physics of Fluids*, 26 :065108, 2014. doi : 10.1063/1.4884555.

[20] D. Coles and E. Hirst. Proceedings : Computation of turbulent boundary layers - 1968 afosr-ifp-stanford conference, stanford univ., calif., 19-24 august 1968. volume ii. compiled data. 1968.

[21] P. Constantin. Geometric statistics in turbulence. *SIAM Review*, 36(1) :73–98, 1994. ISSN 00361445. URL http://www.jstor.org/stable/2132562.

[22] J.W. Deardorff. A numerical study of three-dimensional turbulent channel flow at large reynolds numbers. *Journal of Fluid Mechanics*, 41(2) :453–480, 1970. doi : 10.1017/S0022112070000691.

[23] M.S. Dodd and L. Jofre. Small-scale flow topologies in decaying isotropic turbulence laden with finite-size droplets. *Physical Review Fluids*, 4 :064303, 2019. doi : 10.1103/PhysRevFluids.4.064303.

[24] G.F. Douglas and K.L. Douglas. Numerical simulation of turbulent flows. *Reviews of Geophysics*, 10(1) :51–72, 1972. doi : 10.1029/RG010i001p00051. URL https://agupubs.onlinelibrary.wiley.com/doi/abs/10.1029/RG010i001p00051.

[25] B. Duret. *Simulation numérique directe des écoulements liquide-gaz avec évaporation : application à l'atomisation*. PhD thesis, 2013. URL http://www.theses.fr/2013ISAM0031. Thèse de doctorat dirigée par Demoulin, François-Xavier et Reveillon, Julien Physique Rouen, INSA 2013.

[26] B. Duret, G. Luret, J. Reveillon, T. Ménard, A. Berlemont, and F.X. Demoulin. DNS analysis of turbulent mixing in two-phase flows. *International Journal of Multiphase Flow*, 40 :93 – 105, 2012. ISSN 0301-9322. doi : https://doi.org/10.1016/j.ijmultiphaseflow.2011.11.014.

[27] C. Eckart. An analysis of stirring and mixing processes in incompressible fluids. *Journal of Marine Research*, 7 :265–275, 1948. URL https://images.peabody.yale.edu/publications/jmr/jmr07-03-11.pdf.

[28] S. Elghobashi. Direct numerical simulation of turbulent flows laden with droplets or bubbles. *Annual Review of Fluid Mechanics*, 51(1) :217–244, 2019. doi : 10.1146/annurev-fluid-010518-040401. URL https://doi.org/10.1146/annurev-fluid-010518-040401.

[29] S. Elghobashi and G.C. Truesdell. On the two-way interaction between homogeneous turbulence and dispersed solid particles. i : Turbulence modification. *The Physics of Fluids*, 5(7) :1790–1801, 1993. doi : 10.1063/1.858854. URL https://doi.org/10.1063/1.858854.

[30] J.L. Estivalezes. Une formulation conservative du schéma weno pour améliorer la résolution de la méthode level set. Technical report, Communication interne, ONERA Toulouse, 2002.

[31] G.M. Faeth. Current status of droplet and liquid combustion. *Progress in Energy and Combustion Science*, 3(4) :191 – 224, 1977. ISSN 0360-1285. doi : https://doi.org/10.1016/0360-1285(77)90012-0. URL http://www.sciencedirect.com/science/article/pii/0360128577900120.

[32] G.M. Faeth. Spray combustion phenomena. *Symposium (International) on Combustion*, 26(1) :1593 – 1612, 1996. ISSN 0082-0784. doi : https://doi.org/10.1016/S0082-0784(96)80383-3. URL http://www.sciencedirect.com/science/article/pii/S0082078496803833.

[33] R.P. Fedkiw, T. Aslam, B. Merriman, and S. Osher. A non-oscillatory eulerian approach to interfaces in multimaterial flows (the ghost fluid method). *Journal of Computational Physics*, 152(2) :457–492, 1999. ISSN 0021-9991. doi : https://doi.org/10.1006/jcph.1999.6236. URL https://www.sciencedirect.com/science/article/pii/S0021999199962368.

[34] J.R. Fessler, J.D. Kulick, and J.K. Eaton. Preferential concentration of heavy particles in a turbulent channel flow. *The Physics of Fluids*, 6(11) :3742–3749, 1994. doi : 10.1063/1.868445. URL https://doi.org/10.1063/1.868445.

[35] U. Frisch. *Turbulence : The Legacy of A. N. Kolmogorov*. Cambridge University Press, 1995. doi : 10.1017/CBO9781139170666.

[36] K. Gawcedzki and A. Kupiainen. Anomalous scaling of the passive scalar. *Physical Review Letters*, 75 :3834–3837, Nov 1995. doi : 10.1103/PhysRevLett.75.3834. URL https://link.aps.org/doi/10.1103/PhysRevLett.75.3834.

[37] L. Germes Martinez, B. Duret, J. Reveillon, and F.X. Demoulin. A new dns formalism dedicated to turbulent two-phase flows with phase change. *International Journal of Multiphase Flow*, 143 :

103762, 2021. ISSN 0301-9322. doi : https://doi.org/10.1016/j.ijmultiphaseflow.2021.103762. URL https://www.sciencedirect.com/science/article/pii/S0301932221002020.

[38] C.H. Gibson. Fine structure of scalar fields mixed by turbulence. I. Zero-gradient points and minimal gradient surfaces. *The Physics of Fluids*, 11 :2305–2315, 1968. doi : 10.1063/1.1691820.

[39] S.S. Girimaji and S.B. Pope. Propagating surfaces in isotropic turbulence. *Journal of Fluid Mechanics*, 234 :247–277, 1992. doi : 10.1017/S0022112092000776.

[40] L. Gomet, V. Robin, and A. Mura. Influence of residence and scalar mixing time scales in non-premixed combustion in supersonic turbulent flows. *Combustion Science and Technology*, 184(10-11) :1471–1501, 2012. doi : 10.1080/00102202.2012.690259.

[41] M. Gonzalez and P. Paranthoen. Influence of vorticity alignment upon scalar gradient production in three-dimensional, isotropic turbulence. *Journal of Physics : Conference Series*, 318(5) :052041, dec 2011. doi : 10.1088/1742-6596/318/5/052041.

[42] M. Gorokhovski and M. Herrmann. Modeling primary atomization. *Annual Review of Fluid Mechanics*, 40(1) :343–366, 2008. doi : 10.1146/annurev.fluid.40.111406.102200. URL https://doi.org/10.1146/annurev.fluid.40.111406.102200.

[43] J. Guang-Shan and S. Chi-Wang. Efficient implementation of weighted eno schemes. *Journal of Computational Physics*, 126(1) :202–228, 1996. ISSN 0021-9991. doi : https://doi.org/10.1006/jcph.1996.0130. URL https://www.sciencedirect.com/science/article/pii/S0021999196901308.

[44] D. Gueyffier, J. Li, A. Nadim, R. Scardovelli, and S. Zaleski. Volume-of-fluid interface tracking with smoothed surface stress methods for three-dimensional flows. *Journal of Computational Physics*, 152(2) :423–456, 1999. ISSN 0021-9991. doi : https://doi.org/10.1006/jcph.1998.6168. URL https://www.sciencedirect.com/science/article/pii/S002199919896168X.

[45] P.E. Hamlington, J. Schumacher, and W.J.A. Dahm. Direct assessment of vorticity alignment with local and non-local strain rates in turbulent flows. *The Physics of Fluids*, 20(11) :111703, 2008. doi : 10.1063/1.3021055.

[46] D.F. Harris. The pioneer in the hygiene of ventilation. *The Lancet*, 176(4542) :906 – 908, 1910. ISSN 0140-6736. doi : https://doi.org/10.1016/S0140-6736(00)52420-9. URL http://www.sciencedirect.com/science/article/pii/S0140673600524209. Originally published as Volume 2, Issue 4542.

[47] J. Hasslberger, S. Ketterl, M. Klein, and N. Chakraborty. Flow topologies in primary atomization of liquid jets : a direct numerical simulation analysis. *Journal of Fluid Mechanics*, 859 :819–838, 2019. doi : 10.1017/jfm.2018.845.

[48] M. Holzer and E.D. Siggia. Turbulent mixing of a passive scalar. *The Physics of Fluids*, 6(5) : 1820–1837, 1994. doi : 10.1063/1.868243.

[49] I. Iliopoulos and T.J. Hanratty. A non-gaussian stochastic model to describe passive tracer dispersion and its comparison to a direct numerical simulation. *The Physics of Fluids*, 16(8) : 3006–3030, 2004. doi : 10.1063/1.1760770. URL https://doi.org/10.1063/1.1760770.

[50] F.A. Jaberi, R.S. Miller, C.K. Madnia, and P. Givi. Non-gaussian scalar statistics in homogeneous turbulence. *Journal of Fluid Mechanics*, 313 :241–282, 1996. doi : 10.1017/S0022112096002200.

[51] D. Jacqmin. Calculation of two-phase navier–stokes flows using phase-field modeling. *Journal of Computational Physics*, 155(1) :96–127, 1999. ISSN 0021-9991. doi : https://doi.org/10.1006/jcph.1999.6332. URL https://www.sciencedirect.com/science/article/pii/S0021999199963325.

[52] P. Jenny, D. Roekaerts, and N. Beishuizen. Modeling of turbulent dilute spray combustion. *Progress in Energy and Combustion Science*, 38(6) :846 – 887, 2012. ISSN 0360-1285. doi : https://doi.org/10.1016/j.pecs.2012.07.001. URL http://www.sciencedirect.com/science/article/pii/S0360128512000445.

[53] A. Juneja and S.B. Pope. A dns study of turbulent mixing of two passive scalars. *The Physics of Fluids*, 8(8) :2161–2184, 1996. doi : 10.1063/1.868990. URL https://doi.org/10.1063/1.868990.

[54] S. Junji. Recent advances in computational modeling of primary atomization of liquid fuel sprays. *Energies*, 11(11), 2018. ISSN 1996-1073. doi : 10.3390/en11112971. URL https://www.mdpi.com/1996-1073/11/11/2971.

[55] A. Kalyan and R. William. Interactive processes in gasification and combustion. part i : Liquid drop arrays and clouds. *Progress in Energy and Combustion Science*, 18(3) :221–295, 1992.

ISSN 0360-1285. doi : https://doi.org/10.1016/0360-1285(92)90012-P. URL https://www.sciencedirect.com/science/article/pii/036012859290012P.

[56] R.E. Kohler. The origin of lavoisier's first experiments on combustion. *Isis*, 63(3) :349–355, 1972. ISSN 00211753, 15456994. URL http://www.jstor.org/stable/229275.

[57] B. Lafaurie, C. Nardone, R. Scardovelli, S. Zaleski, and G. Zanetti. Modelling merging and fragmentation in multiphase flows with surfer. *Journal of computational physics (Print)*, 1994. ISSN 0021-9991.

[58] R. Lebas, T. Ménard, P.A. Beau, A. Berlemont, and F.X. Demoulin. Numerical simulation of primary break-up and atomization : DNS and modelling study. *International Journal of Multiphase Flow*, 35(3) :247 – 260, 2009. ISSN 0301-9322. doi : https://doi.org/10.1016/j.ijmultiphaseflow.2008.11.005.

[59] X.D. Liu, R.P. Fedkiw, and M. Kang. A boundary condition capturing method for Poisson's equation on irregular domains. *Journal of Computational Physics*, 160(1) :151 – 178, 2000. ISSN 0021-9991. doi : https://doi.org/10.1006/jcph.2000.6444.

[60] J.L. Lumley. Computational modeling of turbulent flows. 18 :123 – 176, 1979. ISSN 0065-2156. doi : https://doi.org/10.1016/S0065-2156(08)70266-7.

[61] J.L. Lumley and G.R. Newman. The return to isotropy of homogeneous turbulence. *Journal of Fluid Mechanics*, 82(1) :161–178, 1977. doi : 10.1017/S0022112077000585.

[62] A.J. Majda and L. Bertozzi. *Vorticity and Incompressible Flow*. Cambridge Texts in Applied Mathematics, 2001.

[63] J. Martin, A. Ooi, M.S. Chong, and J. Soria. Dynamics of the velocity gradient tensor invariants in isotropic turbulence. *The Physics of Fluids*, pages 2336 – 2346, 1998. ISSN 1089-7666.

[64] A. Mura and S. Zhao. Turbulence topology evolution in weakly turbulent premixed flames. *Physics of Fluids (2021, in press)*.

[65] A. Mura, K. Tsuboi, and T. Hasegawa. Modelling of the correlation between velocity and reactive scalar gradients in turbulent premixed flames based on DNS data. *Combustion Theory and Modelling*, 12 :671–698, 2008.

[66] T. Ménard. *Développement d'une méthode Level Set pour le suivi d'interface. Applications de la rupture de jet liquide*. Theses, Université de Rouen, 2007.

[67] T. Ménard, S. Tanguy, and A. Berlemont. Coupling level set/VOF/ghost fluid methods : validation and application to 3D simulation of the primary break-up of a liquid jet. *International Journal of Multiphase Flow*, 33(5) :510 – 524, 2007. ISSN 0301-9322. doi : https://doi.org/10.1016/j.ijmultiphaseflow.2006.11.001.

[68] L.R.C. NASA. Compressible turbulent boundary layers ; a symposium held at langley research center, hampton, virginia, december 10-11, 1968. 1968.

[69] W.F. Noh and P. Woodward. Slic (simple line interface calculation). In Adriaan I. van de Vooren and Pieter J. Zandbergen, editors, *Proceedings of the Fifth International Conference on Numerical Methods in Fluid Dynamics June 28 – July 2, 1976 Twente University, Enschede*, pages 330–340, Berlin, Heidelberg, 1976. Springer Berlin Heidelberg. ISBN 978-3-540-37548-7.

[70] K. Ohkitani. Eigenvalue problems in three-dimensional euler flows. *The Physics of Fluids*, 5(10) : 2570–2572, 1993. doi : 10.1063/1.858772. URL https://doi.org/10.1063/1.858772.

[71] K. Ohkitani. A miscellany of basic issues on incompressible fluid equations. *Nonlinearity*, 21 (12) :T255–T271, nov 2008. doi : 10.1088/0951-7715/21/12/t02. URL https://doi.org/10.1088/0951-7715/21/12/t02.

[72] K. Ohkitani and S. Kishiba. Nonlocal nature of vortex stretching in an inviscid fluid. *The Physics of Fluids*, 7(2) :411–421, 1995. doi : 10.1063/1.868638. URL https://doi.org/10.1063/1.868638.

[73] A. Ooi, J. Martin, J. Soria, and M.S. Chong. A study of the evolution and characteristics of the invariants of the velocity-gradient tensor in isotropic turbulence. *Journal of Fluid Mechanics*, 381 :141–174, 1999. doi : 10.1017/S0022112098003681.

[74] S. Osher and R.P. Fedkiw. Level set methods : an overview and some recent results. *Journal of Computational Physics*, 169(2) :463 – 502, 2001. ISSN 0021-9991. doi : https://doi.org/10.1006/jcph.2000.6636.

[75] S. Osher and J.A. Sethian. Fronts propagating with curvature-dependent speed : algorithms based on hamilton-jacobi formulations. *Journal of computational physics (Print)*, 1988. ISSN 0021-9991.

[76] M.R. Overholt and S.B. Pope. Direct numerical simulation of a passive scalar with imposed mean gradient in isotropic turbulence. *The Physics of Fluids*, 8(11) :3128–3148, 1996. doi : 10.1063/1.869099. URL https://doi.org/10.1063/1.869099.

[77] A.E. Perry and M.S. Chong. A description of eddying motions and flow patterns using critical-point concepts. *Annual Review of Fluid Mechanics*, 19(1) :125–155, 1987. doi : 10.1146/annurev.fl.19.010187.001013.

[78] C.S. Peskin. *Flow patterns around heart valves : a digital computer method for solving the equations of motion*. Theses, Albert Einstein Coll. Med., Univ. Microfilms, 1972. URL https://hdl.handle.net/20.500.12202/2090.

[79] S. Pirozzoli and F. Grasso. Direct numerical simulations of isotropic compressible turbulence : Influence of compressibility on dynamics and structures. *The Physics of Fluids*, 16(12) : 4386–4407, 2004.

[80] L. Prandtl. Über die ausgebildete turbulenz. *Journal of Applied Mathematics and Mechanics*, pages 136–139, 1925. doi : https://doi.org/10.1007/978-3-662-11836-8_60.

[81] E.G. Puckett, A.S. Almgren, J.B. Bell, D.L. Marcus, and W.J. Rider. A high-order projection method for tracking fluid interfaces in variable density incompressible flows. *Journal of Computational Physics*, 130(2) :269–282, 1997. ISSN 0021-9991. doi : https://doi.org/10.1006/jcph.1996.5590. URL https://www.sciencedirect.com/science/article/pii/S0021999196955904.

[82] A. Pumir. A numerical study of the mixing of a passive scalar in three dimensions in the presence of a mean gradient. *The Physics of Fluids*, 6(6) :2118–2132, 1994. doi : 10.1063/1.868216.

[83] J. Reveillon and F.X. Demoulin. Evaporating droplets in turbulent reacting flows. *Proceedings of the Combustion Institute*, 31(2) :2319–2326, 2007. ISSN 1540-7489. doi : https://doi.org/10.1016/j.proci.2006.07.114. URL https://www.sciencedirect.com/science/article/pii/S1540748906001222.

[84] G.R. Ruetsch and M.R. Maxey. Small-scale features of vorticity and passive scalar fields in homogeneous isotropic turbulence. *The Physics of Fluids*, 3 :1587–1597, 1991.

[85] J. Ryu and D. Livescu. Turbulence structure behind the shock in canonical shock-vortical turbulence interaction. *Journal of Fluid Mechanics*, 756 :R1–1–R1–12, 2014.

[86] F. Sass. *Geschichte des Deutschen Verbrennungsmotorenbaues*. Springer-Verlag Berlin Heidelberg, 1962. ISBN 978-3-662-11842-9. doi : 10.1007/978-3-662-11842-9.

[87] R. Scardovelli and S. Zaleski. Direct numerical simulation of free-surface and interfacial flow. *Annual Review of Fluid Mechanics*, 31(1) :567–603, 1999. doi : 10.1146/annurev.fluid.31.1.567. URL https://doi.org/10.1146/annurev.fluid.31.1.567.

[88] X. Shan and H. Chen. Lattice boltzmann model for simulating flows with multiple phases and components. *Physical Review E*, 47 :1815–1819, Mar 1993. doi : 10.1103/PhysRevE.47.1815. URL https://link.aps.org/doi/10.1103/PhysRevE.47.1815.

[89] H.H. Shen, A.H.D. Cheng, K.H. Wang, M.H. Teng, and C.C.K. Liu. *Environmental Fluid Mechanics : Theories and Applications*. American Society of Civil Engineers, 2002. ISBN 97807844475218.

[90] W. Sirignano. Fluid dynamics and transport of droplets and sprays second edition. 1999.

[91] J. Smagorinsky. General Circulation Experiments with the Primitive Equations : I. The basic Experiment*. *Monthly Weather Review*, 91(3) :99–164, 03 1963. ISSN 0027-0644. doi : 10.1175/1520-0493(1963)091<0099:GCEWTP>2.3.CO;2. URL https://doi.org/10.1175/1520-0493(1963)091<0099:GCEWTP>2.3.CO;2.

[92] J. Soria, R. Sondergaard, B.J. Cantwell, M.S. Chong, and A.E. Perry. A study of the fine-scale motions of incompressible time-developing mixing layers. *The Physics of Fluids*, 6(2) :871–884, 1994.

[93] A.V. Spandan, V. Meschini, R. Ostilla-Mónico, D. Lohse, G. Querzoli, M.D. de Tullio, and R. Verzicco. A parallel interaction potential approach coupled with the immersed boundary method for fully resolved simulations of deformable interfaces and membranes. *Journal of computational physics*, 348 :567–590, o 2017. ISSN 0021-9991. doi : 10.1016/j.jcp.2017.07.036.

[94] A.V. Spandan, R. Verzicco, and D. Lohse. Deformable ellipsoidal bubbles in taylor-couette flow with enhanced euler-lagrangian tracking. *Physical Review Fluids*, 2 :104304, Oct 2017. doi : 10.1103/PhysRevFluids.2.104304. URL https://link.aps.org/doi/10.1103/PhysRevFluids.2.104304.

[95] K.R. Sreenivasan. On local isotropy of passive scalars in turbulent shear flows. *Proceedings : Mathematical and Physical Sciences*, 434(1890) :165–182, 1991. ISSN 09628444. URL http://www.jstor.org/stable/51992.

[96] K.R. Sreenivasan and R.A. Antonia. The phenomenology of small-scale turbulence. *Annual Review of Fluid Mechanics*, 29(1) :435–472, 1997. doi : 10.1146/annurev.fluid.29.1.435. URL https://doi.org/10.1146/annurev.fluid.29.1.435.

[97] M. Sussman and E.G. Puckett. A coupled level set and volume-of-fluid method for computing 3D and axisymmetric incompressible two-phase flows. *Journal of Computational Physics*, 162 (2) :301 – 337, 2000. ISSN 0021-9991. doi : https://doi.org/10.1006/jcph.2000.6537.

[98] M. Sussman, P. Smereka, and S. Osher. A level set approach for computing solutions to incompressible two-phase flow. *Journal of Computational Physics; (United States)*, 114 :1, 9 1994. ISSN 0021-9991. doi : 10.1006/jcph.1994.1155. URL https://www.osti.gov/biblio/7075774.

[99] N. Swaminathan and N. Chakraborty. Influence of the Damköhler number on turbulence-scalar interaction in premixed flames, Part II : model developement. *The Physics of Fluids*, 19 : 045104.1–045104.11, 2007.

[100] S. Tanguy. *Développement d'une méthode de suivi d'interface. Applications aux écoulements diphasiques*. Theses, Université de Rouen, November 2004. URL https://tel.archives-ouvertes.fr/tel-00007613.

[101] Y. Tian, F.A. Jaberi, and D. Livescu. Density effects on post-shock turbulence structure and dynamics. *Journal of Fluid Mechanics*, 880 :935–968, 2019. doi : 10.1017/jfm.2019.707.

[102] Y. Tian, F.A. Jaberi, and D. Livescu. Density effects on post-shock turbulence structure and dynamics. *Journal of Fluid Mechanics*, 880 :935–968, 2019. doi : 10.1017/jfm.2019.707.

[103] G.A. Tokaty. *A History and Philosophy of Fluid Mechanics*. Dover Publications, 2013. ISBN 9780486681030.

[104] A. Tsinober. *An Informal Conceptual Introduction to Turbulence : Second Edition*. Fluid Mechanics and Its Applications. Springer Netherlands, 2009. ISBN 9789048131747.

[105] A. Umemura. Interactive droplet vaporization and combustion : Approach from asymptotics. *Progress in Energy and Combustion Science*, 20(4) :325–372, 1994. ISSN 0360-1285. doi : https://doi.org/10.1016/0360-1285(94)90013-2. URL https://www.sciencedirect.com/science/article/pii/0360128594900132.

[106] S.O. Unverdi and G. Tryggvason. A front-tracking method for viscous, incompressible, multi-fluid flows. *Journal of Computational Physics*, 100(1) :25–37, 1992. ISSN 0021-9991. doi : https://doi.org/10.1016/0021-9991(92)90307-K. URL https://www.sciencedirect.com/science/article/pii/002199919290307K.

[107] P. Vieillefosse. Local interaction between vorticity and shear in a perfect incompressible fluid. *Journal de Physique*, 43 :837–842, 1982.

[108] D.H. Wacks, N. Chakraborty, M. Klein, P.G. Arias, and H.G. Im. Flow topologies in different regimes of premixed turbulent combustion : a direct numerical simulation analysis. *Physical Review Fluids*, 1 :083401, 2016. doi : 10.1103/PhysRevFluids.1.083401.

[109] Z. Warhaft and Jayesh. Probability distribution of a passive scalar in grid-generated turbulence. *Physical Review Letters*, 67 :3503–3506, Dec 1991. doi : 10.1103/PhysRevLett.67.3503. URL https://link.aps.org/doi/10.1103/PhysRevLett.67.3503.

[110] C. Weber. Zum zerfall eines flüssigkeitsstrahles. *ZAMM - Journal of Applied Mathematics and Mechanics / Zeitschrift für Angewandte Mathematik und Mechanik*, 11(2) :136–154, 1931. doi : https://doi.org/10.1002/zamm.19310110207. URL https://onlinelibrary.wiley.com/doi/abs/10.1002/zamm.19310110207.

[111] C.K. Westbrook, W.J. Pitz, M. Mehl, and H.J. Curran. Detailed chemical kinetic reaction mechanisms for primary reference fuels for diesel cetane number and spark-ignition octane number. *Proceedings of the Combustion Institute*, 33(1) :185 – 192, 2011. ISSN 1540-7489. doi : https://doi.org/10.1016/j.proci.2010.05.087. URL http://www.sciencedirect.com/science/article/pii/S1540748910002063.

[112] C. You-Biao and L. Xi-Yun. Topological evolution in compressible turbulent boundary layers. *Journal of Fluid Mechanics*, 733 :414–438, 2013. doi : 10.1017/jfm.2013.399.

[113] L.I. Zaichik and V.A. Pershukov. Influence of particles on the initial stage of homogeneous turbulence degeneration. *Journal of Engineering Physics*, 58(04) :408 – 412, 04 1990. doi : 10.1007/BF00877345. URL https://doi.org/10.1007/BF00877345.

[114] N. Zeoli and S. Gu. Numerical modelling of droplet break-up for gas atomisation. *Computational Materials Science*, 38(2) :282–292, e 2006. ISSN 0927-0256. doi : 10.1016/j.commatsci.2006.02.012.

[115] S. Zhao, A. Er-raiy, Z. Bouali, and A. Mura. Dynamics and kinematics of the reactive scalar gradient in weakly turbulent premixed flames. *Combustion and Flame*, 198 :436 – 454, 2018. ISSN 0010-2180. doi : https://doi.org/10.1016/j.combustflame.2018.10.002.

[116] S. Zhao, Z Bouali, and A Mura. Computational investigation of weakly turbulent flame kernel growths in iso-octane droplet clouds in cvc conditions. *Flow, Turbulence and Combustion*, 104(1) :139 – 177, 2020. ISSN 1573-1987. doi : 10.1007/s10494-019-00051-x. URL https://doi.org/10.1007/s10494-019-00051-x.

Résumé

Dans le cas des écoulements diphasiques, et plus particulièrement dans celui de la combustion diphasique, la représentation des couplages entre mélange turbulent et transfert de masse constitue un enjeu crucial. Les processus correspondants d'évaporation et de mélange (jusqu'aux échelles moléculaires) entre le combustible et l'oxydant constituent en effet une condition préalable au développement éventuel de la réaction chimique. D'un point de vue plus général, l'étude (i) du mélange scalaire en présence d'interfaces — quelle que soit leur nature (flamme mince, onde de choc, interface liquide/gaz ou bien solide/gaz ou encore solide/liquide) — ainsi que (ii) celle de l'influence de ces interfaces sur la topologie de l'écoulement se développant à leur proximité est un domaine de recherche extrêmement actif. Quoique fondamentales les problématiques associées se révèlent essentielles pour les applications pratiques relevant aussi bien de la production d'énergie (et de la propulsion) que de l'astrophysique ... Cette thèse est donc consacrée à améliorer notre compréhension de ces processus de mélange scalaire en écoulements diphasiques turbulents, en s'appuyant sur des simulations numériques directes (DNS) de turbulence diphasique homogène isotrope (TDHI) conduites pour différentes valeurs de la fraction volumique de liquide et de la tension superficielle. Les bases de données numériques sont générées à l'aide d'un code de calcul (ARCHER) qui résout la forme incompressible des équations de Navier-Stokes. Les propriétés eulériennes et lagrangiennes des champs scalaires et de vitesse issues des DNS sont analysées par le biais d'un certain nombre de quantités essentielles telles que les invariants du tenseur des gradients de vitesse, les caractéristiques d'alignement des champs scalaires et de vitesse, la vorticité, l'enstrophie, le taux de dissipation scalaire ...

Mots clés : Écoulement diphasique / Évaporation / Lagrange, Équations de / Navier-Stokes, Équations de / Runge-Kutta, Méthode de / Transfert de masse / Turbulence / Taux de dissipation scalaire / Interaction turbulence-scalaire / Simulation numérique directe (DNS)

Resume

In the case of two-phase flows, and particularly in two-phase flow combustion, the representation of the couplings between turbulent mixing and mass transfer is a crucial issue. The corresponding processes of evaporation and mixing (up to molecular scales) between fuel and oxidizer are indeed a prerequisite for the possible development of the chemical reaction. From a more general point of view, the study of (i) scalar mixing in the presence of interfaces – whatever their nature (thin flame, shock wave, liquid/gas or solid/gas or solid/liquid) – and (ii) the influence of these interfaces on the topology of the flow developing at their location; are two extremely active areas of research. Although fundamental, the associated problems were shown to be essential for practical applications in the fields of power generation (and propulsion) as well as astrophysics ... This thesis is therefore aimed at improving our understanding of these scalar mixing processes in turbulent two-phase flows, based on direct numerical simulations (DNS) of isotropic homogeneous two-phase flow turbulence conducted for different values of liquid volume fraction and surface tension. Numerical databases are generated using a computational code (ARCHER) that solves the incompressible Navier-Stokes equations. The Eulerian and Lagrangian properties of the scalar and velocity fields derived from DNS are analyzed by means of a number of essential quantities such as the invariants of the velocity gradient tensor (VGT), the alignment statistics of the scalar and velocity fields, vorticity, enstrophy, scalar dissipation rate, etc.

Keywords: Two-phase flow / Evaporation / Lagrange equations / Navier-Stokes equations / Runge-Kutta formulas / Mass transfer / Turbulence / Scalar dissipation rate / Turbulence-scalar interaction / Direct numerical simulation (DNS)